2019

Modeling Alzheimer's Disease Using CRISPR/CAS9 Gene Editing and Induced Pluripotent Stem Cells Reveals Conserved Cellular Mechanisms

Dylan Kwart

MODELING ALZHEIMER'S DISEASE USING CRISPR/CAS9 GENE EDITING AND INDUCED PLURIPOTENT STEM CELLS REVEALS CONSERVED CELLULAR MECHANISMS

A Thesis Presented to the Faculty of

The Rockefeller University

in Partial Fulfillment of the Requirements for

The degree of Doctor of Philosophy

by

Dylan Kwart

June 2019

MODELING ALZHEIMER'S DISEASE USING CRISPR/CAS9 GENE EDITING AND INDUCED PLURIPOTENT STEM CELLS REVEALS CONSERVED CELLULAR MECHANISMS

Dylan Kwart, Ph.D.

The Rockefeller University 2019

Alzheimer's disease (AD) is the most common cause of dementia worldwide and a leading cause of death in the United States. Rare cases of autosomal dominant familial AD (fAD) result from genetic mutations in three key genes: amyloid precursor protein (*APP*), and two APP processing-related genes (presenilin-1 (*PSEN1*), and presenilin-2 (*PSEN2*)), supporting the theory that altered APP metabolism is a central cause of AD. However, which product of APP metabolism is causal remains a matter of investigation. A probable source of this lack of understanding stems from the poor disease model systems that have been utilized in the field for many years. Recently, advances in human induced pluripotent stem cell (iPSC) technology has enabled the study of uniquely human diseases, such as AD, in human tissue. However, the inability to precisely and efficiently genetically engineer human iPSCs has limited their use in effectively studying monogenic human diseases like fAD.

In this thesis I first describe my work involved in developing CRISPR/Cas9 gene editing technology for use in human stem cells. Our CRISPR/Cas9-based genome-editing framework allows the selective introduction of mono- and bi-allelic sequence changes, such as single fAD-causing pathogenic mutations, with high efficiency and accuracy. We show that editing accuracy is increased dramatically by incorporating silent CRISPR/Cas-blocking mutations along with pathogenic mutations. As well, by characterizing and exploiting a stereotyped inverse relationship between a mutation's incorporation rate and its distance to the CRISPR/Cas9 cleavage site, we achieve predictable control of zygosity. Homozygous introduction requires using a guide RNA targeting close to the intended mutation, whereas heterozygous introduction can be accomplished by distance-dependent suboptimal mutation incorporation or by using mixed repair templates. Additionally, we establish a method termed "CORRECT" for precise and scarless gene editing. Together, our findings will greatly facilitating the study of human disease and development of more human disease models by enabling efficient introduction of specific sequence changes in human stem cells using CRISPR/Cas9.

In later chapters I discuss how we used our novel CRISPR/Cas9 gene editing framework to investigate in human neurons how *APP* and *PSEN1* mutations may converge in their actions in promoting AD-related phenotypes. We generated a comprehensive panel of isogenic knock-in human iPSCs, which were differentiated into disease-vulnerable cortical neurons. Initial global transcriptomic profiling of

mutant neurons revealed overlapping effects of the mutations on expression of AD-related genes, suggesting an AD gene associated-network effect, as well as endosomal-related genes. Endocytic dysfunction, as measured by enlargement of Rab5+ early endosomes, was found in all *APP* and *PSEN1* pathogenic mutant neurons analyzed. By comparing heterozygous and homozygous cells we found *APP* and *PSEN1* mutations have discordant effects on Aβ production but similar effects on the precursor to Aβ, β-C-terminal fragment of APP (β-CTF), which accumulates in all *APP* and *PSEN1* mutant neurons. Importantly, endosomal dysfunction in these human neurons correlates with endogenous accumulation of β-CTF, and not with longer Aβ peptides, and could be rescued by pharmacological modulation of β-secretase (BACE) but not γ-secretase. These data provide a new piece of evidence for β-CTF being an important common product of APP metabolism that significantly contributes to AD pathology.

In summary, by developing the technology to engineer next-generation human AD model systems using CRISPR/Cas9 and iPSCs, our results not only provide insight into the mechanism by which familial *APP* and *PSEN1* mutations may cause AD, but also provide knowledge that could be critical for the development of novel therapeutics that may help to treat AD.

To everyone ever affected by Alzheimer's Disease.

To all of my family and friends.

To Jerry, my love.

Acknowledgements

The work that will be described in this thesis is a product of many incredibly fruitful collaborations and extensive teamwork. First and foremost, I would like to recognize my thesis advisor, Marc. I would like to thank Marc for all of his support, scientifically and professionally, since the beginning of my rotation in 2013. The amount that I have learned from training with Marc is immense, and these valuable lessons will be carried with me throughout my entire career. I will forever be grateful for your guidance through the unexpected twists and turns that we have endured during my thesis. The scientific rigor and passion that endures in Marc's lab is intoxicating and I could not have asked for a better mentor and lab environment to carry out my PhD work. I also would like to also sincerely thank Olav, our beloved lab manager, who was responsible for making Marc's lab such an incredible place to work, and providing invaluable guidance, especially in the past year of my studies.

I would especially like to acknowledge one of Marc's former postdocs, and now friend and colleague of mine, Dominik. In the first year of my PhD Dominik taught me everything about how to work with iPSCs, which, as we learned together is not an easy system. After initially training with Dominik during my rotation, our work turned into an incredible lasting collaboration, from which multiple exciting discoveries were made and papers published. Dominik, thank you for being an incredible partner in crime, I have learned a lot from your scientific passion and rigor. The work that will be described in Chapters II and III are the product of years' worth

of collaboration with Dominik. More recently I have had the absolute pleasure of working closely with Andy, another student in our lab. I'm grateful that our projects became interconnected, as it has made our science stronger and more captivating. All of the work presented in Chapter IV pertaining to *PSEN1* mutant iPSCs was done in close collaboration with Andy. Andy, working with you has been easy and fun, a testament to our friendship. I look forward to seeing how the story evolves further. In addition to working with Dominik and Andy, "team iPS" was upheld by two incredibly motivated technicians, Mike and Antonia. Mike, Antonia, I am forever to your commitments to the projects we worked on and I look forward to continue working together soon!

I would also like to acknowledge other members of Marc's lab, who provided friendship and support throughout the past several years. Shaun, Deanna, Eliza, Ross and Jason, being able to talk and advise each other on our science and our lives is something I'm thankful for. Additionally, I would like to also thank Kim, Dave, Zhuhao, Nick, Yuya and Nico, for your help and support during our overlapping times here at Rockefeller.

There are many members of the lab who also made significant contributions to the work presented in this thesis. As I already mentioned, all of the work presented in Chapters II and III was done in close collaboration with Dominik Paquet. All of the work presented in Chapter IV was done in close collaboration with Andrew Gregg, who spearheaded much of the *PSEN1* gene editing and early

phenotypic analysis. Shaun Teo did an incredible amount of work in helping analyze CRISPR-editing outcomes using deep-sequencing and bioinformatics (shown in Chapter II), and Kim Olsen performed electrophysiological characterization of our iPSC-derived neurons (Appendix I). In addition, I would like to acknowledge our collaborators at the New York Stem Cell Foundation (Andrew Sproul and Scott Noggle) who helped us generate and characterize the iPSC line used in this thesis (characterization presented in Appendix I). I would also like to thank Dr. Yueming Li for generously providing us with γ-secretase modulators.

Part of my more recent work has also been the product of a fruitful collaboration with members of Bob Darnell's lab. I would like to thank Claudia Scheckel for setting up this valuable project together. My thesis would not be what it is today without your hard work and close collaboration. I would also like to thank Elisabeth Murphey, who has provided invaluable help in more recent data analyses. Claudia and Elisabeth, I value all of your contributions and your friendship. The work done by Claudia and Elisabeth is described in Chapter IV.

Thank you to my thesis committee members, Shai Shaham, Sandy Simon and Sid Strickland. Your support, guidance and insight as my project has evolved will always be cherished. Sid, ever since joining your lab as a summer student in 2010, I knew I wanted to carry out my PhD thesis work at Rockefeller. I thank you Sid for your unwavering support ever since we met when I was a SURF student.

Importantly I would also like to extend my thanks to everyone at the Dean's office. It has been a pleasure to get to work with you ever since I was a SURF student in 2010. You all make doing a PhD at Rockefeller the best experience anyone could ask for. Thank you so much for that.

Notably, I'd like to thank the many resource center staff members here at Rockefeller, who are technically responsible for making a lot of this thesis work possible. At the FCRC, I would like to thank Svetlana and staff; at the genomics core I would like to thank Connie, at the Translational Research Core I would like to thank Juana, and at BIRC I would like to thank Alison. I have learned so much from you all and I am so grateful for your commitment and expertise.

I would like to also thank all of my family and friends, at home in Toronto and here in NYC. Your love and support has made doing 6 years of hard work possible. I will forever be thankful for all of you. I love each and every one of you!

Lastly, I'd like to thank my partner, Jerry. As you know, the rollercoaster ride that is a PhD has brought a multitude of ups and downs. Your love and support has made doing this all possible. Thank you for always saying the right thing, taking care of me when the stress is high, and always being so loving. You put everything into perspective and always keep me moving forward. I'll never be able to thank you enough. I cannot wait for the next chapter of our lives to begin!

Table of Contents

List of Figures

List of Tables

List of Abbreviations

3x-Tg	Triple-transgenic mouse
Aβ	Amyloid-β
AD	Alzheimer's disease
AICD	APP intracellular domain
Aph1	Anterior Pharynx 1
APOE	Apolipoprotein E
APP	Amyloid Precursor Protein
APPswe	APP Swedish mutation
β-CTF	α-C-terminal fragment of APP
α-CTF	β-C-terminal fragment of APP
BACE	β-secretase
CAA	Cerebral amyloid angiopathy
CRISPR	Clustered regularly interspaced short palindromic repeat
dAP	*Swe/M146V* double mutant iPSC line
DE	Differentially expressed
DIV	Day in vitro
DS	Downs Syndrome
DSB	Double stranded break
ECL	Electrochemiluminescent
FACS	Fluorescence activated cell sorting
fAD	Familial Alzheimer's disease
FTD	Frontotemporal dementia
gDNA	Genomic DNA
GFP	Green Fluorescent Protein
GWAS	Genome-wide association studies
HDR	Homology directed repair
HEK293T	Human Embryonic Kidney 293T cell line
Indel	Insertion or deletion
iPSC	Induced pluripotent stem cell
MAP	Microtubule Associated Proteins
MAPT	Microtubule Associated Protein Tau
MEF	Mouse embryonic fibroblast
NCT	Nicastrin
NEHJ	Non-homologus end joining

NFT	Neurofibrillary tangle
NPC	Neural precursor cell
PAM	Proto-spacer adjacent motif
PCR	Polymerase chain reaction
PEN2	Presenilin Enhancer 2
PSEN2	Presenilin-2
PSEN1	Presenilin-1
RFLP	Restriction fragment length polymorphism
sAD	Sporadic AD
sAPPβ	Soluble APPβ
sAPPα	Soluble APPα
sgRNA	Single guide RNA
ssODN	Single stranded oligo DNA nucleotide
TALEN	Transcription activator-like effector nuclease

CHAPTER I: INTRODUCTION

Rationale for thesis work

Ever since the German physician Alois Alzheimer discovered abnormal deposits in the brain of a 51year-old patient suffering from memory impairments in 1906 (Alzheimer, 1916; Alzheimer et al., 1995), the effort to better understand and treat what we now know as Alzheimer's disease (AD) has endured. More than one century later, and after years of research into the basic biological mechanisms underlying AD, researchers are still hard at work trying to discover a cure for this unthinkably devastating disease. The lack of any effective AD therapeutics underscores the underlying complexities of the disease and indicates that new and improved ways of studying AD may be invaluable to the field.

AD is currently defined by the presence of two key neuropathological findings, extracellular plaques composed of amyloid-beta (Aβ) (Tanzi et al., 1987), and intracellular neurofibrillary tangles (NFTs) composed of hyperphosphorylated tau (Grundke-Iqbal et al., 1986; Wischik et al., 1988). While the majority of AD cases occur sporadically (sAD), genetic studies have demonstrated that single mutations in either the amyloid precursor protein (*APP*) gene, or presenilin genes (*PSEN1* and *PSEN2*), are sufficient to cause a rare, early-onset, familial form of AD (fAD) (Alzheimer's Disease Collaborative Group, 1995; Goate et al., 1991; Levy-Lahad et al., 1995; Rogaev et al., 1995; Schellenberg et al., 1992; St George-Hyslop et al., 1992; Van Broeckhoven et al., 1992). These genetic findings, along with the

discovery that presenilins form the catalytic component of the γ-secretase complex responsible for cleaving APP and generating Aβ, implies that APP metabolism is essential to AD pathogenesis (De Strooper et al., 1998; Goldgaber et al., 1987; Kang et al., 1987; St George-Hyslop et al., 1987; Tanzi et al., 1987). As a result, the leading theory of AD pathogenesis is known as the "amyloid cascade hypothesis", which places extracellular Aβ as the most upstream trigger of neurodegenerative processes in the disease (Hardy and Higgins, 1992; Hardy, 2006).

To date, more than 200 fAD mutations in *APP*, *PSEN1* and *PSEN2* have been described, and while the effects of many of these mutations on Aβ production have been studied extensively, a common unifying mechanism describing how these mutations lead to the development of AD has yet to be determined (Barber, 2012). Confounding many of these early studies is their use of non-human and/or non-neuronal cellular systems that rely on massive overexpression of AD-associated proteins, typically in rodent models (Götz and Ittner, 2008). Moreover, these widely used non-physiological models fail to adequately recapitulate all known human AD hallmark pathologies, and therefore may limit the discovery of effective AD therapeutics. Generation of a physiologically relevant human neuronal model system may be the key to unlocking future discoveries of basic disease mechanisms and novel therapeutic targets. This thesis describes an effort to develop gene editing and human stem cell technologies, and ultimately implement these tools to better understand common disease mechanisms underlying AD caused by fAD mutations.

Epidemiology and clinical manifestation of AD

AD is classified as a type of neurodegenerative dementia, which is a broad description of a family of brain disorders that cause chronic and gradual loss of memory, language, problem solving skills and executive functioning. Ultimately, the disease culminates in a loss of ability to perform everyday activities as well as a loss of one's independence (Alzheimer's Association, 2017). AD comprises approximately 60-70% of all dementias, making it the most common type of neurodegenerative disease, affecting over 5 million people in the US and more than 40 million people worldwide (Alzheimer's Association, 2017; Scheltens et al., 2016). The primary risk factor for AD is aging, as epidemiological studies have shown that the risk of developing AD approximately doubles every five years after the age of 65 (Alzheimer's Association, 2017). Prevalence of AD correlates with population lifespan and as global population demographics change in the coming decades, the number of cases of AD worldwide is also expected to dramatically shift. Specifically, it is estimated that today approximately 5.7 million Americans are living with AD, however with predicted future population aging, this number is expected to triple by 2050 (Alzheimer's Association, 2017).

AD is the only one of the top 10 leading causes of death that cannot be prevented, cured or slowed (Alzheimer's Association, 2017). Between years 2000 and 2015 the number of deaths known to be associated with AD has increased 125 percent, while deaths due to the most common cause of death (heart disease) has significantly decreased (Alzheimer's Association, 2017). The lifetime cost of care

for an individual living with AD dementia is estimated to be over $300,000, and it is expected that in the US the total payments in 2018 for all individuals with AD is more than 250 billion dollars. Therefore, if no effective therapies are discovered, the financial burden of AD will increase to a projected 1.1 trillion dollars by 2050 (Alzheimer's Association, 2017).

Clinically, symptoms may present differently amongst patients with AD. Early in AD progression individuals are often able to function independently. However, in more moderate and severe stages of AD individuals may become frequently confused about where they are, have personality and behavioral changes, and ultimately require assistance in basic activities of daily living and may lose their ability to communicate (Alzheimer's Association, 2017). Once the AD progresses to the latest stages, brain regions involved in motor control and other basic bodily functions become affected, ultimately impairing movement and requiring the patient to be cared for full-time or hospitalized. Lung infection (aspiration pneumonia) is a common concomitant issue in late stage AD, contributing to death in many cases (Alzheimer's Association, 2017).

Diagnosis of AD is not straightforward, as many presenting symptoms overlap with other dementias of a different cause. Therefore, diagnosing AD requires careful examination obtaining family medical records, patient reporting, cognitive testing, blood testing to rule out other potential causes of dementia, and, in more recent years, brain imaging for Aβ or tau (Alzheimer's Association, 2017). Despite these improved methods of clinical examination, bona fide AD can only be fully diagnosed

upon autopsy and identification of hallmark AD neuropathological features. In the future, with the development of biomarkers, revised strategies to diagnose AD early are anticipated. While this improvement in no way offsets the demand for novel therapeutics to treat AD, early diagnosis will help ease the burden of the disease by allowing a patient's family and caregivers to adequately prepare for treatment and may aid in the development of interventions to delay AD progression.

AD neuropathology: APP and generation of Aβ

Neurologically, AD is associated with global brain atrophy and loss of synapses (Scheltens et al., 2016). In addition, there are two key hallmark neuropathological features that define AD: 1) Extracellular plaques comprised of an aggregated peptide called amyloid beta (Aβ) (Tanzi et al., 1987), and 2) intracellular neurofibrillary tangles comprised of hyperphosphorylated microtubule-associated protein tau (Grundke-Iqbal et al., 1986; Wischik et al., 1988). Aβ is generated by sequential cleavages of the amyloid precursor protein (APP). Human *APP*, located on chromosome 21, is a ubiquitously expressed transmembrane protein with particularly high expression in the central nervous system (CNS). *APP* is normally alternatively spliced into approximately one of 10 variants 639-770 amino acids in length. The major isoform in the CNS is APP695, however all isoforms can lead to the generation of Aβ (Wang et al., 2017a). Although a consensus as to the normal function of APP has yet to be reached, much is known about how the protein is both

trafficked and metabolized in normal and disease conditions (Gandy and Greengard, 1994; O'Brien and Wong, 2011; Van Der Kant and Goldstein, 2015).

Although Aβ is the most well-known disease-associated derivative of APP, APP actually is both processed by both non-amyloidogenic and amyloidogenic pathways via a series of secretase enzymes or enzyme complexes (**Figure 1**). APP predominantly (~90-99% of the time) is processed in the non-amyloidogenic pathway. APP is first cleaved by α-secretase to generate an N-terminal fragment called soluble APPα (sAPPα) and a C-terminal fragment (CTF) 83 amino acids in length (C83, or α-CTF). α-CTF is then further processed by another secretase complex called γ-secretase, releasing the APP intracellular domain (AICD) and a 3 kDa peptide product (P3). To generate Aβ, APP must be cleaved first by β-secretase at Asp1 (the first amino acid in the Aβ sequence), which yields an N-terminal soluble APPβ fragment (sAPPβ) as well as a CTF that is 99 amino acids in length (C99 or β-CTF). β-CTF can then be further processed by γ-secretase to yield AICD as well as full-length Aβ (Haass et al., 2012; O'Brien and Wong, 2011).

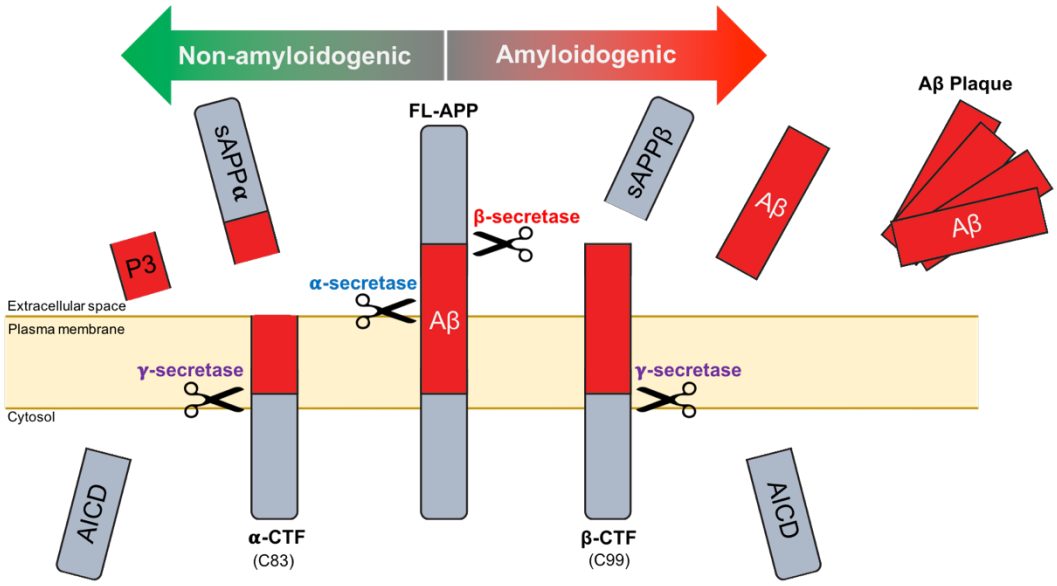

Figure 1. Amyloidogenic and non-amyloidogenic processing of APP.

APP undergoes a serious of catalytic cleavages by different secretase enzymes and enzyme complexes. In the non-amyloidogenic pathway (left) APP is initially cleaved by α-secretase, which results in the production of α-CTF (C83) and sAPPα. α-CTF can then be further processed by γ-secretase, yielding the soluble P3 fragment and the AICD. In the amyloidogenic pathway, APP is instead first cleaved by β-secretase, which results in generation of β-CTF (C99) and sAPPβ. β-CTF is then further cleaved by γ-secretase, which results in the production of AICD as well as full length Aβ. In pathological conditions, Aβ can form aggregates and deposit into extracellular amyloid plaques.

In actuality, the majority of β-secretase processing actually occurs at the Glu11 position in Aβ (β' site), which generates a shorter β'-CTF 89 amino acids in length. β'-CTF can also be further cleaved by γ-secretase, generating AICD as well as truncated Aβ (**Figure 2**) (Wang et al., 2017a). Additionally, APP can be processed by a β-secretase homologue called BACE2, which, as a θ-secretase,

precludes the generation of Aβ (**Figure 2**) (Wang et al., 2017a). BACE 2 is not highly expressed in the brain (Bennett et al., 2000; Sun et al., 2006; 2005).

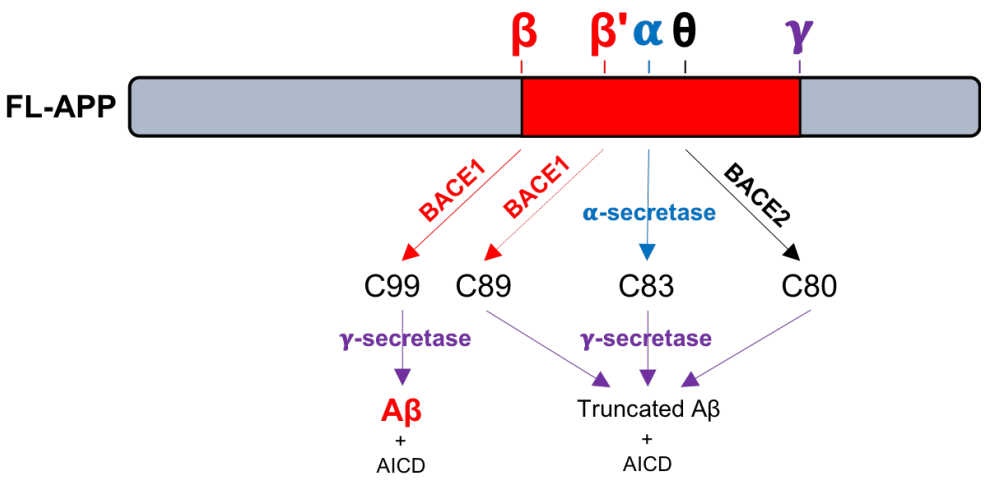

Figure 2. Non-canonical processing of APP

APP is predominantly cleaved by α-secretase (blue) to generate sAPPα and α-CTF (C83), which is further processed by γ-secretase to generate truncated non-pathogenic Aβ peptides. A minority of APP is processed by β-secretase cleavage enzyme 1 (BACE1; β-secretase), which cleaves APP at both Asp1(β, minority of BACE1 cleavage) and Glu11 (β') (numbering of Aβ sequence), generating β-CTFs that are either 99 (C99) or 89 (C89) amino acids in length, respectively. These β-CTFs can be further processed by γ-secretase, however only C99 β-CTF produces full length Aβ. APP can also be cleaved by BACE2 (a θ-secretase) which generates a CTF 80 amino acids in length (C80) and can be further processed by γ-secretase to generate truncated Aβ and AICD. Red portion depicts Aβ sequence of APP. Adapted from (Wang et al., 2017a).

γ-secretase is a highly conserved protein complex composed of homomeric assembly of the catalytic subunit PSEN1 (or PSEN2), nicastrin, anterior pharynx 1 (Aph1) and the presenilin enhancer 2 (PEN2). Recent characterization of γ-secretase structure and function has been illuminating in that we now better understand how γ-secretase processes β-CTF to generate Aβ (**Figure 3**). In an initial endopeptidase cleavage between amino acids 50/49 or 49/48, γ-secretase cleaves β-CTF and releases one of two AICD fragments of different lengths (**Figure 3**). γ-secretase then continues to make several successive tri- or tetra-peptide carboxypeptidase cleavages of the longer Aβ substrate (Takami et al., 2009). This processive activity most commonly yields shorter and less hydrophobic fragments of Aβ, typically 38 or 40 amino acids in length (Aβ38 and Aβ40, respectively) (**Figure 3**). Aβ40 is the most abundant Aβ species generated by γ-secretase processing in normal conditions, however levels of longer Aβs like the 42 or 43 amino acid form (Aβ42 or Aβ43) are increased in disease (Iwatsubo et al., 1995; Scheuner et al., 1996a). Longer Aβs are much more hydrophobic and prone to aggregation and therefore are more predominant in the extracellular Aβ plaques characteristic in AD (Jarrett et al., 2002). Typically, soluble Aβ that is regularly generated and released into the extracellular space can be readily cleared from the brain parenchyma (Castellano et al., 2011; Paresce et al., 1996; Wyss-Coray et al., 2003). In disease conditions, however, Aβ clearance mechanisms can also be impaired, resulting in the greater likelihood of accumulated soluble Aβ to oligomerize, fibrillize and

ultimately aggregate into bona fide amyloid plaques (Selkoe, 2006; Selkoe and Hardy, 2016).

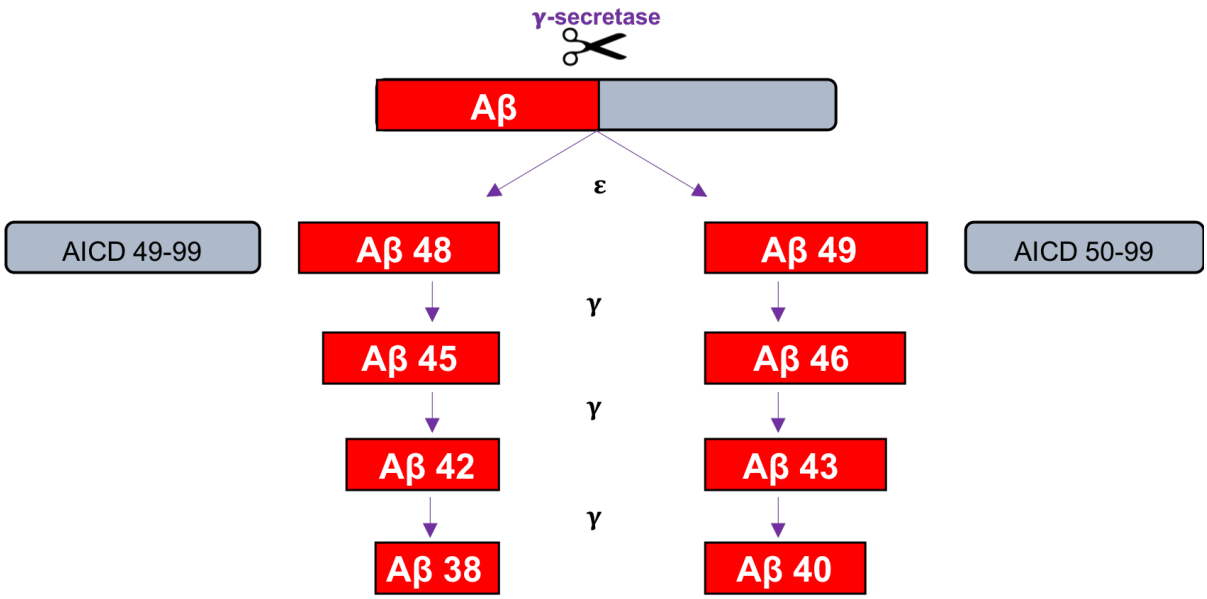

Figure 3. γ-secretase processing of βCTF and Aβ generation.

β-CTF is cleaved intramembranously by the γ-secretase complex. Initially, γ-secretase makes an endopeptidase cleavage of β-CTF between amino acids 49-48 or 50-49, generating Aβ peptides of either 48 or 49 amino acids in length. Additionally, AICDs are generated that differ in length by 1 amino acid. Subsequently, through a series of carboxypeptidase cleavages 3 or 4 amino acids of the Aβ peptides are removed, most commonly resulting in the generation of Aβs 38 or 40 amino acids in length. In AD, there is an accumulation of longer Aβ species, which are more hydrophobic and prone to aggregate.

APP trafficking and proteolytic processing

APP is a type 1 single-pass transmembrane protein that is trafficked through the constitutive secretory pathway (**Figure 4**). After being synthesized in the endoplasmic reticulum (ER), nascent APP polypeptides are transported to the Golgi apparatus and trans-golgi network (TGN) where it undergoes numerous posttranslational modifications (Haass et al., 2012). The TGN is the major residence of APP in neurons (Hartmann et al., 1997; Xu et al., 1997). Only a small fraction of APP (approximately 10%) ultimately reaches the plasma membrane (Haass et al., 2012; Thinakaran and Koo, 2008). At the cell surface, APP can be rapidly internalized by clathrin-mediated endocytosis and is sorted into the early endosome (Haass et al., 2012; Thinakaran and Koo, 2008). Internalized APP is then trafficked into the late endosome-lysosomal pathway for degradation, or trafficked back to the plasma membrane or to the TGN (Haass et al., 2012; Small and Petsko, 2015; Thinakaran and Koo, 2008) (**Figure 4**).

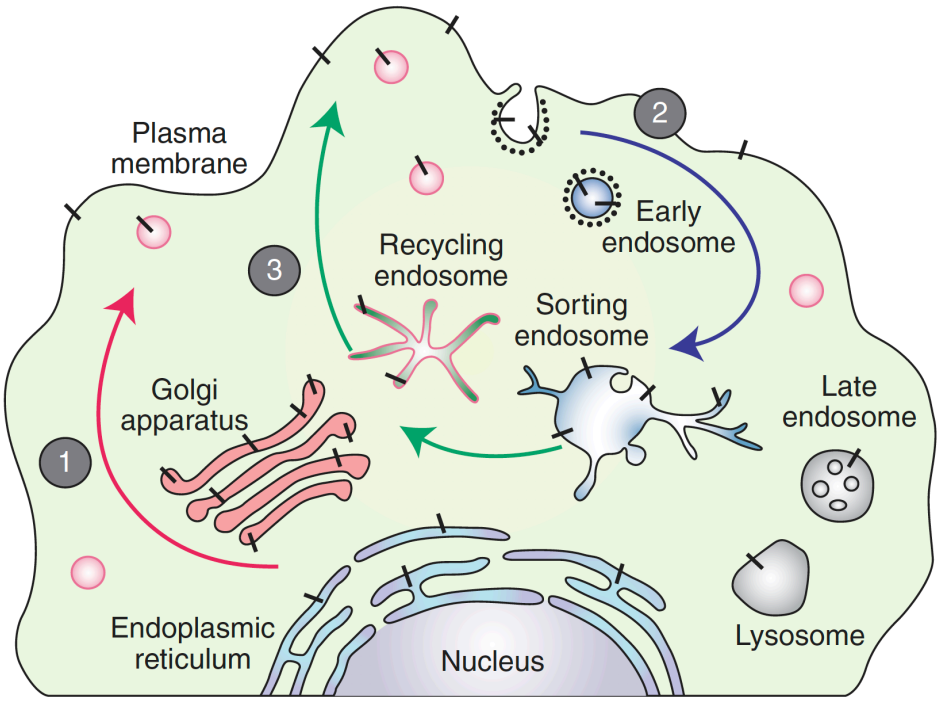

Figure 4. Trafficking and processing of APP.

APP is a single-pass transmembrane protein that matures through the classical secretory pathway. (1) Nascent APP molecules (shown as black bars) are generated and modified through the secretory pathway. Once APP reaches the cell surface it can be rapidly internalized via clathrin-mediated endocytosis (2). (3) Once endocytosed APP is trafficked through early endosomes it can subsequently be trafficked either to the TGN or cell surface through retromer or recycling endosomes, respectively. APP can also be trafficked to late endosomes and lysosomes for degradation. Reprinted with permission from (Haass et al., 2012).

APP is predominantly cleaved by α-secretase at the cell surface (Haass et al., 2012; Sisodia, 1992), whereas amyloidogenic β-secretase cleavage of APP predominantly occurs in endosomal compartments (Haass et al., 2012; Huse et al., 2000; Rajendran et al., 2008) (**Figure 5**). As an aspartyl protease, β-secretase

(BACE1) has an optimal activity at low pH and is therefore most active in both early and late endosomes (Vassar, 1999). Mature and active γ-secretase complexes are located predominantly within both the plasma membrane at the cell surface as well as within endosomal-lysosomal compartments (Dries and Yu, 2008; Kaether et al., 2006). While γ-secretase subunits can be found in other organelles associated with the secretory pathway, these are thought to be unassembled complexes and inactive. Therefore, Aβ is predominantly generated in endosomal compartments, while P3 is mostly generated at the cell surface (**Figure 5**). Aβ resulting from amyloidogenic processing of APP in endosomes can either be secreted or trafficked to late endosomes and lysosomes for degradation (Haass et al., 2012).

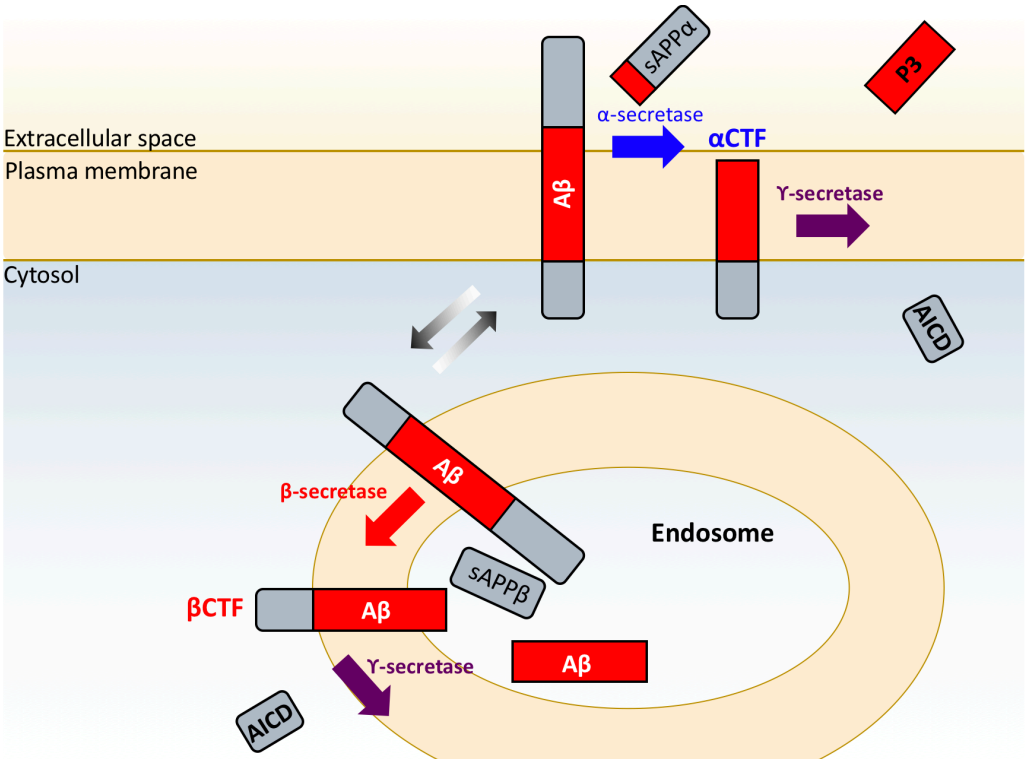

Figure 5. Amyloidogenic versus non-amyloidogenic processing is regulated by trafficking and compartmentalization of APP.

Non-amyloidogenic processing of APP predominantly occurs at the cell surface, as this is where the majority of α-secretase resides. Amyloidogenic processing occurs within endocytic organelles, where β-secretase is more abundant and active. γ-secretase is present both at the cell surface and within endocytic compartments (Haass et al., 2012).

Endocytosis and trafficking of APP is intricately regulated. Much of this regulation is mediated by members of the low-density lipoprotein receptor (LDLR) family (Bu, 2009; Li et al., 2001) (**Figure 6**). Many LDLR family members serve as receptors for apolipoprotein E (APOE) (Bu, 2009; Pitas et al., 1987), which is highly associated with AD pathogenesis, thereby implicating LDLRs in AD biology.

Moreover, variants in a number of LDLRs have been shown to be associated with late-onset AD risk (Gopalraj et al., 2005; Kang et al., 1997; Karch and Goate, 2015; Wang et al., 2017b). LRP1, one LDLR family member, can bind APP directly or indirectly and promote rapid APP endocytosis, which has been shown to significantly increase Aβ production (Bu, 2009; Cam et al., 2005; Liu et al., 2007). In contrast, another LDLR, LRP1B, competes for interaction with APP and retains APP at the cell surface leading to reduced Aβ production (Cam et al., 2004). Similarly, APOER2 decreases APP endocytosis and Aβ generation by enhancing APP interaction with other cell surface proteins and increases its retention at the plasma membrane (Bu, 2009; Hoe et al., 2005). The most widely studied LDLR related to AD is SORL1. SORL1 (and also the related SORCS1) is associated with AD in a variety of ways, most significant, is the discovery of *SORL1* variants associated with sAD (Kuwano et al., 2013; Rogaeva et al., 2009). More recently, even coding mutations in *SORL1* have been found to cause an extremely rare inherited version of AD (Cuccaro et al., 2016; Vardarajan et al., 2015; 2014). SORL1 shares homology with intracellular sorting receptors and is trafficked from endosomes back to the plasma membrane or TGN by the retromer complex. SORL1 binds APP, and therefore co-traffics APP away from endosomes, reducing the likelihood of amyloidogenic processing of APP in endocytic vesicles and Aβ production (Andersen et al., 2005; O'Brien and Wong, 2011; Offe et al., 2006). It is thought that disease-associated SNPs in SORL1 exert pathogenicity by reducing SORL1 expression or affinity for APP, leading to enhanced amyloidogenic APP processing

(Vardarajan et al., 2015; Young et al., 2015). Trafficking of APP is further regulated by a complex network of sorting nexins (SNXs), Rab-GTPases as well as intracellular adaptor proteins (Haass et al., 2012) (**Figure 6**). In sum, perturbations in intracellular trafficking processes may be inherently and intricately associated with AD pathogenesis, perhaps in part by altering APP processing and generation of amyloidogenic peptides.

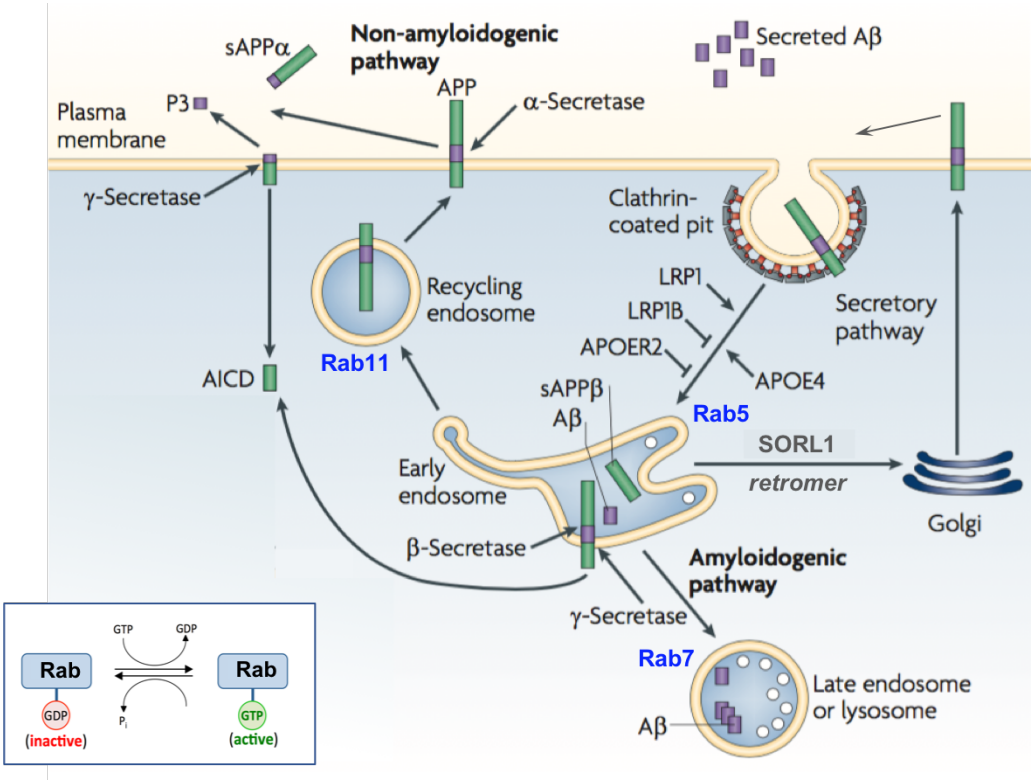

Figure 6. Regulation of APP trafficking in the endosomal-lysosomal system.

APP is predominantly processed in the non-amyloidogenic pathway at the cell surface. When APP is endocytosed APP can be processed to generate Aβ in endocytic compartments. Most Aβ is ultimately secreted into the extracellular space however some is trafficked to late endosomes or lysosomes where it

can accumulate intracellularly. Endocytosis of APP (and therefore regulation of amyloidogenic processing) is coordinated by low-density lipoprotein family members and APOE. LRP1, which is endocytosed rapidly, enhances APP endocytosis and amyloidogenic processing, whereas LRP1B and APOER2 helps to retain APP at the cell surface and promote non-amyloidogenic processing. APOE4 promotes APP endocytosis and amyloidogenic processing. SORL1 is a retromer receptor and shuttles APP out of endosomes back to the TGN (or cell surface) thereby reducing amyloidogenic APP processing. Additionally, trafficking and transit through the endosomal-lysosomal system is regulated by Rab-GTPases (which function by hydrolyzing GTP as shown in the adjacent box). Reprinted and modified with permission (Bu, 2009).

AD neuropathology: Tau

In addition to amyloid plaques, the second hallmark neuropathological feature of AD is neurofibrillary tangles (NFTs). These intracellular inclusions are comprised of hyperphosphorylated microtubule associated protein tau (MAPT or tau) (Grundke-Iqbal et al., 1986). Tau is a soluble cytosolic protein that that normally functions to bind, stabilize, and promote the flexibility of microtubules (Weingarten et al., 1975). In neurons, microtubules are a critical component of axons, serving as a track for shuttling of proteins and vesicles between the cell body and synapse (Avila et al., 2002; Ebneth et al., 1998; Millecamps and Julien, 2013; Spires-Jones and Hyman, 2014). Typically, in neurons tau is not present in dendrites, however in AD, axonal tau becomes hyperphosphorylated, resulting in its dissociation from microtubules and mislocalization to the somatodendritic compartment (Götz et al., 1995; Hoover

et al., 2010; Miller et al., 2014). Mislocalized hyperphosphorylated tau can also aggregate, forming fibrils and the characteristic NFTs (Götz and Ittner, 2008; Guo and Lee, 2011). These pathological changes are detrimental to the health of a neuron, as aggregated hyperphosphorylated tau can form seeds and sequester normal functioning tau and other essential microtubule-associated proteins (MAPs) (Alonso et al., 1997; Guo and Lee, 2011). Together, these changes lead to disruptions in normal microtubule assembly and function, disrupting axon integrity and transport, which may ultimately lead to degeneration.

Interestingly, tau pathology (NFTs) correlates better with cognitive decline and AD severity than does Aβ burden, suggesting that tau may serve as a downstream causal feature of neurodegeneration (Braak and Braak, 1991). Furthermore, within the last decade, there has been a growing consensus that tau may act as a prion-like protein and spread from diseased neurons to non-diseased neurons to propagate pathology (Fu et al., 2016; Kaufman et al., 2016; Sanders et al., 2014; Wu et al., 2016). These two fundamental discoveries provide undeniable evidence that tau plays a critical role in AD progression. However, whether tau truly is the causal effector of degeneration in AD, and how tau neuropathology is related to changes in Aβ metabolism remains a topic of great debate in the field.

AD genetics: Familial AD and the amyloid cascade hypothesis

The majority of AD cases (over 99%) occurs late in life and sporadically (sporadic AD or sAD), that is with no known genetic cause. Approximately less than

1% of AD occurs much earlier in life, due to the inheritance of an autosomal dominant familial AD (fAD) mutation (Karch and Goate, 2015). The idea that rare forms of AD could be inherited came prior to even the identification of APP, from studying patients with Down Syndrome (DS), which is caused by the presence of an additional part or all of chromosome 21. It was discovered that individuals with DS caused by an additional full copy of chromosome 21 develop AD neuropathology (Masters et al., 1985), however patients with a partial trisomy (not including the *APP* gene) do not (Guerreiro et al., 2012). This discovery was particularly meaningful only once Aβ was identified as the major component of the amyloid plaque, and APP was genetically mapped to chromosome 21 (Goldgaber et al., 1987; Kang et al., 1987; Robakis et al., 1987; Roher et al., 1986; St George-Hyslop et al., 1987; Tanzi et al., 1987). Together, this was the earliest evidence that excess Aβ produced in DS is due an additional copy of *APP* may be sufficient to cause AD.

It is now known that early-onset fAD can be caused by mutations in either *APP, PSEN1* or *PSEN2.* To date more than 30 fAD *APP* mutations, including rare fAD caused by *APP* gene duplication (Rovelet-Lecrux et al., 2006), have been identified and account for approximately 14% of all fAD cases. The majority of fAD *APP* point mutations cluster around the sites of Aβ processing (**Figure 7**). Initially, *APP* fAD mutations were extremely valuable discoveries as they revealed numerous aspects of the molecular underpinnings of AD pathology. The widely studied *APP* Swedish mutation (*APPswe*, KM670/671NL) was shown to increases Aβ in patient plasma up to 3-fold by enhancing β-secretase cleavage efficiency and generation of

β-CTF (Citron et al., 1992; 1994; Mullan et al., 1992). Recently, a protective *APP* mutation (*APP-A673T*) lying adjacent to the Swedish mutation was discovered, thereby further implication altered APP processing at the β-secretase cleavage site as inherently associated with development of AD (Jonsson et al., 2012). Similarly, the disease-causing *APP* Flemish mutation (*APP-A692G*) is situated at the site of α-secretase processing and is therefore predicted to exert its pathogenicity by limiting α-secretase cleavage and as a result enhancing amyloidogenic processing by β-secretase (De Jonghe et al., 1998; Hendriks et al., 1992). Some evidence also points to a role of the *APP-A692G* mutation in altering processing of APP by γ-secretase, which leads to enhanced amyloid production(Tian et al., 2010). Multiple pathogenic *APP* mutations exist at the C-terminal region of the Aβ sequence in APP (Chartier-Harlin et al., 1991; Goate et al., 1991; Murrell et al., 2000; 1991). These mutations cluster around the γ-secretase processing site and therefore are thought to exert their pathogenicity by altering γ-secretase function. Past cellular studies have demonstrated that these C-terminal *APP* mutations may not alter total Aβ levels, but instead shift processing to increase the levels of longer more amyloidogenic Aβ42, highlighting a potential important role of Aβ aggregation in AD pathogenesis (De Jonghe et al., 2001; Tamaoka et al., 1994). Together, the discovery of multiple fAD patients with characteristic pathology and mutations in the *APP* gene makes it clear that the processing of APP plays a central causal role in AD pathogenesis.

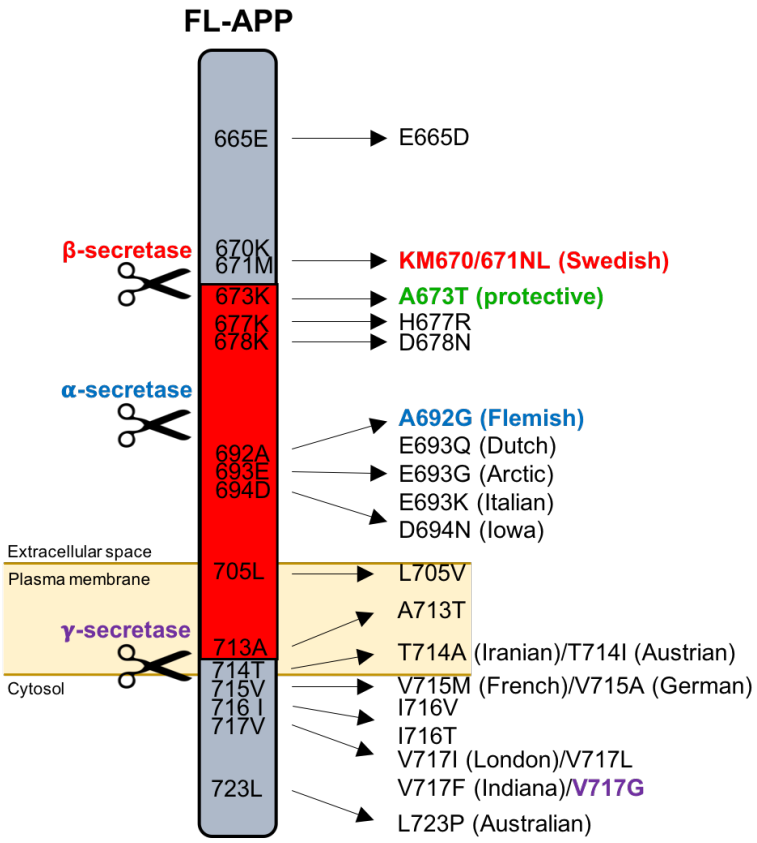

Figure 7. APP fAD mutations.

Schematic of APP, fAD mutations and processing sites. Mutations associated with early-onset familial AD are shown. *APP* fAD mutations tend to cluster around sites of secretase cleavages, thereby influencing processing patterns. One mutation is protective against AD (A673T, shown in green). The Aβ region of APP is indicated in red. Mutations studied in this thesis (*APPswe, APP-A763T, APP-A692G, APP-V717G*) are colored.

Since the discovery of *APP* fAD mutations, nearly 200 other fAD mutations have been discovered, mapping to chromosome 14 and chromosome 1 (Kelleher and Shen, 2017a; Levy-Lahad et al., 1995; Rogaev et al., 1995; Schellenberg et al., 1992; St George-Hyslop et al., 1992). These two genes are now known to be

PSEN1 and *PSEN2*, respectively, which, as describes above, encode the catalytic component of the γ-secretase complex necessary for the generation of Aβ (De Strooper et al., 1998; De Strooper, 2007). While only 13 dominant mutations in *PSEN2* have been identified, over 180 mutations have been found in *PSEN1*, accounting for nearly 80% of all fAD cases (Giri et al., 2016). Generally, mutations in *PSEN1* and *PSEN2* are distributed throughout the protein. Similar to the C-terminal mutations in *APP*, *PSEN1* and *PSEN2* mutations have been shown to also shift processing of APP to generate relatively more of the longer Aβ42 peptides compared to the shorter Aβ40 (increasing the Aβ 42:40 ratio) (Borchelt et al., 1996; Citron et al., 1992; Duff et al., 1996; Kelleher and Shen, 2017a; Scheuner et al., 1996b). While the mechanistic explanation for how these mutations affect γ-secretase are still being fully fleshed out, the discovery of mutations in these two genes that are inherently related to Aβ generation amplifies the causal relationship between AD and APP processing, and places emphasis on the relative amounts of longer Aβs as the primary contributing factor important in AD pathogenesis.

These abovementioned discoveries of causal direct genetic links between altered APP processing, Aβ and disease, bolstered the development of the "amyloid cascade hypothesis". The amyloid cascade hypothesis posits that changes in APP processing and/or brain Aβ homeostasis can result in the aggregation of Aβ and formation of amyloid plaques (Hardy and Higgins, 1992). Importantly, the hypothesis predicts that these early changes in Aβ metabolism are sufficient to initiate a series of related pathological changes including the hyperphosphorylation

and aggregation of tau into NFTs, and ultimately neurodegeneration. While the strongest evidence supporting this hypothesis comes from the familial AD genetics described above, a large amount of *in vitro* and *in vivo* evidence has also accumulated over the past two decades. In particular, *in vitro* evidence has shown that Aβ can be toxic to primary mouse neurons, and that toxicity appears to be abolished when tau is knocked-out (Rapoport et al., 2002; Roberson et al., 2007). Moreover, Aβ has been shown to induce tau phosphorylation, promote synapse loss, and trigger neuroinflammation, all of which are characteristic of AD pathogenesis (Jin et al., 2011; Koffie et al., 2009). *In vivo*, overexpression of mutant *APP* and *PSEN1* dramatically enhances tau aggregation in a mouse model expressing human tau, and augments cognitive and behavioral impairments in these animals (Oddo et al., 2003).

Although these genetic and experimental data provide a considerable amount of support for the amyloid cascade hypothesis, other findings call the hypothesis into question. Most notable is the finding that some individuals have very high amyloid burden in their brains but up until death they are cognitively normal, suggesting that amyloid deposits may not always trigger toxicity (Davis et al., 1999). Moreover, in a related neurodegenerative disorder called frontotemporal dementia (FTD) – caused by familial mutations in the *MAPT* (tau) gene – there is tau pathology (NFTs) and neurodegeneration in the absence of changes in Aβ (Dumanchin et al., 1998; Hong et al., 1998; Hutton et al., 1998). This indicates that Aβ is not always necessary to trigger tau pathology and neurodegeneration. Regardless, it seems undeniable that

APP and Aβ play a critical role in AD development, although the exact mechanism by which altered APP metabolism results in disease remains elusive.

AD genetics: Sporadic AD and genetic risk factors

The complexity of AD pathogenicity has been further underscored by more recent discoveries of genetic risk factors of late-onset sAD. For a long time, the only known late-onset AD-associated risk gene was *APOE*. *APOE* encodes the protein apolipoprotein E and is located in humans on chromosome 19. There are 3 *APOE* alleles called ε2, ε3 and ε4. One copy of the *APOE* ε4 allele increases risk for developing late-onset AD by 3-fold while two copies of ε4 increases risk for AD 12-fold (Corder et al., 1993; Scheltens et al., 2016; Strittmatter et al., 1993; Verghese et al., 2011). *APOE* ε2 allele carriers tend to be protected from development of AD (Corder et al., 1994). APOE is the primary cholesterol carrier in the brain and plays a role in a variety of biological processes in the central nervous system. Specifically, APOE is associated with cholesterol metabolism, lipid trafficking, inflammation, synaptic function, neurogenesis, as well as APP trafficking, endocytosis and Aβ production (Bu, 2009; Liu et al., 2013). The underlying mechanism linking APOE ε4 to AD is seemingly complex and has been shown to involve aberrant changes in Aβ deposition and aggregation as well as clearance (Corder et al., 1993; Scheltens et al., 2016; Strittmatter et al., 1993; Verghese et al., 2011). Non Aβ-associated mechanisms linking APOE ε4 and AD include an effect on the endosomal-lysosomal

system, tau homeostasis, synaptic plasticity, neuroinflammation and lipid homeostasis (Chung et al., 2016; Krasemann et al., 2017; Nuriel et al., 2017a; 2017b; Shi et al., 2017).

Recent technological advances in genome-wide association studies (GWAS) and next generation sequencing (NGS) have been revolutionary in discovering other sAD-associated genes. sAD risk genes broadly can be categorized into three main pathways –immune response, lipid metabolism and endocytosis – with many of these risk genes falling into two or even more of these biological categories (**Table 1**).

Table 1. Late-onset AD risk genes and their biological associations.

Gene	Function	Pathway	References
APOE	Lipid transport, endocytosis, cytoskeletal dynamics	Lipid metabolism, endocytosis	(Corder et al., 1993; Roses M D, 1996; Saunders, 2000; Saunders et al., 1993)
CLU	Synapse turnover, endocytosis, chaperone protein	Lipid metabolism, immune response, endocytosis	(Byun et al., 2014; Harold et al., 2009; Jones and Jomary, 2002; Rosenberg and Silkensen, 1995)
SORL1	Endocytosis, APOE receptor, processing/trafficking of APP	Endocytosis, lipid metabolism	(Andersen et al., 2005; Cuccaro et al., 2016; Gustafsen et al., 2013; Kuwano et al., 2013; T Cuenco et al., 2008; Vardarajan et al., 2015; Young et al., 2015)
ABCA7	Lipid homeostasis, Phagocytosis	Lipid metabolism,, Immune response	(Hollingworth et al., 2011; Holton et al., 2013)
CR1	Complement activation, Aβ clearance	Immune response	(Biffi et al., 2012; Kok et al., 2011; Kucukkilic et al., 2018; Wilson et al., 1987)
CD33	Clathrin-mediated endocytosis, Cell signalling	Endocytosis, immune response	(Siddiqui et al., 2017; The Alzheimer Disease Neuroimaging Initiative et al., 2013)
MS4A	Immune function, signal transduction	Immune response	(Antúnez et al., 2011; Ma et al., 2015; Zhu et al., 2017)
TREM2	Inflammatory response	Immune response	(Guerreiro et al., 2013; Jonsson et al., 2013; Ulrich et al., 2017)
BIN1	Synaptic vesicle endocytosis, APP trafficking, cytoskeletal dynamics	Endocytosis, synapse function	(Calafate et al., 2016; Harold et al., 2009; Ubelmann et al., 2017)
CD2AP	Receptor-mediated endocytosis, cytokinesis, cytoskeletal dynamics, synapse funciton	Endocytosis, synapse function	(Chen et al., 2015; Hollingworth et al., 2011; Monzo et al., 2005; Ubelmann et al., 2017)
PICALM	Clathrin-mediated endocytosis	Endocytosis, synapse function	(Harold et al., 2009; Kok et al., 2011; Schjeide et al., 2011; Xiao et al., 2012)
EPHA1	Synaptic development, immune function, neural development	Immune response, synapse function	(Hollingworth et al., 2011; Karch and Goate, 2015; Karch et al., 2012; Lambert et al., 2013; Wang et al., 2015)
HLA-DRB5/HLA-DRB1	Immune function, histocompatibility	Immune response	(Giri et al., 2016; Karch and Goate, 2015; Lu et al., 2017)

INPP5D	Cytokine signaling, Immune function	Immune response	(Jing et al., 2016; Karch and Goate, 2015; Scheltens et al., 2016; Yoshino et al., 2017)
MEF2C	Myogenesis, synapse formation	Immune response, synapse function	(Clark et al., 2013; Karch and Goate, 2015; Lambert et al., 2013; Nowakowska et al., 2010)
CASS4	Cell migration, cell adhesion		(Beck et al., 2014; Giri et al., 2016; Karch and Goate, 2015)
PTK2B	Calcium homeostasis, MAP kinase signaling	Synaptic function	(Alier and Morris, 2005; Beck et al., 2014; Jiao et al., 2015)
NME8	Ciliary function, neuronal cell proliferation		(Karch and Goate, 2015; Kim et al., 2002; Liu et al., 2016; 2014b)
ZCWPW1	Epigenetic regulation, neural development		(Allen et al., 2015; Karch et al., 2016)
CELF1	mRNA editing, Pre-mRNA splicing		(Giudice et al., 2016; Hinney et al., 2014; Karch et al., 2016)
FERMT2	Cell-cell adhesion, angiogenesis		(ADGC, Alzheimer's Disease Neuroimaging Initiative et al., 2016; Apostolova et al., 2018; Karch and Goate, 2015)
SLC24A4/RIN3	Cell signaling, neural development, endocytosis	Endocytosis	(Giri et al., 2016; Kajiho et al., 2003; Karch and Goate, 2015; Nixon, 2017)
DSG2	Cell-cell adhesion		(Hartlieb et al., 2014; Karch and Goate, 2015; Lambert et al., 2013)
PLD3	Signal transduction, epigenetic modification, endosomal-lysosomal defects	Lipid metabolism	(Cruchaga et al., 2014; Fazzari et al., 2017; Karch and Goate, 2015)
UNC5C	Neural development		(Wetzel-Smith et al., 2014)
AKAP9	Signal transduction, tau dynamics		(Logue et al., 2014; Venkatesh et al., 2016)
ADAM10	Neurogenesis, cell adhesion, APP processing		(Kim et al., 2009; Suh et al., 2013; Vassar, 2013)
SORCS1	Endocytosis, APOE receptor, processing/trafficking of APP	Endocytosis, lipid metabolism	(Reitz et al., 2011; Xu et al., 2013)
LRP1	Endocytosis, APOE receptor, processing/trafficking of APP	Endocytosis, lipid metabolism	(Bu, 2009; Shinohara et al., 2017; Wang et al., 2017b)

Neuroinflammation is a central feature in AD and several immune-associated genes with variants that are associated with late-onset AD have been identified (Karch and Goate, 2015). It has been shown in numerous rodent and human studies that amyloid plaques in the brain are surrounded by activated immune cells (Condello et al., 2015; Nimmerjahn et al., 2005; Yuan et al., 2016) and that many of the late-onset associated genes that have been identified by GWAS are uniquely expressed at high levels in brain immune cells (e.g., microglia) (Efthymiou and Goate, 2017; Sims et al., 2017). Some of these immune-related risk genes include CR1, CD33, CLU, EPHA1, MS4A and TREM2. Neuroimmune cells are important phagocytic scavenging cells necessary for the maintenance of a healthy brain. Therefore, it is thought that perturbations in these processes may alter protein homeostasis in the brain parenchyma and lead to the accumulation of Aβ (Hickman et al., 2008; Nimmerjahn et al., 2005). For example, CD33 and TREM2 are thought to contribute to disease by impairing clearance of Aβ (Griciuc et al., 2013; Rivest, 2015; Ulrich et al., 2017). It has also been shown that the complement cascade is elevated in AD and can contribute to disease pathology (Eikelenboom et al., 1989; Hong et al., 2016; Shen et al., 1997), therefore variants in CR1, which could confer risk to AD or be neuroprotective, may be associated with disease by either enhancing or attenuating the complement response (Karch and Goate, 2015).

Besides *APOE*, late-onset AD genes associated with lipid metabolism include *CLU, ABCA7, SORL1, DSG2. APOE* and *CLU* (also known as Apolipoprotein J, APOJ) are thought to share similar roles in AD pathogenesis, with their contribution

to Aβ clearance being most widely studied (Castellano et al., 2011; DeMattos et al., 2004; Verghese et al., 2013; Zandl-Lang et al., 2018). These lipoproteins can directly bind to Aβ and also lipoprotein receptors that may play a role in Aβ clearance and APP metabolism (Bu, 2009; Cam et al., 2004; Offe et al., 2006; Sagare et al., 2007). *ABCA7* is important mediator of cholesterol metabolism and is associated with plaque burden in AD brains as well as cognitive decline (Karch et al., 2012; Kim et al., 2013; Shulman et al., 2013). Genes involved in lipid metabolism also play a pivotal role in regulating endocytosis and intracellular trafficking, all of which depend on the regulation and coordination of lipoproteins and lipoprotein receptors (Bu, 2009; Holtzman et al., 2012; Pitas et al., 1987).

Many genes known to regulate endocytic processes, which are important in APP processing and synaptic activity, have been implicated in late-onset AD risk. These endocytosis genes include *SORL1*, *SORCS1, LRP1, BIN1, PICALM, CD2AP, EPHA1, RIN3, MEF2C* (Giri et al., 2016; Karch and Goate, 2015). SORL1, SORCS1 and LRP1 are all APOE receptors and are known to regulate endocytosis and intracellular trafficking of multiple cargos including APP (Andersen et al., 2005; Karch and Goate, 2015; Reitz et al., 2011; Rogaeva et al., 2009; Shinohara et al., 2017; Young et al., 2015). *BIN1, PICALM* and *CD2AP* are associated with receptor-mediated endocytosis and not only play a role in trafficking APP and Aβ production, but may also affect overall cellular proteostasis and aberrant protein aggregation (Calafate et al., 2016; Cormont et al., 2003; Monzo et al., 2005; Moreau et al., 2014; Tian et al., 2013; Ubelmann et al., 2017). In addition, these genes may play a vital

role in synaptic vesicle trafficking and recycling (Di Paolo et al., 2002; Dustin et al., 1998; Harel et al., 2008). *EPHA1* is a critical gene involved in synapse formation and neurodevelopment. Through involvement in cell membrane processes, *EPHA1* is implicated in immune function, and synaptic plasticity (Lai and Ip, 2009; Martínez et al., 2005; Sakamoto et al., 2011). *RIN3* encodes a protein that functions as a guanine nucleotide exchange for small GTPases, including Rab5. RIN3 stimulates and stabilizes Rab5 on early endocytic/endosomal vesicles (Kajiho et al., 2003; 2011; Nixon, 2017). In addition, *APOE* and *CLU* are important regulators of endocytosis, capable of binding a variety of endocytic lipoprotein receptors (Bu, 2009; Byun et al., 2014). A more detailed discussion of endocytic sAD risk genes and endosomal-lysosomal dysfunction in AD is provided below.

Endosomal-lysosomal trafficking dysfunction in AD

The endocytic pathway is integral to the normal functioning of neurons. Through endocytosis neurons respond to extracellular trophic factors; recycle plasma membrane receptors and other integral membrane proteins in response to neurotransmitters; and relay extracellular signals to intracellular biosynthetic pathways (Cosker and Segal, 2014; Parton and Dotti, 1993). By endocytosis, molecules from the cell surface (such as APP, neurotransmitter receptors, signaling molecules, etc.) are trafficked through a series of intracellular compartments, where they can be modified or degraded in a biologically meaningful way (Haass et al., 2012; Hu et al., 2015; Nixon et al., 2000). Upon internalization by endocytosis, cell

surface proteins are first sorted into early endosomes, where they can then be recycled back to the plasma membrane or TGN, or transported to late-endosomes and lysosomes for degradation (**Figure 6**) (Hu et al., 2015). Endocytosed molecules can be recycled and sorted away from the degradative pathway in a few different ways (**Figure 8**): Cargos can be recycled back to the PM in a fast and direct manner; or in slow recycling, where cargos are first directed to recycling endosomes before reaching the cell surface (Hu et al., 2015). Additionally, cargos in endocytic compartments can be trafficked by the retromer complex, in a retrograde direction from the endosome to the TGN, or directly for the endosome back to the cell surface (Small and Petsko, 2015). Endosomal and lysosomal compartments are characteristically acidic, necessary for the many degradative hydrolases and other proteases important for protein homeostasis, which function optimally in these acidic conditions (Hu et al., 2015). The careful coordination of trafficking of cargos and vesicles through endosomal and lysosomal compartments is carefully controlled by a family of GTPase proteins called Rab proteins (**Figures 6 and 8**) (Doherty and McMahon, 2009; Stenmark, 2009).

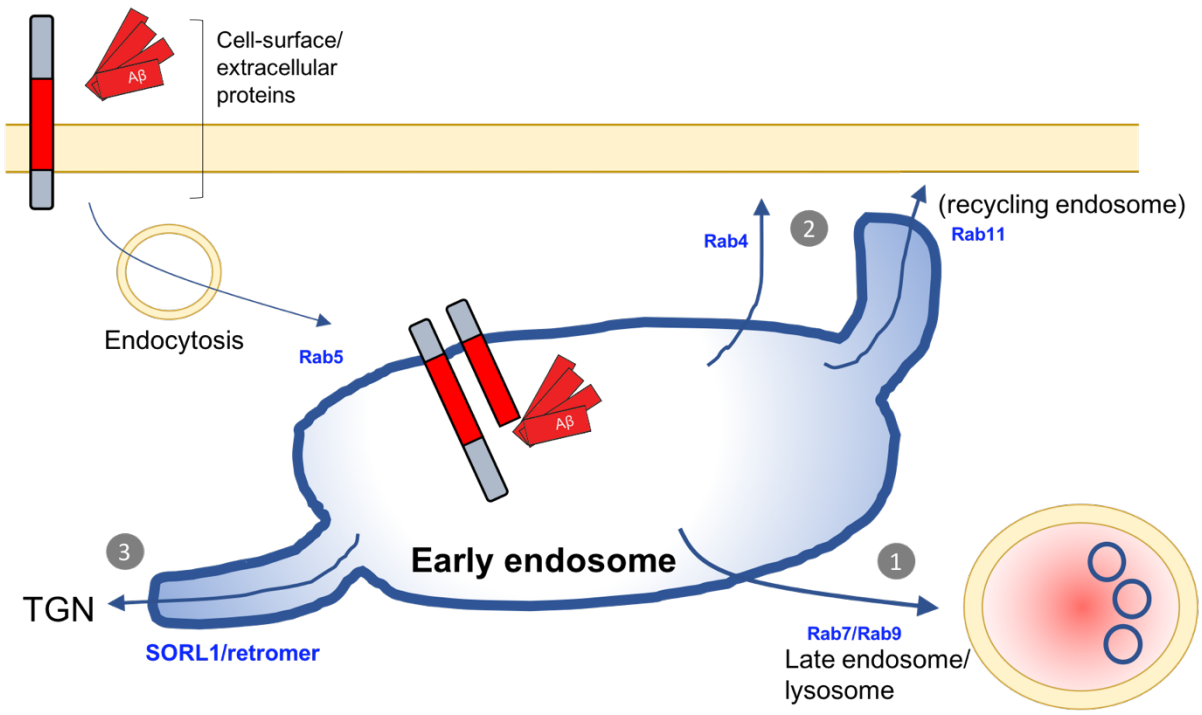

Figure 8. Endocytic trafficking into and out of the early endosome.

Cargos (such as cell surface proteins or extracellular proteins) are sorted into the early endosome by endocytosis (mediated by Rab5). There are subsequently three trafficking pathways out of the early endosome. (1) Cargos may be trafficked towards the degradation pathway. This results in the formation of intraluminal vesicles and degradation in the late endosome and lysosome. (2) Cargos may be trafficked back to the cell surface. This can occur rapidly and directly (mediated by Rab4) or through the recycling endosome (mediated by Rab11). (3) In the retrograde pathway, cargos are trafficked back to the TGN in a process coordinated by the retromer complex. Given its role as a "central hub" in endocytic sorting, pathological changes in early endosome function/morphology can have broad and dramatic effects on overall intracellular trafficking and the endosomal-lysosomal system. Adapted from (Small et al., 2017).

As described above, APP is a type 1 transmembrane protein that is endocytosed and trafficked through the endosomal-lysosomal system. Moreover, amyloidogenic versus non-amyloidogenic processing of APP occurs in a tightly regulated fashion almost entirely dependent upon its intracellular trafficking. Specifically, early endosomes are of particular relevance to AD, as it is thought that it is in these structures where APP meets β- and γ-secretases to generate Aβ (Haass et al., 2012). Therefore, any perturbation in the endocytic pathway that alters the trafficking of APP and influences the time APP spends in endosomal compartments may have consequential effects on the development of AD pathology.

Early endosomal dysfunction is one of the earliest neuronal pathologies of AD observed in sAD patients prior to deposition of extracellular Aβ (Cataldo et al., 2000; Ginsberg et al., 2010a; 2010b). These endosomal changes suggest that neurons may become intracellularly compromised much earlier than when overt Aβ plaque or tau tangle pathology accumulates. Early endosomes are a central hub in intracellular membrane and protein trafficking. Imbalances in trafficking into- and out of this organelle may therefore have severe consequences on the overall health of a neuron (Small et al., 2017) (**Figure 8**). While it remains elusive what exactly causes upstream early endosome dysfunction in AD pathogenesis, multiple studies which have focused on using non-human overexpression models have indicated that intracellular accumulations of APP fragments, either β-CTF or longer Aβs (e.g., Aβ42) may be the drivers (Jiang et al., 2010; Treusch et al., 2011; Xu et al., 2016).

As will be discussed in later chapters, this hypothesis remains to be adequately tested in human neurons, particularly in the absence of transgenic overexpression.

As described in detail above, genetic association studies have revealed variants in multiple different endocytic/endosomal trafficking-related genes (e.g., *SORL1, BIN1, CD2AP, PICALM, RIN3,* etc.) as strongly linked to late-onset sAD (Karch and Goate, 2015). These genetic findings implicate, at least in some cases of AD, endocytic dysfunction as an initial primary upstream pathological event. For example, *SORL1* mutations or SORL1 knock-down/knockout reduces transport of cargos (including APP) out of endosomes via retromer-mediated routes (Andersen et al., 2005; Gustafsen et al., 2013; Reitz et al., 2011; Small and Petsko, 2015). This leads to dysregulated sorting of endosomal proteins, including APP, accelerated Aβ generation and endosome enlargement (Andersen et al., 2005; Gustafsen et al., 2013; Reitz et al., 2011; Small and Petsko, 2015). Similarly, BIN1 and CD2AP also functions to traffic cargos out of early endosome (Ubelmann et al., 2017). BIN1 is important in shuttling cargos out of endosomes towards the cell surface via the recycling pathway, while CD2AP is important in mediating sorting out of early endosomes and towards the degradative pathway (Ubelmann et al., 2017). Deficiencies in retromer core proteins (VPS26, VPS35) as well as variants in other key retromer genes have been linked with AD (Small and Petsko, 2015). These AD-related changes in retromer biology are thought to reduce the overall function of retromer, leading to impaired sorting of cargos out of endosomes and dysfunction/enlargement of early endosomes. Mutations in PICALM, which is an

important regulator of trafficking into the endosome, suggest that endocytic influx, and not just efflux, is also inherently linked to AD (Thomas et al., 2016). Furthermore, genetic associations with RIN3 directly implicate activity of Rab proteins, such as Rab5, as being associated with AD pathogenesis (Kajiho et al., 2003; 2011; Xu et al., 2018).

As mentioned above, neuronal APOE receptors are key regulators of endocytosis, thereby implicating APOE in endosomal dysfunction. In studies investigating the pathogenicity of the *APOE4* allele, it was found that *APOE4* can result in endosomal enlargement by accelerating endocytosis and impair normal endosomal recycling (Chen et al., 2010; He et al., 2007; Li et al., 2012; McColl et al., 2003; Nuriel et al., 2017b; Ye et al., 2005; Zhao et al., 2017). *APOE* is one of many different lipid/cholesterol-associated genes linked with AD. Interestingly, it is known that altering overall levels or trafficking of cholesterol in neurons also leads to alterations in endocytosis and endosomal enlargement (Jin et al., 2004; Marquer et al., 2014).

Taken together, all of these lines of evidence provide a compelling case for endosomal dysfunction being a principle upstream pathological event. Enlarged endosomes, caused by increased endocytosis or reduced recycling may also result in more APP residing in early endosomes, leading to greater amyloidogenic processing and Aβ generation (Haass et al., 2012; Jiang et al., 2010; Small et al., 2017). Whether or not endosomal dysfunction in sAD is a pathogenic mechanism converging on Aβ production or is instead itself a principle driver of disease remains

unclear. Furthermore, whether or not the early endosome abnormalities hallmark in late-onset AD are also common to fAD caused by *APP* and *PSEN* mutations is in great need of further investigation.

AD models

Much of the knowledge we have today about AD pathogenesis and underlying AD mechanisms has critically depended on the development of adequate and representative experimental model systems. The breakthrough discoveries of familial mutations capable of causing early-onset AD (and FTD) has enabled the development of numerous *in vivo* and *in vitro* experimental model systems, with the hope that discoveries made in these systems would translate to more common sAD as well. The most widely used models in the AD field have been transgenic mouse models. These models have been instrumental in the discovery of many important disease mechanisms, however, as will be described below, they also are undeniably problematic. The first ever APP transgenic mouse model was published in 1991 (Quon et al., 1991), however it was not until 1995 that the first models actually demonstrating AD-associated amyloid pathology were published. Specifically, these mice were called the PDAPP and Tg2576 mouse and were designed to transgenically overexpress human APP with either the Indiana (V717F) or Swedish (KM670/671NL) fAD mutations, respectively (Games et al., 1995; Hsiao et al., 1996; Rockenstein et al., 1995). While in both of these models amyloid plaques similar to those in human AD patients are found in mouse brains by approximately 10-11

months of age, neither of these mice develop NFTs (or any robust tau pathology) nor have measurable neurodegeneration and neuronal loss. This, of course, contrasts greatly with human patients, who have only a single heterozygous fAD *APP* mutation, yet develop a brain full of amyloid plaques, NFTs and have profound neuronal loss. Similar problems were also seen in early PSEN1 transgenic models. Namely, overexpression of mutant *PSEN1* (such as *M146V*) results in a predictable increase in longer Aβ 42 peptides in the brain, however these mice don't display any plaque pathology, NFTs, neurodegeneration, or cognitive deficits even at up to 2.5 years of age (Duff et al., 1996; Qian et al., 1998). Furthermore, even transgenic mice overexpressing both mutant human *APP* and *PSEN1* fail to demonstrate any NFT pathology or robust neurodegeneration, despite the accelerated accumulation of Aβ plaques in the brain (Borchelt et al., 1997; Holcomb et al., 1998). The failure of these mouse models to recapitulate the seminal pathological features of human AD highlights how the use of mouse models in AD research may be confounding, and points to the many key differences between rodents and humans.

Years later, the first AD mouse model was developed that demonstrates both Aβ as well as NFT pathology. Specifically, it took the expression of three different mutant transgenes (*APPswe, PSEN1-M146V* and *MAPT-P301L*) to result in both hallmark clinical AD pathologies, with corresponding synaptic and cognitive changes. This mouse is commonly known in the field as the triple-transgenic (or 3xTg) mouse (Oddo et al., 2003). The mere notion that it took additional overexpression of human tau (*MAPT*) with an FTD-causing familial mutation, further

highlights the differences between human and mouse tau biology, and raises questions as to the degree to which conclusions made from these mice are broadly relevant to human AD. More recently, the first non-overexpression AD mouse models have been generated and used to study disease mechanisms. Briefly, researchers replaced the mouse *APP* gene with human *APP* bearing up to 3 different fAD mutations (*APPswe, APP-I716F, APP-E693G*), which is expressed at normal physiological levels controlled by the endogenous mouse *APP* promoter (Saito et al., 2014). These mice develop aggressive amyloidosis and demonstrate plaque pathology starting at 2 months. These mice also show microgliosis and increased numbers of reactive astrocytes, synaptic loss and cognitive impairment. However, likely due to the absence of mutant tau overexpression, *APP* knock-in mice fail demonstrate any NFT pathology, once again underscoring the limitations of even the "best" mouse models (Saito et al., 2014). Most interestingly, the scientists behind this novel *APP* knock-in mouse reported that many of the phenotypes reported in *APP* overexpression models could not be reproduced in their system. This led the authors to conclude that up to 60 percent of the phenotypes identified in *APP*-overexpressing mice could in fact be artifacts of overexpression, therefore potentially calling into question the findings of thousands of past research papers (Saito et al., 2014).

In vitro cell culture models have also been abundantly used in the AD field. In particular, these models have been instrumental in the understanding of the mechanism of Aβ production, APP trafficking, and endosomal-related changes in

AD. Many *in vitro* studies utilize primary cultures of mouse disease-vulnerable neurons, often comparing wildtype and transgenic mice overexpressing mutant human *APP* and or *PSEN1* (Saraceno et al., 2013; Trinchese et al., 2004). This approach has been instrumental in deciphering how APP is processed and trafficked in neurons, however, as described above, is confounded by overexpression of mutant protein in non-human cells. Mouse primary neurons are somewhat difficult to maintain in culture, and therefore have in many cases been supplanted by the use of proliferating non-neuronal (and in many cases non-human) cell lines. For example, human embryonic kidney cells (HEK) and mouse neuroblastoma (N2A) cells have been engineered to stably overexpress wildtype and mutant APP and/or PSEN1 (Borchelt et al., 1996; Jiang et al., 2010; Kim et al., 2015; Tarassishin et al., 2004; Xu et al., 1997). These models have revealed interesting insights into the potential pathogenicity of fAD mutations and have been widely used to investigate APP trafficking in wildtype and mutant conditions (Choy et al., 2012; Sannerud et al., 2016; Sullivan et al., 2011). Furthermore, overexpression of full-length APP and APP cleavage products have provided insight into the pathways contributing to endosomal dysfunction in AD (Jiang et al., 2010; Kim et al., 2015; Xu et al., 2016).

In vitro non-neuronal cell culture models are often chosen for use as they are self-renewing and can be easily genetically manipulated. Although these systems are scalable and easy to use, they also have considerable drawbacks. As with most mouse models, *in vitro* cell culture models heavily rely on transgenic overexpression of fAD mutant APP and/or PSEN1, which is a dramatic departure from patients who

contain only a single heterozygous fAD mutation. Moreover, studying AD phenotypes in non-neuronal cells calls into question whether findings are also applicable to neurons, which are post-mitotic, highly compartmentalized and polar. Importantly, in terms of studying intracellular trafficking, overexpression models are especially concerning, as the normal trafficking and processing of proteins (including APP which is intricately processed) is likely aberrantly affected by being present in cells at a saturating level.

The abovementioned drawbacks of common *in vivo* and *in vitro* models highlight the imminent need for the generation of new model systems that are more physiologically comparable to the AD patient condition. Specifically, being able to study AD processes in human neurons in the absence of overexpression will not only help to decipher which previously identified phenotypes may be relevant to human neurons but will undoubtedly enable the discovery of novel disease mechanisms or serve as a valuable platform for testing novel therapies. Fortunately, with the recent development of iPSC and CRISPR/Cas9 technology, generating models that enable the study of genetically tractable human AD-vulnerable neurons is now feasible.

Induced pluripotent stem cell (iPSC) technology

Yamanaka and colleagues first demonstrated that mouse fibroblasts could be reprogrammed into pluripotent embryonic-like cells. They showed that expression of only 4 transcription factors (Oct4, Sox2, Klf4 and c-Myc) was sufficient to induce

reprogramming in both mouse and human somatic cells into iPSCs (Park et al., 2008; Takahashi and Yamanaka, 2006). Since this initial discovery, many different protocols have been developed to generate iPSCs from a wide variety of donor cell types (fibroblasts, glia, B lymphocytes, amniotic fluid-derived cells, cells in blood and urine) and using a diversity of strategies (viral delivery of reprogramming factors, liposome or electroporation-mediated transfection of linear DNA, direct protein deliver, etc.) (Singh et al., 2015). iPSCs are like embryonic stem cells (ESCs) in that they are self-renewing and are capable of differentiating all three germ layers (mesoderm, ectoderm and endoderm). As a result, iPSCs are capable of generating virtually any cell type, including many different types of neurons similar to those found in the human brain. The potential of this technology to propel biomedical science forward led Dr. Yamanaka to receive the 2012 Nobel Prize in Medicine.

iPSC technology provides great promise for modeling and studying monogenic diseases, such as fAD caused by *APP* or *PSEN1* mutations. Since the development of iPSC technology, dozens of papers have been published describing the use of iPSCs to study neurodegenerative diseases (Bahmad et al., 2017; Xie and Zhang, 2015; Yang et al., 2016). Of these studies, several groups have utilized iPSCs for modeling AD. Most studies proceeded in the following manner: Dermal fibroblasts are isolated from skin biopsies of AD patients (with a known fAD mutation or with sAD). At the same time, fibroblasts are also obtained from an unaffected individual to serve as a control. These somatic cells are then reprogrammed into iPSCs, which can be differentiated into AD-vulnerable cells such as cortical neurons

following a variety of established protocols. Using this approach, past studies have demonstrated that *APP* and *PSEN1* fAD and even sAD patient-derived iPSCs display disease-relevant phenotypes associated with APP processing, Aβ generation and tau pathology, and have even revealed potential new mechanisms underlying AD pathogenesis (Duan et al., 2014; Israel et al., 2012; Kondo et al., 2013; Moore et al., 2015; Muratore et al., 2014; Ortiz-Virumbrales et al., 2017; Shi et al., 2012; Sproul et al., 2014).

Patient-derived iPSCs have demonstrated the potential applications of this technology for modelling AD but many of these past studies are complicated by several outstanding technical issues. One of the greatest and most poorly understood problems with human iPSCs is the donor-to-donor variability and cellular heterogeneity. For example, in past studies using patient-derived iPSCs, it was found that some iPSC lines with an fAD mutation successfully demonstrated AD-associated phenotypes while other iPSC lines (even with the same fAD mutation) failed to do so (Israel et al., 2012; Kondo et al., 2013). This issue of clonal iPSC-line heterogeneity is concerning, as it raises the question of what the most appropriate control should be. If phenotypic variability is common between different patient-derived iPSC lines, then surely, variability exists across non-diseased "control" iPSC lines too. This unexplained variation may come from the differences in genetic background between the diseased and healthy donors' cells. Therefore, one confounding factor in using patient-derived iPSCs and comparing them to control iPSCs is that it is generally unclear whether phenotypic differences seen are due to

a particular disease-associated mutation of interest or differences in genetic background between control and patient samples. This is of particular importance when comparing subtle phenotypes, which may be expected in iPSC-derived neurons with only a single heterozygous mutation and no transgenic overexpression. Furthermore, iPSC-derived neurons are typically analyzed only approximately 30-60 days after induction of differentiation, whereas patients with fAD mutations typically develop AD after approximately 40 years. Therefore, an additional concern is that a single heterozygous mutation may not be sufficient to allow for subtle phenotypes to be resolved.

Taken together, the drawbacks described above highlight the need to generate isogenic iPSC control and mutant cell lines differing only at the site of the mutation of interest. Additionally, tools to be able to study mutations in both a heterozygous and homozygous context would be very helpful to amplify subtle disease-relevant phenotypes while maintaining physiological levels of mutant protein expression. Fortunately, the recent developments in genome editing technology now means generating isogenic wildtype, homo- and heterozygous fAD mutant iPSCs is a possibility.

CRISPR/Cas9 gene editing

For over a decade there has been a considerable effort made in developing gene editing technology for use in human cells, such as iPSCs. These initially included zinc finger nucleases (ZFNs) as well as transcription activator-like effector

nucleases (TALENs), but more recently CRISPR/Cas9 has supplanted both of these early technologies. While the potential utility of CRISPR/Cas9 gene editing technology in biomedicine is vast, one of the most promising uses of the technology is for engineering next-generation iPSC model systems that overcome confounding issues associated with patient-derived stem cell models.

The bacterial CRISPR/Cas9 (clustered regularly interspaced short palindromic repeats /CRISPR-associated protein 9) system is a versatile tool for precise, sequence-specific gene editing in many organisms and model systems (Cho et al., 2013; Cong et al., 2013; Hruscha et al., 2013; Hsu et al., 2014; Jinek et al., 2013; Mali et al., 2013), including iPSCs (Hsu et al., 2014; Mali et al., 2013). The CRISPR/Cas9 gene editing system, derived from the bacterial adaptive immune system in Streptococcus pyogenes (Horvath and Barrangou, 2010), consists of the nuclease Cas9 and a guide RNA, which directs Cas9 to the DNA target through a 20 bp programmable sequence. The guide RNA targets Cas9 to a specific genomic locus by RNA-DNA base pairing adjacent to an NGG protospacer adjacent motif (PAM) on the DNA (**Figure 9A**). Both the presence of the PAM and guide RNA binding are required for Cas9 to introduce a site-specific double-strand break (DSB), which occurs 3 bp upstream of the PAM motif (Jiang et al., 2015; Marraffini and Sontheimer, 2010). The CRISPR/Cas9 complex has been shown to be very efficient at introducing DSBs in the DNA of many cell types and model systems, commonly resulting in bi-allelic modifications (Canver et al., 2014; Dow et al., 2015; Platt et al., 2014). In most cases these DSBs are repaired by the non-homologous end-joining

(NHEJ) pathway, leading to nonspecific insertions, deletions or other mutations, commonly referred to as 'indels' (Hsu et al., 2014; Jinek et al., 2013). This is convenient for generating gene knockouts, which are most easily created by non-specific modification of both alleles by NHEJ (**Figure 9B**).

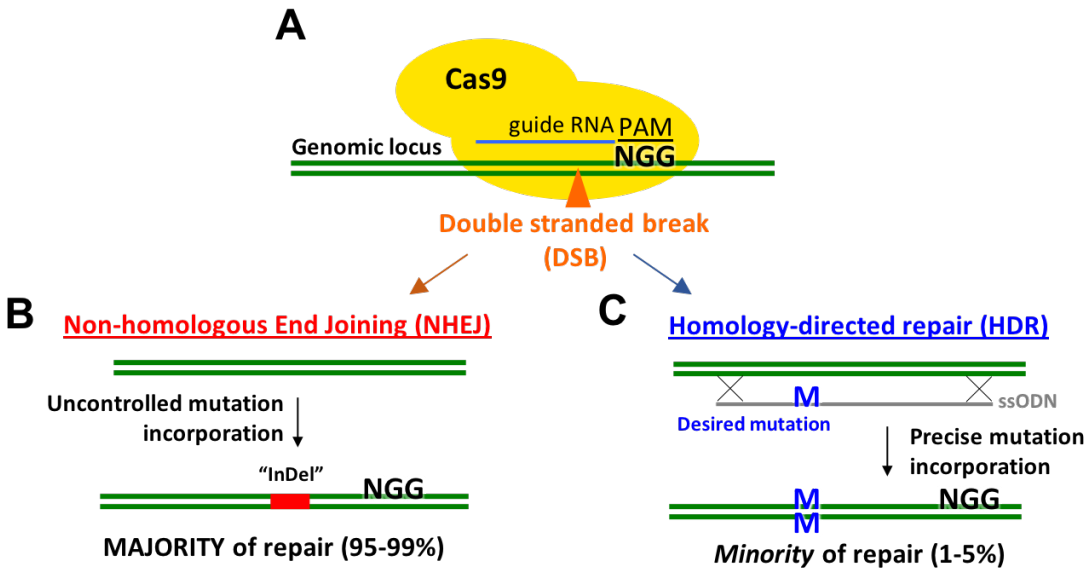

Figure 9. CRISPR/Cas9 gene editing.

A) CRISPR/Cas9 gene editing works by targeting to any genomic NGG (PAM) sequence a guide RNA (commonly a single guide RNA called an sgRNA) and Cas9 nuclease. This results in a double-stranded DNA break (DSB). **B**) DSBs are most commonly repaired by the error prone non-homologous end-joining pathway (NHEJ), which results in random base insertions or deletions (called "indel" mutations). **C**) In rare cases, the cell may utilize homology-directed repair (HDR), which makes use of a DNA template provided (such as a single stranded DNA oligo, ssODN) with homology to the sequence surrounding the DSB. If this repair template is modified to contain a specific mutation of interest, that change will be incorporated into the edited genome.

In rare cases the cellular repair mechanism can utilize another DNA molecule, such as the homologous allele or an exogenously introduced DNA template, to repair the chromosome break by homology-directed repair (HDR)(Hsu et al., 2014). Introducing a modified donor template, such as a single-stranded oligo DNA nucleotide (ssODN), can yield intended base changes that can be utilized to knock-in (KI) specific mutations (Cong et al., 2013; Horvath and Barrangou, 2010) (**Figure 9C**). For example, patient derived iPSCs containing a fAD *APP* or *PSEN1* mutation can be engineered using CRISPR/Cas9 to correct the pathogenic mutation back to the wildtype allele to generate isogenic control cell lines. More promising, however, is the use of CRISPR/Cas9 editing in a standardized wildtype iPSC line, to introduce any disease-causing mutations desired and generate (heterozygous and homozygous) isogenic mutant iPSCs without ever needing to access patient material. Although CRISPR/Cas9 has already been extensively and efficiently used to study gene function by engineering gene knockouts (KO) through NHEJ (Jiang et al., 2015; Marraffini and Sontheimer, 2010; Wang et al., 2013), precise editing by HDR to engineer sequence-specific changes such as disease-causing point mutations is inefficient (Canver et al., 2014; Cong et al., 2013; Dow et al., 2015; Platt et al., 2014; Wang et al., 2013). This limitation has unfortunately prevented the widespread use of CRISPR/Cas9-mediated gene editing for use in disease modeling. Furthermore, systematic, targeted introduction of base-changes by HDR at only a single allele using CRISPR/Cas9 had not been reported, making it difficult

to use this gene editing system for modeling the many important human diseases (such as fAD) that are caused or influenced by heterozygous changes.

Overview of thesis work

In this introduction, I have described how decades of research have mostly converged on altered APP metabolism, and more specifically Aβ, as the key pathological trigger in AD. This work has focused predominantly on studying causal fAD mutations in *APP* and *PSEN1,* using transgenic overexpression of mutant human protein in mouse models as an approach for deciphering how Aβ may confer pathogenicity. Despite the clear genetic link between *APP*, *PSEN1* (or *PSEN2*) and Aβ, it is still uncertain how a variety of mutations in one of three different genes causes a common disease. Furthermore, recent discoveries have called into question whether or not Aβ is the only disease-associated pathological protein fragment important in the development of AD (Kim et al., 2015; Xu et al., 2016). This apparent complexity is underscored by the recent failures of clinical trials testing the efficacy of multiple novel anti-amyloid therapeutics (Egan et al., 2018; Mullard, 2017). It is therefore now, more than ever, time to reassess the state of the AD research field and consider what experimental and technical improvements can be made to help better understand AD biology.

Early on in our attempt to study neurodegeneration, our group presumed that to better understand the mechanisms underlying a uniquely human disease such as AD, it would be valuable to perform experiments in *human tissue*. Naturally we

turned to using human iPSCs, which, as described above, can be used to generate human disease-vulnerable cortical neurons. We were particularly drawn to the unresolved basic question in the field of how a large number of fAD mutations in *APP* and *PSEN* genes can result in a common disease signature. Given the promise of CRISPR/Cas9 editing, we thought that instead of depending on the highly variable process of obtaining biopsies from rare fAD patients, reprogramming patient fibroblasts into iPSCs and differentiating cells into neurons, it would be helpful instead to generate a standardized wildtype iPSC line into which we could knock-in any fAD mutation we wished to study. With this approach in mind, the main goal of my thesis work was as follows: ***Use CRISPR/Cas9 gene editing and iPSC technology to determine in human neurons common cellular mechanisms underlying both APP and PSEN1 fAD mutations***.

Initially, I began my first CRISPR/Cas9 gene editing experiments in January 2013, only days after the manuscripts detailing the first usage of the technology in human cells were made publicly available. Quickly we realized that CRISPR/Cas9 technology was particularly underdeveloped, specifically for its use in engineering specific sequence changes in stem cells. In Chapter II, I will begin by describing two major prohibitive issues we noticed with using CRISPR/Cas9 in iPSCs. Specifically, CRISPR/Cas9-mediated knock-in is incredibly inaccurate, and it is virtually impossible to efficiently generate both heterozygous and homozygous mutant knock-in cell lines using standard approaches. I will describe how we overcame these issues by systematically interrogating patterns of HDR-mediated mutation

incorporation using next generation sequencing (NGS) technology ultimately to develop a universal framework for precise and efficient introduction of mutations with CRISPR/Cas9. In Chapter III, I will expand on this established approach and discuss a related CRISPR/Cas9-based strategy we developed called CORRECT, which specifically enables scarless introduction of an intended sequence or mutation.

Chapter IV will focus on describing how we actually implemented our novel CRISPR/Cas9 gene editing platform to generate and study a large and comprehensive panel of isogenic *APP* and *PSEN1* fAD mutant iPSCs. Probing differentiated mutant iPSC-derived neurons revealed unexpected overlapping common cellular and molecular AD-relevant phenotypes. Specifically, using "-omics" technologies, we discovered that dysregulation of both AD- and endocytosis-associated genes is a pathogenic feature common to *APP* and *PSEN1* mutant cells. Endocytic dysfunction was confirmed in all mutant neurons analyzed and was shown to be specifically correlated with endogenous accumulation of β-CTF, and not changes in Aβ levels. Furthermore, endosomal enlargement phenotypes could be pharmacologically rescued by inhibition of β-secretase, but not by treatment with novel γ-secretase modulators. Together these data reinforce a developing consensus in the AD field, namely, that β-CTF may be an important common product of APP metabolism that significantly contributes to AD pathology. At the end of each chapter describing experimental results I will discuss the significance and implications of the work presented. I will discuss how our work fits in the broader scientific literature and

describe some future research directions. Chapter V will contain a final outlook and perspective of the work presented in this thesis, and Appendix I includes details of important methods and materials relevant to Chapters II-IV.

CHAPTER II: EFFICIENT INTRODUCTION OF SPECIFIC HOMOZYGOUS AND HETEROZYGOUS MUTATIONS USING CRISPR/Cas9

Background and rationale

CRISPR/Cas9 is a versatile system for gene editing, which, when applied to iPSC technology, holds great potential for enabling the development of next-generation model systems of neurodegenerative diseases such as AD. Our goal was to leverage these two technologies and to use CRISPR/Cas9 to introduce a series of disease-causing fAD *APP* and *PSEN1* mutations in wildtype human iPSCs. Moreover, we aimed to generate both homozygous and heterozygous knock-in cell lines, so that in differentiated AD-vulnerable cortical neurons, mutation-load dependent phenotypes could be adequately determined and subtle phenotypes could be more significantly exaggerated (in homozygous cells).

At the time of our initial experiments using CRISPR/Cas9, little was known about how useful the technology would be for editing human stem cells. When we started the project, the only published work on CRISPR/Cas9 editing was studies demonstrating that the CRISPR/Cas9 complex is very efficient at introducing DSBs in the DNA of many cell types (Canver et al., 2014; Dow et al., 2015; Platt et al., 2014) and was convenient for generating gene knockouts, easily created by generating shifts in the reading frame of the targeted gene leading to premature stop codons on both alleles (Hsu et al., 2014; Jinek et al., 2013). This is because most

commonly after a DSB occurs, the broken chromosome is repaired by the error-prone process of NHEJ, which does not allow introduction of specific sequence changes but rather random base insertions or deletions, also known as “indel” mutations (Hsu et al., 2014; Jinek et al., 2013). Generating a specific sequence change, like the introduction of a single *APP* or *PSEN1* fAD mutation, requires the cell to utilize a much rarer DNA repair mechanism called HDR (Hsu et al., 2014). Accomplishing this most commonly involves simultaneously introducing a modified DNA repair template, such as a single stranded oligonucleotide (ssODN), containing both homologous sequence to the genomic region around the DSB and the intended sequence changes, which can be incorporated into the edited genome (**Figure 9**).

Unfortunately, we quickly realized CRISPR/Cas9-mediated mutation knock-in by HDR was incredibly difficult, and overcoming this problem needed to be the first major focus of our experimental efforts. Furthermore, we expected these same issues were being faced by multiple groups around the world trying to implement CRISPR/Cas9 in their favorite model system. Therefore, improving CRISPR/Cas9 technology and developing a new approach for efficient and precise knock-in would be a widely valued effort. The following results are adapted from our recent publications (Kwart & Paquet et al., 2017; Paquet & Kwart et al., 2016).

CRISPR/Cas-blocking mutations increase HDR accuracy by preventing re-editing

Knocking-in pathogenic mutations requires that only the amino acid change caused by these mutations occurs at a targeted locus, while the neighboring amino acids stay unaltered. While attempting to introduce either the *APPswe* or *PSEN1-M146V* fAD mutations into iPSCs using CRISPR/Cas9, we detected HDR by presence of an intended mutation provided via the cognate ssODNs, however most HDR events also contained unwanted indels (**Figure 10**). This was a problematic result as such indels would lead to unwanted amino acid changes.

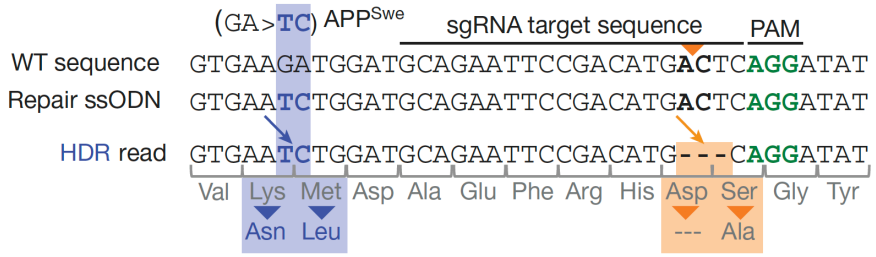

Figure 10. HDR is usually corrupted by unwanted indels.

APP sequencing alignment showing concomitant HDR (blue arrow) and indels (orange arrow) after editing.

The additional unwanted indels we noticed in HDR sequencing reads presumably resulted from the known high nuclease activity of CRISPR/Cas9 (Cong et al., 2013; Dow et al., 2015; Wang et al., 2013), which may continuously re-cut edited loci until sufficient modification by NHEJ prevents further targeting. If so, we

reasoned that this re-editing may be blocked by simultaneously introducing mutations into the NGG PAM sequence or guide RNA binding sequence, which CRISPR/Cas9 requires for targeting (Hsu et al., 2014), as shown in prokaryotes (Jiang et al., 2013). The efficacy of potential blocking mutations had not yet been systematically studied in eukaryotic cells, therefore we tested their effect on HDR accuracy in our established wildtype human iPSCs (see **Appendix I** for info on iPSC generation) and, for comparison, HEK293T cells. We introduced Cas9-eGFP and a single-guide RNA (sgRNA) plasmid together with five pooled repair ssODN templates, which in addition to the *APPswe* or *PSEN1-M146V* pathogenic mutation also contained a putative silent CRISPR/Cas-blocking mutation (**Figure 11A-B**). Although we expect mutations in either of the guanines of the PAM to be most effective in blocking CRISPR/Cas9 activity because the PAM (NGG) sequence is required for Cas9 binding to DNA (O'Connell et al., 2014; O'Geen et al., 2015; Wu et al., 2014), insertion of silent mutations is not always possible at that site due to individual reading frames and codon usages of different edited loci. Therefore, we tested CRISPR/Cas-blocking mutations at various positions upstream in the 20 bp guide RNA targeting sequence that are believed to disturb guide RNA hybridization to target DNA (Hsu et al., 2013; Pattanayak et al., 2013) and thus reduce CRISPR/Cas9 activity. As a control, we added an ssODN containing a silent mutation outside of the guide RNA targeting sequence, which allowed identification of its incorporation by deep sequencing, but should not block CRISPR/Cas-targeting (**Figure 11B**).

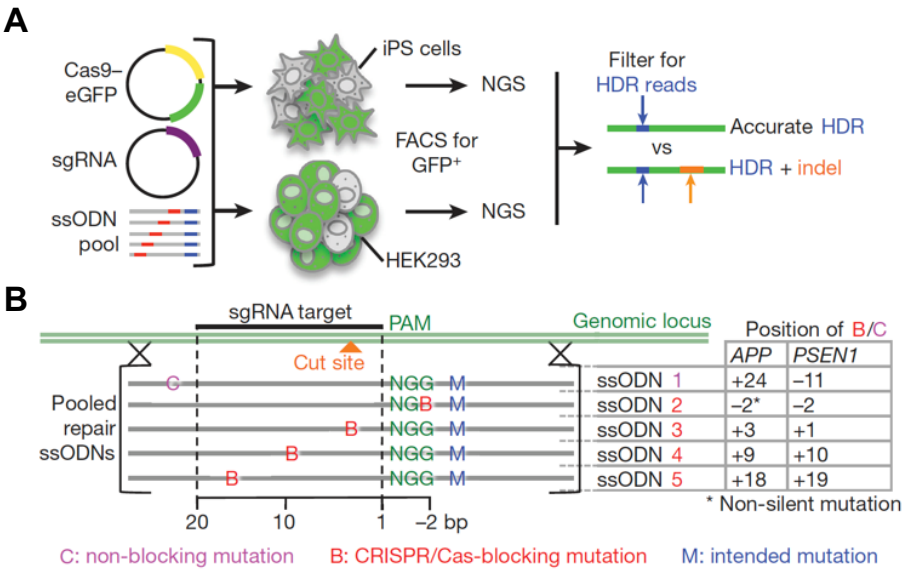

Figure 11. Schematic of experimental setup for CRISPR/Cas-blocking mutation analysis.

A) Experimental setup for gene editing analysis by NGS. Cas9 and sgRNA expressing plasmids were transfected along with ssODNs. GFP+ cells were sorted out by FACS and CRISPR/Cas9 editing was analyzed by NGS. **B)** Schematic of pooled ssODNs used to test effects of CRISPR/Cas-blocking mutations.

We analyzed genomic loci of Cas9-eGFP-expressing cells by Next Generation Sequencing (NGS) (See **Appendix I** for details of sequencing analysis) and determined the fraction of HDR reads (reads where there was incorporation of the pathogenic mutation on the ssODN template). Overall HDR rates for these experiments were approximately 2-3% (data not shown). Next, we filtered to determine the number of HDR reads that were "accurate", i.e., without undesirable indel modifications. We found that a large majority of genomes that incorporated the

pathogenic and control mutation had further indel modifications at both loci, resulting in low levels of accurate HDR (only 6 to 35%; see **Figure 12A-B**). In contrast, the presence of a CRISPR/Cas-blocking mutation in the PAM dramatically increased accurate HDR rates in iPSCs and HEK293 cells at both loci (**Figure 12A-B**). The remaining "inaccurate" HDR reads all contained indel mutations, which were likely generated by NHEJ events prior to or during homology-directed repair that did not block further editing. Silent mutations in the sgRNA targeting site increased accurate HDR in both iPSCs and HEK293 cells at the *APP* locus, illustrating that for this locus, optimal guide RNA binding is crucial for CRISPR/Cas9 activity (**Figure 12A**). At the *PSEN1* locus accurate HDR was only modestly increased by some of the guide RNA targeting site mutations (**Figure 12B**). This indicates that the activity of the *PSEN1*-targeting sgRNA is less affected by mutations at the guide RNA binding sequence. Results did not differ when ssODN templates from the abovementioned pool were transfected separately into HEK293 cells (**Figure 13**).

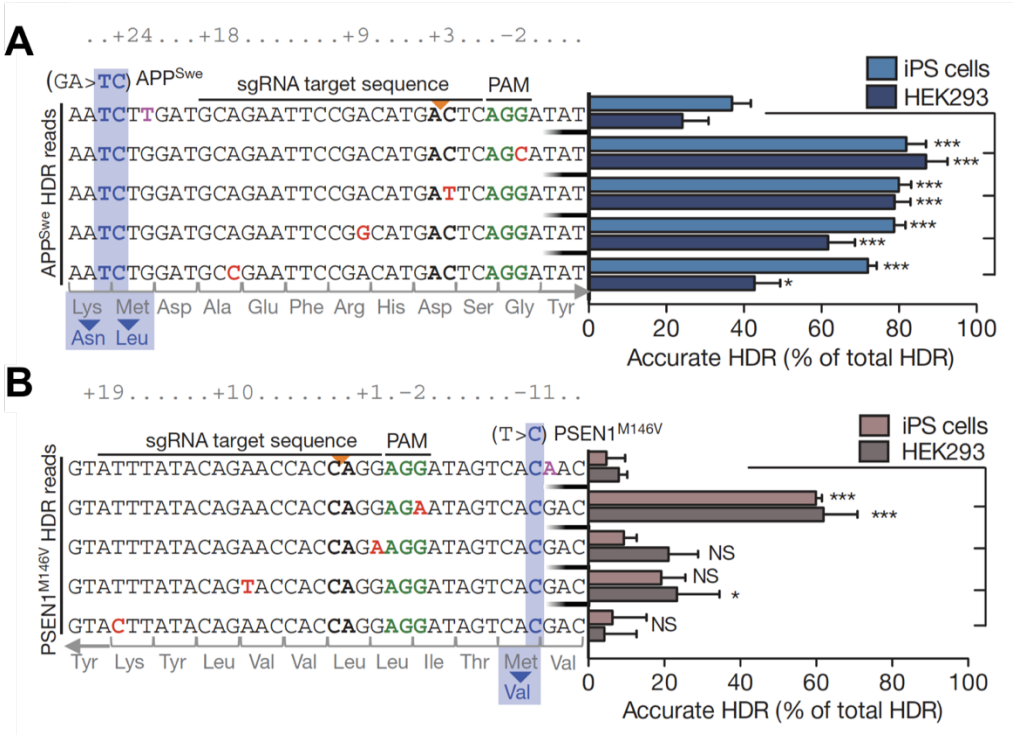

Figure 12. CRISPR/Cas-blocking mutations increase HDR accuracy.

A-B) Percentages of accurate HDR (HDR only events, i.e., without concomitant indels) for blocking or control mutations at *APP* (**A**) and *PSEN1* (**B**) loci in pooled transfected iPSCs and HEK293 cells. Values represent mean ± SEM (n=3). ***$P < 0.001$, **$P < 0.01$, *$P < 0.05$, 1-way ANOVA.

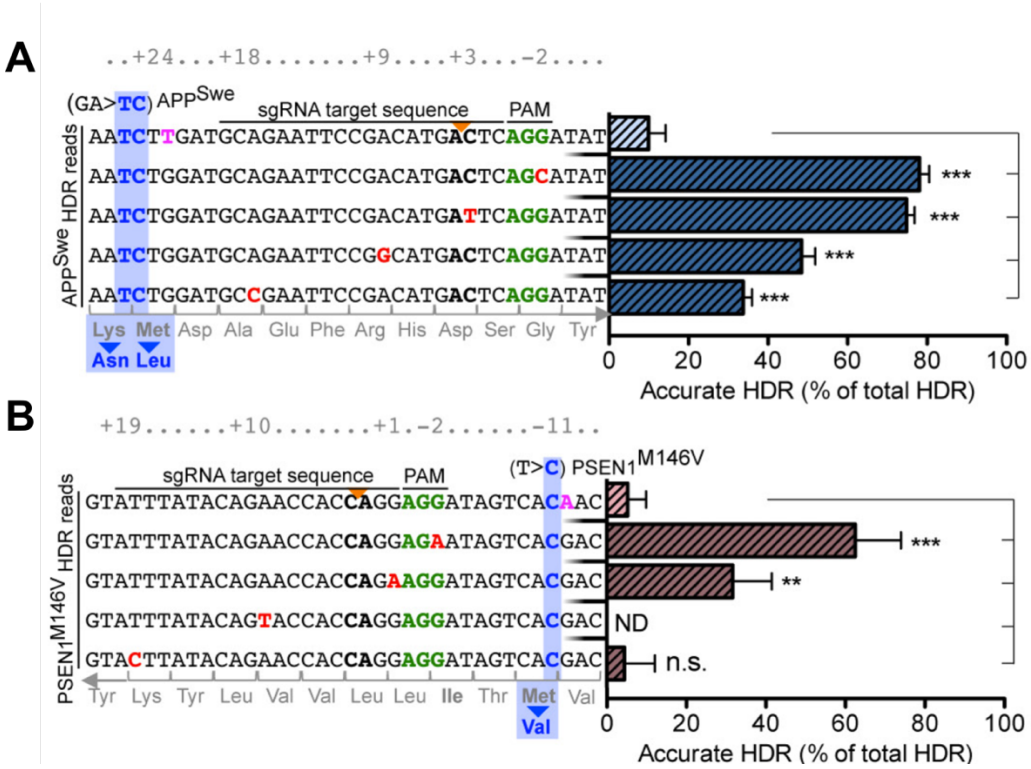

Figure 13. Analysis of CRISPR/Cas-blocking mutations using un-pooled ssODNs

Accurate HDR editing rates (HDR only events, i.e., without concomitant indels) from 5 unpooled templates containing intended pathogenic and CRISPR/Cas-blocking or non-blocking control mutations. Percentages of accurate HDR for reads containing B or C mutations at the *APP* (**A**) and *PSEN1* (**B**) locus in HEK293 cells. Values represent mean ± SEM (n=3). ND = not detected; n.s. = not significant. $^{***}P < 0.001$, $^{**}P < 0.01$, 1-way ANOVA.

Single CRISPR/Cas-blocking had much reduced efficacy in the sgRNA target sequence at the *PSEN1* locus compared to *APP*, suggesting the *PSEN1* sgRNA can overcome minimal sequence mismatches. We therefore tested the efficacy of using multiple blocking mutations positioned in the guide RNA target seed sequence and found an improvement of editing accuracy that was comparable to that of PAM-

blocking mutations (**Figure 14A**). This result corroborates previous studies, which found that multiple consecutive mismatches within the guide RNA seed sequence largely prevent targeting by the CRISPR/Cas9 complex (Hsu et al., 2013; Kuscu et al., 2014; Pattanayak et al., 2013). Unfortunately, it may be impossible to use multiple consecutive sgRNA-blocking mutations that are silent. Therefore, we tested the efficacy of using multiple silent blocking mutations in the guide-RNA target sequence. We also found that improvements in editing accuracy comparable to that of PAM-blocking mutations were seen when multiple silent blocking mutations in the sgRNA sequence were incorporated (**Figure 14B**). Additionally, we confirmed that the frequency, position, and size of all indels detected in these abovementioned experiments followed the distribution expected from previous studies (Mali et al., 2013; Yang et al., 2013) (**Figure 15**).

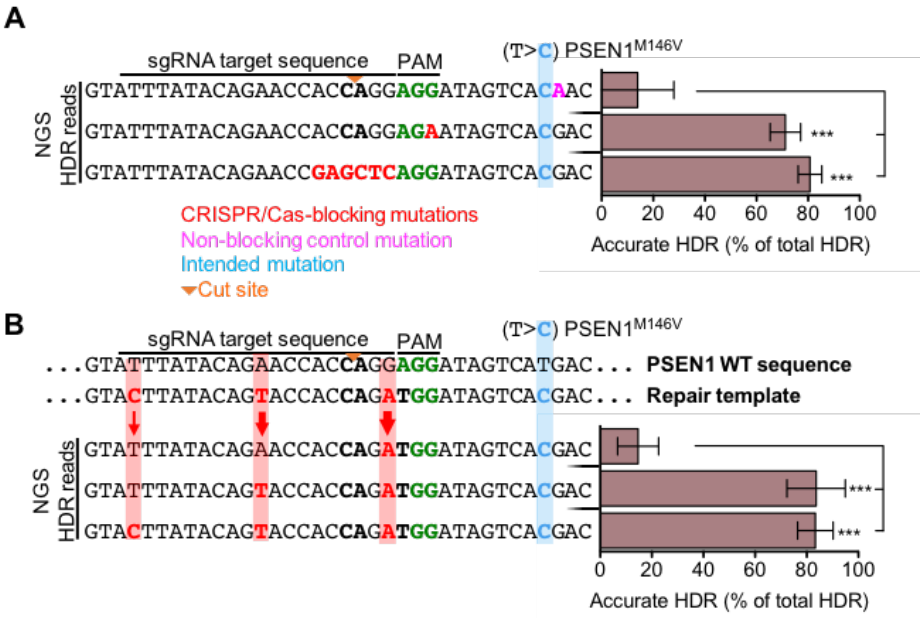

Figure 14. Multiple CRISPR/Cas-blocking mutations in the sgRNA target sequence increase editing accuracy.

Accurate HDR editing rates (HDR only events, i.e., without concomitant indels) in a pool of transfected iPSCs determined for the *PSEN1-M146V* locus. **A**) Introducing several blocking mutations within the first 6 bases of the guide RNA target sequence blocks re-editing as efficiently as PAM-altering CRISPR/Cas-blocking mutations. **B**) Accurate HDR editing rates using an ssODN with three interspersed silent guide RNA-altering CRISPR/Cas-blocking mutations as a repair template in a pool of transfected iPSCs. HDR events with only partial incorporation of blocking mutations result in reduced overall HDR-mediated editing accuracy (see top read, only 'A' incorporated). For (**A**) and (**B**) values represent mean ± SEM (n = 3). ***$P < 0.001$, one-way ANOVA.

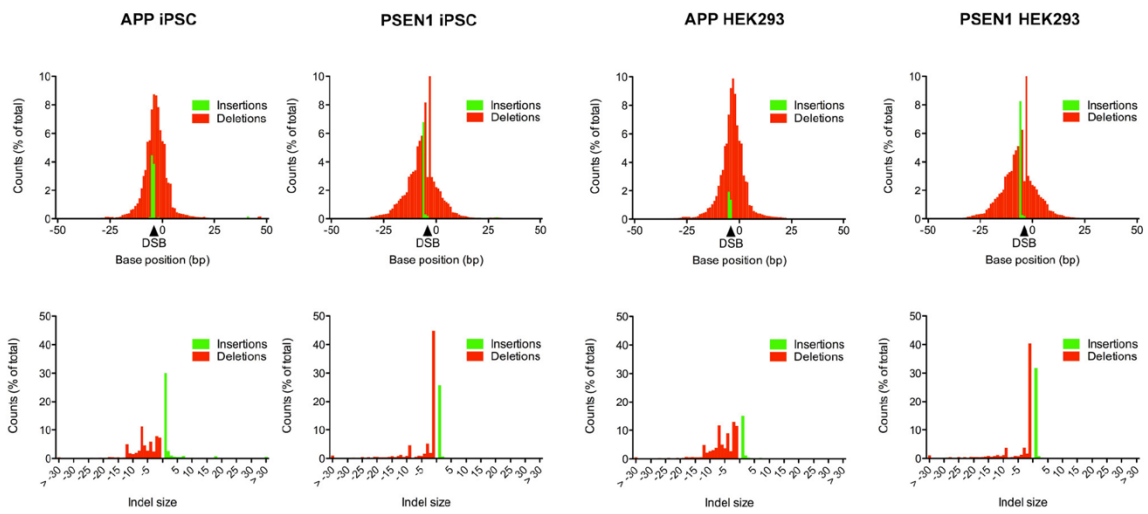

Figure 15. Analysis of CRISPR/Cas9-induced indels in gene edited iPSCs and HEK293T cells.

Plots depicting frequency of indels at each position around the targeted locus in all NGS reads with editing events from the analysis shown in Figure 12. Insertions are plotted at the location where they begin, and deletions are plotted across all deleted base positions (top). Histogram illustrating distribution of indel sizes (bottom).

Surprisingly, when studying the HDR events at *APP* and *PSEN1* loci in detail, we noticed that between 6% and 11% of the HDR reads contained more than one CRISPR/Cas-blocking or non-blocking control mutation (**Figure 16**). Since each ssODN repair template provides only one control or CRISPR/Cas-blocking mutation, the cells must have used multiple distinct ssODNs from the pool for repair, presumably in multiple rounds of HDR that occurred after repeated Cas9 editing. These data indicate that at a given locus at least 3 rounds of cut-and-repair events can occur before a genomic edit is final. This hypothesis is further supported by the

fact that at both loci these “double HDR” events more often contain a non-blocking control mutation than a CRISPR/Cas-blocking mutation (**Figure 16**).

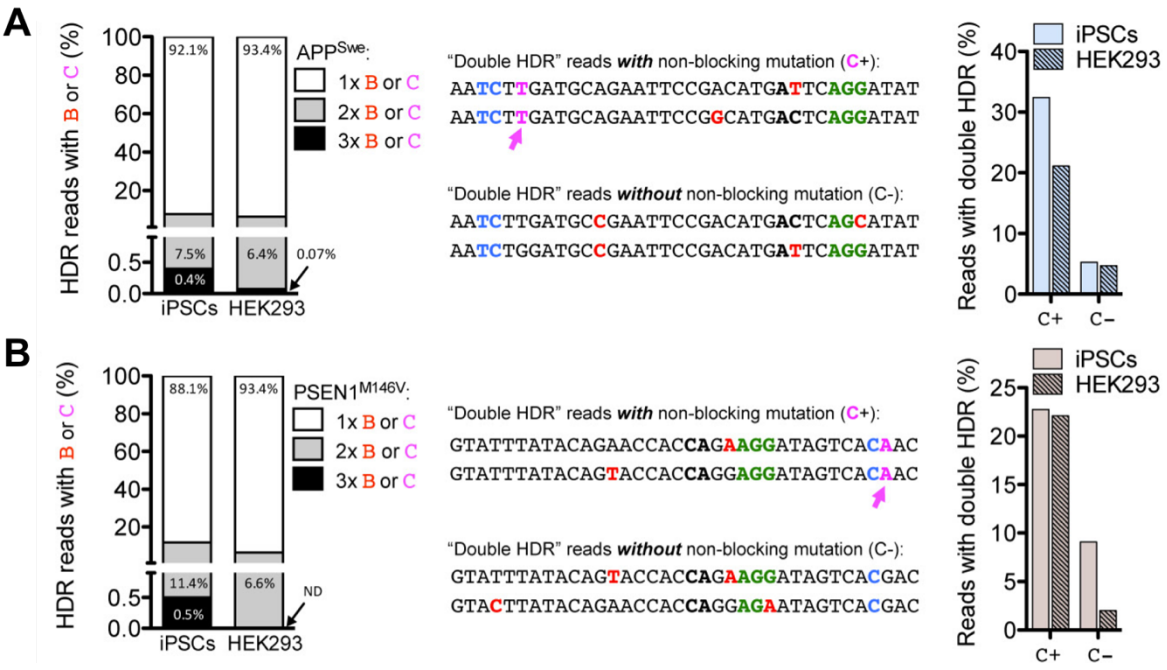

Figure 16. CRISPR/Cas-blocking mutations are incorporated in multiple rounds of re-editing.

A-B) Proportion of NGS reads containing putative single, double, or triple HDR events (left) for *APP* (**A**) and *PSEN1* (**B**). Putative “double HDR” examples of the most frequent reads that either contain a non-blocking control mutation C with an additional CRISPR/Cas-blocking mutation B, or do not contain C and have two different CRISPR/Cas-blocking mutations (middle). Reads that contain the non-blocking mutation (C+) are more frequently re-edited to incorporate a CRISPR/Cas-blocking mutation (“double HDR”) than reads containing a blocking mutation B instead of the non-blocking mutation C (C-). To facilitate data analysis, all replicates were pooled to increase read numbers for rare events.

Taken together, our results provide direct evidence that CRISPR/Cas9 will continuously re-edit a genomic locus, even after HDR occurs, until sufficient modification prevents further activity. This prevalent and deleterious process can be blocked by introducing a modified repair template with CRISPR/Cas-blocking mutations, preferably in the PAM. This simple modification can increase the number of accurately edited alleles up to tenfold (6% for non-blocking vs. 60% for blocking mutations at the *PSEN1* locus, see **Figure 12**), which in diploid cells has the potential to increase the probability of editing both alleles accurately by 100-fold (6% x 6% = 0.36% vs. 60% x 60% = 36%, assuming independent editing of both alleles). Therefore, CRISPR/Cas-blocking mutations can dramatically influence the feasibility of a desired genome editing experiment.

CRISPR/Cas9 editing results mostly in bi-allelic changes

We tested our approach of simultaneous introduction of either the *APPswe* or *PSEN1-M146V* mutations together with CRISPR/Cas-blocking mutations by generating single-cell-derived clones of iPSCs. While we could readily isolate a number of clones with bi-allelic HDR-mediated incorporation of both pathogenic and CRISPR/Cas-blocking mutations without additional indels (data not shown), almost all clones that had seemingly undergone only mono-allelic mutation incorporation (HDR at only one allele as assessed using an RFLP assay; see methods **Appendix I** for details) contained unwanted indels at the “non-HDR” allele (**Figure 17**). Therefore, heterozygous lines could not be readily isolated by mono-allelic HDR

alone. Previous studies have identified a similar tendency for CRISPR/Cas9 editing to mostly result in bi-allelic indel modifications (Dow et al., 2015; Wang et al., 2013). This tendency, in addition to the established known high activity of the CRISPR/Cas9 complex (Cong et al., 2013; Dow et al., 2015; Wang et al., 2013), makes it plausible that potential targets in a cell are all edited at a similar rate in the presence of Cas9 and sgRNA, thereby dramatically reducing the probability of isolating cells in which only one allele is edited by HDR while the other allele is unmodified. This observation raised the question of how, if not by mono-allelic HDR, to isolate clones heterozygous at the intended site without indels at the other allele.

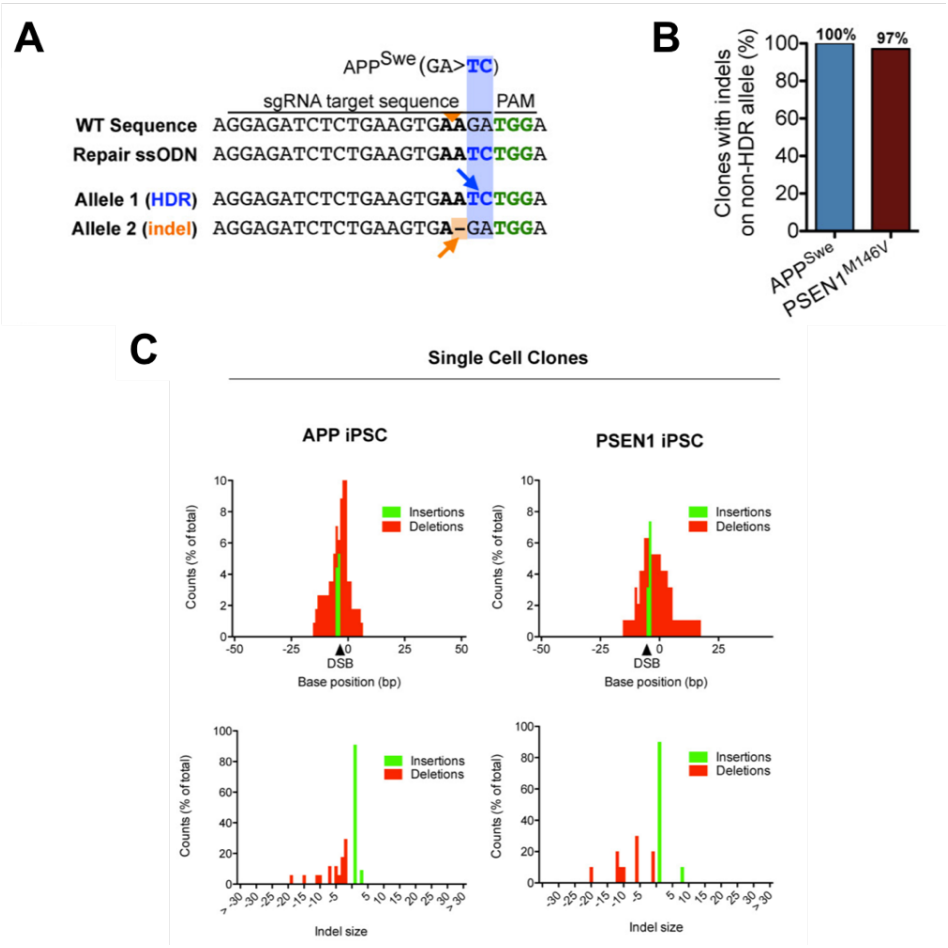

Figure 17. Mono-allelic HDR clones contain indels on the other non-HDR allele.

A) Sanger sequencing reads of both *APP* alleles of a single-cell clone with mono-allelic HDR (blue arrow), determined using the PolyPeak Parser tool (see **Appendix I**). The non-HDR allele is altered by NHEJ in the sgRNA target sequence (orange arrow). **B**) Single-cell clones with HDR on one allele are mostly altered by NHEJ on the non-HDR allele (*APP* n=26, *PSEN1* n=34). **C**) Indel position and size in mono-allelic HDR single-cell-derived iPSC clones.

A monotonic inverse relationship between the rate of mutation incorporation and distance from the CRISPR/Cas9 cleavage site

While studying deep sequencing data from genomes edited using ssODNs bearing both pathogenic and PAM-altering CRISPR/Cas-blocking silent mutations, we observed that sequencing reads that had incorporated a silent CRISPR/Cas-blocking mutation by HDR did not always contain the pathogenic mutation (**Figure 18**). These reads were most abundant when the pathogenic mutation and CRISPR/Cas9 cleavage site were not in close proximity. This observation is consistent with earlier reports of a distance effect influencing mutation incorporation by HDR using other gene editing systems (Beumer et al., 2013; Elliott et al., 1998; Rivera-Torres et al., 2014; Taghian and Nickoloff, 1997; Yang et al., 2013). More recent studies in mouse and human cancer cells (Bialk et al., 2015; Inui et al., 2014) suggested a similar effect for CRISPR/Cas9 editing, however, the molecular basis of this distance phenomenon, and how it depends on guide RNA sequence, repair template composition, base position or genomic context remains to be elucidated. We reasoned that if a predictable relationship between distance and mutation incorporation exists at multiple loci, it could be exploited to selectively control mutation incorporation at each allele based on probability alone. In other words, if the two HDR events depicted by NGS reads in **Figure 18** represented the two alleles of a single cell, heterozygous editing of a pathogenic mutation will be achieved.

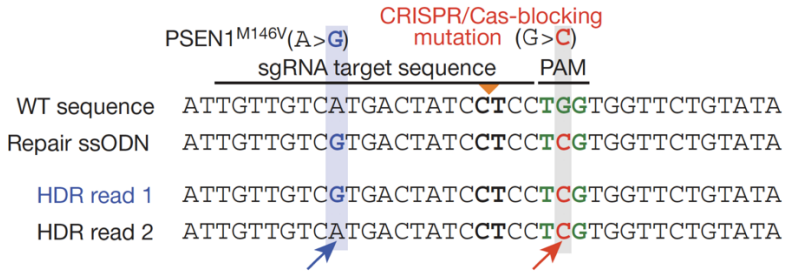

Figure 18. Pathogenic mutation is not always incorporated by CRISPR/Cas9-mediate HDR.

PSEN1 sequencing alignment showing HDR-mediated introduction of a CRISPR/Cas-blocking mutation (red arrow) with or without the pathogenic mutation (blue arrow).

To systematically characterize this distance effect, we performed an unbiased scan of oligo mutation incorporation rates at both the *APP* and *PSEN1* locus, using one sgRNA per locus combined with a pool of 20 different ssODNs. Each ssODN contained a unique CRISPR/Cas-blocking 3 bp barcode sequence (in this experiment we did not restrict ourselves to silent mutations) as well as a single intended point mutation at increasing distances from the CRISPR/Cas9 cleavage site (**Figure 19A**, oligo sequences can be found in **Appendix I**). Cas9, sgRNA and ssODN pools were transfected into iPSCs and HEK293T cells. Gene editing outcomes at *APP* and *PSEN1* loci was assessed by NGS, using the CRISPR/Cas-blocking barcode sequence to identify reads with HDR-mediated incorporation of each ssODN. Strikingly, we found a clear monotonic inverse relationship between the rate of mutation incorporation and distance from the CRISPR/Cas9 cleavage site that did not differ significantly for *APP* and *PSEN1* in either iPSCs or HEK293 cells

(**Figure 19B-C**). Moreover, when comparing 100bp ssODNs to longer ssDNA or dsDNA HDR repair templates the distance relationship was similar (**Figure 20**), suggesting that such a phenomenon is not influenced by the repair templates themselves but instead arises from an intrinsic property of the CRISPR/Cas9-mediated DSB.

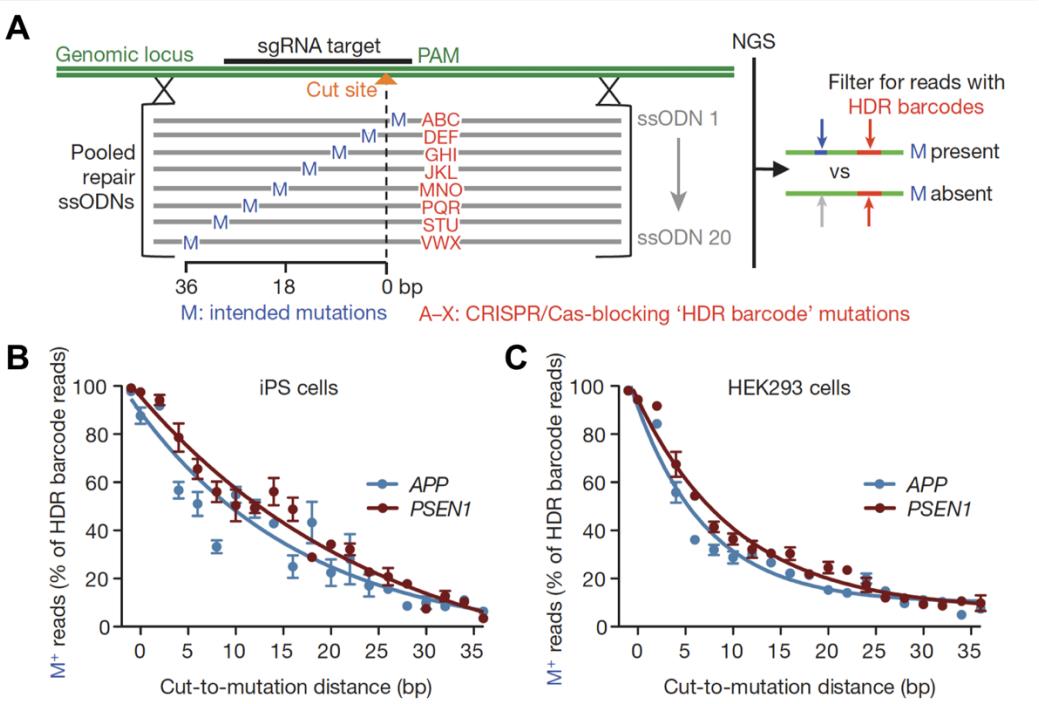

Figure 19. A monotonic inverse relationship between mutation incorporation and distance from the CRISPR/Cas9 cleavage site.

A) Pooled ssODNs used to scan mutation incorporation rates based on cut-to-mutation-distance. Barcode mutations (red) identify HDR-reads and mutation M position during NGS analysis. **B-C**), A monotonic relationship underlies the rate of mutation M incorporation and cut-to-mutation distance during HDR in both iPSCs (**B**) and HEK293 cells (**C**) (n=4 for iPSCs, n=3 for HEK293); goodness of fit: R^2(*APP*) = 0.75(iPSC) / 0.96(HEK293), R^2(*PSEN1*)

= 0.94(iPSC) / 0.97(HEK293); curves for *APP* and *PSEN1* are not significantly different, two-tailed t-test: p=0.31(iPS) / 0.06(293).

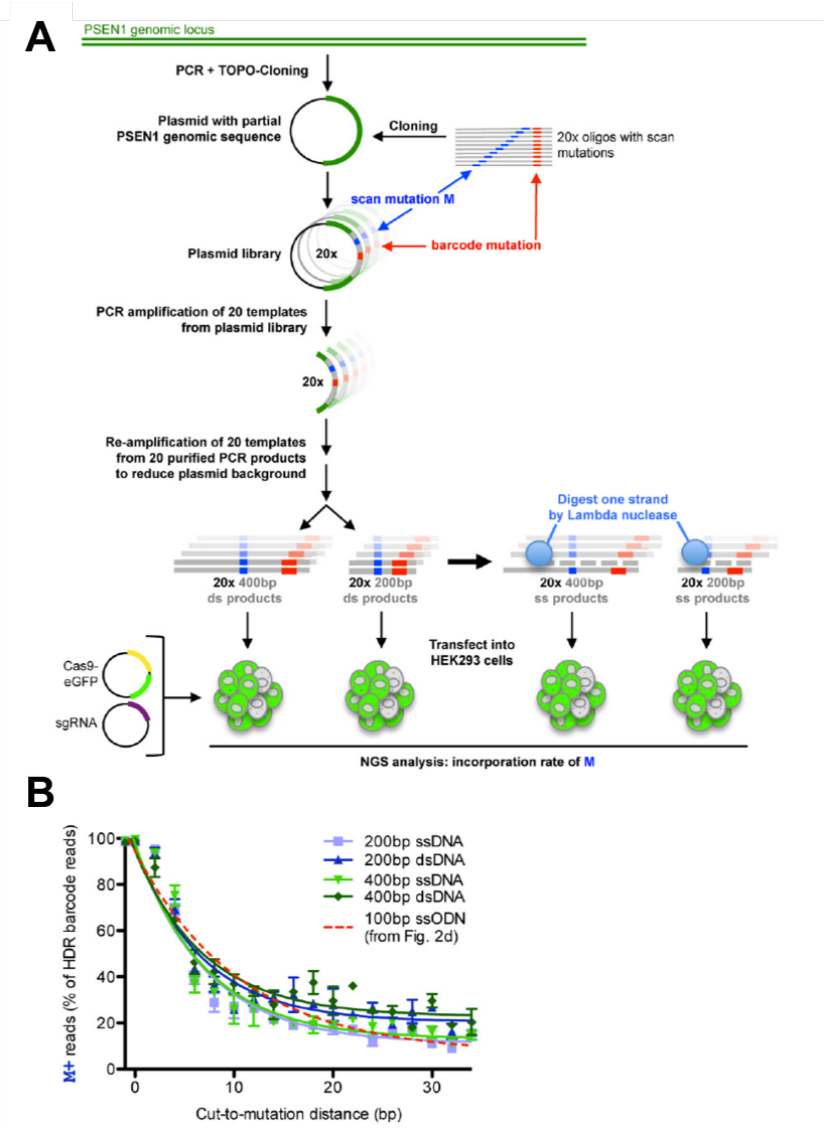

Figure 20. Longer ssDNA or dsDNA HDR templates do not influence mutation incorporation probabilities related to cut-to-mutation distance.

A) Schematic describing the generation of large ssDNA and dsDNA HDR repair templates for the *PSEN1* locus (see **Appendix I** for more details). **B**) The monotonic relationship between incorporation of intended mutations (M)

by HDR and cut-to-mutation distance is not altered by providing longer ssDNA and dsDNA templates (n=2). Red hashed trendline shows previously determined 100-nt oligo scan result (from **Figure 19B**) for comparison.

To address whether loci, guide RNA activity or ssODNs sequence differences also influence this relationship we utilized three sgRNA/ssODN pairs (see oligo sequences in **Appendix I**) to target a DSB at short, intermediate and long distances from the *APPswe* or *PSEN1-M146V* pathogenic mutation sites in iPSCs (**Figure 21**). Each ssODN repair template contained a silent CRISPR/Cas-blocking mutation in addition to the intended pathogenic mutation, and the presence of both mutations was analyzed by NGS.

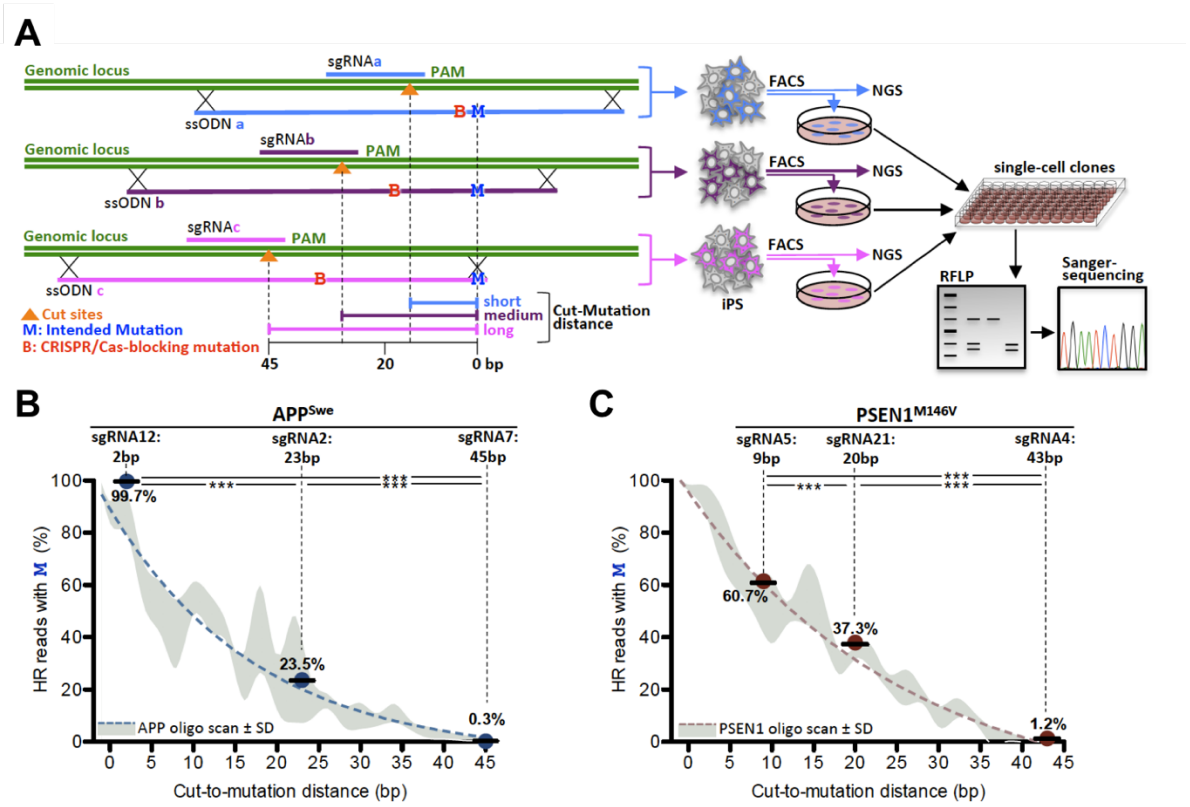

Figure 21. Analysis of the "distance effect" using 3 independent sgRNA-ssODN pairs in iPSCs.

A) Experimental setup using three sgRNA/ssODN pairs per locus with increasing cut-to-mutation distance. Edited iPSCs were analyzed by NGS (or grown for clonal analysis in **Figure 22**). **B-C**) Incorporation rate of APP and PSEN1 pathogenic mutations at increasing distance from the cut site targeted by three distinct sgRNA/ssODN pairs is governed by distance. Incorporation rates (solid dots represent mean ± SEM, note SEM is too small to be visible, (n=3)) match almost exactly the curves for each locus previously determined by oligo scan (hashed trend line ± SD of raw data from **Figure 19B**). ***P < 0.001, 1-way ANOVA.

As expected, we found that at both the *APP* and *PSEN1* locus, sgRNAs targeting a DSB at short distances from the pathogenic mutation (2bp for APP-

sgRNA12, 9bp for PSEN1-sgRNA5) resulted in very efficient incorporation of both mutations, whereas the rate of incorporation of the pathogenic mutation dropped significantly with increasing distance (**Figure 21B-C**). Notably, the incorporation rates for each sgRNA/ssODN pair matched almost exactly the curves for each locus determined by the oligo scan data (**Figure 19B**, plotted as dashed lines in **Figure 21B-C**). Together, the finding of similar distance-incorporation relationships for multiple independent sgRNAs, as well as multiple ssODN and longer repair templates at several genomic loci in two cell types suggests that a generalizable and predictable "distance effect" may govern incorporation of any intended sequence change during gene editing by HDR.

Using the distance effect for efficient introduction of targeted homo- and heterozygous mutations

Our data imply that the cut-to-mutation distance needs to be minimized for efficient homozygous incorporation of a mutation. For example, to yield 25% homozygous clones the probability of mutation incorporation per allele needs to be above 50% (50% x 50% = 25%), which requires a cut-to-mutation distance below approximately 10 bp (see **Figure 19B-C**). The distance effect also predicts that as cut-to-mutation distances increase and probability of mutation incorporation drops, the odds of generating a mono-allelic alteration should increase. To examine whether the distance effect could be exploited to not only introduce targeted homozygous but also heterozygous mutations, we first determined an overall

probability of mutation incorporation (i.e. single allele frequencies for pathogenic mutation) for iPSCs by combining our oligo scan data from *APPswe* and *PSEN1-M146V* loci (determined in **Figure 19B**). By assuming that HDR takes place independently at both alleles, we calculated the expected distance ranges that would favor homozygous, heterozygous and wildtype genotypes at a given distance by multiplying single allelic probabilities (**Figure 22A**, see **Appendix I** for details of calculation).

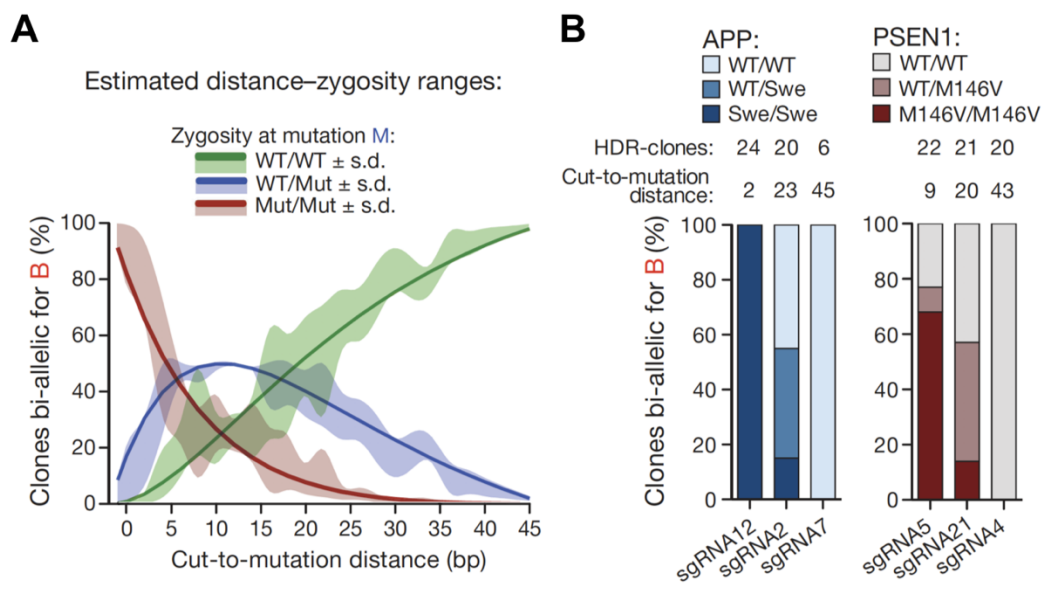

Figure 22. Exploiting the "distance effect" to predict zygosity using CRISPR/Cas9-mediated HDR in iPSCs.

A) Predicted distance ranges for desired zygosities, calculated based on oligo scan data (**Figure 19B** and **Appendix I**). **B**) Frequency of different *APP* and *PSEN1* mutation genotypes in single cell clones with bi-allelic HDR of blocking mutations. Indicated zygosities fit to predicted values. HDR clones = number of Sanger sequenced clones that had all undergone bi-allelic incorporation of a CRISPR/Cas-blocking mutation as determined by RFLP analysis.

To experimentally test these predictions, we derived single-cell clones from iPSCs electroporated with the three sgRNA/ssODN pairs as described in **Figure 21A**. We isolated clones that had undergone bi-allelic incorporation of the silent CRISPR/Cas-blocking mutation as determined by RFLP assay (approximately 2-3% of clones on average) and assessed their zygosity for the pathogenic mutation by Sanger sequencing (**Figure 22B**). Notably, we found that the rate of homo- and heterozygosity correlated well with our predictions based on the "distance effect" (**Figure 22A**). The *APP* sgRNA/ssODN pair targeting 2 bp away from the pathogenic mutation yielded 100% clones homozygous for the pathogenic mutation, whereas the *APP* sgRNA/ssODN pair targeting 23 bp away yielded more than twice as many heterozygous as homozygous clones. About half of the clones for this distance did not contain the pathogenic mutation on either allele. The *APP* sgRNA/ssODN pair targeting 45 bp away from the mutations did not yield any clones containing the pathogenic mutation, even though this mutation was present in the ssODNs used as an HDR template (**Figure 22B**). Similar results were also obtained for PSEN1 (**Figure 22B**). We noted that for *PSEN1* sgRNA5 (cut-to-mutation distance 9 bp), more homozygous clones were generated than predicted based on distance (67% actual vs. 20-40% predicted). This may reflect differences in usage of the other allele as a repair template for HDR at some loci or arise from subtle differences in DSB response and repair. Taken together, our results demonstrate that (1) choosing the optimal cut-to-mutation distance is crucial for efficient HDR-based genome editing,

and (2) the distance effect facilitates selection of the most efficient guide RNAs for engineering both homo- and heterozygous HDR-mediated gene modifications.

Selection for heterozygous mutations using mixed HDR templates

As shown above, the selection of a suitable guide RNA is limited not only by its specificity and activity for the targeted locus, but also by the requirement for a PAM close to the intended target site. For a given sequence these requirements may be too restrictive and result in cases where no suitable guide RNA is available for homo- or heterozygous knock-in by our approach. Choosing a guide RNA with a targeting site more than 10 bp away from the mutation may still yield homozygous clones, albeit at much lower efficiencies, however obtaining heterozygous clones with a guide RNA that targets very close to the mutation site (<3 bp, **Figure 22A**) is highly unlikely.

We reasoned that this problem could be circumvented by equimolar mixing of two ssODNs that both harbor a CRISPR/Cas-blocking mutation, with only one containing the pathogenic mutation (**Figure 23**). We tested this approach on the APP locus using the most closely targeting sgRNA available, which in our previous analysis did not yield any heterozygous clones (APP-sgRNA12, see **Figure 23A**). When analyzing single cell-derived clones with bi-allelic incorporation of the CRISPR/Cas-blocking mutation by RFLP and Sanger sequencing, we did indeed find an appreciable number of clones heterozygous for the intended pathogenic mutation, thereby validating the approach. Unexpectedly, we observed a higher

frequency of clones homozygous for the pathogenic mutation than the predicted 50% (**Figure 23A**). This increased frequency is consistent with the increased incorporation rate of the ssODN containing both the CRISPR/Cas-blocking and pathogenic mutation, as determined by NGS of edited loci in pooled cells from the same experiment (**Figure 23A**). The ssODN containing the pathogenic mutation might be favored because the mutation lies in the sgRNA seed sequence, which may more effective at blocking CRISPR/Cas as described above.

This observation motivated us to test an alternative approach of again using APP-sgRNA12 and mixing two ssODNs that contained either only the intended pathogenic mutation, or a CRISPR/Cas-blocking mutation, but at identical positions in the sgRNA target site (**Figure 23B**). Strikingly, and as expected, nearly half of the clones were heterozygous for the pathogenic mutation at one allele and contained the CRISPR/Cas-blocking silent mutation at the other. Deep sequencing confirmed incorporation of both oligos at nearly equal rates (**Figure 23B**). The rate of wildtype clones was not assessed, because the silent mutation present in the wildtype ssODN template did not introduce a restriction site for RFLP screening. However, given the ~50% ssODN incorporation rates determined by deep sequencing, about 25% of HDR clones are predicted to be wildtype. We also demonstrated at the *PSEN1* locus the ability to mix repair templates to predictably and significantly increase the number of heterozygous clones obtained using the *PSEN1* sgRNA that cleaves closest to the *M146V* mutation site (PSEN1-sgRNA5, **Figure 23C**). Together, these data support the strategy of using a mixture of two oligonucleotides

to introduce different sequences at each allele and thereby obtain desired heterozygous modifications in spite of the constraints of the targeted locus.

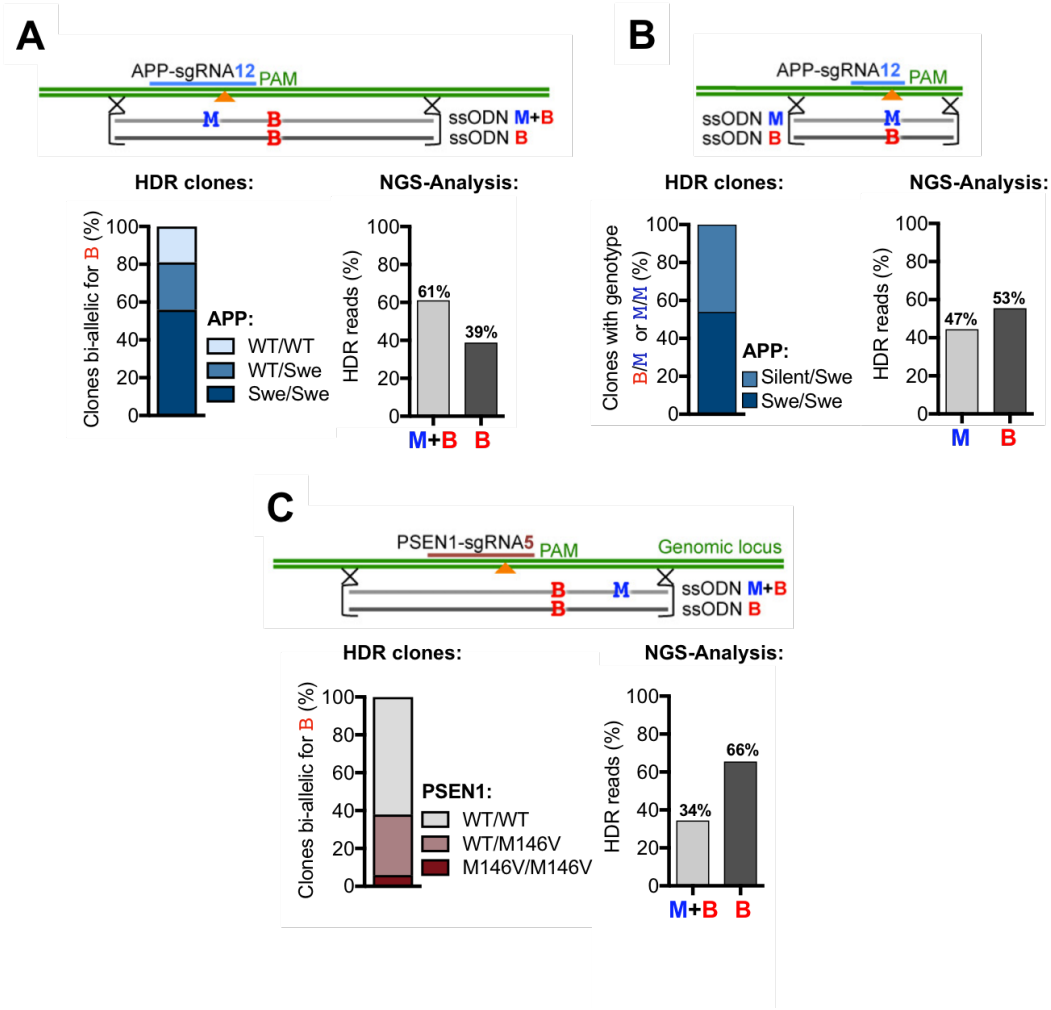

Figure 23. Introduction of heterozygous or homozygous mutations into iPSCs by using mixed HDR templates.

A-B) Mixed ssODN editing approach at the *APP* locus with blocking mutations in both (**A**) or one (**B**) ssODNs (top); zygosity quantification of single-cell clones and incorporation rates of CRISPR/Cas-blocking mutation B and pathogenic mutation M determined by NGS analysis (bottom). Note that for the M/B approach in **B**, both oligos are incorporated at near equal levels,

as they have similar blocking activities, whereas for the M+B/B approach in **A**, the M+B ssODN is preferentially incorporated, presumably due to a synergistic blocking effect of both M and B. For the clone quantification in (**B**) the rate of wildtype clones was not assessed, because the silent mutation did not introduce a restriction site for screening. **C**) Mixed ssODN editing approach at the *PSEN1-M146V* locus (top). Using an sgRNA with the smallest possible cut-to-mutation distance (PSEN1-sgRNA5, 9bp), two ssODNs were provided, each containing the same silent PAM-altering CRISPR/Cas-blocking mutation B, but only one containing the pathogenic mutation M. Frequencies of pathogenic mutation genotypes in single cell clones with bi-allelic HDR of B (left) and incorporation rates of CRISPR/Cas-blocking and pathogenic mutations by NGS (right). Note that due to the 9bp distance to the cleavage site, the incorporation of M is lower than 50% (as expected from the distance effect).

Conclusions

I began this chapter by highlighting a major problem with CRISPR/Cas9 gene editing technology, which, at the time of these studies, was not very well communicated. Specifically, we noticed early in our utilization of CRISPR/Cas9 in wildtype iPSCs that not only was HDR-mediated mutation incorporation rare, it was incredibly inaccurate due to the innate high activity of the CRISPR/Cas9 complex. As a result, HDR-mediated mutation incorporation is almost always corrupted by additional unwanted indel mutations, making it nearly impossible to use CRISPR/Cas9 for precise gene editing in iPSCs. Related to this is also the problem

of generating heterozygous clones, since the highly active CRISPR/Cas9 complex virtually always introduces unwanted indel mutations at the non-HDR allele in a single cell. In the work described above, we overcame these two technological barriers and report a CRISPR/Cas9-based genome editing framework that allows for selective introduction of specific mono- and bi-allelic sequence changes with high efficiency.

Utilizing human iPSCs and HEK293 cells, we first established that by simultaneously introducing a CRISPR/Cas9-blocking point mutation in the PAM or guide RNA binding sequence, accurate HDR-mediated incorporation of an intended pathogenic mutation can be significantly increased up to 10-fold per allele. Next, by systematically characterizing HDR-mediated mutation introduction at varying distance to the CRISPR/Cas9 cleavage site, we determined a predictable, monotonic inverse relationship between distance of an intended sequence change and its rate of incorporation, thereby corroborating and extending previous evidence of such a distance effect (Beumer et al., 2013; Bialk et al., 2015; Elliott et al., 1998; Inui et al., 2014; Rivera-Torres et al., 2014; Taghian and Nickoloff, 1997; Yang et al., 2013). Additionally, we exploited this relationship to derive distance ranges that enable the selection of the most suitable sgRNAs for the efficient generation of homo- and heterozygous clones. Furthermore, we demonstrated that heterozygous changes can also be achieved by reducing the relative concentration of the intended mutation in the repair template by mixing mutant with non-mutant repair templates. In this work we introduced pathogenic mutations, but it should be noted that our

approach of manipulating cut-to-mutation distance or repair template concentration can be applied to any intended sequence change at virtually any loci.

Discussion

The findings in this study establish a framework for efficient CRISPR/Cas9-mediated introduction of targeted mono- and bi-allelic mutations into eukaryotic cells by characterizing the dynamics of homologous recombination and highlight the utility of this technology for studying genetic disorders. The widespread use of CRISPR/Cas9 to induce specific genomic changes depends on strategies to increase homologous recombination, while at the same time reducing non-specific repair, such as NHEJ. Recently, several groups have demonstrated increased HDR rates by either cell cycle synchronization (Lin et al., 2014), activation of β3-adrenergic-receptors (Yu et al., 2015), or shRNA knockdown or pharmacological inhibition of components of the NHEJ pathway (Chu et al., 2015; Maruyama et al., 2015). Although these studies provide valuable improvements, they do not block CRISPR/Cas9 activity after HDR has occurred, which we show leads to repeated editing of genomic loci in a majority of cases due to the high activity of the CRISPR/Cas9 complex. One approach to reduce this undesirable re-cutting may be to titrate down Cas9 or guide RNA levels to reduce overall activity or use a modified Cas9 that does not fully cleave the DNA (e.g., a nickase) (Ran et al., 2013). However, in our hands this resulted in a drop in overall HDR rates to a level that makes manual single cell clone picking impractical (data not shown). We therefore

kept Cas9, sgRNA and ssODNs at a constant concentration at which HDR was most efficient. Our approach of using CRISPR/Cas-blocking silent mutations significantly increases accurate HDR events up to 10-fold for a given allele, with the potential to provide a nearly 100-fold increased probability of detecting desired HDR events at both alleles. These dramatic benefits provided by CRISPR/Cas-blocking mutations can be combined with other complementary approaches described above to further improve HDR efficiency.

In addition to improving the rate of accurate HDR, understanding the dynamics of homologous recombination of a repair template at a genomic locus targeted by CRISPR/Cas9 is crucial to efficiently direct the outcome of such a targeting event. We addressed this by systematically interrogating HDR-mediated incorporation of multiple repair templates at two independent genomic loci in two different cell types by high-throughput NGS analysis. This unbiased approach allowed us to extend previous evidence for a distance effect (Beumer et al., 2013; Bialk et al., 2015; Elliott et al., 1998; Inui et al., 2014; Rivera-Torres et al., 2014; Taghian and Nickoloff, 1997; Yang et al., 2013) and define a specific inverse relationship between the distance of a base from the site of CRISPR/Cas9 cleavage and the rate of its incorporation by HDR. The length of gene conversion tracts we determined for CRISPR/Cas9 editing in human iPSCs and HEK293 cells was very similar to tract length observed for TALENs in human iPSCs and other human cell types (i.e., incorporation drops significantly between 10-20 bp) (Rivera-Torres et al., 2014; Yang et al., 2013), however, it differed markedly from that observed with zinc

finger nucleases in Drosophila (over 3,000 bp) (Beumer et al., 2013) and restriction enzymes in rodent cells (80-200 bp) (Elliott et al., 1998; Taghian and Nickoloff, 1997). This divergence might reflect species differences, for example varying activities of repair pathways, or differences in the types of cleavage, e.g. sticky ends for restriction enzymes versus blunt ends for TALENs and CRISPR/Cas9, which may affect strand resection and repair. Variations in analysis may also play a role, for example some studies used selection markers, which may increase the representation of rare events, especially if the number of analyzed clones is small. We therefore note that controlling zygosity by exploiting the distance effect may work best in systems where short gene conversion tracts are more likely, whereas oligo mixing is a more universally applicable approach.

The distance effect we observed for CRISPR/Cas9 editing in human cells seems likely to reflect intrinsic features of the repair mechanism since in our initial survey it did not depend markedly on cell type, genomic locus, guide RNA, or nature of the repair template. What determines this dependence on distance? One possible explanation, described two decades ago in the context of restriction-enzyme-induced transgene conversion by HDR in mouse ESCs (Elliott et al., 1998), is that different size deletions arise after nuclease-mediated DSBs and that only the part of the repair template overlapping these deletions is used during HDR. If small deletions or resections are more common than large ones, this would result in fewer incorporations of mutations more distal to the cleavage site (**Figure 24**). Our data support this idea, because they not only confirm that deletions are more likely small

than large and center around the Cas9-mediated DSB, but also indicate no significant change of the distance dependency by altering the size and type of HDR repair templates used.

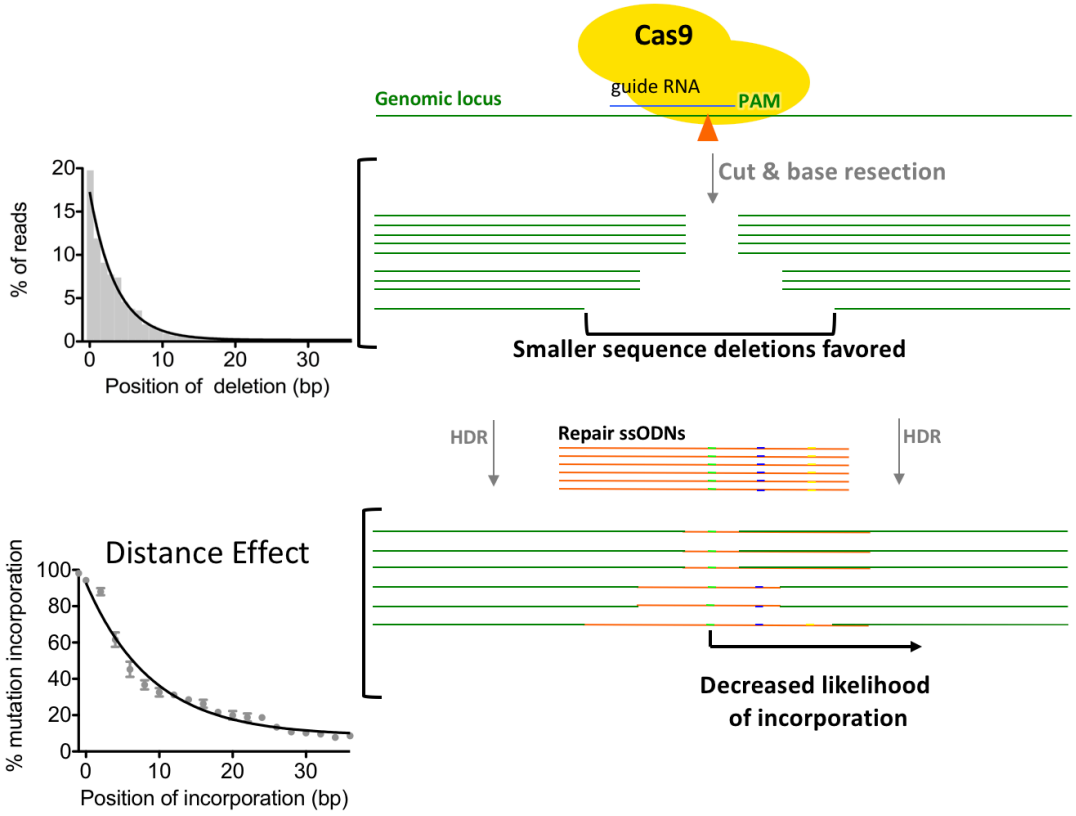

Figure 24. Possible mechanism underlying the distance effect for HDR-mediated mutation incorporation with CRISPR/Cas9.

CRISPR/Cas9 causes a DSB at a genomic locus, which leads to variable size deletions or strand resections in different cells. Genomes with small deletions or resections are more common than large ones, which is reflected in the distribution of deleted bases after NHEJ (top left). During HDR, only the part of the repair template overlapping this deletion may be used, which results in fewer mutations incorporations more distal to the cleavage site (bottom left,

data pooled for *APP* and *PSEN1* from **Figure 19C**). Graphs depict our actual data.

Although it remains to be determined whether our proposed mechanism is the correct explanation, the observation of a reproducible and stereotyped distance effect has two major implications for the field of gene editing: First, it demonstrates that HDR is most efficiently achieved by selecting a guide RNA that causes a DSB close to the intended sequence change. Second, it defines optimal distance ranges to generate mono- or bi-allelic modifications, significantly improving guide RNA selection procedures that until now have focused principally on on-target activity and predicted off-target effects. As we show, the most efficient way of obtaining a clone heterozygous for a pathogenic mutation is to introduce it together with bi-allelic CRISPR/Cas-blocking silent mutations, which prevent destruction of both alleles by NHEJ. The different zygosities at both alleles are achieved by reducing the probability of the introduction of the pathogenic mutation by either modulating distance between cleavage site and mutation (distance effect) or mixing pathogenic-mutant and non-mutant oligos.

Our improved CRISPR/Cas9-based gene editing framework also streamlines the modeling of genetic diseases in human iPSC models, by avoiding typical drawbacks associated with use of patient-derived models. These include scarce availability or low quality of patient cell lines with mutations of interest, particularly for rare diseases, as well as the potential for inefficient reprogramming and/or poor

somatic cell differentiation quality. Furthermore, making comparisons in isogenic cell lines prevents confounding genetic background effects (Bellin et al., 2012; Tiscornia et al., 2011). Knocking-in pathogenic mutations in human disease-relevant cells is more physiological than overexpression, which is commonly used in transgenic animal or cellular disease models, and also permits study of heterozygous mutations that underlie many important human diseases. When performed in a standardized iPSC or embryonic stem cell line, our approach not only allows efficient generation of knock-in models, but also cross-comparison between lines with different mutations in the same genetic background.

Since the completion of the CRISPR/Cas9 studies presented in this thesis there has been a large amount of work to further develop and improve the gene editing field. Specifically, the development of a new CRISPR technology, CRISPR/Cpf1 has offered promise for enabling efficient and precise sequence changes (Zetsche et al., 2015). However, as will be described below, we believe there are considerable drawbacks to this new technology and Cpf1 may not be a widely useful replacement for CRISPR/Cas9. Cpf1 is another bacterial RNA-guided nuclease which is a member of a class II CRIPSR/Cas system. Cpf1 differs from Cas9 in many ways. Cpf1 is a much smaller and simpler nuclease compared to Cas9 and is guided by a smaller sgRNA molecule than is needed for Cas9 targeting. Unlike Cas9, Cpf1 targets a T-rich PAM (TTTN) at the 5' end of the sgRNA target sequence (Cas9 targets NGG at the 3' end of the target sequence) and makes a staggered cleavage of the DNA at 19bp after the PAM on the targeted strand and

23bp on the other strand (Zetsche et al., 2015). As a result, the DSB has 5' overhangs ("sticky ends"). The fact that Cpf1 results in a cleavage with overhangs in intriguing, as strand resection and overhang generation is known to be as an essential first step for initiating HDR (Elliott et al., 1998). Furthermore, many researchers believe that the generation of sticky ends may greatly facilitate the insertion of much longer tracts of DNA more effectively. Unfortunately, there have been no investigations in human cells (including stem cells) demonstrating whether Cpf1 indeed improves HDR rates or conversion tract length. Furthermore, future studies would be necessary to determine whether the distance effect we determined for Cas9 editing in human cells holds true or is altered when instead using Cpf1.

There are potentially other drawbacks to using Cpf1 over Cas9. Since Cpf1 cleaves 19-23bp from the PAM site and since most editing events (HDR or indels) take place closest to the cut-site, repetitive editing is more likely, since modifications would less commonly alter the PAM and prevent re-editing. Furthermore, if blocking mutations are also proven to be effective for Cpf1, then incorporating these mutations in the PAM, which is at a considerable distance from the cut site, may be difficult due to the distance effect. Therefore, even if HDR rates are somewhat improved using Cpf1, the problems of re-editing and inaccurate HDR may be considerably worse when using Cpf1. At this time, all of these concerns are speculative, and therefore additional studies are required to address them.

While CRISPR/Cas9, as reported here and by others, mostly generates bi-allelic modifications, TALENs are capable of introducing heterozygous changes,

likely due to their known lower editing activities, such that when HDR occurs at one allele the unedited allele is spared from NHEJ. However, compared to CRISPR/Cas9, efficient and widespread use of TALENs has been hampered by their difficult design and assembly, and the need for extensive clone screening because of lower editing rates (Ding et al., 2013). The strategy we describe, by harnessing the efficiency of CRISPR/Cas9-based targeting with approaches to enabling precise control of zygosity, provides a more efficient method for introducing both homo- and heterozygous sequence changes in a predictable manner. What's more, this approach facilitates the simultaneous modification of several loci in the same standardized model systems, helping open important research avenues such as studying combinations of disease-associated mutations or risk factors to better understand multifactorial diseases.

Chapter III: PRECISE AND EFFICIENT SCARLESS GENOME EDITING IN STEM CELLS USING "CORRECT"

Background and Rationale

While attempting to edit the *APP* and *PSEN1* loci in human iPSCs, we noted that up to 95% of the genomes that had incorporated the intended sequence change by CRISPR/Cas9-mediated HDR were corrupted by additional indel mutations (described in **Chapter II**). These "inaccurate" edits arise from subsequent re-editing of a previously edited locus by the CRISPR/Cas9 complex (**Figure 25A**), which will re-cut target loci until they are sufficiently modified to prevent further detection by CRISPR. We demonstrated that undesirable re-editing could be largely prevented by inserting mutations into HDR repair templates within sequences required by CRISPR/Cas9 for targeting (**Figure 25B**). These simple repair template modifications can increase editing accuracy up to 10-fold per allele, and therefore assuming independent allelic editing, may increase the probability of accurately editing both alleles in a single cell by up to 100-fold, which, for manual clone picking, can make the difference between a practical versus impractical genome editing experiment. Furthermore, we found that in most cases CRISPR/Cas9 editing in iPSCs is bi-allelic, because non-HDR edited alleles are virtually always disrupted by indels caused by NHEJ. Therefore, the only way to generate precise accurately edited iPSCs was to introduce CRISPR/Cas-blocking mutations at both alleles in the genome (see **Chapter II**).

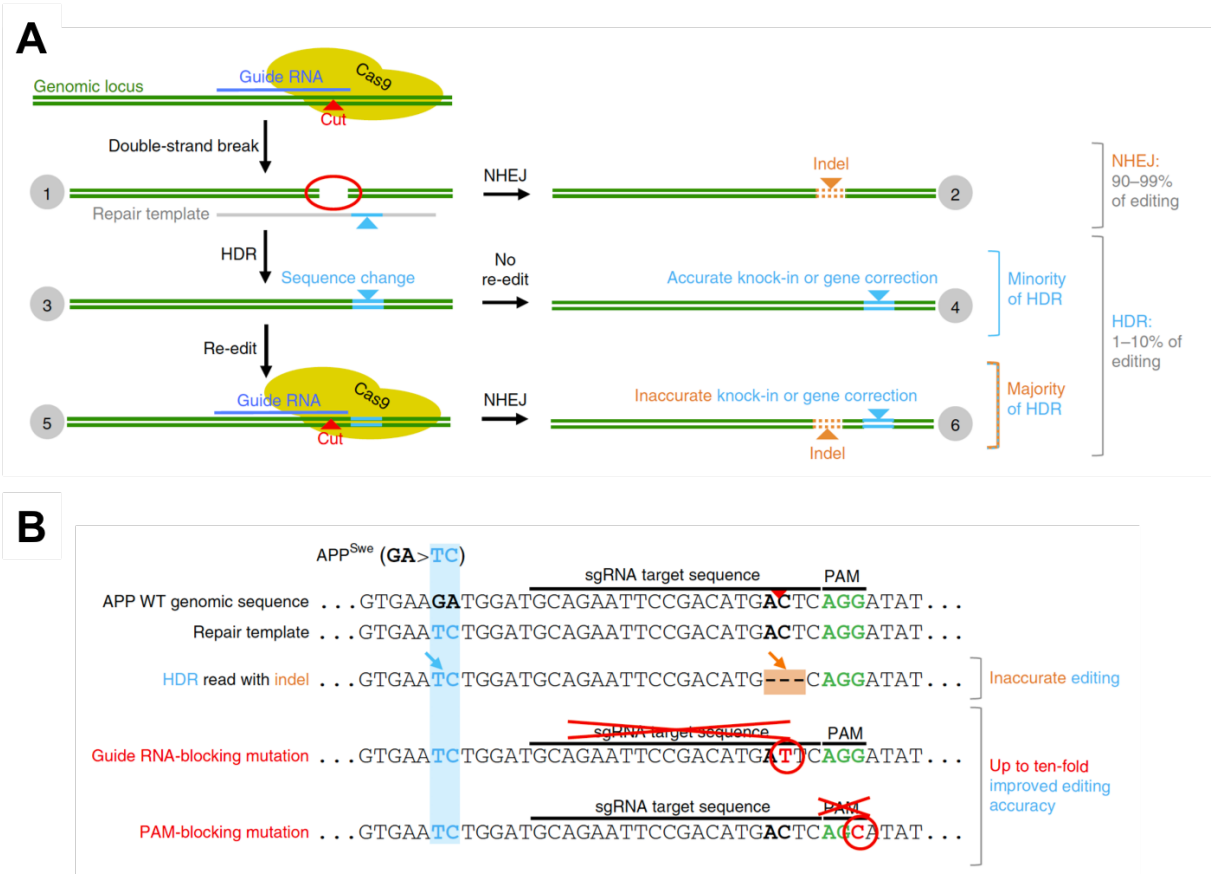

Figure 25. Schematic summarizing editing outcomes and CRISPR/Cas-blocking mutations in human stem cells.

A) Following a CRISPR/Cas9-mediated double strand break (1) a majority of loci will be repaired through the error-prone NHEJ pathway resulting in random indel mutations (2). In approximately 1-10% of cases HDR introduces an intended sequence change provided by a homologous DNA repair template (3). However, this sequence change is accurate (i.e. not corrupted by additional CRISPR/Cas9 editing) only in a very small minority of cases (as low as 6% as described above) (4). In the majority of the HDR events, the CRISPR/Cas9 complex will re-cut (5) and cause additional indels (up to 95% of HDR events at the PSEN1 locus as described above) (6). (**B**) HDR-mediated editing using an sgRNA targeting near the *APPswe* site (light blue arrow). Commonly, re-editing after incorporation of the intended *APPswe*

mutation by HDR results in inaccurately edited genomes (orange arrow). Introducing CRISPR/Cas-blocking mutations in the guide RNA target sequence or PAM prevents further target detection and re-cutting and therefore improves HDR accuracy up to 10-fold per allele.

While the introduction of CRISPR/Cas-blocking mutations in coding regions should in most cases not cause any unexpected problems, as they can be silent (leaving the encoded amino acid unchanged), introducing these additional mutations into non-coding regions such as introns, regulatory regions or non-coding RNAs may have unwanted consequences. Furthermore, introducing silent mutations in coding sequence at or near splice sites, splicing enhancers or inhibitors may cause unwanted effects. In some cases, the use of additional mutations can be avoided by simply choosing guide RNAs where the intended sequence change doubles as a blocking mutation (if they lie within the PAM or guide RNA target sequence) but this is not universally applicable. Therefore, there was a need to develop a strategy that takes advantage of the efficacy of CRISPR/Cas9 but can be utilized for scarless introduction of specific sequence changes by HDR, with the absence of additional CRISPR/Cas-blocking mutations. The following work is adapted from our recent publications (Kwart & Paquet et al,. 2017; Paquet & Kwart et al., 2016).

Scarless genome editing using CORRECT

To address this limitation, we devised a two-step gene editing strategy termed "CORRECT" (Consecutive Re-Guide or Re-Cas steps to Erase CRISPR/Cas-

blocked Targets), which, by taking advantage of CRISPR/Cas-blocking mutations in both steps enables efficient “scarless” introduction of a single intended mutation sequence, while minimizing clone picking. Moreover, each step of *CORRECT* is compatible with manipulating cut-to-mutation distance or using a mixed oligo approach (see **Chapter II**) to favor homo- or heterozygous mutation incorporation. We have developed two variants of CORRECT: re-Guide (**Figure 26A**) and re-Cas (**Figure 26B**).

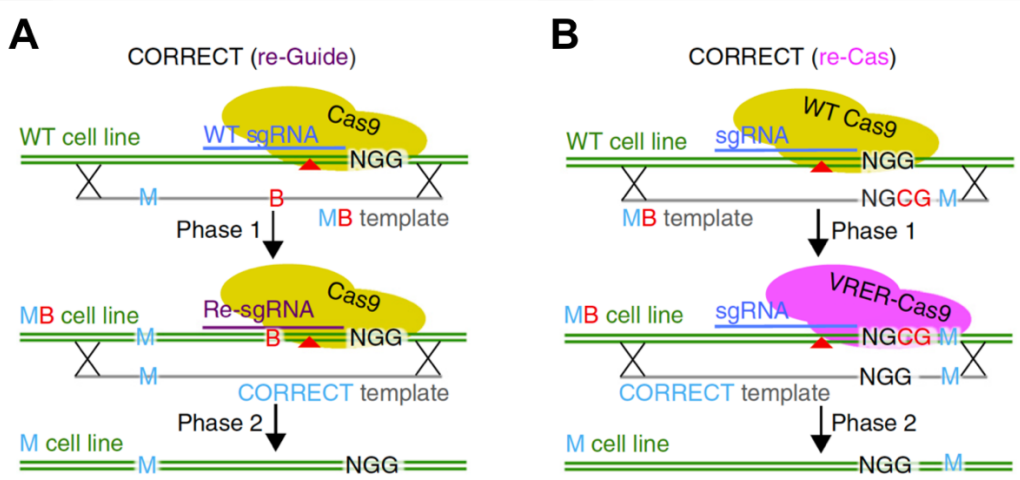

Figure 26. Schematic describing scarless editing using CORRECT by re-Guide and re-Cas.

(**A**) For re-Guide editing a CRISPR/Cas-blocking mutation B in the guide RNA target sequence is introduced in addition to the intended mutation M with the MB template by HDR. B is subsequently removed in the second Phase using a modified guide RNA (re-sgRNA) with Cas9 and the CORRECT template, resulting in scarless introduction of the intended mutation M. (**B**) For re-Cas editing a PAM-altering CRISPR/Cas9 blocking mutation is introduced in addition to the intended mutation M with the MB template by HDR. The altered PAM is targeted by VRER-Cas9 in Phase 2 resulting in scarless introduction of M alone. In Phase 1 and Phase 2 of both CORRECT

variants CRISRP/Cas9-blocking mutations enable efficient and accurate scarless mutation incorporation.

In both re-Guide and re-Cas, a blocking mutation B is introduced at both alleles together with the intended mutation M by an ssODN template (MB template) in the first phase, thus preventing unwanted indels. In the second phase a modified "CORRECT template" is used to remove the blocking mutations but preserve the intended mutation. While the re-Guide blocking mutations are located in the guide RNA targeting sequence and therefore prevent further targeting of the single guide RNA (sgRNA), the re-Cas blocking mutation prevents PAM detection by mutating the NGG (e.g., to NGCG). Targeted re-editing of the blocked locus is achieved in the second phase with a modified set of reagents: For re-Guide, a modified sgRNA ("re-sgRNA", targeting the 20bp sequence containing the introduced CRISPR/Cas-blocking mutations) is used in combination with wildtype (WT) Cas9. For re-Cas, the sgRNA from phase 1 is reused, but WT-Cas9 is replaced by a Cas9 variant (e.g., the recently described VRER-Cas9) (Kleinstiver et al., 2015), which targets the modified PAM sequence introduced as a blocking mutation in the first step (**Figure 26A-B**). Both variants utilize a modified repair template in phase 2 (CORRECT template), which removes the blocking mutations by HDR, but leaves the pathogenic mutation in place. By choosing guide RNAs with specific cut-to-mutation distance or using mixed repair templates strategically as described in the previous chapter, each step of CORRECT allows homo- or heterozygous incorporation of the intended mutation.

Assessing CORRECT feasibility in pooled gene editing experiments

To test the feasibility and efficiency of CORRECT by both re-Guide and re-Cas we selected two mutations to introduce (*APPswe* and *APP-A673T*) by either CORRECT variant based on the situation of the mutation site around the PAM or sgRNA target sequence (**Figure 27**). We also determined restriction endonuclease sites that would be uniquely introduced by MB and CORRECT templates, which enable RFLP screening for accurately edited clones in each phase of CORRECT (**Figure 27**).

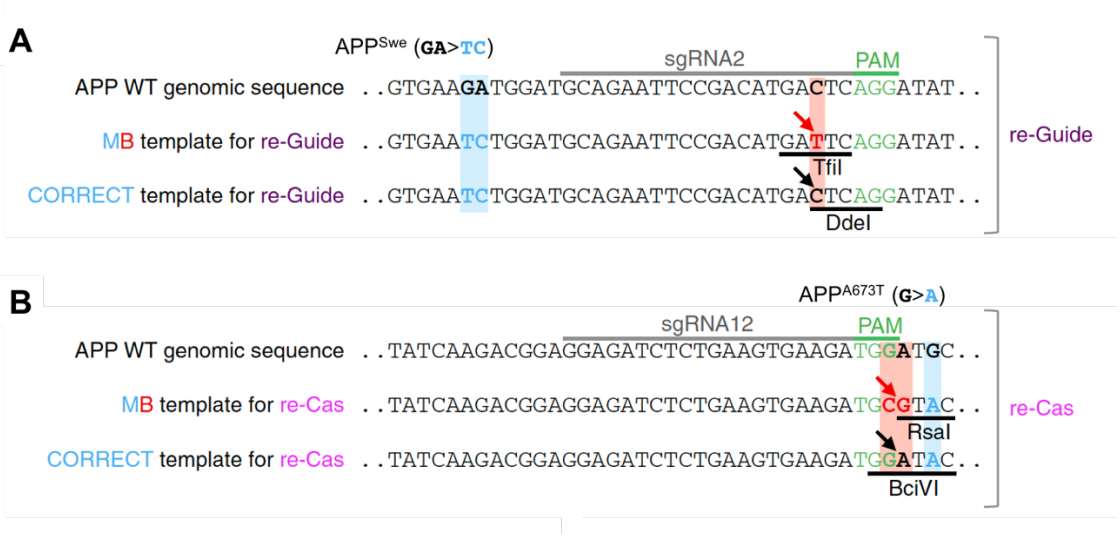

Figure 27. Experimental design for scarless mutation introduction using CORRECT.

Design of MB and CORRECT ssODN repair templates that were designed for re-Guide (**A**) and re-Cas (**B**) experiments such that MB and CORRECT templates introduce different restriction sites for RFLP screening (shown with black underlines).

We began by generating two homozygous “MB” iPSC lines containing (1) the homozygous *APPswe* pathogenic mutation and a CRISPR/Cas-blocking mutation in the guide RNA target sequence, or (2) the *APP-A673T* (a protective APP mutation) and NGCG PAM-altering mutations (**Figure 28A-B**). Using both the wildtype parent iPSCs as well as these MB iPSCs, we showed by SURVEYOR assay, combinations of WT-Cas9 and sgRNAs were highly active on their respective targets in wildtype unedited iPSCs, whereas combinations of WT-Cas9/re-sgRNA or VRER-Cas9/sgRNA were not (**Figure 28C, E**). In contrast, WT-Cas9/re-sgRNA efficiently targeted the modified locus in *APPswe* MB iPSCs, and VRER-Cas9/sgRNA efficiently targeted the modified locus in *APP-A673T* MB iPSCs (**Figure 28C, E**). As anticipated, WT-Cas9/sgRNAs combinations were virtually inactive on modified loci, illustrating efficient blocking of unwanted re-editing after HDR in all cases. We then attempted to specifically remove the blocking mutations from both MB cell lines by introducing CORRECT-templates and the above-mentioned combinations of WT-Cas9/re-sgRNA or VRER-Cas9/sgRNA (**Figure 28A-B**), respectively, and measured the resulting allele frequencies by NGS. Strikingly, we detected the expected scarless genome editing events with high efficiency (**Figure 28D, F**). Thus, in this preliminary test of CORRECT, we demonstrated this approach enables increased editing accuracy provided by blocking mutations in each step, and at the same time allows scarless introduction of intended pathogenic mutations.

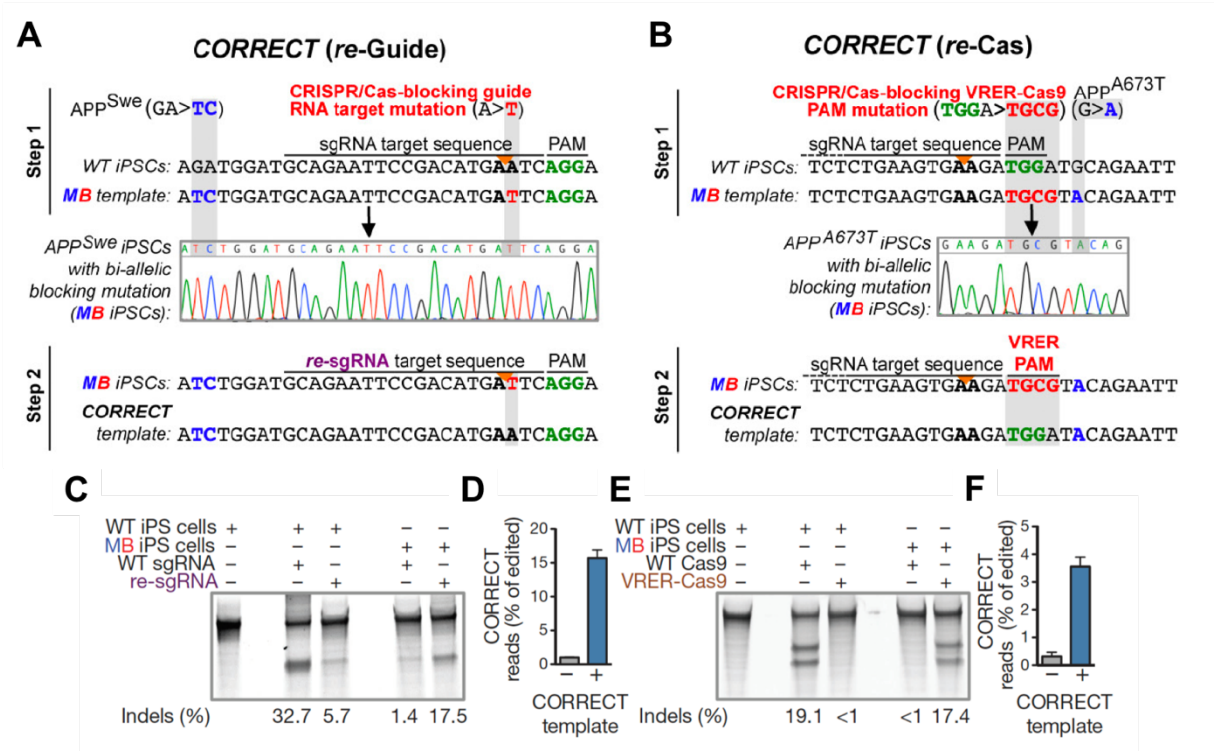

Figure 28. Assessing feasibility of CORRECT by pooled re-Guide or re-Cas editing.

A-B) Schematics depicting details of the two tested CORRECT approaches: In step 1 of re-Guide (**A**) the *APPswe* mutation was introduced together with a CRISPR/Cas-blocking guide RNA target mutation, which is to then be removed in step 2 using a re-sgRNA specific for the mutated sequence and WT-Cas9. In step 1 of re-Cas (**B**) the *APP-A673T* mutation was introduced together with a CRISPR/Cas-blocking PAM-altering NGCG mutation that is then removed in step 2 using the VRER Cas9 variant, which specifically detects the NGCG PAM. We chose to incorporate the *APP-A673T* mutation using the very active APP-sgRNA12 to test CORRECT by re-Cas since the *APPswe* mutation is located in the target sequence of this sgRNA, which may block re-editing by CRISPR/Cas and could therefore complicate the interpretation of results. The *APP-A673T* mutation lies outside of the target sequence (**B**). In both cases, the blocking mutations were removed using a CORRECT ssODN repair template, which restored the original sequence at

the site of the blocking mutation (which blocks further re-cutting in this step) but retained the pathogenic APP mutation. **C**, **E**) SURVEYOR assays showing specificity of WT-Cas9/WT-sgRNAs for WT targets, and WT-Cas9/*re*-sgRNA (**C**) or VRER-Cas9/WT-sgRNA (**E**) for mutated loci. **D, F**) NGS quantification of genomes with intended incorporation of CORRECT templates by HDR in pooled iPSCs (n=2).

Increasing HDR rates as a strategy to improve CORRECT efficiency

The greatest drawback of CORRECT is the need for two rounds of gene editing, single cell sorting, colony picking, screening and expansion. All of these steps together add additional time, albeit most of this time is not "hands-on". As described in the previous chapter, bi-allelic HDR rates in single cell-derived iPSC clones was approximately 2%, which means in the first phase of CORRECT editing picking hundreds of colonies to obtain a handful of clones for subsequent quality control analysis and expansion prior to the next round of editing. To minimize needing to pick hundreds of colonies more than one time, we sought to determine a simple strategy to significantly increase the rate of isolating HDR clones with minimal additional optimizations. One approach we tested was to alter the FACS sorting paradigm we had previously established to isolate iPSCs that were electroporated with Cas9, sgRNA and ssODN repair templates. As described above (and in **Appendix I**), we sorted out electroporated iPSCs that were expressing GFP, which is co-expressed from the Cas9 plasmid (we assumed GFP+ cells would have also taken up sgRNA plasmid and ssODNs as these other DNAs are significantly smaller

than the pCas9_GFP plasmid). In all of our early experiments we simply sorted out the entirety of the GFP+ population and analyzed all of those cells together, which would yield the approximately 2-3% biallelic HDR clones as described above (see an example in **Figure 29**)

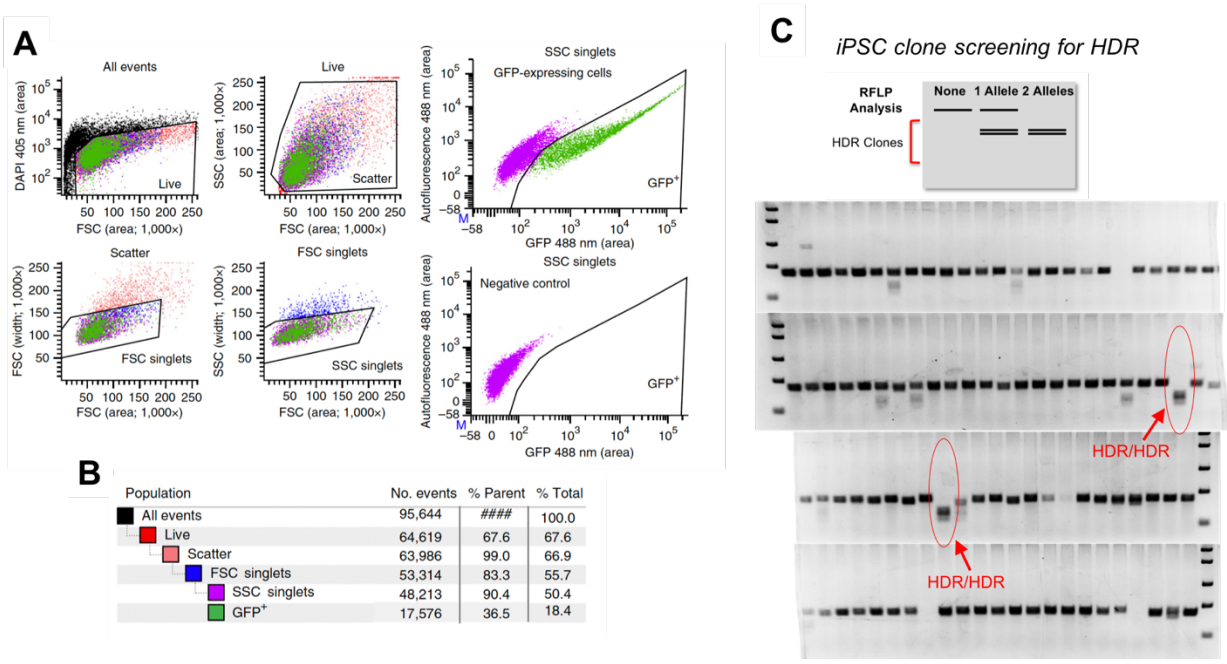

Figure 29. Original approach for FACS enrichment of gene edited iPSCs and RFLP analysis.

A-B) Enrichment of GFP-expressing iPSCs by FACS sorting. Note setup of gates based on GFP/DAPI-negative and GFP positive samples. Only live single GFP-positive cells were collected (top right panel). **C**) RFLP screening strategy (example for *APPswe* incporporation). Bi-allelic HDR clones are pointed to by red arrows (~2%). HDR/HDR clones were confirmed to have accurate mutation incorporation by Sanger sequencing (not shown).

Given that the overall level of HDR depends on both CRISPR/Cas9 activity as well as presence of the ssODN repair template, we hypothesized that perhaps the population of cells that have the most CRISPR/Cas9 and repair template would also be the cells that have undergone the most number of desired HDR-mediated changes. We tested what HDR rates would be in sorted GFP+ cell populations split based on either low, medium, or high GFP fluorescence intensity (**Figure 30A**). In this proof-of-principle experiment, we chose to target the *APPswe* locus using APP-sgRNA12 described in the previous chapter. After isolating single cell-derived colonies and performing RFLP analysis to screen for HDR clones we noticed striking differences in the sorted populations (**Figure 30B-C**). Specifically, both mono-allelic and bi-allelic HDR clones were most rare in the GFP low population (1% for each). In the GFP middle population there were more of both mono-allelic (7%) and bi-allelic (2%) HDR clones. Most strikingly, however, was the GFP high population, which had a remarkably high number of both mono-allelic (18%) and bi-allelic (17%) HDR clones. Together, in the GFP high population, 47% of all clones picked had undergone HDR at one or more alleles. (**Figure 30B-C**). These data were exciting, as we demonstrated that simply by changing the FACS gating strategy, we could dramatically increase the frequency of HDR clones thereby dramatically reducing the number of colonies that would need to be picked and screened to identify accurately edited iPSCs. This approach has become an invaluable development that has enabled us to rapidly generate isogenic iPSCs by either a one-step or two-step (via CORRECT) CRISPR/Cas9 editing approach.

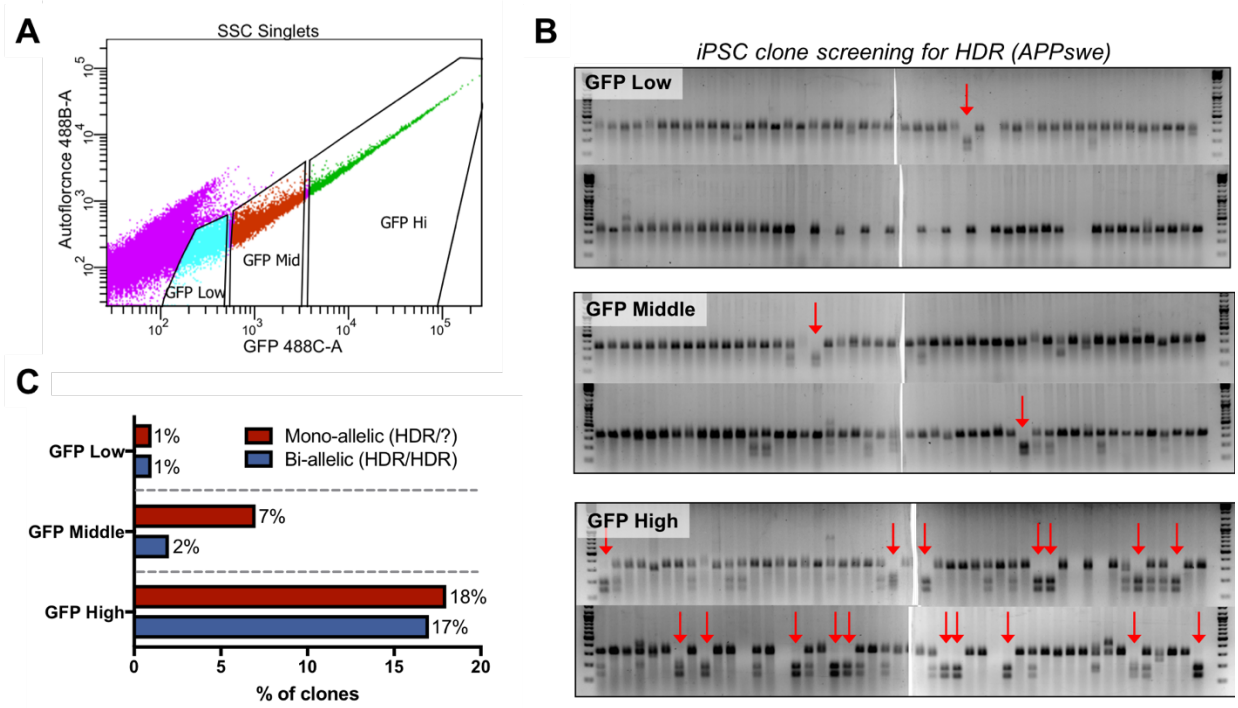

Figure 30. Enriching for high GFP intensity in electroporated iPSCs by FACS dramatically increases probability of identifying bi-allelic accurately edited HDR clones.

A) FACS gating strategy to sort low, medium, or high GFP+ expressing iPSCs. **B**) RFLP analysis from GFP low, medium and high expressing populations. Red arrows indicate bi-allelic HDR clones. Example shown for TfiI digestion indicating *APPswe* incorporation. **C**) Quantification of mono-allelic and bi-allelic HDR clones from 2 96-well plates of picked iPSC clones. HDR/HDR clones were confirmed to have accurate mutation incorporation by Sanger sequencing (not shown).

Using CORRECT for generation of scarless mutant iPSCs

With the confidence that CORRECT is a feasible method for scarless editing gained from the pooled analysis combined with the novel FACS gating approach we

identified for making identification of HDR clones more efficient, we set out to fully utilize CORRECT by re-Guide and re-Cas to generate scarless homozygous *APPswe* (re-Guide) and *APP-A673T* (re-Cas) iPSC lines. We took the two "MB" clones we generated (see **Figure 28** and **Figure 31**) and completed the second phase of CORRECT by re-editing the MB locus using the "CORRECT template" (**Figure 31A-B**). After screening single cell-derived iPSC clones by RFLP analysis for incorporation of the CORRECT template, we successfully identified a number of accurately edited "M clones" that only contain the pathogenic or protective *APP* mutation and no other CRISPR/Cas-blocking mutations. We picked only a few hundred clones in both phases of re-Guide and re-Cas and were able to efficiently identify several accurately edited clones in each step (**Figure 31C**). Taken together, this work demonstrates that CORRECT, which, by exploiting the use of highly efficacious CRISPR/Cas-blocking mutations in two rounds of genome editing, enables accurate, efficient and scarless introduction of specific base changes in difficult to edit cell lines such as iPSCs.

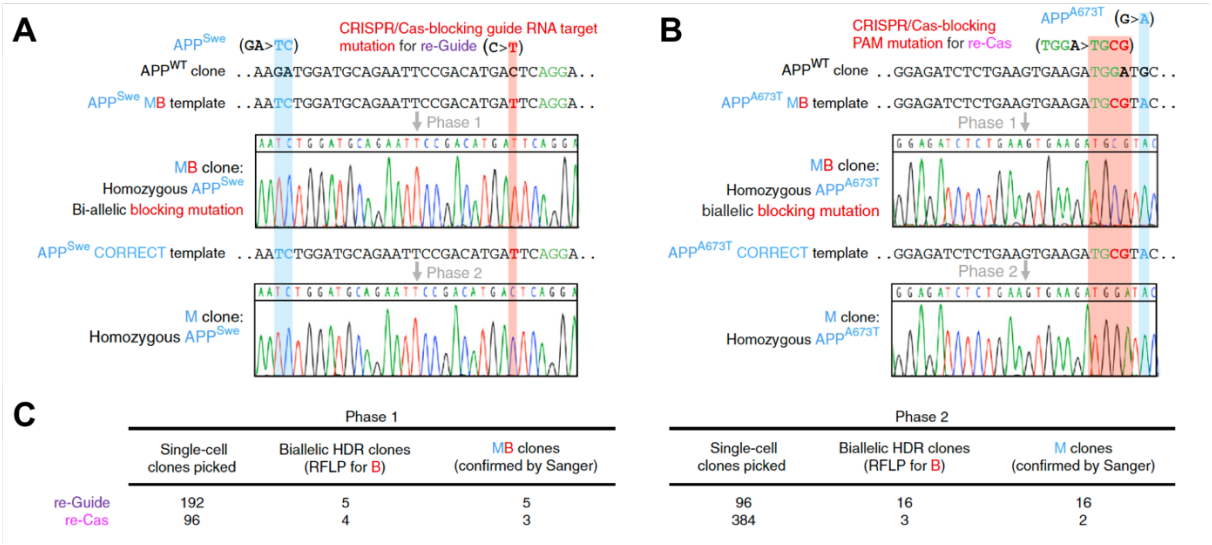

Figure 31. Derivation of scarless *APP* mutant isogenic iPSC clones by CORRECT.

Genotypes of selected re-Guide (**A**) and re-Cas MB and M clones (**B**) were confirmed by Sanger sequencing. **C**) Number of single-cell derived clones that had bi-allelic incorporation of the MB or CORRECT template for both re-Guide and re-Cas experiments, as determined by RFLP assay and confirmed by Sanger sequencing.

When to use CORRECT: Re-Guide or re-Cas

The first decision to make is whether or not CORRECT is required to achieve the desired gene editing outcome. If scarless editing is not required, for example at protein-coding loci where silent CRISPR/Cas-blocking mutations in PAM or sgRNA target sequence are effective and compatible (see above), the desired change can be achieved in a single round of gene editing without CORRECT. When this is not

possible, such as when studying a defined genetic mutation requires scarless editing, CORRECT is advisable.

Next, one should determine whether the re-Guide or re-Cas variation is more suitable. While PAM-blocking mutations utilized by the re-Cas variant may be more universally applicable, in our hands the re-Guide variant seemed to yield more efficient CORRECT editing (**Figure 28D, F** and **Figure 31C**). We therefore recommend to choose re-Guide or re-Cas based on the editing efficiencies of the available guide RNAs (for example, by performing Surveyor nuclease assays) and the position of their targeting site relative to the intended mutation M (**Figure 32**). In the rare instance that the intended mutation falls within the two guanines of the NGG PAM site or within the guide RNA seed sequence (the first 7 to 13 bases upstream of the NGG (Jinek et al., 2012; Semenova et al., 2011)) the mutation itself will likely be blocking, making re-Guide or re-Cas unnecessary (unless one wishes to introduce a specific screening mutation for RFLP analysis). However, CORRECT should be used when the intended mutation is upstream of the guide RNA seed sequence or downstream of the PAM. First, a guide RNA should be chosen that minimizes the distance between cut site and intended mutation to ensure efficient incorporation (as described in **Chapter II**). This also means the distance between the intended mutation M and the blocking mutation B should be minimized, as increasing the distance between these two mutations, for example by placing them on opposite sides of the Cas9 cut site, reduces probability of incorporation of both mutations together. When the intended mutation is located within the first base of

the PAM or downstream of it, re-Cas should be utilized, whereas re-Guide should be employed when the intended mutation falls within or upstream of the 20-nt guide RNA sequence. A useful guide summarizing these experimental design tips is highlighted below (**Figure 32**).

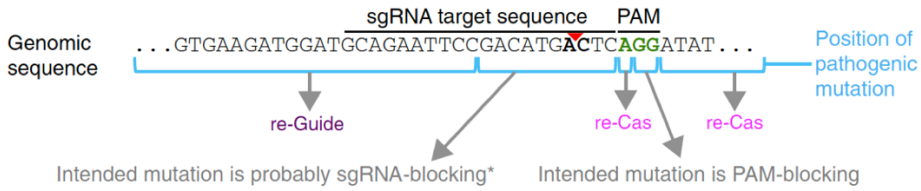

Figure 32. Schematic summarizing criteria for selecting re-Guide versus re-Cas CORRECT variants.

(**A**) Selection of the re-Guide or re-Cas variant of CORRECT depends on the intended mutation M position at the locus being targeted. Asterisk (*): If the intended mutation is not blocking, use re-Guide.

Considerations for ssODN design: MB and CORRECT templates

For both re-Guide and re-Cas, an MB and a CORRECT template should be obtained. These templates can be ordered as custom synthetic oligos ready for use with CORRECT. We use 100-nt ssODN templates centered around the cut site, using the sequence of the non-targeted strand, i.e. the strand that has the same sequence as the guide RNA, to avoid base-pairing of guide RNA and repair oligo. However, recent evidence suggests that HDR repair can be further improved by using the sequence of the targeted strand and by optimizing repair template position

relative to the edited locus (Richardson et al., 2016). For re-Guide, the MB template should contain the intended mutation plus the CRISPR/Cas-blocking mutations in the guide RNA targeting site. For re-Cas, the MB template should contain the intended mutation plus the NGG>NGCG (for VRER Cas9) PAM-altering CRISPR/Cas-blocking mutation. For both re-Guide and re-Cas, the CORRECT template should retain the intended mutation sequence, but replace the CRISPR/Cas-blocking mutations with the original guide RNA or NGG PAM sequence (for re-Guide and re-Cas, respectively).

Ultimately, Sanger sequencing of the edited loci of individual iPSC clones must be performed to confirm accurate CORRECT editing. However, to minimize the number of clones to be sequenced, we recommend incorporating restriction endonuclease sites by the intended or CRISPR/Cas-blocking mutation(s) in both the MB and CORRECT templates. Alternatively, loss of a restriction endonuclease site by incorporation of either MB or CORRECT templates can be used to indicate accurately edited clones, however this may lead to identification of more false-positive clones since indel mutations arising from NHEJ could also disrupt a restriction site if near the Cas9 cut site. Following RFLP analysis only clones that demonstrate the expected DNA fragment lengths on an agarose gel will be sequenced. If necessary, unwanted additional mutations introduced in the MB template for screening purposes in the first round of editing can be removed with the CORRECT template in the second round of editing, and loss of restriction endonuclease cleavage can be used to identify edited clones.

Using re-Guide allows changing multiple bases in the guide RNA target sequence, which gives more flexibility for the introduction and/or removal of a restriction endonuclease site for clone screening by RFLP analysis. re-Cas requires a specific mutant Cas9 PAM in the MB template (e.g., NGCG for the VRER-Cas9), which may make the introduction of restriction endonuclease sites for screening more difficult to determine. As illustrated above, we have applied re-Cas to introduce the A673T mutation in the wildtype *APP* locus with sgRNA12, and used RFLP-mediated screening to identify MB and M clones: First, we incorporated the VRER PAM and A673T mutation by the MB template (**Figure 27**). These two changes (**TGG**ATGC > **TGCG**TAC) generated a RsaI site (GTAC). In the second phase of editing, correcting the PAM back to the wildtype TGG sequence with the CORRECT template (**TGCG**TAC > **TGG**ATAC) introduced a BciVI site (GGATAC). Alternatively, we could have used several other strategies. For example, we could have used APP sgRNA2 for re-Cas (used for re-Guide scarless introduction of *APPswe*) by changing the wildtype PAM to incorporate the VRER PAM in the MB template (CTC**AGG**ATAT>CTC**CGCG**TAT), which introduces a BstUI site (CGCG), and removes a DdeI site (CTNAG). The DdeI site can then be restored by correcting the PAM back to the wildtype AGG sequence by the CORRECT template. In summary, we believe CORRECT is a framework for efficient scarless genome editing that can be broadly utilized at virtually any genomic loci in a variety of model systems.

Applications of CORRECT and comparison with other methods

Here we present the use of CORRECT for scarless introduction of disease-associated homo- and heterozygous mutations into wildtype human iPSCs. We have demonstrated that generating knock-in mutant iPSCs cell lines makes it possible to study disease-associated mutations in disease-relevant cell types, which has great impact on the broader field of disease modeling (Paquet et al., 2016). Moreover, CORRECT makes it possible to use CRISPR/Cas9-mediated gene editing to efficiently edit non-coding genomic sequence, where silent blocking mutations cannot be utilized. CORRECT also provides alternatives for more effective editing of coding sequence, especially in cases where using silent blocking mutations is not possible either due to incompatibility with the reading frame or insufficient blocking activity. Instead of generating knock-in cell lines, researchers may choose to obtain patient samples with known genomic mutations. To generate isogenic wildtype control cell lines, CORRECT can easily be modified to replace patient-specific mutations with wildtype sequence by incorporating these modifications in the MB and CORRECT templates. Furthermore, CORRECT has the added benefit that customizable sequences, such as restriction endonuclease recognition sites, can be introduced into MB templates, which allow simple RFLP screening analysis to identify correctly targeted clones.

Gene editing with CORRECT is advisable when scarless editing is imperative to faithfully study a defined genetic mutation. If silent blocking mutations are effective and compatible with the locus, the desired change can be achieved in a single round

of gene editing without CORRECT. When scarless mutation introduction is desired, this can also be achieved in a single step using a repair ssODN containing only the intended sequence change, but no blocking mutation. However, except in the rare case that the intended mutation doubles as a CRISPR/Cas-blocking mutation we would not recommend the latter strategy, because accurate editing efficiencies could be reduced up to 10-fold per allele (see **Chapter II**). Although accurately edited clones can still be identified at this low editing efficiency by other cellular enrichment strategies such as sib-selection (Miyaoka et al., 2014), this requires laborious sequential cellular selection, clonal expansion and genomic analysis and therefore the overall time required for this approach is similar to CORRECT editing.

Alternatively, one could use a different scarless genome editing approach such as the *piggyBac* transposon, which has been shown to be effective in human iPSCs (Yusa, 2013). Similar to CORRECT, this method requires two rounds of genetic manipulation, clone picking and screening. Therefore, generating scarlessly edited clones with *piggyBac* would take approximately the same time as CORRECT. Since the *piggyBac* transposon system uses antibiotic resistance markers for screening, it facilitates isolating larger genomic changes, such as gene or exon insertions, or deletion of protein domains, which are usually very rare events. However, for smaller edits, such as base changes, CORRECT performs better in our hands for several reasons: (1) transfection of the large *piggyBac* repair template in iPSCs and its genomic incorporation is inefficient; (2) editing with *piggyBac* requires a TTAA sequence near the target site of interest, which is more restrictive than the

NGG PAM requirement for Cas9 and could severely limit the number of targetable loci; (3) construction and cloning of the *piggyBac* targeting vector containing the intended sequence changes is laborious compared to simply ordering custom synthetic ssODNs, which are used as repair templates for CORRECT. Finally, excision of the *piggyBac* transposon can be inefficient and lead to integration elsewhere in the genome, which requires subsequent southern blot analysis for quality control.

More recently, a new CRISPR-based technology has been developed for scarless mutation incorporation called “base editing” (Gaudelli et al., 2017; Komor et al., 2016). Briefly, this approach negates the necessity for Cas9-mediated DSB generation. Specifically, a catalytically inactive version of Cas9 is tethered to a cytidine or adenosine deaminase, which can mediate C-G to A-T or A-T to C-G changes without DNA cleavage when targeted to a genomic locus by an sgRNA. This approach has its many advantages, namely, by bypassing DNA cleavage there is no NHEJ that occurs and therefore no problem of additional unwanted indels alongside desired changes or need for CRISPR/Cas-blocking mutations. This means base editing can be performed in a single round of gene editing. Although the efficacy of base editing in human stem cells remains to be adequately tested, studies in other cell types have shown high C to T and A to C editing efficiencies (up to 75% of cells). While base editing holds great promise for use wide use in multiple scientific fields, it does have its disadvantages over our described one- or two-step gene editing approaches using Cas9-mediate HDR. Specifically, the greatest

disadvantage is that base editing is unspecified, only occurring between a predicted sequence range near the sgRNA target site. To adjust the editing window, different deaminases tethered to inactive Cas9 must be used. This of course means that in order to be able to use base editing one would need the guide RNA sequence to match the necessary location for the optimal base editing range for a given deaminase, which may not always be possible depending on the genomic sequence. Furthermore, because the exact base being edited cannot be specified (only a 4-5 nucleotide window (Gaudelli et al., 2017; Komor et al., 2016)) every single clone picked will have to be sequenced, as there is no way to introduce specific RFLP screening sites in addition to the desired mutation by base editing. Lastly, while base editing may be effective for engineering a single C-G to A-T or A-T to C-G mutation, introducing multiple specific base changes (such as the double base change seen for the *APPswe* mutation) is difficult without two rounds of base editing. Therefore, while base editing holds great promise, any desired gene-edit involving more than one base change at this point should be done using CRISPR/Cas9-mediated HDR in a one-step (using blocking mutations) or two-step (using CORRECT) approach.

Limitations of CORRECT

CORRECT currently works best in dividing cells in culture, limiting its use *in vivo* in animal models. The two rounds of genomic manipulations and clone picking required to generate pure cultures of accurately edited human stem cell lines with

CORRECT take approximately 3 months, twice as long as scarless editing without the benefit of blocking mutations. However, because CORRECT may increase the editing efficiency up to 100-fold, the longer time required is made up for by less manual labor, especially during the clone picking steps. In an extreme case, CORRECT would require picking only a couple hundred clones, while tens of thousands may be required if a CRISPR/Cas9 blocking-mutation strategy is not used. In the future CORRECT may be further streamlined by multiplexing both editing steps in a single cell pool, for example by using cell lines with inducible forms of wildtype or variant Cas9 (Dow et al., 2015).

The two rounds of genome editing required for CORRECT may potentially increase the risk of off-target modifications. However, this potential increase will likely not expand the number of potential off-target sites, since the same (for re-Cas) or very similar (for re-Guide) guide RNAs are used in both editing steps. Furthermore, since using blocking mutations significantly increases editing accuracy, CORRECT facilitates isolating multiple clones for phenotypic comparison. Finally, the VRER Cas9 variant used in phase 2 of re-Cas has only more recently been engineered and is far less studied. Therefore, the degree of on-target activity and specificity at multiple genomic loci in a variety of cell types remains to be elucidated. We expect that as CRISPR/Cas9 technologies are further developed, variant Cas9 enzymes will be enhanced with improved on-target activity and specificity (Kleinstiver et al., 2015) and may make re-Cas the future CORRECT variant of choice.

Our two variants of CORRECT offer the choice of either using well-characterized wildtype Cas9 in both steps together with a modified guide RNA (re-Guide) or a Cas9 variant with altered PAM specificity in step 2, which benefits from using the same sgRNA in both steps, and potentially more robust blocking effects by the PAM mutation (re-Cas). In our laboratory, however, we have noticed reduced rates of HDR using the VRER Cas9 compared to wildtype Cas9 when employing CORRECT to target the amyloid precursor protein (APP) gene (see **Figure 28D, F** and **Figure 31C**). Prior to choosing CORRECT by re-Guide or re-Cas the HDR efficiency for wildtype and mutant Cas9 can be determined at the intended locus of interest in a pool of transfected cells by either NGS detection of intended sequence incorporation (Paquet et al., 2016) or RFLP detection of a restriction endonuclease site introduced by an HDR template (Cong et al., 2013). We recommend using the CORRECT variant that yields the highest HDR rates to minimize manual clone picking during each gene editing phase. Regardless of Cas9 variant used, CORRECT can be combined with novel NHEJ inhibitor and HDR improvement strategies (Chu et al., 2015; Lin et al., 2014; Maruyama et al., 2015; Richardson et al., 2016; Yu et al., 2015), as well as other recently published cellular enrichment methods (Miyaoka et al., 2014) to minimize clone picking and improve recovery of accurately edited clones in each step of the protocol.

CHAPTER IV: STUDYING ISOGENIC MUTANT *APP* AND *PSEN1* IPSC-DERIVED NEURONS REVEALS CONSERVED CELLULAR AD MECHANISMS

Background and Rationale

The "amyloid cascade hypothesis" is the most prominent theory describing the pathogenesis of AD (Hardy and Higgins, 1992), and places Aβ as the early key initiator of all downstream changes necessary for the development of AD. This notion is most significantly supported by genetics, as more than 200 fAD mutations in *APP, PSEN1* and *PSEN2* – all genes associated with the generation of Aβ – have been described to date. While the effects of many of these mutations on Aβ production have been studied extensively, *a common unifying mechanism by which fAD mutations lead to the development of AD has yet to be determined*. For example, fAD mutations in *APP* appear to have variable effects on Aβ production. fAD caused by *APP* duplication or N-terminal mutations, such as the widely studied *APP* Swedish mutation (*APPswe*), indiscriminately increase Aβs (Citron et al., 1992; Mullan et al., 1992; Rovelet-Lecrux et al., 2006). In contrast, *APP* C-terminal mutations that cluster around the γ-secretase processing site appear to increase the amount of longer, more hydrophobic Aβs (such as Aβ42), relative to shorter Aβs (such as Aβ40), resulting in an increase in the Aβ 42:40 ratio with variable effects on total Aβ production (Eckman et al., 1997; Herl et al., 2009) (**Figure 7**). Similarly, it is now widely agreed upon that mutations in *PSEN1* also act to increase the Aβ 42:40

ratio, in some cases even decreasing total Aβ production (Borchelt et al., 1996; Citron et al., 1992; Duff et al., 1996; Scheuner et al., 1996b). However, whether these relative changes correspond with increased total Aβ42 production, decreased Aβ40 production, or a combination of both remains debated (Kelleher and Shen, 2017b). Taken together, it remains unclear whether specific changes in APP processing are common amongst all *APP* and *PSEN1* fAD mutations, and whether these potential common changes may be disease-relevant.

Aberrant changes in intracellular trafficking and the endocytic system have become another plausible common underlying pathological mechanism in AD. Genome-wide association studies and other human genetics approaches have consistently identified variants in genes associated with endocytic trafficking to be significantly associated with sAD risk (Giri et al., 2016; Karch and Goate, 2015). Endosomal pathologies have also been observed in post-mortem sAD patient brains and more recently in some cellular fAD models, and found to precede Aβ accumulation (Cataldo et al., 2000; 2008; Israel et al., 2012; Raja et al., 2016; Woodruff et al., 2016). Some studies have reported that early endosomal abnormalities seen in AD, such as enlargement of Rab5+ early endosomes, may be driven not by Aβ, but by β C-terminal fragments of APP (β-CTFs) (Jiang et al., 2010; Kim et al., 2015; Woodruff et al., 2016; Xu et al., 2016), but others have reported Aβ-dependent endocytic trafficking defects (Treusch et al., 2011). These studies are confounded by their use of non-human and/or non-neuronal cellular systems that rely on massive overexpression of AD-associated proteins. Consequently, it

remains to be determined in human neurons with physiologically relevant APP and PSEN1 protein expression whether early endosomal abnormalities are a broadly unifying disease-relevant phenotype associated with different fAD mutations.

With these open questions in mind we took advantage of our established CRISPR/Cas9 gene editing frameworks described in Chapter II and Chapter III to generate and study a comprehensive panel of isogenic homozygous and heterozygous *APP* and *PSEN1* fAD mutant human iPSCs. Upon differentiation into human cortical neurons expressing APP and PSEN1 at endogenous levels, we tested whether these mutations result in any common disease-associated phenotypes. To address this question in an unbiased manner, we performed global transcriptomic profiling of *APP* and *PSEN1* mutant neurons, which revealed common dysregulation in overlapping networks of AD-implicated genes as well as in endocytosis-associated genes. Directed by these global pathway changes, we identified functional early endosomal abnormalities in every homozygous pathogenic fAD mutant iPSC-derived neuron line we generated, as measured by Rab5+ early endosome enlargement, suggesting an effect of altered APP processing on the endosomal system. We show that while *APP* and *PSEN1* mutations have discordant effects on the precise processing of APP and production of Aβ peptides, all fAD mutations studied cause a robust accumulation of longer Aβ species (Aβ43 and/or Aβ42) as well as β-CTF. Taking advantage of established small molecules, we show that early endosome enlargement could be rescued by inhibition of β-secretase (BACE), but not modulation of γ-secretase. Importantly, we also confirm,

for the first time in human cortical neurons, that AD-associated Rab5+ early endosome enlargement is associated specifically with endogenous accumulation of β-CTF, and not longer Aβ peptides or other APP CTF fragments. Together, our study amplifies the relevance of Aβ-independent endosomal defects as a common, early pathological feature of fAD, and supports growing evidence that β-CTF may be a significant contributor to AD pathology.

Unbiased molecular profiling of fAD mutant neurons reveals transcriptional dysregulation of AD- and endocytic-associated genes.

As outlined in Chapter II, we employed our novel CRISPR/Cas9 gene editing framework (Kwart et al., 2017; Paquet et al., 2016) to introduce two of the most widely studied fAD mutations (*APPswe* and *PSEN1-M146V*) in wildtype human iPSCs. In a preliminary analysis of differentiated disease-vulnerable neurons (details of differentiation can be found in **Appendix I**), we noticed disease-associated Aβ-related phenotypes that were different in *APPswe* neurons compared to *PSEN1-M146V* neurons (Paquet et al., 2016). To investigate whether these two different canonical fAD mutations result in any common disease-relevant phenotypes we performed unbiased global transcriptomic profiling of wildtype, homozygous *APPswe* and homozygous *PSEN1-M146V* iPSC-derived neurons by RNA sequencing (RNA-seq). Additionally, to exaggerate cellular and molecular changes in pathways affected by both *APP* and *PSEN1* mutations, we profiled neurons from an additional *Swe/M146V* "double knock-in" iPSC line (also shown as "dAP" below) that we

generated (**Figure 33**), which contains both homozygous *APPswe* and *PSEN1-M146V* fAD mutations.

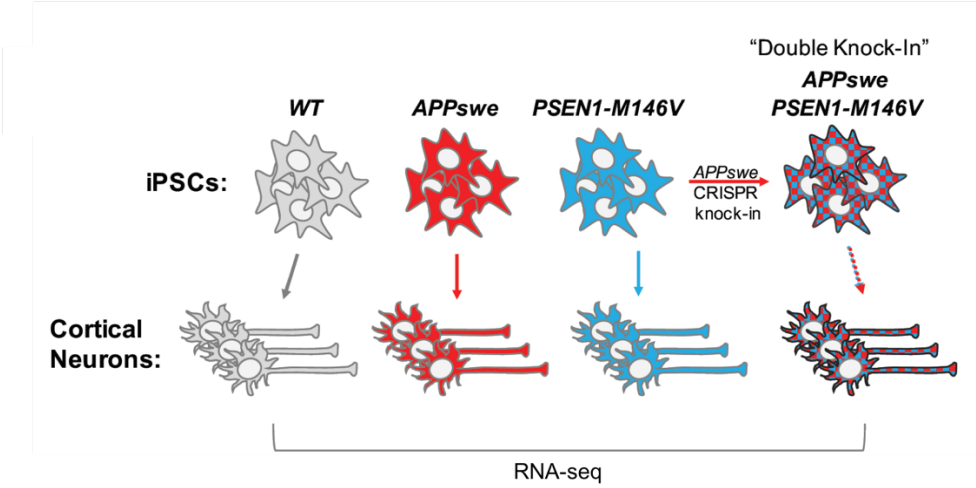

Figure 33. Strategy for molecular profiling of isogenic *APP* and *PSEN1* fAD mutant neurons.

Schematic describing strategy for generation of *Swe/M146V* double knock-in iPSCs and molecular profiling strategy. *APPswe* and *PSEN1-M146V* iPSCs were generated using the CIRSPR/Cas9 strategy outlined in Chapter II (and see Appendix I). *Swe/M146V* iPSCs were generated by re-editing *PSEN1-M146V* homozygous iPSCs and introduction of the *APPswe* mutation using CRISPR/Cas9. All iPSCs were differentiated and cultured until DIV80 then were used for molecular profiling.

We isolated RNA from mature (days *in vitro* 80 (DIV80)) wildtype and mutant iPSC-derived neurons and performed RNA sequencing (RNA-seq) (see **Appendix I** for sequencing library quality control analyses). We wished to determine at the whole-genome level what types of genes and gene pathways are being differentially regulated in mutant cells. Therefore, we performed a differential expression analysis

to decipher all significantly differentially expressed genes in the three different mutant neuron cell lines compared to wildtype (FDR < 0.05 and $|Log_2FC| > 1$) (**Figure 34A**). Intriguingly, over 32% of all differentially expressed genes (856 genes) were common between one or more mutant cell lines, suggesting overlapping gene expression and pathway perturbations may be an underlying feature of both *APP* and *PSEN1* fAD mutation pathogenicity (**Figure 34B**). To get a handle on what these common differentially expressed genes are, we performed an unbiased gene-ontology (GO) pathway analysis on the 856 genes commonly dysregulated in the mutants compared to wild-type. The top most significantly enriched GO-terms were related to synaptic functioning, GPCR signaling, and neuronal development (**Figure 34C**). Interestingly, we noticed that a handful of the genes in the top Synaptic Signaling GO-term hit were genes known previously to be involved in AD (e.g., *CLU, APOE, SORL1, GRIN3A, etc.*). This lead us to wonder whether there may be a more generalized change in expression of known AD-associated genes in fAD mutant neurons compared to wildtype. To assess expression patterns of AD-associated genes in our fAD mutant cell lines we curated a list of 114 putative “AD genes”, with identified AD-linked variants as determined by GWAS (downloaded from https://www.ebi.ac.uk/gwas/) (see Appendix I for complete list). We then determined the base Mean expression of these AD genes in our data to give us an overview of similarities and differences in AD gene expression between genotypes. Hierarchical clustering analysis revealed that *P1SEN1-M146V* and *Swe/M146V* double mutant neurons had more similar expression patterns of AD

genes, while *APPswe* neurons clustered more closely with wildtype neurons (**Figure 34D**). All mutant neurons were notably less correlated with wildtype cells. By performing a hypergeometric statistical test, we found that AD genes were significantly enriched amongst all genes differentially expressed in *APPswe, PSEN1-M146V* and *Swe/M146V* neurons compared to wildtype. In fact, between 20-25% of analyzed AD genes were differentially expressed in each mutant cell line compared to wildtype (**Figure 34E-G**). Individual gene expression of these 39 differentially expressed AD genes is shown (**Figure 34F**). These data suggest *APP* and *PSEN1* fAD mutations may commonly perturb an AD-associated gene network.

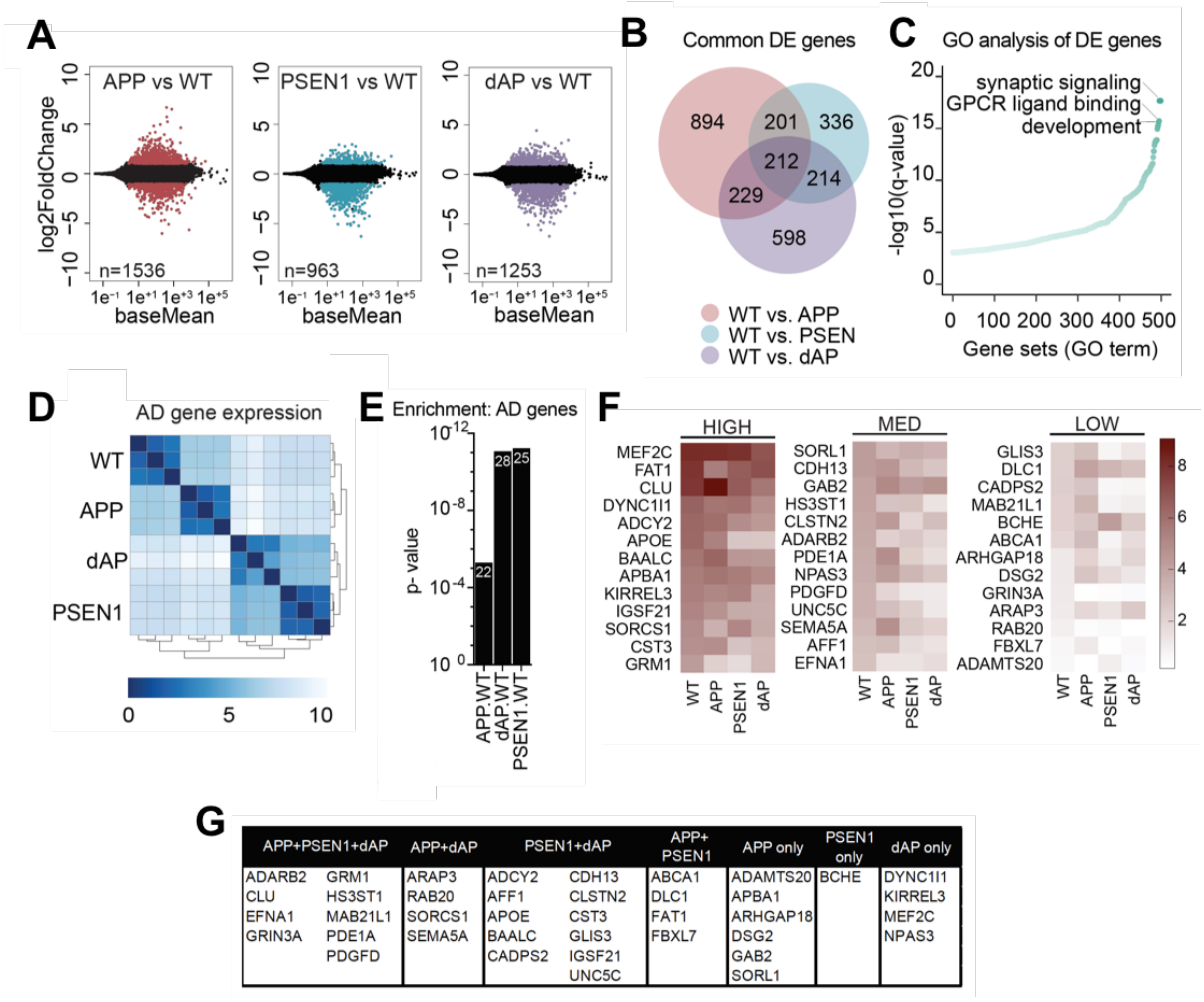

G

APP+PSEN1+dAP		APP+dAP	PSEN1+dAP		APP+ PSEN1	APP only	PSEN1 only	dAP only
ADARB2	GRM1	ARAP3	ADCY2	CDH13	ABCA1	ADAMTS20	BCHE	DYNC1I1
CLU	HS3ST1	RAB20	AFF1	CLSTN2	DLC1	APBA1		KIRREL3
EFNA1	MAB21L1	SORCS1	APOE	CST3	FAT1	ARHGAP18		MEF2C
GRIN3A	PDE1A	SEMA5A	BAALC	GLIS3	FBXL7	DSG2		NPAS3
	PDGFD		CADPS2	IGSF21		GAB2		
				UNC5C		SORL1		

Figure 34. RNA-seq differential expression analysis reveals AD-associated genes as dysregulated in fAD mutant neurons.

A) MA-plots depicts the Log_2FC (Y axis) and expression (TPM, X axis) of differentially expressed genes in mutant neurons compared to wildtype cells. **B**) Venneuler diagram showing the overlap of significantly differentially enriched genes in mutant neurons as compared to wild-type. Determined by R package DESEQ2. FDR < 0.05 & absolute $Log_2FC > 1$. **C**) Metascape GO analysis, plotted significance (log_{10} q-value) of top 500 enriched GO terms determined by overlapping gene lists (B). X-axis = Ranked GO-term number; Y-axis = -log_{10} q-value per GO-term. **D**) Heatmap of p value for Euclidean distance analysis of AD gene expression in wildtype and mutant neurons.

Each tile represents a single replicate (n=3); as expected replicates from each genotype cluster closest together. Scale represents the Euclidean distance between samples, calculated using the rlog-transformed values to avoid dominating the distance measure by a few highly variable genes. **E**) Plotted hypergeometric p-values of AD genes enriched within all significantly differentially expressed genes (FDR < 0.05 & absolute LFC > 1). Numbers in bars indicate number of AD genes enriched in differentially expressed gene sets. **F**) Heatmap depicting expression (Log_2 TPM) of all AD genes significantly differentially expressed in mutant neurons (from E). **G**) Table of AD genes differentially expressed in mutant cells compared to wildtype. Column headers indicate in which mutant neurons listed AD genes are differentially expressed (all compared to wildtype). Determined by R package DESEQ2. FDR < 0.05 & absolute $Log_2FC > 1$. dAP = *Swe/M146V* double mutant.

Given that we were most interested in deciphering the molecular pathways commonly perturbed by both *APP* and *PSEN1* mutations, we next sought to determine what gene expression differences are driven by *APP* and *PSEN1* mutation combination in *Swe/M146V* double mutant neurons compared to *APPswe* and *PSEN1-M146V* neurons alone. Using our differential expression analysis data, we compared *Swe/M146V* neurons to *APPswe* and *PSEN1-M146V* single mutant neurons independently and noticed a considerable number of differentially expressed genes in each comparison. There were substantially more significantly differentially expressed genes that either increased or decreased expression in double mutant neurons compared to single mutant neurons than in single mutant cells compared to wildtype. For example, we found *PSEN1* mutant cells had 963

differentially expressed genes compared to wildtype cells, but over 1.5 times more (1465 genes) when compared to *Swe/M146V* cells (**Figure 35A-B** compared to **Figure 34A**). These patterns of gene expression differences suggest that the combination of fAD mutations in *Swe/M146V* neurons may be exaggerating or augmenting AD-relevant transcriptomic changes. Interestingly, 60-70% of genes differentially expressed in double mutant cells compared to single mutant cells are non-overlapping, implying some unique "double-mutant effect" gene expression signature may exist compared to when mutations are expressed alone (**Figure 35C**).

To better understand the nature of these changes, we performed another GO analysis, this time inputting the list of all genes significantly differentially expressed in *Swe/M146V* cells compared to single mutant neurons. Remarkably, we noticed that of all the significant GO-terms identified a substantial number were associated with endocytosis and lipid trafficking (**Figure 35D**). Of these enriched terms, the largest gene-sets included the annotated ontologies "early endosome" ($P = 10^{-4}$), "endocytic vesicle" ($P = 10^{-8}$) and "early endosome membrane" ($P = 10^{-4}$). Moreover, between 20 and 30% of all genes that comprise these GO-terms were differentially expressed in our analysis. Together, approximately 100 unique differentially expressed endocytic-related genes were included in these enriched gene sets (see complete list of genes in Appendix I). When we compared expression of these endocytic genes across all genotypes by hierarchical clustering, we found that *PSEN1-M146V* and *Swe/M146V* neurons cluster more closely together than with *APPswe* or wildtype neurons (**Figure 35E**), implying a similar

pattern of endocytic gene expression between these two genotypes. Interestingly, *APPswe* neurons showed patterns of endocytic gene expression that were markedly uncorrelated with *PSEN1-M146V* and *Swe/M146V* neurons (see differences in **Figure 35E** heatmap), supporting the idea that while both fAD mutations may commonly affect endocytosis and endosomal related processes, they may do so by influencing different molecular pathways. Expression levels of the top 45 expressed endocytic genes is shown in **Figure 35F**.

Intriguingly, in addition to pinpointing the endocytic pathway, by comparing genes differentially expressed in double mutant neurons compared to single mutant neurons we also identified a substantial number of significantly enriched GO-terms associated with known AD processes and neurodegeneration (**Figure 35G)**. These data indicate that the combination of *APP* and *PSEN1* mutations may further interact to activate AD-relevant downstream molecular neurodegenerative signaling pathways. Taken together, these transcriptomic analyses indicate that our *APP* and *PSEN1* fAD mutant human neurons demonstrate a common signature of AD-associated molecular phenotypes, which, in part, may converge on endocytic dysfunction.

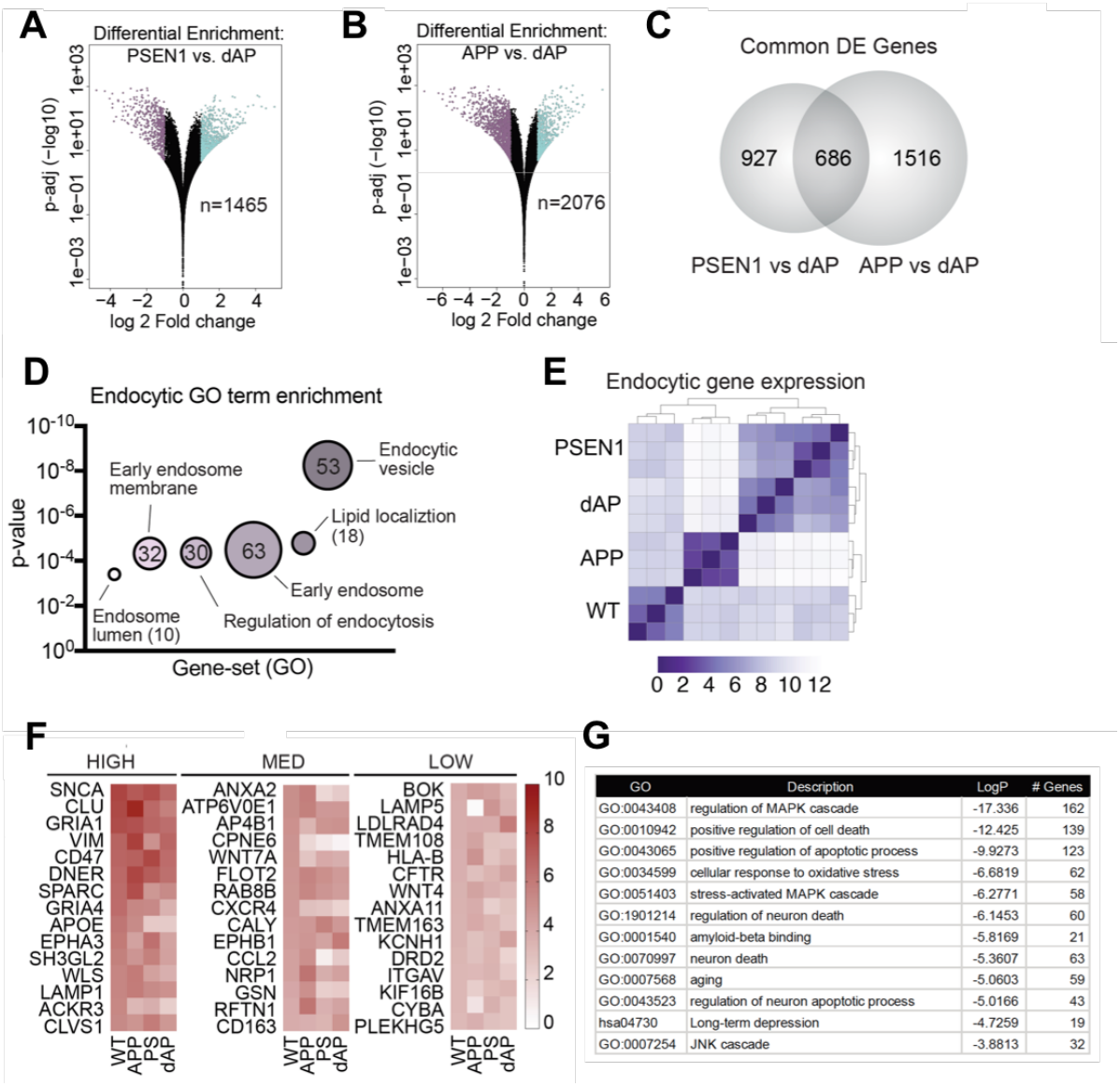

GO	Description	LogP	# Genes
GO:0043408	regulation of MAPK cascade	-17.336	162
GO:0010942	positive regulation of cell death	-12.425	139
GO:0043065	positive regulation of apoptotic process	-9.9273	123
GO:0034599	cellular response to oxidative stress	-6.6819	62
GO:0051403	stress-activated MAPK cascade	-6.2771	58
GO:1901214	regulation of neuron death	-6.1453	60
GO:0001540	amyloid-beta binding	-5.8169	21
GO:0070997	neuron death	-5.3607	63
GO:0007568	aging	-5.0603	59
GO:0043523	regulation of neuron apoptotic process	-5.0166	43
hsa04730	Long-term depression	-4.7259	19
GO:0007254	JNK cascade	-3.8813	32

Figure 35. Genes differentially expressed in *Swe/M146V* neurons are associated with endocytic processes.

A-B) Volcano plots representing adjusted p value (-Log_{10}) over the Log_2 fold change of *Swe/M146V* neurons compared to *PSEN1-M146V* (**A**) and *APPswe* (**B**) neurons. Each dot is representative of a gene ID. Differential analysis performed with R package DESEQ2. Blue and purple dots represent genes that show significantly increased or decreased expression, respectively. **C**) Venneuler diagram showing the overlap of significantly

differentially enriched genes in *Swe/M146V* mutant neurons as compared to *PSEN1-M146V* and *APPswe* neurons. Determined by R package DESEQ2. FDR < 0.05 & absolute $Log_2FC > 1$. **D**) Metascape GO analysis, plotted significance (log_{10} q-value) of enriched endocytic/trafficking GO terms determined by gene lists derived from (C). Y-axis = $-Log_{10}$ q-value per GO-term. Size of spot and number indicate number of differentially expressed genes enriched in each GO term. **E**) Heatmap of p value for Euclidean distance analysis of endocytic gene expression in wildtype and mutant neurons. Each tile represents a single replicate (n=3); as expected replicates from each genotype cluster closest together. Scale represents the Euclidean distance between samples, calculated using the Log-transformed values to avoid dominating the distance measure by a few highly variable genes. **F**) Heatmap depicting expression (Log_2 TPM) of top 45 expressed endocytic genes significantly differentially expressed in *Swe/M146V* mutant neurons compared to single mutant cells (from D). dAP = *Swe/M146V* double mutant; PS = *PSEN1-M146V*.

Early endosomal abnormalities are a unifying common phenotype in multiple *APP* and *PSEN1* fAD mutant iPSC-derived neurons.

Although *APPswe* and *PSEN1-M146V* are two of the most widely studied mutations, they represent only a small fraction of the hundreds of fAD mutations that have been identified, many of which alter amino acids within different gene domains and contribute to variable clinical manifestations (Giri et al., 2016; Shea et al., 2016). In order to better understand whether endosomal dysfunction is a shared common phenotype across a variety of fAD mutations, we set out to generate a large and

comprehensive panel of isogenic mutant human iPSCs. We strategically chose to include in our study 3 different known *APP* mutations that are differentially distributed across the *APP* gene and predicted to differentially influence β-secretase- (*APPswe*), α-secretase- (*APP-A692G*) or γ-secretase- (*APP-V171G*) related processing (Chartier-Harlin et al., 1991; Hendriks et al., 1992; Mullan et al., 1992) (**Table 2** and see schematic in **Figure 7**). Four *PSEN1* mutations (*PSEN1-M146V, PSEN1-L166P, PSEN1-M233L and PSEN1-A246E)* distributed across the gene with different predicted severities were also selected for our analyses (Aldudo et al., 1999; Alzheimer's Disease Collaborative Group, 1995; Moehlmann et al., 2002; Sherrington et al., 1995) (**Table 2**). Mutant iPSC lines were all generated by CRISPR/Cas9-mediated mutation knock-in using our established common wildtype parental cell line (see **Appendix I**), therefore making all additional cell lines studied completely isogenic and avoiding any contribution of non-specific phenotypes due to background genetic heterogeneity. iPSCs were then differentiated into human cortical neurons to study endosomal phenotypes (differentiation procedure described in **Appendix I**).

Table 2. List of all isogenic mutant iPSC lines and mean age of AD onset.

WT parental line: 7889SA			Mean age of onset (SD)
Cell line	**CRISPR edit**	**Genotype**	
1	*APP* Knock-In (pathogenic)	WT/Swe	52.25 (5.74)[1]
2		Swe/Swe	
3		WT/A692G	47.00 (3.37)[1]
4		A692G/A692G	
5		WT/V717G	50.00 (6.0)[1]
6		V717G/V717G	
7	*PSEN1* Knock-In (pathogenic)	WT/M146V	39.00 (NA)[1]
8		M146V/M146V	
9		WT/L166P	28 (NA)[2]
10		L166P/L166P	
11		WT/M233L	35.5 (7.78)[1]
12		WT/A246E	50.14 (4.30)[1]
13		A246E/Null	
14	Double Knock-In (pathogenic)	Swe/Swe M146V/M146V	
15	*APP* Knock-In (protective)	A673T/A673T	
16	*APP* Knock-Out	APP-KO/KO	

1- From DIAN study (Ryman et al., 2014)

2- From (Moehlmann et al., 2002)

It has now been demonstrated in a variety of different model systems that early endocytic dysfunction, such as an aberrant enlargement of Rab5+ early endosomes, may be a common upstream pathological hallmark feature of AD (Cataldo et al., 2000; 2008; Israel et al., 2012; Raja et al., 2016; Woodruff et al., 2016). However, it is unclear whether early endosome pathology can be assayed in isogenic mutant human iPSC-derived neurons, and not known whether it is common to multiple different *APP* and *PSEN1* fAD mutations. To explore this, we used high resolution and quantitative immunofluorescence to study Rab5+ early endosome

morphology in all our *APP, PSEN1* and double knock-in mutant iPSC-derived neurons. Strikingly, we noticed in all homozygous mutant neurons a significant increase in the size of Rab5+ early endosomes (**Figure 36A-B**), which also corresponded with increased fluorescence intensity (**Figure 36C**). Interestingly, we did not see any consistent differences in the total number of Rab5+ early endosomes per cell across our panel of isogenic mutant iPSC-derived neurons (**Figure 36D**). This endosome size change is specifically driven by an overall decrease in the number of small endosomes (<0.5μm^2) and a much larger increase in the number of larger (>1μm^2) endosomes (**Figure 36E**). Interestingly, Rab5+ endosome enlargement was significantly exaggerated in the *Swe/M146V* double knock-in neurons compared to single homozygous and wildtype cells (**Figure 36A-B**), suggesting the mutations in these two genes may pathologically converge on a common cellular mechanism. While heterozygous mutant cells did not all demonstrate significant differences in mean endosome area or frequency of enlarged endosomes, many heterozygous mutant neurons displayed intermediate phenotypes compared to homozygous counterparts (**Figure 36F-G**).

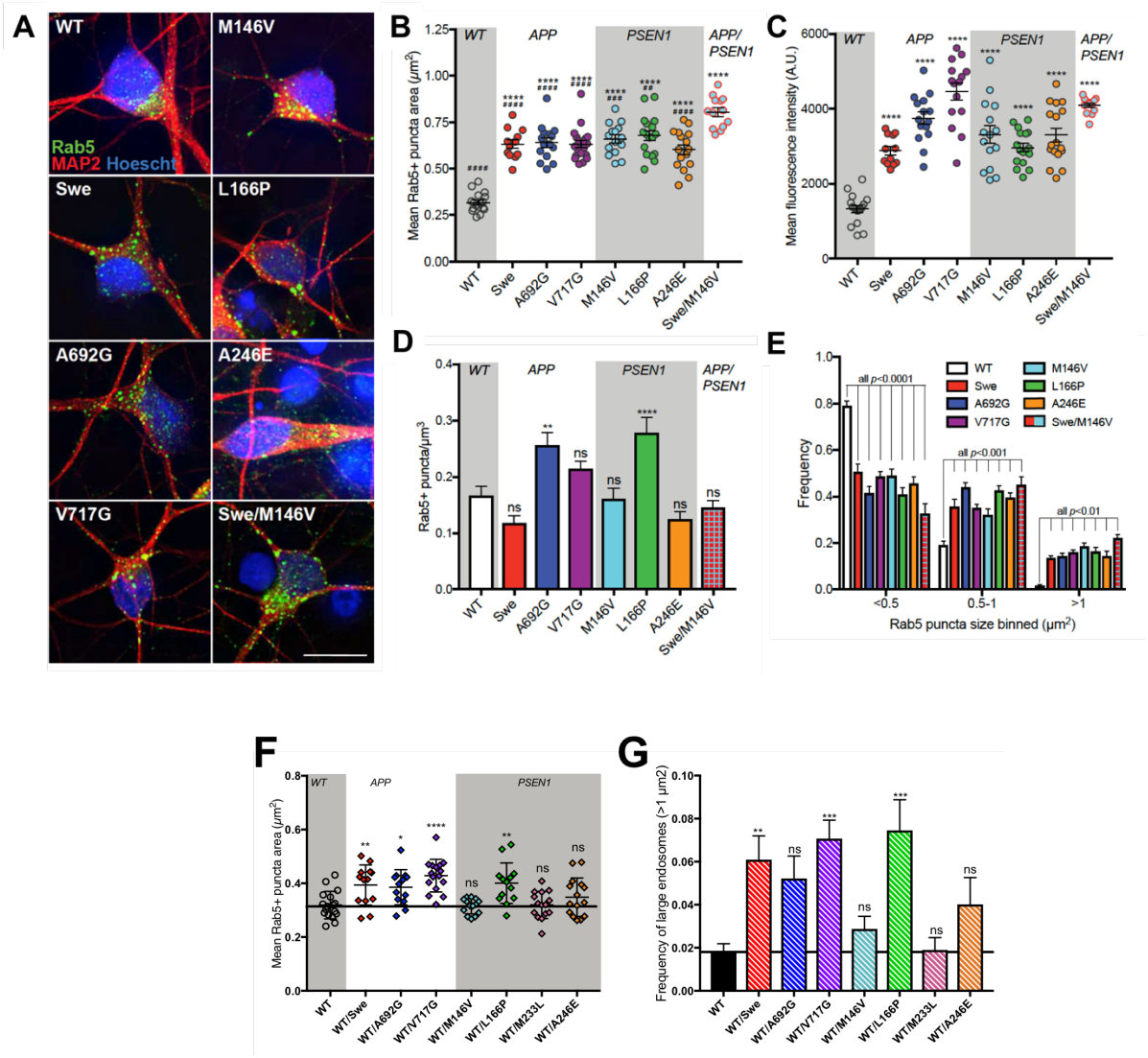

Figure 36. Early endosomal abnormalities are a shared APP-dependent common phenotype in APP and PSEN1 fAD mutant iPSC-derived neurons.

A) Representative immunofluorescence images from homozygous mutant human neurons stained for Rab5 (green), MAP2 (red) and Hoechst (blue). The sizes of Rab5+ puncta were quantified using Imaris. **B**) All mutant cells demonstrate increased mean Rab5+ endosome size compared to wildtype. **C**) Mean fluorescence intensity of Rab5+ punta increases in all fAD mutatnt cells compared to wildtype. **D**) Total number of Rab5+ early endosomes per

cell does not consistently change in each fAD mutant line. Values represent mean ± SEM. $^{**}P < 0.05$ and $^{***}P < 0.001$, $^{****}P < 0.0001$, one-way ANOVA with comparison to wildtype. $^{\#\#}P < 0.05$ and $^{\#\#\#}P < 0.001$, $^{\#\#\#}P < 0.0001$, one-way ANOVA with comparison to Swe/M146V. **E**) The size distribution of Rab5+ puncta of all fAD mutant neurons compared to wildtype shows a shift from smaller to larger Rab5+ early endosomes. Values represent mean ± SEM and *P* values represent two-way ANOVA with comparisons to wildtype. Mean endosome size (**F**) and frequency of large endosomes (**G**) of all heterozygous *APP* and *PSEN1* mutant neurons compared to wildtype. Values represent mean ± SEM. $^{**}P < 0.05$ and $^{***}P < 0.001$, $^{****}P < 0.0001$, one-way ANOVA with comparison to wildtype. $^{\#\#}P < 0.05$ and $^{\#\#\#}P < 0.001$, $^{\#\#\#}P < 0.0001$, one-way ANOVA with comparison to Swe/M146V WT = wildtype. n=12-20 cells analyzed. Scale bar, 10μm.

APP and *PSEN1* fAD mutations increase accumulation of longer Aβs and APP β-CTFs in human neurons.

It is widely thought that fAD mutations contribute to AD pathogenesis by aberrantly affecting APP processing and Aβ production. Therefore, we next sought to characterized how *APP* and *PSEN1* mutations affect APP metabolism and to pinpoint which APP peptides may represent a common correlate associated with endosomal dysfunction. APP is cleaved initially and most often by α-secretase at the cell surface, which, by cleaving within the amyloid portion of the protein, precludes the generation of Aβ (**Figure 37A**). To generate Aβ, APP is first endocytosed, and within an early endocytic vesicle is subsequently cleaved by β-secretase cleavage enzyme (BACE), as the activity of BACE is favored by the acidic endocytic

environment. BACE cleavage of APP produces APP β-CTF, which is then further processed by γ-secretase to yield Aβs of varying length (**Figure 37A-B**). It is now widely accepted that the mechanism by which γ-secretase cleaves APP β-CTF is processive in nature. In short, γ-secretase cleaves β-CTF in 3-4 amino acid increments generating Aβs of different lengths, most commonly 38 or 40 amino acids in length (**Figure 37B**) (Szaruga et al., 2017; Takami et al., 2009).

When we analyzed various species of Aβ secreted by mutant human cortical neurons, we noted only one common trend across all pathogenic fAD mutant lines. Levels of longer Aβs, namely Aβ43 and/or Aβ42, were increased in cell culture supernatants of all *APP* and *PSEN1* mutant neurons compared to wildtype cells (**Figures 37C-D**). Levels of shorter Aβ, however, were not changed in a consistent way across *APP* and *PSEN1* mutant neurons. Specifically, all *APP* mutants had increased Aβ38 compared to wildtype, whereas all *PSEN1* mutants significantly decreased Aβ38 (**Figure 37E**). Similarly, the *APPswe* and *APP-A692G* mutants increased Aβ40, whereas all *PSEN1* mutants decreased Aβ40 (**Figure 37F**). Interestingly, the *APP-V717G* mutant, which lies at the γ-secretase cleavage site, decreased Aβ43 and Aβ40 compared to wildtype, highlighting how this mutation shifts γ-secretase processing toward the Aβ42 and Aβ38 pathway (**Figures 37B, D and F**). When levels of all Aβ species measured were summed together to quantify total Aβ levels compared to wildtype, *APP* and *PSEN1* mutant cells again had opposite effects, with *APPswe* and *APP-A692G* mutants increasing total Aβ, and all *PSEN1* mutants decreasing total Aβ (**Figure 37G**).

We next calculated the Aβ 42:40 ratio, which has been widely used to determine AD severity in cases of both sAD and fAD. We observed that the *APPswe* and *APP-A692G* mutants had no effect on the Aβ 42:40 ratio, whereas the *APP* V717G mutants, and all *PSEN1* mutants increased the Aβ 42:40 ratio (**Figure 37H**). *PSEN1-L166P* most dramatically affected the Aβ 42:40 ratio (~14-fold increase compared to wildtype), which corresponds with how clinically severe this mutation is known to be (age of onset in 20's, **Table 2**). Interestingly, *Swe/M146V* double knock-in neurons demonstrated an Aβ profile consistent with combinatorial effects of both the *APPswe* and *PSEN1-M146V* mutation, i.e., *Swe/M146V* neurons had substantially higher levels of all Aβ peptides measured, as well as elevated Aβ 42:40 ratio (**Figure 37C-H**).

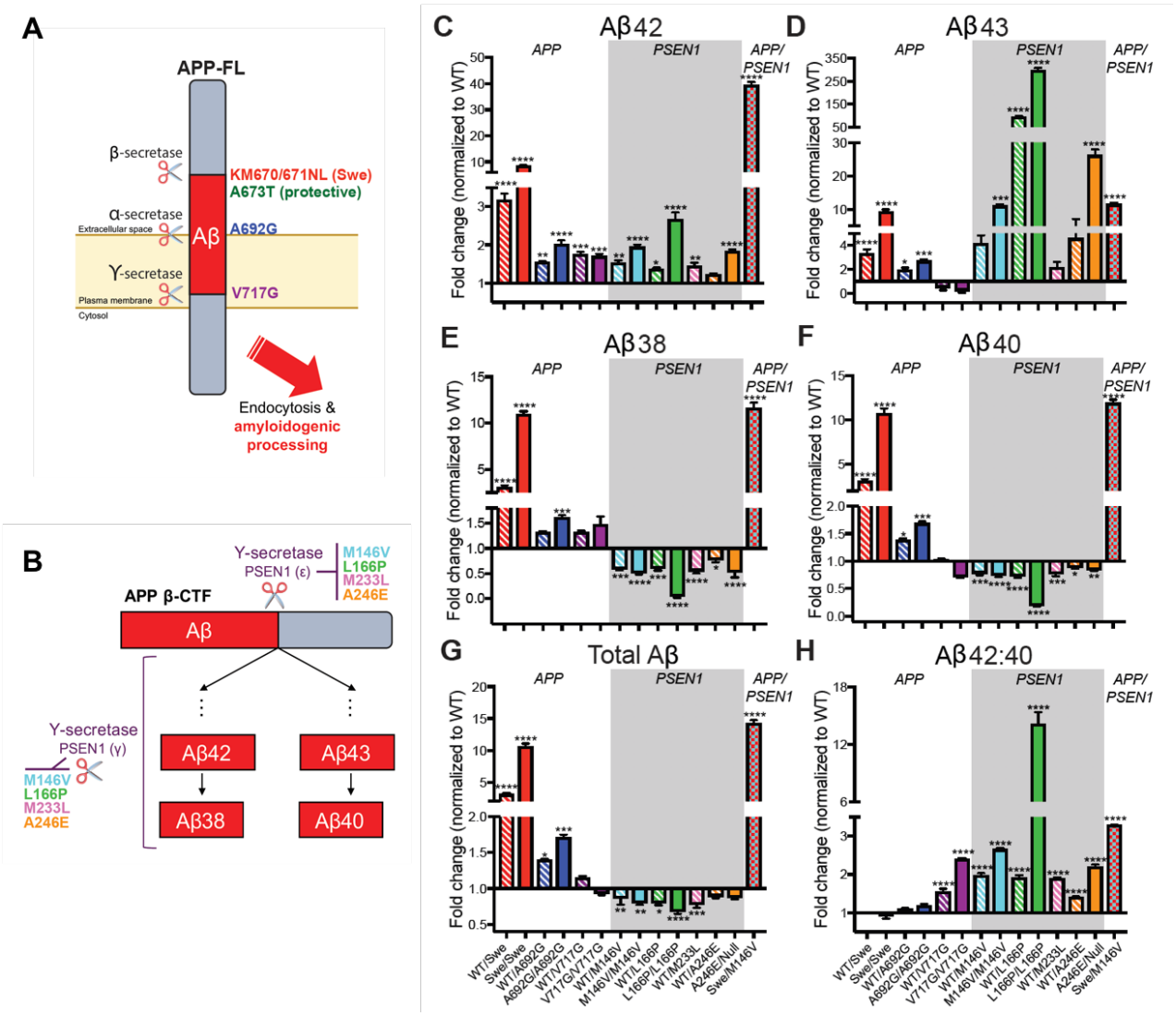

Figure 37. *APP* and *PSEN1* mutations increase production of longer Aβ peptides.

A) Schematic of APP processing and representation of distribution of APP mutations engineered as described in Table 1. **B**) Schematic of γ-secretase processing of β-CTF to generate Aβs of varying length. *PSEN1* mutations depicted to represent the γ-secretase cleavages processes that may be affected. **C-H**) Aβ measurements in *APP*, *PSEN1* and *Swe/M146V* double mutant neurons (DIV60-70) compared to wildtype. Represented as fold-change compared to wildtype. Supernatants analyzed for **C**) Aβ42, **D**) Aβ43, **E**) Aβ38 and **F**) Aβ40 by ELISA. **G**) All Aβs measured were summed together

to determine total Aβ, and **H**) the ratio of Aβ 42:40 was calculated. Values represent mean (n=3 biological replicates) ± SEM $^{**}P < 0.05$ and $^{***}P < 0.001$, $^{****}P < 0.0001$, one-way ANOVA, outliers identified by ROUT method (Q = 1%).

Amyloidogenic processing of APP for Aβ generation depends on β-secretase-mediated generation of β-CTF, whereas non-amyloidogenic processing occurs when APP is instead first cleaved by α-secretase to generate a 16 amino acid shorter peptide called α-CTF. Both β- and α-CTF are substrates for subsequent cleavage by γ-secretase. Therefore, in addition to Aβ production, fAD mutations, by affecting α-, β- and γ-secretase cleavage, may also affect the metabolism of β- and/or α-CTF. When examining APP CTFs by Western blot, we noted the presence of five distinct bands, which have previously been reported to be the phosphorylated and dephosphorylated β-CTFs (C99/p-C99 and C89/p-C89) and α-CTFs (C83/p-C83), with C89 and p-C83 overlapping (Buxbaum et al., 1998) (**Figures 38A-B**). We noticed that *APP* and *PSEN1* mutants demonstrated variable effects on α-CTF metabolism (**Figure 38C**). However, all *APP* and *PSEN1* mutant human neurons exhibited an accumulation of β-CTF (**Figure 38D**). *Swe/M146V* neurons further demonstrated an additive effect of the *PSEN1* and *APP* mutations on CTF accumulation, resulting in substantially higher levels of accumulated β-CTF compared to all single mutant and wildtype neurons (**Figure 38**).

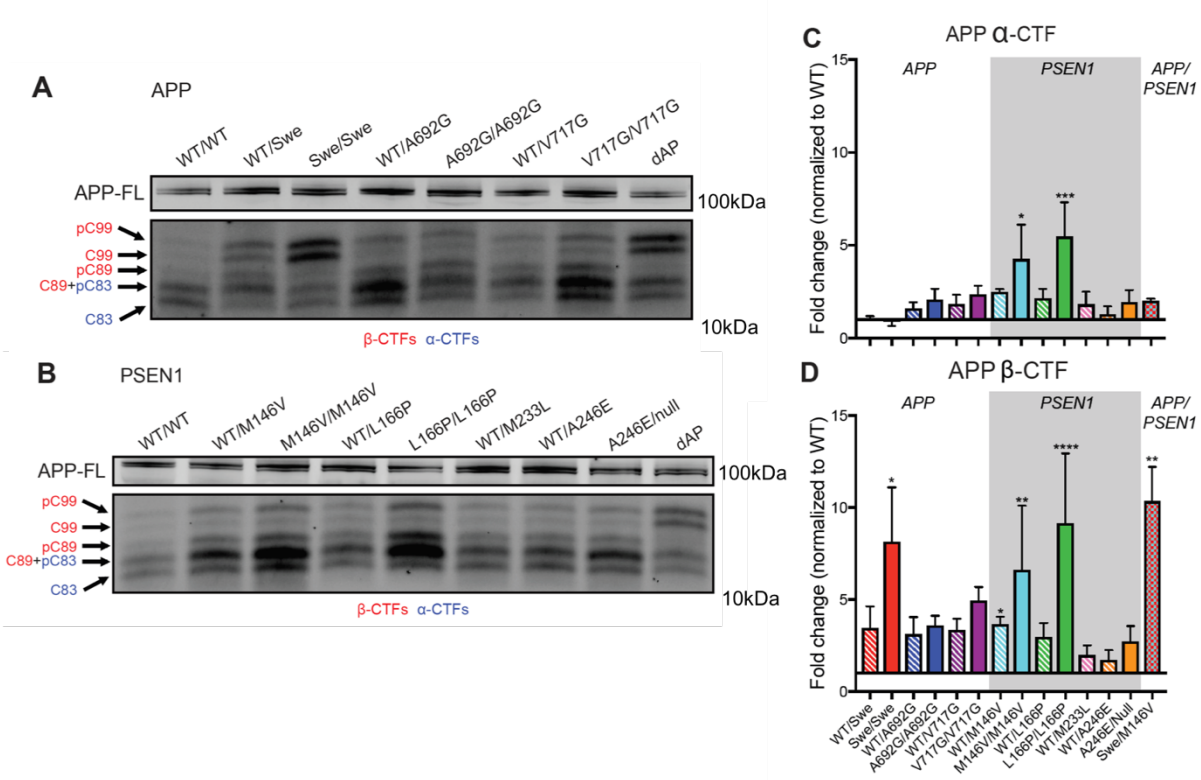

Figure 38. *APP* and *PSEN1* fAD mutations increase accumulation of APP β-CTFs.

α-CTF and β-CTF levels were analyzed by western blot in *APP* (**A**) and *PSEN1* (**B**) mutant neurons and were quantified using densitometry (**C** and **D**). *Swe/M146V* double mutant neurons were included in both blots for comparison. Western blot densitometry values represent mean (n=3 replicates) ± SEM $^{**}P < 0.05$ and $^{***}P < 0.001$, $^{****}P < 0.0001$.

Taken together, these data demonstrate that although different *APP* and *PSEN1* fAD mutations may variably affect APP processing and Aβ generation, common trends across all mutations do exist. Specifically, in all *APP* and *PSEN1* fAD mutant cells we detected increased levels of longer Aβs and β-CTF, which are

therefore candidates for being critical APP-derivatives most relevant to the development of AD.

Early endosomal enlargement in human fAD mutant neurons is dependent on APP processing and can be rescued by BACE inhibition.

fAD mutant iPSC-derived neurons all demonstrate endosome enlargement as well as elevated longer Aβs and accumulation of β-CTF. Therefore, if these cellular and biochemical changes are related, then genetic manipulations to lower Aβs and β-CTF may reverse the endosomal phenotype. To test this we used our isogenic mutant iPSC line with the protective *APP-A673T* mutation knocked-in at both alleles (Jonsson et al., 2012; Kwart et al., 2017; Paquet et al., 2016). The *APP-A673T* mutation is directly adjacent to the *APPswe* mutation near the β-secretase processing site of APP (**Figure 37A** and **Figure 7**). When we examined the various β-CTFs, we noted no change in total β-CTFs between *APP-A673T* and WT (**Figure 39B and D**). However, *APP-A673T* mutant neurons demonstrated a shift in APP processing that trended (albeit not significantly) towards an increase in the production of non-amyloidogenic C89 β-CTFs (**Figure 39B-C**), along with a reduction in total Aβ (**Figure 39A**). In addition, we studied an isogenic APP knockout (*APP-KO*) iPSC line that we generated using CRISPR/Cas9-mediated deletion of the conserved APP transcription start-site (see details on *APP-KO* iPSC generation in **Appendix I**). As expected, *APP-KO* iPSC-derived neurons had undetectable levels of Aβ (**Figure 39A**). When studying endosome morphology, *APP-KO* neurons

demonstrated a highly significant reduction in Rab5+ endosome size compared to wildtype; *APP-A673T* neurons also showed a trend towards reduction, but it was not significant (**Figure 39E-F**). When analyzing the frequency distribution of endosome size, we found *APP-KO* neurons have a significant increase in the number of small endosomes (<0.5μm^2) and reduction in the number of medium-sized endosomes (0.5-1μm^2) (**Figure 39G**). These results support the view that endosome pathology seen in *APP* and *PSEN1* mutant neurons is indeed dependent on APP and its altered processing caused by fAD mutations, confirming recent findings. Taken together, these data further support the notion that amyloidogenic APP processing is capable of causing endocytic abnormalities seen in mutant human neurons.

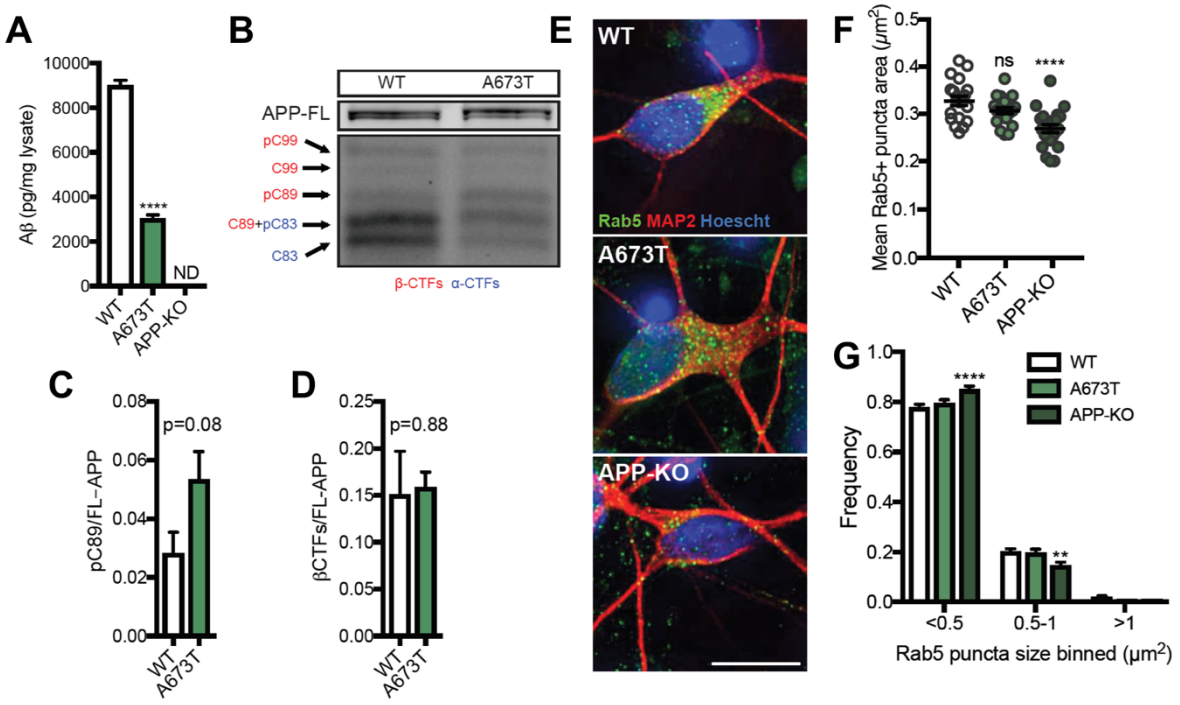

Figure 39. Rab5+ early endosomes enlargement is APP-processing dependent.

Total Aβ (**A**), Aβ 42:40 ratios (**B**) as well as FL-APP and APP-CTFs (**C**) were measured in protective *APP-A673T* mutant and *APP-KO* neurons by ELISA and western blot, respectively. **D**) *APP-A673T* shifts APP processing towards α-CTF generation. **E**) Representative immunofluorescence images from wildtype, *APP-A673T* and *APP-KO* stained for Rab5 (green), MAP2 (red) and Hoechst (blue). **F**) Mean Rab5+ endosome area per cell (n=18-23 cells), and **G**) frequency distribution of endosome size. Values represent mean ± SEM. $^{**}P < 0.05$ and $^{****}P < 0.0001$, one-way ANOVA (**F**) or two-way ANOVA (**G**) with comparisons to controls. $^{\#\#}P < 0.001$, one-way ANOVA compared to wildtype. Scale bar, 10μm.

In pathogenic fAD mutant neurons, endogenous Aβ and β-CTF levels can be manipulated by treatment with a β-secretase inhibitor (BACEi), which should prohibit

amyloidogenic processing of APP. We confirmed in *Swe/M146V* neurons, which demonstrated the largest increase in Aβ production, that BACEi treatment significantly decreases total Aβ production (**Figure 40A**), and almost completely prevents the generation of β-CTF in L166P homozygous neurons, which showed the largest increase in all detectable APP-CTFs (**Figure 40B**). Interestingly, endosome enlargement seen in all *APP* and *PSEN1* mutant iPSC-derived neurons was significantly rescued by BACEi treatment (**Figure 40C-D**). Taken together, these rescue experiments further support that in human neurons, Rab5+ early endosome morphological changes seen in fAD are mediated by endogenous changes in APP processing caused by *APP* and *PSEN1* mutations and can be rescued pharmacologically by BACEi treatment.

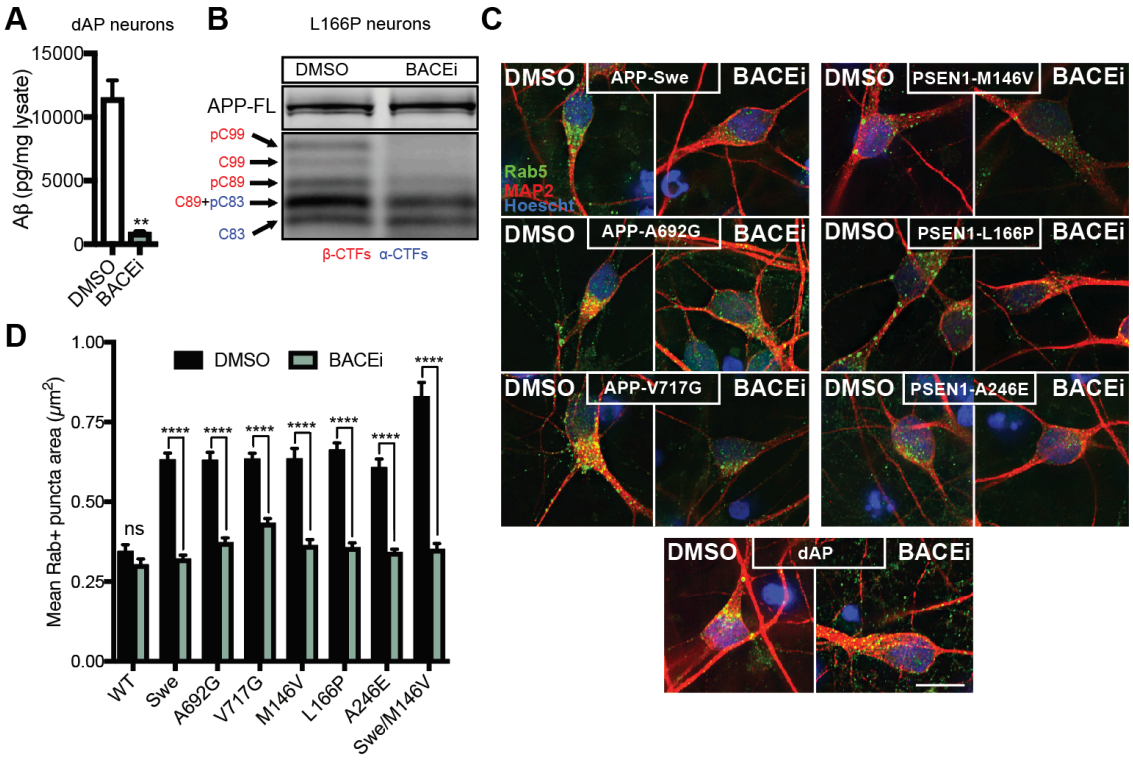

Figure 40. Rab5+ early endosomes enlargement can be rescued by BACEi treatment in fAD mutant neurons.

A) Compared to DMSO control, BACEi treatment of *Swe/M146V* double mutant neurons nearly abolishes Aβ production with concomitant reduction of β-CTF, as determined by western blot (**B**). Representative images of Rab5 (green), MAP2 (red) and Hoescht (blue) staining (**C**) and quantification (**D**) showing BACEi treatment of homozygous mutant *APP* and *PSEN1* neurons significantly reduces endosome size (n=10-20 cells). The sizes of Rab5+ puncta were quantified using Imaris. Values represent mean ± SEM. $^{**}P < 0.05$ and $^{****}P < 0.0001$, two-way ANOVA with comparisons to controls. Scale bar, 10μm.

Rab5+ early endosomes enlargement is not rescued by reducing longer Aβ peptides with a γ-secretase modulator.

Although some previous studies have also implicated APP β-CTF as a plausible contributor to intracellular trafficking defects in AD (Jiang et al., 2010; Kim et al., 2015; Woodruff et al., 2016; Xu et al., 2016), other studies suggesting longer Aβs are relevant to endocytic dysfunction have also been reported (Treusch et al., 2011). Many of these studies did not investigate AD-related endosomal defects in human neurons, were confounded by their use of non-physiological APP (or β-CTF or Aβ) overexpression, or did not precisely separate the contribution of Aβs from that of β-CTF. We therefore aimed to determine in mutant iPSC-derived neurons with endogenous *APP* and *PSEN1* expression whether endosome enlargement seen in fAD neurons is specifically associated with longer Aβs and/or β-CTF.

We tested the contribution to endosome dysfunction of longer Aβs by treating neurons with a γ-secretase modulator (GSM). GSMs are a class of AD therapeutics engineered to alter γ-secretase function without blocking activity (Crump et al., 2013) (inhibitors of γ-secretase were found to be ineffective in clinical trials and actually made patient symptoms worse). We tested the effect of a GSM on *PSEN1-M146V, PSEN1-L166P and Swe/M146V* homozygous mutant neurons, all of which accumulate longer Aβs through a consistent loss of γ-secretase processivity (**Figures 37 and 38**). Wildtype neurons were treated for comparison. GSM treatment had no apparent effect on total Aβ production (**Figure 41A**), but in wildtype, *M146V* and *Swe/M146V* cells GSM resulted in a robust reduction of longer

Aβ production concomitant with an increase in production of shorter Aβ (**Figure 41B-F**). Interestingly, GSM treatment did not result in any significant overall changes in longer versus shorter Aβ levels in *PSEN1-L166P* homozygous mutant neurons (**Figure 41B**). This result is of particular interest, since the *PSEN1-L166P* mutation is the most severe mutation we studied (see **Table 2**), and suggests that this mutation is so detrimental to γ-secretase that the GSM had no effect.

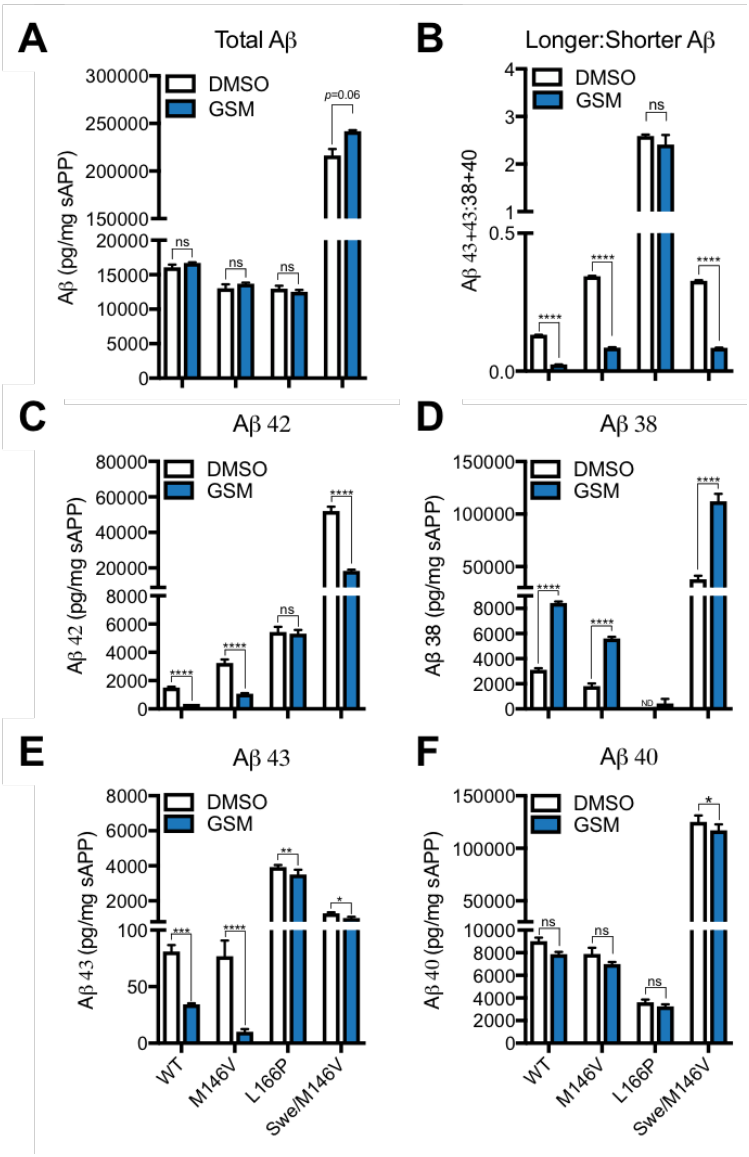

Figure 41. Aβ analysis of GSM treated wildtype and fAD mutant iPSC-derived neurons.

A) Wildtype and mutant neurons treated with a GSM does not alter total Aβ production (Aβ 38+40+42+43) but shifts processing to increase longer Aβs (42+43) relative to shorter Aβs (38+40) (**B**) compared to DMSO control. **C**) Treatment of GSM results in Aβ42 levels to be significantly reduced in all neurons except for *PSEN1-L166P* homozygous cells. **D**) GSM treatment results in a corresponding increase in Aβ38 levels. **E**) Aβ43 is more subtly

reduced in all neurons with treatment of GSM. **F**) Aβ40 levels are relatively unchanged by GSM treatment compared to DMSO. Values represent mean (n=3 biological replicates) ± SEM. $^{**}P < 0.05$ and $^{***}P < 0.001$, $^{****}P < 0.0001$, two-way ANOVA, outliers identified by ROUT method (Q = 1%).

GSM treatment did not affect β-CTF (or α-CTF) levels as analyzed by western blot (**Figure 42A-B**), highlighting how this class of drug selectively affects γ-secretase processivity (carboxypeptidase) and not endopeptidase (ε) cleavage in human neurons (**Figure 37B)**. Remarkably, treatment with GSM failed to rescue the Rab5+ endosome enlargement in mutant neurons compared to control conditions (**Figure 42C-D**), suggesting that endogenous accumulation of longer Aβ in fAD mutant neurons alone does not contribute to the early endocytic dysfunction in AD.

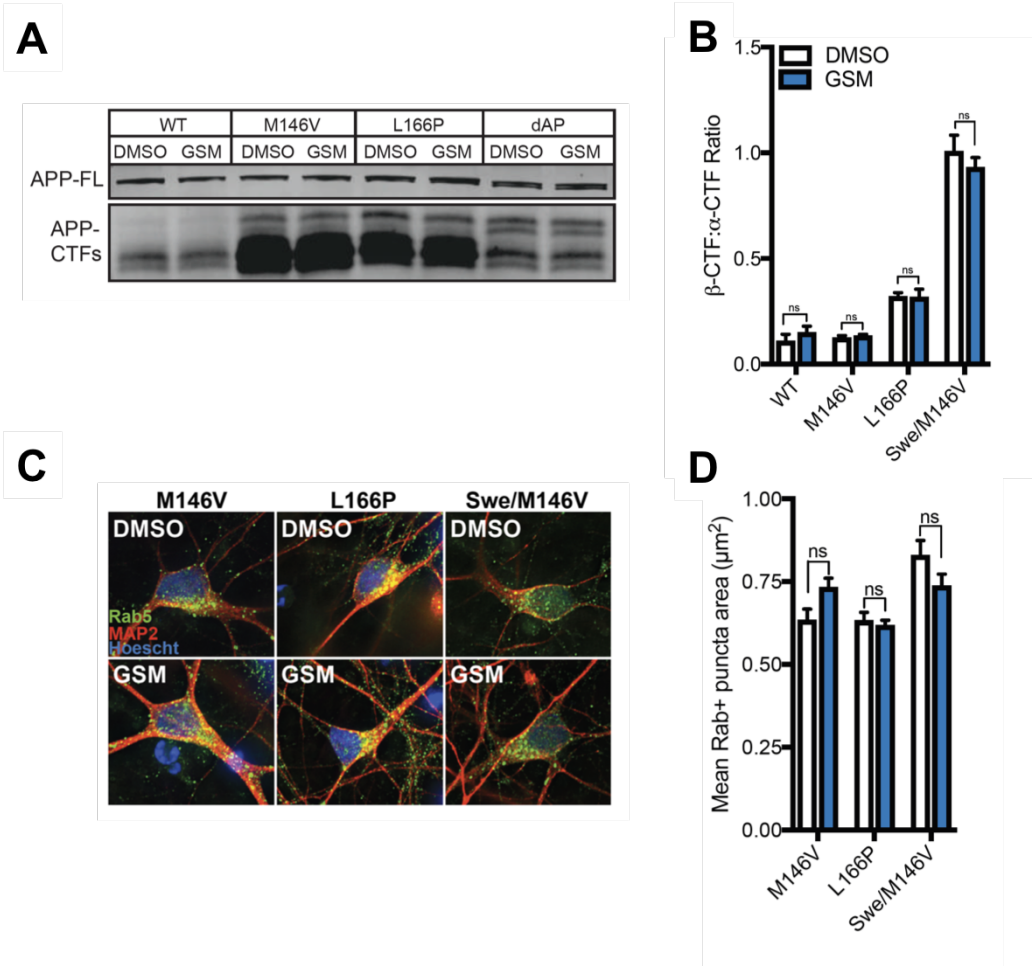

Figure 42. GSM treatment does not affect APP-CTF levels nor rescue endosome enlargement in mutant neurons.

GSM treatment does not alter α-CTF and β-CTF, as analyzed by western blot (**A**) and quantified by densitometry (**B**). Representative images of Rab5 (green), MAP2 (red) and Hoescht (blue) staining (**C**) and quantification (**D**) for GSM treated *PSEN1-M146V, L166P* and *Swe/M146V* double mutant neurons (n=10-20 cells). Values represent mean ± SEM. ns = not significant, two-way ANOVA with comparisons to control. Scale bar, 10*μ*m.

Increasing endogenous APP β-CTF in wildtype human neurons causes early endosome enlargement.

Recent studies have relied on using overexpression of APP β-CTF in either rodent neurons or non-neuronal cell lines to test whether APP β-CTF is sufficient to cause early endosome dysfunction (Jiang et al., 2010; Kim et al., 2015; Xu et al., 2016). APP β-CTF is a rare and transient intermediate APP metabolite, and its generation and trafficking is tightly regulated by concerted β-, α- and γ-secretase activity (Haass et al., 2012). Therefore, β-CTF overexpression is not only non-physiological, but more importantly may inadequately recapitulate the normal trafficking and biological relevance of the peptide. We therefore aimed to study the effect of increasing endogenous APP β-CTF on early endosome morphology without overexpression in wildtype human iPSC-derived neurons pharmacologically. Wildtype neurons were treated with a γ-secretase inhibitor (GSi), which effectively eliminates secreted Aβ production (**Figure 43A**). Since γ-secretase cleaves β-CTF to generate Aβ, γ-secretase inhibition also results in an accumulation of β-CTF in wildtype neurons (**Figure 43B**). In wildtype neurons, γ-secretase more commonly cleaves α-CTF, which exists at much higher levels than β-CTF. Therefore, GSi treatment also much more robustly increases the levels of α-CTF compared to β-CTF in human neurons (**Figure 43B**). β-CTF only subtly differs from α-CTF, which lacks the N-terminal 16 amino acids of β-CTF. To be able to separate β-CTF from α-CTF, we combined GSi and BACEi treatment, which results in an increase in levels of endogenous α-CTF but not β-CTF (**Figure 43B**). We found that GSi and

BACEi treatment together did not affect endosome size, however treatment with GSi alone was sufficient to induce the enlargement of Rab5+ early endosomes compared to DMSO (**Figure 43C-E**).

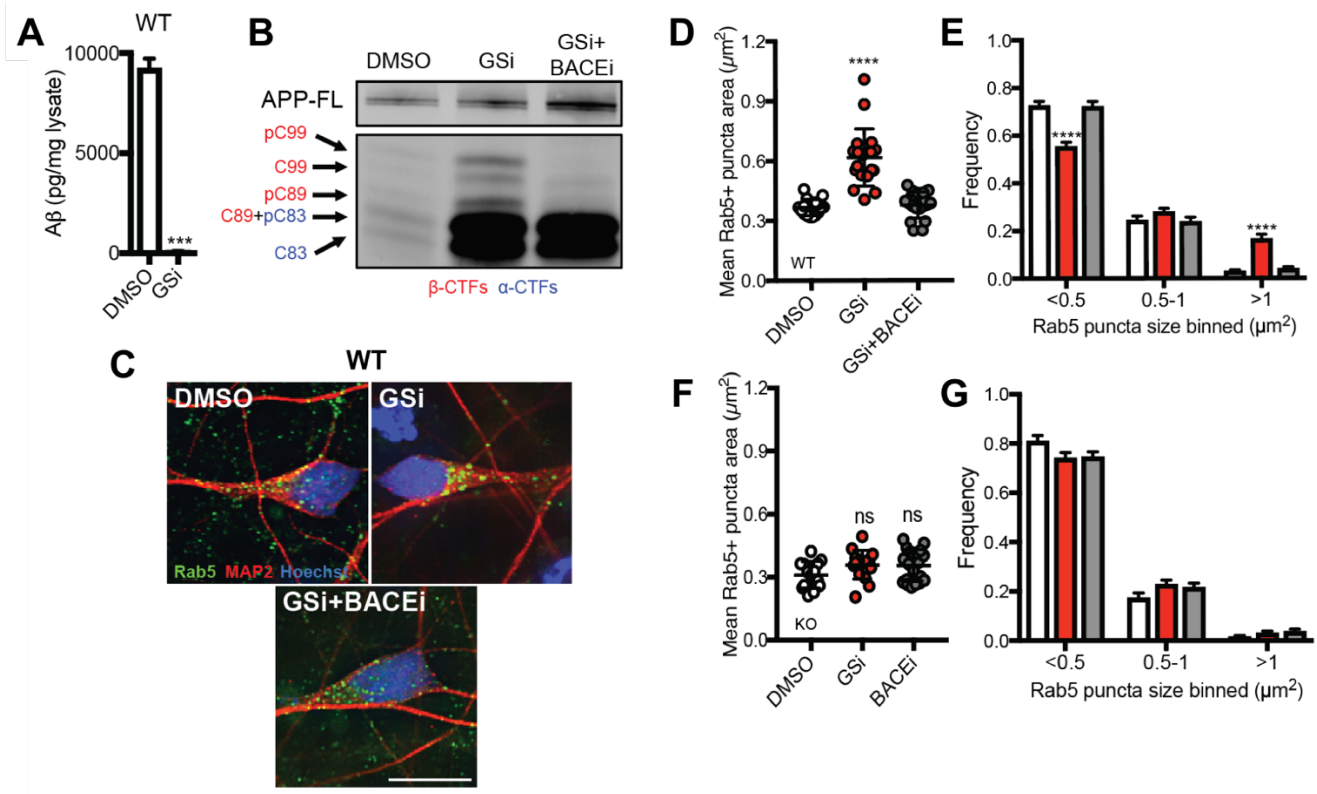

Figure 43. Increasing endogenous APP β-CTF in wildtype human neurons causes Rab5+ early endosome enlargement.

A) Wildtype neurons treated with a GSi nearly abolishes total Aβ production. **B**) GSi treatment of wildtype neurons dramatically increases both α-CTF and β-CTF, while co-treatment of wildtype neurons with GSi and BACEi results in an increase of only α-CTF measured by western blot. Representative images of Rab5 (green), MAP2 (red) and Hoescht (blue) staining (**C**) and quantification (**D**) showing wildtype neurons treated with GSi results in significantly increased mean Rab5+ endosome size and number of larger (>1 μm^2) endosomes (**E**), while co-treatment with GSi and BACEi has no effect.

F) and **G**) treatment of *APP KO* neurons with GSi has no effect on endosome size compared to DMSO control. The sizes of Rab5+ puncta were quantified using Imaris. Values represent mean ± SEM (n=16-19 cells). $^{**}P < 0.05$ and $^{***}P < 0.001$, $^{****}P < 0.0001$, one-way ANOVA (D), two-way ANOVA (E and G) or t-test (A and F) compared to control. Comparisons in F and G are all not significant. Scale bar, 10μm.

Lastly, to confirm that GSi and BACEi treatment are on-target and influencing endosome morphology through APP β-CTF, we repeated the GSi treatment in *APP-KO* iPSC-derived neurons. GSi treatment had no effect on Rab5+ early endosome size in *APP-KO* neurons (**Figure 43F-G**), indicating that GSi-induced endosome enlargement depends on *APP* and therefore most likely β-CTF. In summary, these data confirm that pathological endogenous APP β-CTF accumulation seen in fAD mutant human neurons may be both sufficient and necessary for common early endosome dysfunction associated with AD.

Conclusions

It has been known for nearly 30 years that mutations in *APP* and *PSEN1* cause AD, but precisely how these mutations in two distinct genes result in the same disease remains incompletely understood. In this study we generated a large panel of isogenic fAD mutant iPSC-derived neurons to study underlying common AD-relevant pathological processes in human neurons. Guided by unbiased molecular profiling, we found that select *APP* and *PSEN1* mutant neurons share common sets

of dysregulated genes enriched in pathways associated with AD and with endocytic/endosomal processes. We expanded on these transcriptomic analyses to show functionally that all fAD mutant neurons studied displayed early endosome abnormalities, as assessed by assaying Rab5+ early endosome morphology. Since *APP* and *PSEN1* converge mechanistically on APP processing, we studied APP metabolism in fAD mutant neurons to decipher the precise common disease-associated APP peptide correlates, which may be relevant to endosome biology. We found that while *APP* and *PSEN1* mutations tend to have largely dissimilar effects on APP metabolism, all mutations increase levels of longer, more hydrophobic Aβs, as well as β-CTF. Most importantly, we showed in human neurons that fAD-associated endosomal dysfunction is correlated specifically with accumulation of β-CTF, not increased longer Aβ peptide production. These results expand the understanding of disease-relevant phenotypes shared between *APP* and *PSEN1* mutations and contribute to a growing body of literature implicating endosomal-lysosomal dysfunction and elevated β-CTF as a common underlying pathological feature of both fAD and sAD (Nixon, 2017; Small et al., 2017).

Discussion

Our study relied on recently developed CRISPR/Cas9 technology to generate one of the largest and most diverse panel of human iPSC lines carrying autosomal dominant fAD *APP* and *PSEN1* mutations knocked into a single wildtype parental cell line. This approach has many advantages, including the ability to study

phenotypes in disease-relevant cell types by differentiating iPSCs into AD-vulnerable cortical neurons and studying these phenotypes under endogenous and more physiological levels of mutant protein expression. Most importantly, this approach eliminates potential off-target contribution of reprogramming or differences in genetic background when comparing cell lines from non-isogenic donors. To date, multiple groups have used iPSC-derived neurons to study fAD, but these past investigations either used non-isogenic controls (Israel et al., 2012; Liu et al., 2014a; Moore et al., 2015; Nieweg et al., 2015; Sproul et al., 2014; Yagi et al., 2011), used overexpression of mutant transgenes (Honda et al., 2016; Koch et al., 2012), or narrowly focused on only one or two different fAD mutations (Karch and Goate, 2015; Maloney et al., 2014; Oksanen et al., 2017; Ortiz-Virumbrales et al., 2017; Paquet et al., 2016; Woodruff et al., 2016; 2013). In our study, using a CRISPR/Cas9 gene-editing framework that we recently described (Kwart et al., 2017; Paquet et al., 2016), we engineered and studied 16 different isogenic iPSC lines with different mutations in *APP* and *PSEN1* (**Table 1**), including an *APP* protective mutation and *APP* knock-out. Additionally, using CRISPR/Cas9-mediated "double knock-in", we report findings from an *APPswe/PSEN1-M146V* double mutant iPSC-line. As with mouse models, we found that the combination of *APPswe* and *PSEN1-M146V* mutations causes more robust AD-relevant phenotypes, such as aberrant changes in APP processing and endosomal morphology. In the future, this cell line may serve as a valuable platform for basic disease mechanism discovery as well as novel drug testing. With this comprehensive collection of fAD stem cell lines

in hand, we are well positioned to compare the effects of multiple different fAD mutations and identify relevant changes in APP metabolism and downstream cellular consequences that may have not previously been fully appreciated.

We took advantage of these isogenic lines to carry out unbiased genome-wide molecular profiling of mutant cells. Our RNA-sequencing data, comprising differential expression and pathway analyses, will soon be made publicly available. These comprehensive datasets will assist future studies probing differential gene expression and pathway dysregulation in AD. In the present study, we aimed to identify commonly perturbed disease-associated cellular processes. The fact that there are distinct genes differentially expressed in *APP* and *PSEN1* mutant iPSC-derived neurons is interesting but not entirely unexpected, since both *APP* and *PSEN1* are integral to a variety of overlapping but also distinct cellular processes. It was of interest, then, that we found multiple common endocytic/endosomal trafficking-associated genes that were significantly differentially expressed in all fAD mutant neurons. Many of these trafficking-related genes have previously been implicated in late-onset AD risk (e.g., *SORL1*, *CLU*, *APOE*, etc.), suggesting there is a common network of cellular and molecular changes that may underlie both sAD and fAD pathogenesis.

Our molecular profiling data support the emerging view that intracellular trafficking defects may be an important common pathological process associated with AD and other neurodegenerative diseases (Wang et al., 2014). Less clear, however, is whether trafficking deficits broadly characterize both sAD and fAD

caused by *APP* and *PSEN1* mutations. Previous clinical work has strongly implicated early endosome dysfunction in sAD as a preclinical change preceding amyloid plaque and tangle deposition (Cataldo et al., 2000). A few studies investigating early endosomal-related defects in fAD have been reported, though they are limited by use of non-human and non-neuronal cell lines with overexpression or non-isogenic human iPSC-derived neurons, and are all limited by studying only a small number of fAD mutations (Israel et al., 2012; Kim et al., 2015; Muratore et al., 2014; Xu et al., 2016). Our analysis using multiple different isogenic fAD *APP* and *PSEN1* knock-in mutant human iPSC-derived neurons revealed the presence of significant Rab5+ early endosome enlargement in all lines, supporting endocytic changes as a potentially unifying pathological hallmark of AD.

When characterizing the effects of *APP* and *PSEN1* mutations on APP processing, we found that the total amounts of longer Aβ species (Aβ43 and/or Aβ42) as well as β-CTFs were consistently elevated in a zygosity-dependent manner for all fAD mutant cell lines studied. We found in neurons that mutations in APP at the β-secretase and α-secretase sites generally increase the total amount of Aβ, as seen in the *APPswe* and *APP-A692G* mutants, respectively. Furthermore, by shifting secretase processing, both *APPswe* and *APP-A692G* mutations increase levels of β-CTFs. Interestingly, mutations at the γ-secretase site of APP, such as *APP-V717G,* result in altered γ-secretase processing of β-CTF, shifting the processing of Aβ towards Aβ42 and Aβ38. In addition, we found that the *APP-*

V717G mutation also causes an accumulation of both α- and β-CTFs, suggesting that the mutation also globally impairs γ-secretase peptidase cleavage.

We strategically chose to study 3 different *APP* mutations, as these represent the vast majority of known *APP* fAD mutations which confer pathogenicity by modifying APP processing by either β-, α- or γ-secretase. Interestingly, there are a few *APP* mutations very close to the *APP-A692G* site (E693 and D694) that in past studies have been shown not to affect secretase cleavage of APP at all. In fact, these mutations tend to result in clinically distinct versions of AD, namely, cerebral amyloid angiopathy (CAA), which unlike more widely studied forms of AD involves more vascular defects including strokes, hemorrhages and resulting cognitive decline (Bugiani et al., 2010; Grabowski et al., 2001; Levy et al., 1990; Van Broeckhoven et al., 1990). In CAA, Aβ (typically Aβ40) accumulates in cerebral vessels and plaques are diffuse in the brain parenchyma (Bugiani et al., 2010; Timmers et al., 1990). Past studies have mostly shown that these mutations have no effect on Aβ production, but instead alter the propensity of Aβs to aggregate and fibrillize (Van Nostrand et al., 2001; 2002; Wisniewski et al., 1991). These mutations therefore should not affect production of β- or α-CTF and therefore may not influence endosome morphology, however this hypothesis has yet to be adequately tested. Given the marked differences in clinical and symptomatic presentation between *APP E693/D694* mutations and other *APP* fAD mutations near secretase processing sites, it is possible these different types of mutations reflect distinctly

different diseases, and endosome dysfunction/β-CTF may commonly underlie the pathogenicity of non-CAA types of AD.

In contrast to *APP*, all *PSEN1* mutations appear to alter the processing of APP by impairing γ-secretase activity. Previous studies probing the effects of *PSEN1* fAD mutations have often converged on a common increase in the Aβ 42:40 ratio. However, multiple conflicting studies have led to a debate whether this change in the ratio is caused by increasing Aβ42, decreasing Aβ40, or a combination of both. Moreover, given that multiple *APP* mutations have little or no effect on the Aβ 42:40 ratio, it is unclear how relevant this measure is to pathology. Furthermore, recent studies have shown that some *PSEN1* mutations may be so severe they result in complete loss of Aβ40 and Aβ42 generation (Veugelen et al., 2016; Xia et al., 2015), thereby underscoring the need to understand how all Aβ peptides, including longer Aβs such as Aβ43, are affected by mutations in human neurons.

Our analysis of specific Aβ peptides is consistent with a growing appreciation in the field that *PSEN1* mutations confer a partial loss of γ-secretase processivity. In all *PSEN1* mutant neurons, Aβ42 and Aβ43 were increased, while Aβ38 and Aβ40 were correspondingly decreased, suggesting the mutations impair γ-secretase ability to adequately process β-CTF and Aβs into the shortest possible peptides. Furthermore, all *PSEN1* mutant neurons displayed decreased production of total measured Aβ, which may be a result of overall reduced γ-secretase activity. On the other hand, this may reflect a shift in production towards longer Aβ peptides (e.g., 45 or 46 amino acids) that our assay did not detect (Szaruga et al., 2017). Interestingly,

mutant neurons harboring the L166P mutation (one of the most aggressive fAD mutations known (Moehlmann et al., 2002)) demonstrated the most severe alterations in Aβ production, particularly in a drastic increase in Aβ43, and corresponding reduction in Aβ40 and Aβ38. As a result of these alterations in Aβ production, the Aβ 42:40 ratio, and even more so the Aβ 42:38 and Aβ 43:40 ratios (data not shown), were significantly increased. In addition, all *PSEN1* mutants showed increased levels of β-CTF, which likely explains the corresponding reduction in total amount of Aβ generated. Importantly, α-CTF is also consistently increased in all *PSEN1* mutant neurons, further suggesting global impairment of γ-secretase processivity. In this study we only analyzed 4 different *PSEN1* mutations, however to date over 150 pathological *PSEN1* fAD mutations have been discovered. While new experimental evidence (including ours) continues to overwhelmingly converge on a common mechanism of pathogenicity involving loss of γ-secretase processivity, it would still be meaningful to continue to assess how consistent our detected changes in Aβ, CTF and endosome morphology are with other *PSEN1* mutations, for example mutations that are known to more severely alter γ-secretase activity and Aβ production.

Our study compared multiple mutations known to cause fAD in both *APP* and *PSEN1* genes. As mentioned before, mutations in another gene, *PSEN2*, have also been found to cause fAD. Therefore, one outstanding question is whether or not the effects we see in *APP* and *PSEN1* mutant neurons would also be seen in *PSEN2* mutant cells. *PSEN2* and *PSEN1* are highly homologous and each can form the

catalytic subunit of the γ-secretase complex (De Strooper et al., 2012). In neurons expression of *PSEN2* is much lower than *PSEN1* (we also found this in our RNA-seq analysis) and many believe that there may be different substrate specificities for PSEN1- versus PSEN2-containing γ-secretase (De Strooper et al., 2012; Sannerud et al., 2016). There are over 150 mutations in *PSEN1* known to cause fAD, whereas only about a dozen have been identified in *PSEN2* (An et al., 2015). As a result, *PSEN1* has been much more studied in the literature. Furthermore, *PSEN2* mutations tend to result in disease with later onset age and are less penetrant (An et al., 2015). Many studies including in human iPSC-derived neurons, have concluded that similar to *PSEN1* mutations, many mutations in *PSEN2* also result in an increase in the Aβ 42:40 ratio, which is most likely due to increased Aβ42 and reduced Aβ40 production (Ortiz-Virumbrales et al., 2017; Walker et al., 2005). If this is indeed true, it is likely that impaired PSEN2-containing γ-secretase would also result in an increase of both α- and β-CTF. It has been recently shown that PSEN1 and PSEN2 may most greatly differ in their subcellular localization and trafficking, with PSEN2-containing γ-secretase complexes being much more highly concentrated in endosomal and lysosomal compartments (Sannerud et al., 2016). Given this differential localization it would be expected that impaired activity of PSEN2-containing γ-secretase within endosomes may cause a significant accumulation of β-CTF within these compartments, since it is predominantly within endosomes where β-CTF is cleaved by γ-secretase. If this prediction holds true, I

would predict *PSEN2* mutations disrupt endosome morphology similarly or even more severely than *PSEN1* mutations.

We strategically combined widely available pharmacological agents to manipulate endogenous levels of both Aβs and APP CTFs in our wildtype and mutant human neurons. Specifically, under endogenous gene expression, we were able to isolate the effect of longer Aβs from that of APP CTFs by using GSMs, and showed the effect of β-CTF could be discriminated from that of α-CTF using the combination of γ-secretase inhibitor and β-secretase inhibitor. Such simple pharmacological manipulations could easily be applied to other cellular systems that are similarly difficult to manipulate, such as primary rodent neurons. Using these approaches, we show that Rab5+ endosome enlargement is associated with elevated β-CTF, not α-CTF or Aβ.

It is interesting that β-CTF and α-CTF can have such dramatically different effects on early endosome morphology considering the two peptides only differ by 16 N-terminal amino acids. One recent study speculated that this difference in phenotype may be attributed to a unique gain of function by the 16 amino acids (Xu et al., 2016), whereas another similar study instead suggests the C-terminal YENPTY domain of APP (present in both α- and β-CTF) induces endosome enlargement by recruiting APPL1 and stabilizing Rab5 activity (Kim et al., 2015). Regardless of mechanism, α-CTF is known to mostly be generated at the cell surface, whereas β-CTF is mostly generated in the endosome (Haass et al., 2012). Therefore, compartmentalization of β-CTF in the endosome may enable specific

protein interactions that induce endosome abnormalities, while α-CTF at the cell surface may have no such effect.

Further studies are needed to help decipher the cellular consequences of early endosome morphological changes and how early endosome enlargement phenotypes contributes to neurodegeneration. Rab5+ early endosomes are important for the retrograde trafficking of trophic signals (such as NGF or BDNF) from the axon towards the cell body. Recent overexpression studies in rodent neurons demonstrated that APP-mediated Rab5+ early endosome enlargement slows normal axonal retrograde trafficking, potentially impinging on delivery of pro-survival signals to the soma (Kim et al., 2015; Xu et al., 2016). In one example, researchers found evidence of neuronal atrophy as a consequence of early endosome enlargement (Xu et al., 2016). Whether similar results will be seen in human neurons or *in vivo* remains to be tested, and whether such deficits can trigger neurodegeneration is unclear.

It is also possible that early endosome enlargement can feed into AD pathology in a different way. Specifically, it is possible that enlarged dysmorphic early endosomes provide a site for seeding aggregation of pathological proteins. For example, Aβ, which is mostly generated within endocytic compartments, may be better able to form oligomers or fibrils in enlarged endosomes prior to extracellular release, augmenting plaque deposition. Furthermore, tau, which has recently been shown to be endocytosed and degraded through the endosomal-lysosomal system in human neurons (Evans et al., 2018), may also be more likely to aggregate within

enlarged early endosomes. As well, it has been shown that important lysosomal hydrolases, which normally traffic to the lysosome through the early to late endosome to carry out normal protein degradation, are dysregulated in cells with enlarged endosomes (Cataldo et al., 2008). Impaired trafficking of essential lysosomal hydrolases not only would impair overall proteostasis but may also augment pathological amyloid and tau protein aggregation or spreading. Human neurons provide a valuable system to evaluate the physiologically-relevant consequences of early endocytic defects.

In this study we interrogate a specific Aβ-independent cellular phenotype driven by β-CTF. Although increasing attention is being directed towards β-CTF as a plausible key contributor to AD, a majority of studies continue to focus on the amyloid cascade hypothesis and the neurotoxicity of Aβ. We found that levels of longer Aβs are elevated in all fAD mutations studied. Longer Aβs, such as Aβ42 and Aβ43, are more hydrophobic and have greater propensity to aggregate and deposit within plaques. Although we ruled out the contribution of longer Aβs to Rab5+ endosome enlargement, the effect of changes in Aβ secretion and aggregation on neurodegeneration was not addressed. Interestingly, from the molecular profiling experiments, we also noticed that sets of genes associated with synaptic functioning and neurodegeneration were significantly differentially expressed in *APPswe*, *PSEN1-M146V*, and *Swe/M146V* mutant neurons compared to wildtype (**Figure 34** and **35**). Aβ is thought to potentially be neurotoxic by impeding normal synaptic function, so the gene expression changes we detected in mutant cells may reflect a

compensatory change in gene expression to overcome the neurotoxic effect of pathological Aβ production. It is also possible that the neurotoxicity of Aβ is in part mediated through a non-cell autonomous mechanism, which was also not addressed in our study. Specifically, it has been shown recently that longer Aβ peptides are capable of initiating an inflammatory response, for example through microglia activation (Hong et al., 2016; Sondag et al., 2009). Such an immune response has been suggested to lead to synapse degeneration and ultimately cell death. Future studies, such as co-culturing fAD mutant iPSC-derived neurons with wildtype and mutant human microglia, are necessary to determine whether the increased longer Aβs produced by human fAD mutant neurons are capable of causing an immune response and neurodegeneration.

Our study raises the concern that GSMs and other anti-Aβ therapies which are being developed and tested in the clinic all fail to target β-CTF and therefore may have no effect on rescuing endosomal abnormalities in AD. We and others have shown that inhibiting β-secretase, which reduces both Aβ and β-CTF, rescues endosomal defects (Jiang et al., 2010; Woodruff et al., 2016). Recent BACEi clinical trials have been prematurely ended as no significant positive outcomes were evident (Mullard, 2017), but these trials focused on patient groups that either already had significant AD neuropathology, or patients in a “prodromal” AD stage. The endosomal phenotypes we see in iPSC-derived neurons are detectable very early in development. Since early endosome dysregulation precedes any amyloid or tau pathology, it is likely that to target endosomal dysregulation, patients may need to be

treated prior to detectable AD pathology presentation. While future studies are necessary to understand the precise pathway through which β-CTF results in Rab5+ early endosome enlargement and dysregulation, interventions targeted at this pathway deserve consideration as a therapeutic strategy.

Chapter V: Concluding Remarks

The work presented in this thesis is all focused on addressing an open question in the field of AD, namely, how a multitude of mutations in *APP* and *PSEN1* genes commonly contribute to a singular pathological disease state. We hypothesized that studying these different fAD mutations in a human neuronal model system with the absence of any transgenic overexpression would provide valuable insights and help clear up outstanding mechanistic debates. However, first we needed to take the time necessary to generate the tools needed to develop such a "gold-standard" model system. In doing so, we began to learn a lot about iPSCs and gene editing using CRISPR/Cas9. We developed strategies to improve outcomes of CRISPR-mediated knock-in in human stem cells by studying how HDR-mediated repair works in these cells after a CRISPR edit. In addition, we developed a novel framework for gene editing in iPSCs called "CORRECT", which enables efficient and scarless mutation incorporation. These findings have broad implications for multiple different scientific fields as useful tools for model system development and disease modeling. More recently we have implemented our CRISPR/Cas9 framework to

study common features of diverse *APP* and *PSEN1* mutations, as we initially intended to do. By generating a comprehensive panel of 16 different fAD mutant iPSC lines, we deciphered how *APP* and *PSEN1* mutations commonly contribute to early endosome dysfunction, which we showed to be correlated with APP β-CTF, rather than α-CTF or longer Aβs.

In our analysis we looked at 3 different representative pathogenic *APP* mutations as well as 4 different *PSEN1* mutations using isogenic human iPSC-derived neurons. Although there were some phenotypes that were not consistent across the *APP* and *PSEN1* mutant cells, we did identify 3 common features that were similar across all mutant lines:

1) Increased production of longer Aβs (Aβ43 and/or Aβ42);

2) Increased levels of APP β-CTF;

3) Increased Rab5+ early endosome size.

The identification of these common changes in APP processing across all mutant lines studied is significant, as past studies that may have simply focused on looking at the effect of mutations on total Aβ or the Aβ42:40 ratio would fail to capture these results. What's more, levels of these two types of APP-derived peptides may be more meaningful biomarkers than any other APP metabolite. These phenotype consistencies, and more so the correlation between β-CTF and endosome dysfunction, provide compelling evidence that Aβ may not be the only pathological player in development of AD, although the degree to which longer Aβ peptides and endosome enlargement may synergize in neurodegenerative pathways has yet to be

studied. Our results from studying 7 different mutations lays the groundwork necessary for pursuing additional studies that should assess for different mutations whether APP processing and endosome morphology is similarly affected.

Previous studies have demonstrated that overexpression of full-length APP or β-CTF is capable of inducing early endosome dysfunction, however all of this work had been performed in non-human and/or non-neuronal cellular systems. Furthermore, overexpressing APP or APP β-CTFs would also indiscriminately result in increased production of α-CTF and Aβs in these cells, as both α-secretase and γ-secretase are fairly ubiquitously expressed. Our approach has the advantage not only that we are studying phenotypes in human neurons with the absence of overexpression, but also, we can manipulate and precisely compare the effects of endogenous levels of both β-CTF versus α-CTF as well as longer versus shorter Aβs on endosome dysfunction using pharmacology alone. Specifically, we were able to separate the contribution of longer Aβs from that of β-CTF by using GSM, which specifically reduces longer Aβ levels without affecting β-CTF levels. These experiments allowed us to conclude that increased longer Aβs seen in mutant cells was unrelated to the common endosome enlargement phenotype we identified. Moreover, we were able to strategically isolate the effect of β-CTF from that of α-CTF, which only differ in composition by their N-terminal most 16 amino acids. Specifically, we could increase both α-CTF and β-CTF levels using a γ-secretase inhibitor, which we showed induces endosome enlargement. However, this phenotype was fully rescued by the additional treatment of a β-secretase inhibitor,

which we showed depletes β-CTF without affecting α-CTF. How β-CTF specifically contributes to endosome dysfunction while α-CTF has no effect remains a particular fascinating aspect of APP biology and needs be further investigated using human neurons in the future.

As described at length in previous chapters, a growing number of AD genetic studies have pointed to variants in endocytic-associated genes as important risk factors for sporadic AD development, including GWAS-identified trafficking-related genes such as *SORL1, BIN1, PICALM.* Our study of fAD mutations in *APP* and *PSEN1* and our finding of consistent changes in Aβ, β-CTF and endosomes, begs the question of whether or not variants in AD risk-associated endocytic genes also lead to similar or even the same changes. Future studies should take advantage of our CRISPR/Cas9 gene editing and iPSC platform to expand on our results by engineering disease-associated mutations in AD-relevant endocytic genes in iPSCs and studying APP processing and endosome dysfunction in differentiated neurons. Such future studies will help clarify whether our findings of common changes in Aβ, β-CTF and early endosomes are unique to familial forms of AD or are more widely relevant to both genetically defined as well as spontaneous late-onset AD.

Other major questions remain unanswered, namely, what the cellular consequences of enlarged early endosomes may be and how endosome dysfunction contributes to neurodegeneration. Our human iPSC-derived neuron model has its advantages, namely, the ability to study the effect of many different fAD mutations on APP processing and subtle cellular changes in a controlled

manner. However, in its current state, the technology is ill-equipped to assess neurodegeneration. Even in the most severe mutant iPSC-derived neurons we engineered with both *APP* and *PSEN1* mutations present, cells can be maintained in culture for hundreds of days. This is not so surprising, as it normally takes decades before fAD mutations result in noticeable disease phenotypes in humans. Therefore, it remains open in the field to determine ways to accelerate aging in these human neurons and to promote or activate pro-neurodegenerative pathways. It would also be valuable to decipher novel strategies to mimic cellular stresses associated with AD, which may also be useful for actively promoting degeneration in these cells. Once such technological advances are made, it would be valuable to see whether and how endosomal dysfunction contributes to neurodegeneration and degenerative signaling pathways. Developing an *in vitro* platform to address the effect of endosomal dysfunction on neurodegeneration would be valuable in many ways, namely, for the discovery of novel AD-relevant cellular pathways as well as new targets for the development of better AD therapeutics.

Appendix I: Materials and Methods

sgRNA & Cas9-VRER plasmid design and construction.

sgRNAs were designed using the Zhang lab CRISPR design tool (crispr.mit.edu). sgRNA sequences targeting *APP* or *PSEN1* (**Table 3**) were cloned into plasmid MLM3636 (a gift from Keith Joung, Addgene # 43860) as previously described (Fu et al., 2013).

Table 3. List of sgRNAs sequences used in Chapters I, II and III.

locus	guideRNA	sequence*	Chapters
APPswe	2	GCAGAATTCCGACATGACTC**AGG**	II, III, IV
APPswe	7	**G**TATGATGTAATACAGGTTCT**GGG**	II
APPswe/APP-A673T	12	GGAGATCTCTGAAGTGAAGA**TGG**	II, III, IV
re-APPswe	2	GCAGAATTCCGACATGATTC**AGG**	III
APP-A692G	14	GGTGTTCTTTGCAGAAGATG**TGG**	IV
APP-V717G	1	GACAGTGATCGTCATCACCT**TGG**	IV
APP-KO	16	GCAGGGTCGCGATGCTGCC**CGG**	IV
PS1-M146V	4	GCATTCAGAATTGAGTGC**AGA**	II
PS1-M146V	5	GTTGTCGTGACTATCCTCC**TGG**	II, III, IV
PS1-M146V	21	**G**AACAATGACACTGATCATGA**TGG**	II
PS1-M146V	22	**G**ATTTATACAGAACCACCAGG**AGG**	II
PSEN1-L166P	10	GAGATGATATAATAAGCC**AGG**	IV
PSEN1-M233L	18	GATTAGTGCCCTCATGGCCC**TGG**	IV
PSEN1-A246E	17	**G**ATGGACTGCGTGGCTCATCT**TGG**	IV
		* **G** = added for use with pMLM3636, **green** = NGG	

To generate the Cas9-VRER variant (Kleinstiver et al., 2015) with human codon usage, we introduced the 4 mutations into pCas9_GFP (a gift from Kiran Musunuru, Addgene plasmid # 44719). Briefly, we amplified fragments around the

intended mutation sites by PCR with mutated primers (**Table 4**), digested the plasmid with BamHI/BsrGI and fused all fragments by Gibson assembly.

Table 4. Primers for Gibson assembly of Cas9-VRER plasmid.

Primers for Cas9-VRER Gibson assembly:		
Name	**purpose**	**sequence**
Cas9-VRER-D1135V-F	PCR	AAGCGACTGTAGGAGAAACGAATCCGCCGTATTTC
Cas9-VRER-D1135V-R	PCR	GAAATACGGCGGATTCGTTTCTCCTACAGTCGCTT
Cas9-VRER-G1218R-F	PCR	CTCGCTAGTGCGCGCGAGCTGCAGA
Cas9-VRER-G1218R-R	PCR	TCTGCAGCTCGCGCGCACTAGCGAG
Cas9-VRER-R1335E-T1337R-F	PCR	ACACCACCATAGACAGAAAGGAGTACCGCTCTACAAAGGAGGTCCTGG
Cas9-VRER-R1335E-T1337R-R	PCR	CCAGGACCTCCTTTGTAGAGCGGTACTCCTTTCTGTCTATGGTGGTGT

Design of ssODN repair templates.

100-nt ssODN repair templates (PAGE-purified, IDT) were designed with homologous genomic flanking sequence centered around the predicted CRISPR/Cas9 cleavage site and containing pathogenic and/or CRISPR/Cas-blocking mutations. CRISPR/Cas-blocking silent mutations (i.e. that do not alter the amino acid sequence) were selected based on codon-usage of the edited gene by changing the codon to another codon already used in the same mRNA for the respective amino acid. All ssODNS used in the work described in this thesis are summarized below in **Tables 5-10**.

Table 5. ssODNs used for analysis of CRISPR/Cas-blocking mutation efficacy (Chapter II).

* **guideRNA-binding site = 20-1, N = 0, G = -1, G = -2**

****bold** = cut site, **blue** = intended mutation, **red** = CRISPR/Cas-blocking mutation, **pink** = non-blocking control mutation, **green** = NGG

locus	gRNA	strand	oligo #	codon mutation	position of CRISPR/Cas-blocking mutation*	sequence**
APPSwe	2	+	-	none	none	AAGACGGAGGAGATCTCTGAAGTGAATCTGGATGCAGAATTCCGACATGACTCAGGATATGAAGTTCATCATCAAAAATTGGTACGTAAAATAATTTACC
APPswe	2	+	1	GGA>GCA	-2	AAGACGGAGGAGATCTCTGAAGTGAATCTGGATGCAGAATTCCGACATGACTCAGCATATGAAGTTCATCATCAAAAATTGGTACGTAAAATAATTTACC
APPswe	2	+	2	GAC>GAT	+3	AAGACGGAGGAGATCTCTGAAGTGAATCTGGATGCAGAATTCCGACATGATTCAGGATATGAAGTTCATCATCAAAAATTGGTACGTAAAATAATTTACC
APPswe	2	+	3	CGA>CGG	+9	AAGACGGAGGAGATCTCTGAAGTGAATCTGGATGCAGAATTCCGGCATGACTCAGGATATGAAGTTCATCATCAAAAATTGGTACGTAAAATAATTTACC
APPswe	2	+	4	GCA>GCC	+18	AAGACGGAGGAGATCTCTGAAGTGAATCTGGATGCCGAATTCCGACATGACTCAGGATATGAAGTTCATCATCAAAAATTGGTACGTAAAATAATTTACC
APPswe	2	+	5	CTG>CTT	+24	AAGACGGAGGAGATCTCTGAAGTGAATCTTGATGCAGAATTCCGACATGACTCAGGATATGAAGTTCATCATCAAAAATTGGTACGTAAAATAATTTACC
PSEN1-M146V	22	-	-	none	none	ATCTGTGTCTCATGCTCACCTTATAGCACCTGTATTTATACAGAACCACCAGGAGGATAGTCACGACAACAATGACACTGATCATGATGGCAGCATTCAG
PSEN1-M146V	22	-	1	GAT>AAT	-2	ATCTGTGTCTCATGCTCACCTTATAGCACCTGTATTTATACAGAACCACCAGGAGATAGTCACGACAACAATGACACTGATCATGATGGCAGCATTCAG
PSEN1-M146V	22	-	2	GAG>AAG	+1	ATCTGTGTCTCATGCTCACCTTATAGCACCTGTATTTATACAGAACCACCAGAAGGATAGTCACGACAACAATGACACTGATCATGATGGCAGCATTCAG
PSEN1-M146V	22	-	3	AAC>TAC	+10	ATCTGTGTCTCATGCTCACCTTATAGCACCTGTATTTATACAGTACCACCAGGAGGATAGTCACGACAACAATGACACTGATCATGATGGCAGCATTCAG
PSEN1-M146V	22	-	4	TTT>CTT	+19	ATCTGTGTCTCATGCTCACCTTATAGCACCTGTACTTATACAGAACCACCAGGAGGATAGTCACGACAACAATGACACTGATCATGATGGCAGCATTCAG
PSEN1-M146V	22	-	5	GAC>AAC	-11	ATCTGTGTCTCATGCTCACCTTATAGCACCTGTATTTATACAGAACCACCAGGAGGATAGTCACAACAACAATGACACTGATCATGATGGCAGCATTCAG

Table 6. ssODNs used for oligo scan for "distance effect" (Chapter II).

* **guideRNA-binding site = 20-1, N = 0, G = -1, G = -2**

****bold** = cut site, **blue** = intended mutation, **red** = CRISPR/Cas-blocking mutation, **pink** = non-blocking control mutation, **green** = NGG

locus	gRNA	strand	oligo #	barcode	position of mutation M	sequence**
					WT sequence	AAGACGGAGGAGATCTCTGAAGTGAAGATGGATGCAGAATTCCGACATGACTCAGGATATGAAGTTCATCATCAAAAATTGGTACGTAAAATAATTTACC
APPswe	2	+	01	AGC	-1	AAGACGGAGGAGATCTCTGAAGTGAAGATGGATGCAGAATTCCGACATGACCCAGCATATGAAGTTCATCATCAAAAATTGGTACGTAAAATAATTTACC
APPswe	2	+	02	AAC	0	AAGACGGAGGAGATCTCTGAAGTGAAGATGGATGCAGAATTCCGACATGGCTCAACATATGAAGTTCATCATCAAAAATTGGTACGTAAAATAATTTACC
APPswe	2	+	03	ATC	2	AAGACGGAGGAGATCTCTGAAGTGAAGATGGATGCAGAATTCCGACACGACTCATCATATGAAGTTCATCATCAAAAATTGGTACGTAAAATAATTTACC
APPswe	2	+	04	AGA	4	AAGACGGAGGAGATCTCTGAAGTGAAGATGGATGCAGAATTCCGATATGACTCAGAATATGAAGTTCATCATCAAAAATTGGTACGTAAAATAATTTACC
APPswe	2	+	05	AAA	6	AAGACGGAGGAGATCTCTGAAGTGAAGATGGATGCAGAATTCCAACATGACTCAAAATATGAAGTTCATCATCAAAAATTGGTACGTAAAATAATTTACC
APPswe	2	+	06	CTC	8	AAGACGGAGGAGATCTCTGAAGTGAAGATGGATGCAGAATTTCGACATGACTCCTCATATGAAGTTCATCATCAAAAATTGGTACGTAAAATAATTTACC
APPswe	2	+	07	CGC	10	AAGACGGAGGAGATCTCTGAAGTGAAGATGGATGCAGAACTCCGACATGACTCCGCATATGAAGTTCATCATCAAAAATTGGTACGTAAAATAATTTACC
APPswe	2	+	08	CAC	12	AAGACGGAGGAGATCTCTGAAGTGAAGATGGATGCAGGATTCCGACATGACTCCACATATGAAGTTCATCATCAAAAATTGGTACGTAAAATAATTTACC
APPswe	2	+	09	CTA	14	AAGACGGAGGAGATCTCTGAAGTGAAGATGGATGCGGAATTCCGACATGACTCCTAATATGAAGTTCATCATCAAAAATTGGTACGTAAAATAATTTACC
APPswe	2	+	10	CGA	16	AAGACGGAGGAGATCTCTGAAGTGAAGATGGATACAGAATTCCGACATGACTCCGAATATGAAGTTCATCATCAAAAATTGGTACGTAAAATAATTTACC
APPswe	2	+	11	TAC	18	AAGACGGAGGAGATCTCTGAAGTGAAGATGGGTGCAGAATTCCGACATGACTCTACATATGAAGTTCATCATCAAAAATTGGTACGTAAAATAATTTACC
APPswe	2	+	12	TTC	20	AAGACGGAGGAGATCTCTGAAGTGAAGATAGATGCAGAATTCCGACATGACTCTTCATATGAAGTTCATCATCAAAAATTGGTACGTAAAATAATTTACC
APPswe	2	+	13	TGC	22	AAGACGGAGGAGATCTCTGAAGTGAAGGTGGATGCAGAATTCCGACATGACTCTGCATATGAAGTTCATCATCAAAAATTGGTACGTAAAATAATTTACC
APPswe	2	+	14	TTA	24	AAGACGGAGGAGATCTCTGAAGTGAGGATGGATGCAGAATTCCGACATGACTCTTAATATGAAGTTCATCATCAAAAATTGGTACGTAAAATAATTTACC
APPswe	2	+	15	GGC	26	AAGACGGAGGAGATCTCTGAAGTAAAGATGGATGCAGAATTCCGACATGACTCGGCATATGAAGTTCATCATCAAAAATTGGTACGTAAAATAATTTACC
APPswe	2	+	16	GAC	28	AAGACGGAGGAGATCTCTGAAATGAAGATGGATGCAGAATTCCGACATGACTCGACATATGAAGTTCATCATCAAAAATTGGTACGTAAAATAATTTACC
APPswe	2	+	17	GCC	30	AAGACGGAGGAGATCTCTGGAGTGAAGATGGATGCAGAATTCCGACATGACTCGCCATATGAAGTTCATCATCAAAAATTGGTACGTAAAATAATTTACC
APPswe	2	+	18	GGA	32	AAGACGGAGGAGATCTCCGAAGTGAAGATGGATGCAGAATTCCGACATGACTCGGAATATGAAGTTCATCATCAAAAATTGGTACGTAAAATAATTTACC
APPswe	2	+	19	GAA	34	AAGACGGAGGAGATCCTCGAAGTGAAGATGGATGCAGAATTCCGACATGACTCGAAATATGAAGTTCATCATCAAAAATTGGTACGTAAAATAATTTACC
APPswe	2	+	20	GCA	36	AAGACGGAGGAGACCTCTGAAGTGAAGATGGATGCAGAATTCCGACATGACTCGCAATATGAAGTTCATCATCAAAAATTGGTACGTAAAATAATTTACC
locus	gRNA	strand	oligo #	barcode	position of mutation M	sequence**
					WT sequence	ATCTGTGTCTCATGCTCACCTTATAGCACCTGTATTTATACAGAACCACCAGGAGGATAGTCATGACAACAATGACACTGATCATGATGGCAGCATTCAG
PSEN1-M146V	22	-	01	AGC	-1	ATCTGTGTCTCATGCTCACCTTATAGCACCTGTATTTATACAGAACCACCAAGAGCATAGTCATGACAACAATGACACTGATCATGATGGCAGCATTCAG
PSEN1-M146V	22	-	02	AAC	0	ATCTGTGTCTCATGCTCACCTTATAGCACCTGTATTTATACAGAACCACCTAGGAACATAGTCATGACAACAATGACACTGATCATGATGGCAGCATTCAG
PSEN1-M146V	22	-	03	ATC	2	ATCTGTGTCTCATGCTCACCTTATAGCACCTGTATTTATACAGAACCGCCAGGATCATAGTCATGACAACAATGACACTGATCATGATGGCAGCATTCAG
PSEN1-M146V	22	-	04	AGA	4	ATCTGTGTCTCATGCTCACCTTATAGCACCTGTATTTATACAGAATCACCAGGAGAATAGTCATGACAACAATGACACTGATCATGATGGCAGCATTCAG
PSEN1-M146V	22	-	05	AAA	6	ATCTGTGTCTCATGCTCACCTTATAGCACCTGTATTTATACAGGACCACCAGGAAAATAGTCATGACAACAATGACACTGATCATGATGGCAGCATTCAG
PSEN1-M146V	22	-	06	CTC	8	ATCTGTGTCTCATGCTCACCTTATAGCACCTGTATTTATACGGAACCACCAGGCTCATAGTCATGACAACAATGACACTGATCATGATGGCAGCATTCAG
PSEN1-M146V	22	-	07	CGC	10	ATCTGTGTCTCATGCTCACCTTATAGCACCTGTATTTATGCAGAACCACCAGGCGCATAGTCATGACAACAATGACACTGATCATGATGGCAGCATTCAG
PSEN1-M146V	22	-	08	CAC	12	ATCTGTGTCTCATGCTCACCTTATAGCACCTGTATTTGTACAGAACCACCAGGCACATAGTCATGACAACAATGACACTGATCATGATGGCAGCATTCAG
PSEN1-M146V	22	-	09	CTA	14	ATCTGTGTCTCATGCTCACCTTATAGCACCTGTATCTATACAGAACCACCAGGCTAATAGTCATGACAACAATGACACTGATCATGATGGCAGCATTCAG
PSEN1-M146V	22	-	10	CGA	16	ATCTGTGTCTCATGCTCACCTTATAGCACCTGTGTTTATACAGAACCACCAGGCGAATAGTCATGACAACAATGACACTGATCATGATGGCAGCATTCAG
PSEN1-M146V	22	-	11	TAC	18	ATCTGTGTCTCATGCTCACCTTATAGCACCTATATTTATACAGAACCACCAGGTACATAGTCATGACAACAATGACACTGATCATGATGGCAGCATTCAG
PSEN1-M146V	22	-	12	TTC	20	ATCTGTGTCTCATGCTCACCTTATAGCACTTGTATTTATACAGAACCACCAGGTTCATAGTCATGACAACAATGACACTGATCATGATGGCAGCATTCAG
PSEN1-M146V	22	-	13	TGC	22	ATCTGTGTCTCATGCTCACCTTATAGCGCCTGTATTTATACAGAACCACCAGGTGCATAGTCATGACAACAATGACACTGATCATGATGGCAGCATTCAG
PSEN1-M146V	22	-	14	TTA	24	ATCTGTGTCTCATGCTCACCTTATAACACCTGTATTTATACAGAACCACCAGGTTAATAGTCATGACAACAATGACACTGATCATGATGGCAGCATTCAG
PSEN1-M146V	22	-	15	GGC	26	ATCTGTGTCTCATGCTCACCTTACAGCACCTGTATTTATACAGAACCACCAGGGGCATAGTCATGACAACAATGACACTGATCATGATGGCAGCATTCAG
PSEN1-M146V	22	-	16	GAC	28	ATCTGTGTCTCATGCTCACCTCATAGCACCTGTATTTATACAGAACCACCAGGGACATAGTCATGACAACAATGACACTGATCATGATGGCAGCATTCAG
PSEN1-M146V	22	-	17	GCC	30	ATCTGTGTCTCATGCTCACTTTATAGCACCTGTATTTATACAGAACCACCAGGGCCATAGTCATGACAACAATGACACTGATCATGATGGCAGCATTCAG
PSEN1-M146V	22	-	18	GGA	32	ATCTGTGTCTCATGCTCGCCTTATAGCACCTGTATTTATACAGAACCACCAGGGGAATAGTCATGACAACAATGACACTGATCATGATGGCAGCATTCAG
PSEN1-M146V	22	-	19	GAA	34	ATCTGTGTCTCATGCCCACCTTATAGCACCTGTATTTATACAGAACCACCAGGGAAATAGTCATGACAACAATGACACTGATCATGATGGCAGCATTCAG
PSEN1-M146V	22	-	20	GCA	36	ATCTGTGTCTCATACTCACCTTATAGCACCTGTATTTATACAGAACCACCAGGGCAATAGTCATGACAACAATGACACTGATCATGATGGCAGCATTCAG

Table 7. ssODNs used to verify distance effect with independent sgRNAs (Chapter II).

* guideRNA-binding site = 20-1, N = 0, G = -1, G = -2

**bold = cut site, blue = intended mutation, red = CRISPR/Cas-blocking mutation, pink = non-blocking control mutation, green = NGG

locus	gRNA	strand	oligo #	codon mutation	position of CRISPR/Cas-blocking mutation*	sequence**
APPswe	12	+	1	none	none	CAGGTTCTGGGTTGACAAATATCAAGACGGAGGAGATCTCTGAAGTG**AA**TCTGGATGCAGAATTCCGACATGACTCAGGATATGAAGTTCATCATCAAAA
APPswe	2	+	2	GAC>GAT	+3	CAAGACGGAGGAGATCTCTGAAGTGAA**TC**TGGATGCAGAATTCCGACATG**AT**TCAGGATATGAAGTTCATCATCAAAAATTGGTACGTAAAATAATTTAC
APPswe	7	+	3	GGG>GGA	-2	TAAAACTAATTGGTTGTCCTGCATACTTTAATTATGATGTAATACAGG**TT**CTGGATTGACAAATATCAAGACGGAGGAGATCTCTGAAGTGAA**TC**TGGAT
PSEN1-M146V	5	+	1	CTG>CTC	-1	AATTCTGAATGCTGCCATCATGATCAGTGTCATTGTTGTC**G**TGACTATCC**CT**CCTC**G**TGGTTCTGTATAAATACAGGTGCTATAAGGTGAGCATGAGACAC
PSEN1-M146V	21	-	2	GGC>AGC	-1	TTTATACAGAACCACCAGGAGGATAGTCA**C**GACAACAATGACACTGATC**AT**GATA**G**CAGCATTCAGAATTGAGTGCAGGGCTCTCTGGCCCACAGTCTCG
PSEN1-M146V	4	-	3	GGC>AGC	-2	TAGTCA**C**GACAACAATGACACTGATCATGATGGCAGCATTCAGAATTGA**GT**GC**A**GAGCTCTCTGGCCCACAGTCTCGGTATCTTCTGTGAATGGGGTATA

Table 8. ssODNs used for single cell-derived clonal analysis of distance effect (Chapter II).

* guideRNA-binding site = 20-1, N = 0, G = -1, G = -2

**bold = cut site, blue = intended mutation, red = CRISPR/Cas-blocking mutation, pink = non-blocking control mutation, green = NGG

locus	gRNA	strand	oligo #	codon mutation	position of CRISPR/Cas-blocking mutation*	sequence**	Enzyme for RFLP
APPswe	12	+	1	none	none	CAGGTTCTGGGTTGACAAATATCAAGACGGAGGAGATCTCTGAAGTG**AA**TCTGGATGCAGAATTCCGACATGACTCAGGATATGAAGTTCATCATCAAAA	TfiI
APPswe	2	+	2	GAC>GAT	+3	CAAGACGGAGGAGATCTCTGAAGTGAA**TC**TGGATGCAGAATTCCGACATG**AT**TC**AG**GATATGAAGTTCATCATCAAAAATTGGTACGTAAAATAATTTAC	TfiI
APPswe	7	+	1	TCT>TCC	+1	TAAAACTAATTGGTTGTCCTGCATACTTTAATTATGATGTAATACAGG**TT**C**C**GGGTTGACAAATATCAAGACGGAGGAGATCTCTGAAGTGAA**TC**TGGAT	ScrFI
PSEN1-M146V	5	+	1	CTG>CTC	-1	AATTCTGAATGCTGCCATCATGATCAGTGTCATTGTTGTC**G**TGACTATCC**CT**CCTC**G**TGGTTCTGTATAAATACAGGTGCTATAAGGTGAGCATGAGACAC	BsssI
PSEN1-M146V	21	-	2	GGC>CGC	-1	TTTATACAGAACCACCAGGAGGATAGTCA**C**GACAACAATGACACTGATC**AT**GATC**G**CAGCATTCAGAATTGAGTGCAGGGCTCTCTGGCCCACAGTCTCG	BsaBI
PSEN1-M146V	4	-	3	GGC>AGC	-2	TAGTCA**C**GACAACAATGACACTGATCATGATGGCAGCATTCAGAATTGA**GT**GC**A**GAGCTCTCTGGCCCACAGTCTCGGTATCTTCTGTGAATGGGGTATA	SacI

Table 9. ssODNs used for oligo mixing strategy for increasing heterozygous clones (Chapter II).

* guideRNA-binding site = 20-1, N = 0, G = -1, G = -2

**bold = cut site, blue = intended mutation, red = CRISPR/Cas-blocking mutation, pink = non-blocking control mutation, green = NGG

locus	gRNA	strand	oligo #	codon mutation	position of CRISPR/Cas-blocking mutation*	sequence**	Enzyme for RFLP
APPswe	12	+	1	none	none	CAGGTTCTGGGTTGACAAATATCAAGACGGAGGAGATCTCTGAAGTG**AA**TCTGGATGCAGAATTCCGACATGACTCAGGATATGAAGTTCATCATCAAAA	TfiI
APPswe	12	+	2	AAG>AAA	+2	CAGGTTCTGGGTTGACAAATATCAAGACGGAGGAGATCTCTGAAGTG**AA**A**A**TGGATGCAGAATTCCGACATGACTCAGGATATGAAGTTCATCATCAAAA	
APPswe	12	+	3	GAT>CAT	-2	CAGGTTCTGGGTTGACAAATATCAAGACGGAGGAGATCTCTGAAGTG**AA**GA**T**G**C**ATGCAGAATTCCGACATGACTCAGGATATGAAGTTCATCATCAAAA	SphI
APPswe	12	+	4	GAT>CAT	-2	CAGGTTCTGGGTTGACAAATATCAAGACGGAGGAGATCTCTGAAGTG**AA**TCTG**C**ATGCAGAATTCCGACATGACTCAGGATATGAAGTTCATCATCAAAA	SphI
PSEN1-M146V	5	+	1	CTG>CTC	-1	AATTCTGAATGCTGCCATCATGATCAGTGTCATTGTTGTC**G**TGACTATCC**CT**CCTC**G**TGGTTCTGTATAAATACAGGTGCTATAAGGTGAGCATGAGACAC	BsssI
PSEN1-M146V	5	+	2	CTG>CTC	-1	AATTCTGAATGCTGCCATCATGATCAGTGTCATTGTTGTCATGACTATCC**CT**CCTC**G**TGGTTCTGTATAAATACAGGTGCTATAAGGTGAGCATGAGACAC	BsssI

Table 10. ssODNs used for CORRECT (Chapter III).

* guideRNA-binding site = 20-1, N = 0, G = -1, G = -2

**bold = cut site, blue = intended mutation, red = CRISPR/Cas-blocking mutation, pink = non-blocking control mutation, green = NGG

locus	gRNA	strand	oligo #	codon mutation	position of CRISPR/Cas-blocking mutation*	sequence**	Enzyme for RFLP
APPswe	2	+	1	GAC>GAT	+3	CAAGACGGAGGAGATCTCTGAAGTGAA**TC**TGGATGCAGAATTCCGACATG**AT**TC**AG**GATATGAAGTTCATCATCAAAAATTGGTACGTAAAATAATTTAC	RsaI
APPswe	re-2	+	2	GAT>GAC	+3	CAAGACGGAGGAGATCTCTGAAGTGAA**TC**TGGATGCAGAATTCCGACATG**AC**TC**AG**GATATGAAGTTCATCATCAAAAATTGGTACGTAAAATAATTTAC	
APP-A673T	12	+	1	TGG>TGCG	-2	TACAGGTTCTGGGTTGACAAATATCAAGACGGAGGAGATCTCTGAAGTG**AA**GATG**CG**TACAGAATTCCGACATGACTCAGGATATGAAGTTCATCATCAA	TfiI
APP-A673T	12	+	2	TGCG>TGG	-2,-3	TACAGGTTCTGGGTTGACAAATATCAAGACGGAGGAGATCTCTGAAGTG**AA**GATG**GA**TACAGAATTCCGACATGACTCAGGATATGAAGTTCATCATCAA	

Generation of long ssDNA and dsDNA repair templates.

To generate 200bp and 400bp ssDNA and dsDNA repair templates for repair, a 1000bp piece of the *PSEN1* locus around the edited locus was first PCR-amplified and TOPO-cloned. Then, a library of 20 ssODN oligos or gBlocks (IDT) containing the required mutations was integrated into the TOPO-vector by Gibson assembly (NEB), resulting in a library of 20 plasmid templates, each containing CRISPR/Cas-blocking barcode mutations and an intended mutation at varying cut-to-mutation distances (as described in **Figure 19**). From each plasmid template, 200 bp and 400 bp dsDNA PCR amplicons were generated (primers in **Table 11**) and mixed in equal amounts to generate pools of either size PCR template amplicons. Template pools were then gel extracted to remove residual plasmid. These were then re-amplified by PCR and concentrated prior to transfection. To generate ssDNA templates, dsDNA amplicons were generated as described above with 5' phosphorylated forward primers. Re-amplified dsDNA amplicons were then digested with Lambda Exonuclease (NEB) to generate ssDNA. Reactions were column purified prior to transfection (see **Figure 20** for graphical illustration).

Table 11. Primers used for amplificatin of 200/400bp repair templates

Name	purpose	sequence
PS1-M146V-200bp-F	PCR	CATTCACAGAAGATACCGAGACTG
PS1-M146V-200bp-R	PCR	TACTGTGACAAGAATACCCAACCA
PS1-M146V-400bp-F	PCR	GAAAAAGAAAATTCTGTGTTGGAG
PS1-M146V-400bp-R	PCR	TTTTGTATTTTTTGAATGTTCCACA

Wildtype iPSC line

iPSCs were reprogrammed from human skin fibroblasts (Coriell Institute, Catalog ID: AG07889) of an 18-year old male individual using the Cytotune-iPS Sendai Reprogramming Kit (Life Technologies) according to the manufacturer's instructions, following Rockefeller University Institutional Review Board approval. Informed consent was obtained from all subjects upon sample submission to Coriell Institute. Fibroblasts were confirmed to be wildtype for all studied loci by genotyping. Multiple clones were selected based on characteristic morphology. Genetic fingerprinting confirmed iPSCs were derived from corresponding fibroblast lines. Expression of pluripotency markers Oct4, Tra160, SSEA4 and Nanog was confirmed by immunofluorescence (**Figure 44A**). Clone 7889SA possessed a normal karyotype (Cell Line Genetics) and was characterized for typical iPSC properties and absence of Mycoplasma contamination (**Figure 44B**).

Expression of pluripotency genes was analyzed by NanoString nCounter gene expression system using a pre-designed codeset (Kahler et al., 2013) (**Figure 44C**). Data was normalized to the geometric mean of three housekeeping genes (ACTB, POLR2A, ALAS1) using the nSolver Analysis Software v1.0 (NanoString). 100 ng of total RNA from line 7889SA was compared to RNA extracted from the human ESC lines HUES9 (Cowan et al., 2004). Gene expression for 7 pluripotency markers and the 4 Yamanaka factors introduced as Sendai transgenes (s-t) was compared. Note that the s-tSox2 probe detects some expression of endogenous Sox2, leading to larger values for both lines.

In vivo pluripotency was confirmed by teratoma analysis as described (Kahler et al., 2013; Sproul et al., 2014). Briefly, undifferentiated iPSCs were embedded into Matrigel and subcutaneously injected into the dorsal flank of immune-compromised mice (NOD-SCID *Il2rg-null* mice, Jackson Laboratory). Paraffin sections of the teratomas were subjected to hematoxylin and eosin (H&E) staining and structures characteristic for the three germ layers (ectoderm, mesoderm and endoderm) were identified by microscopy (**Figure 44D**). Animal work was approved by the Columbia Institutional Animal Care and Use Committee.

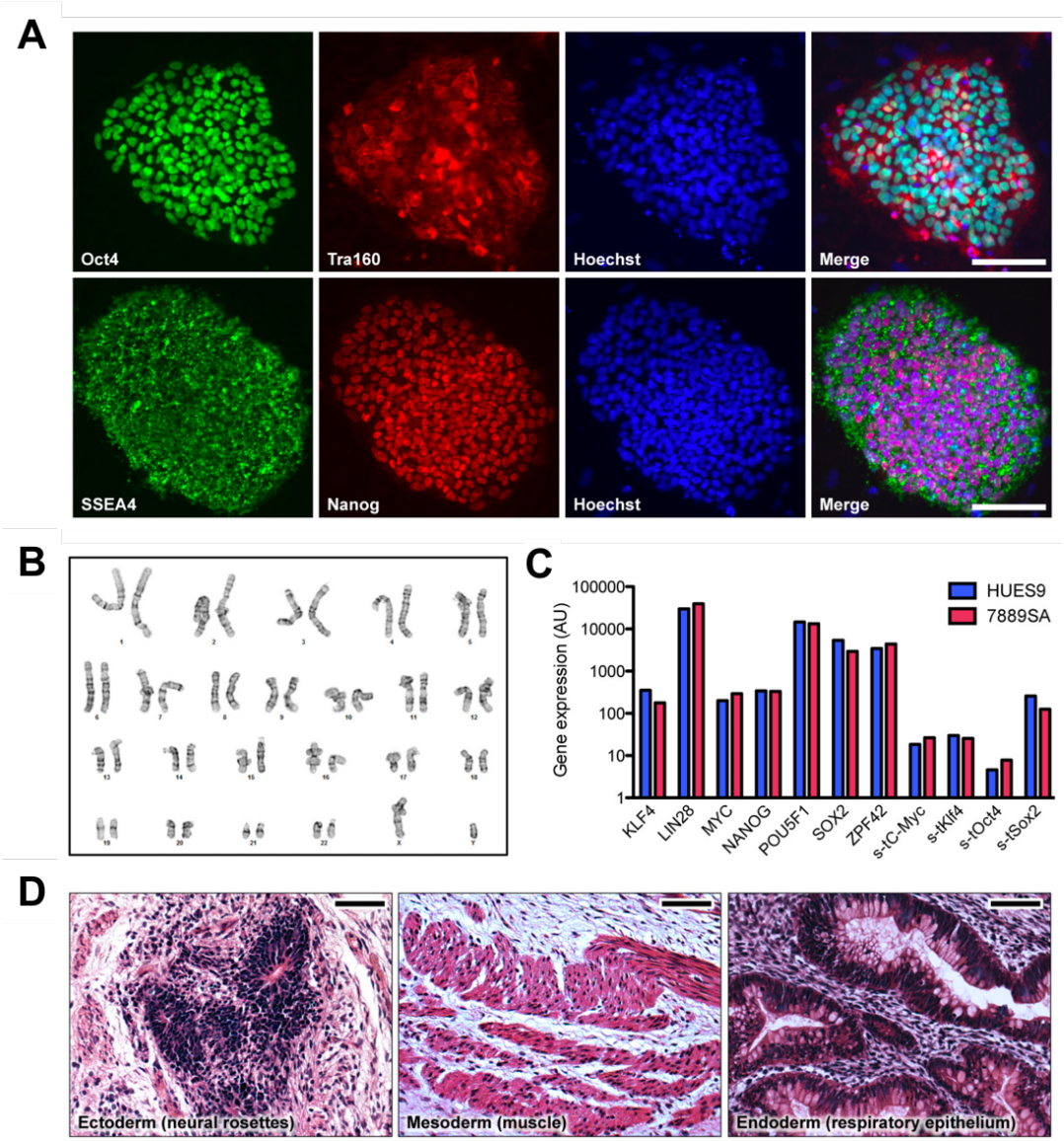

Figure 44. In vitro and in vivo characterization of the wildtype 7889SA human iPSC line.

A) Immunofluorescence stainings of pluripotent stem cell markers. **B**) iPSCs possess a normal human male karyotype. **C**) Nanostring expression analysis of pluripotent stem cell genes in reprogrammed iPSCs compared to HUES9. **D**) *In vivo* differentiation and analysis of iPSC-derived teratoma containing tissues of all germ cell layers. Scale bars, 100 μm.

Cell culture and transfection.

iPSCs were maintained on irradiated MEFs (Globalstem) plated on cell culture plates coated with 0.1% gelatin and grown in HUESM (Knock-out Dulbecco's modified Eagle's Medium (KO-DMEM), 20% knock-out serum, 0.1 mM non-essential amino acids, 2 mM Glutamax, 100 U/mL-0.1 mg/mL penicillin-streptomycin (all Life Technologies), 0.1 mM 2-Mercaptoethanol (Sigma-Aldrich), 10 ng/mL FGF2 (Stemgent), at 37 °C with 5% CO_2. Prior to transfection, iPSCs were transferred to Geltrex-coated (Life Technologies) cell culture plates and grown in MEF-conditioned HUESM containing 10 μM ROCK inhibitor (Stemgent).

iPSCs were transfected with Cas9- and sgRNA-expressing plasmids, and ssODNs by electroporation. 2 million cells were resuspended in 100 μL cold BTXpress electroporation buffer (Harvard Apparatus) with 20 μg pCas9_GFP, 5 μg sgRNA plasmid, and 30 μg ssODN (100bp ssODN, PAGE-purified, IDT). Cells were electroporated at 65 mV for 20 ms in a 1 mm cuvette (Harvard Apparatus). After electroporation cells were transferred to Geltrex-coated cell culture plates and grown in MEF-conditioned HUESM containing ROCK inhibitor for 2 days. In all transfections, 7889SA-derived iPSCs wildtype at genome-edited loci were used. Human embryonic kidney (HEK) 293T cells (Life Technologies) were maintained in DMEM with 10% FBS, 2 mM Glutamax and 100 U/mL-0.1 mg/mL penicillin-streptomycin (all Life Technologies) at 37 °C with 5% CO_2. HEK293 cells were seeded on 12-well plates at 250,000 cells/mL. When approximately 70% confluent,

HEK293 cells were transfected with 800 ng Cas9 plamid, 400 ng sgRNA plasmid and 1 μg ssODN Cells using X-tremeGENE 9 (Roche).

Fluorescence activated cell sorting.

All GFP positive cells regardless of expression levels were collected in the Rockefeller University Flow Cytometry Resource Center using a FACSAria II flow cytometer (BD Biosciences). 48h following transfection, cells were resuspended in PBS with 0.5% BSA fraction V solution, 10 mM HEPES, 100 U/mL-0.1 mg/mL penicillin-streptomycin (all from Life Technologies), 0.5 M EDTA, 20 mM glucose, 10 ng/L DAPI in the presence of ROCK inhibitor for iPSC sorts. For pooled cell NGS analysis 150,000 to 250,000 cells were collected and immediately frozen in liquid N_2 for further study. For single-cell derived iPSC clonal analysis 30,000-60,000 GFP+ cells were immediately plated on a 10 cm plate of MEFs in HUESM and ROCK inhibitor following cell sorting.

NGS analysis of HDR-mediated mutation incorporation.

Genomic DNA was extracted from sorted cells and the genomic region around the CRISPR/Cas9 target site for *APP* and *PSEN1* genes was amplified by PCR with primers positioned outside of the HDR repair template sequence to avoid template amplification for 25 cycles using Q5 polymerase (NEB) according to the

manufacturer's protocol (PCR primers listed in **Table 12**). Primers contained additional sample-specific barcodes. 25 cycles were previously determined to be optimal for exponential amplification of the template as well as visibility for gel extraction (data not shown). To eliminate PCR byproducts and genomic DNA, PCR products were gel purified. 25-100 ng of pooled barcoded PCR products were submitted to the Rockefeller University Genomics Resource Center for targeted MiSeq (Illumina) 300 bp paired-end next generation sequencing with library preparation using the v3 reagent kit (Illumina).

Table 12. PCR primers for amplification of genomic targets for NGS analysis.

Name	purpose	sequence
APPswe-F1	NGS	GGGTAGGCTTTGTCTTACAGTGTTAT
APPswe-R1	NGS	GGATGAACCAGAGTTAATAGGTCATT
PS1-M146V-F1	NGS	GACCTAGGGCTTTTGTGTTTGT
PS1-M146V-R1	NGS	AGTTAAGTTACTGTGACAAGAATACCC
PS1-M146V-F3	NGS - longer templates	GGTGAGTTGGGGAAAAGTGA
PS1-M146V-R4	NGS - longer templates	CTGGCATTACACATGCACCT

Data analysis was performed using Galaxy (Blankenberg et al., 2010b; Goecks et al., 2010) (usegalaxy.org) or Unix-based software tools listed below (summarized in **Figure 45**). First, quality of paired-end sequencing reads (R1 and R2 fastq files) was assessed using FastQC (http://www.bioinformatics.babraham.ac.uk/projects/fastqc). Raw paired-end reads were combined using Paired End ReAd MeRger (PEAR) (Zhang et al., 2014) to generate single merged high quality full-length reads. Reads with sample-specific

forward and reverse barcodes were de-multiplexed using the FASTX-Toolkit (Pearson et al., 1997) barcode splitter. The barcodes were then trimmed using seqtk (https://github.com/lh3/seqtk). Reads were then filtered by quality (using Filter FASTQ (Blankenberg et al., 2010a)) removing reads with a mean PHRED quality score under 30 and a minimum per base score under 24. Only reads shorter than or equal to the length of the PCR amplicons plus 40bp (to account for insertions) were considered for analysis.

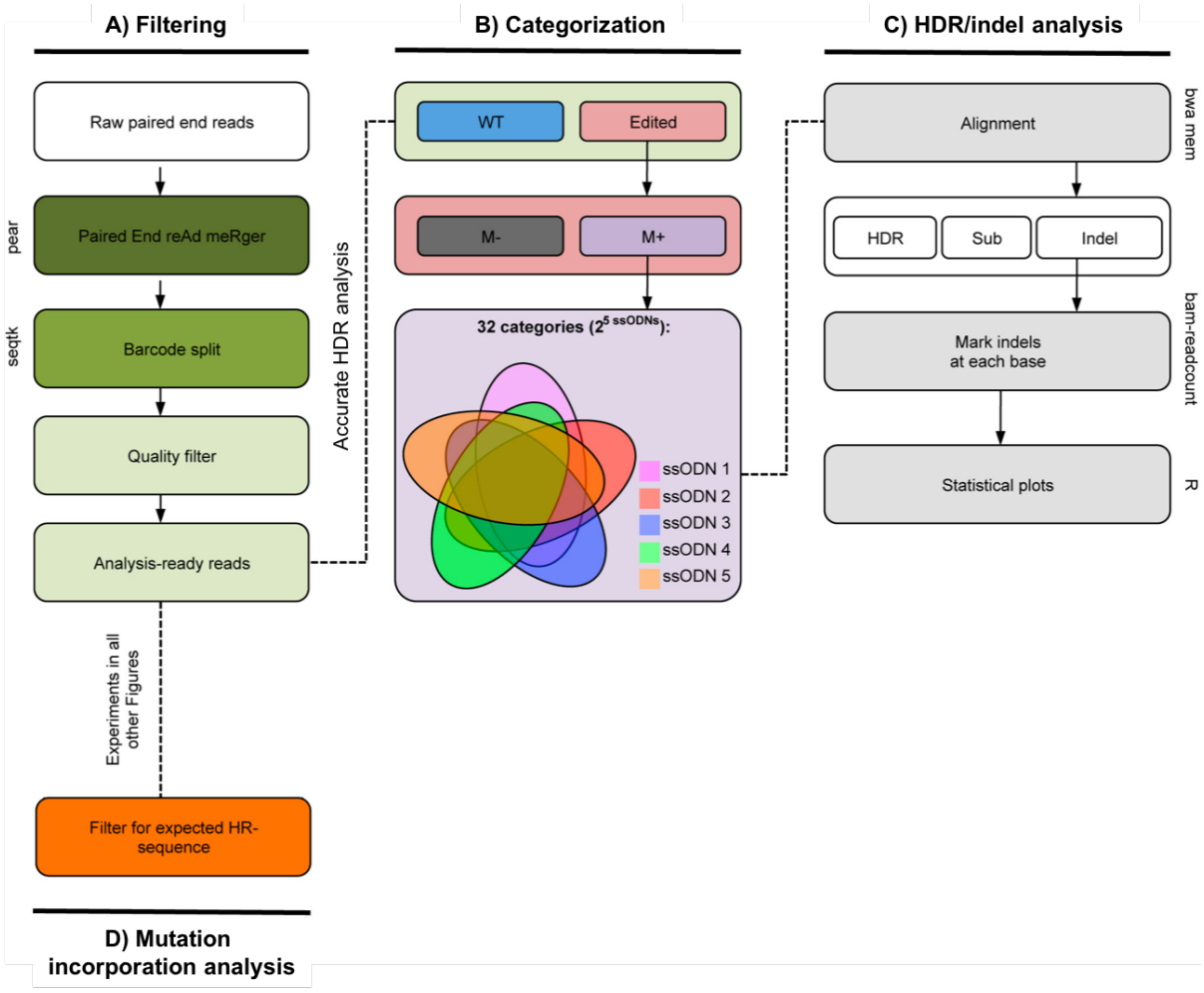

Figure 45. Next-generation sequencing data analysis pipeline for HDR and indel detection.

A) For all NGS experiments, raw forward and reverse paired NGS reads were first merged to obtain single high quality reads (tool: pear), de-multiplexed to separate experiment-specific barcoded reads (seqtk) then filtered to remove low quality reads. **B**) For experiments using pooled oligos containing CRISPR/Cas-blocking mutations, reads were separated into wildtype (WT) and edited reads, which were then filtered to include only reads that had incorporated the pathogenic mutation (M+) (i.e. containing a pathogenic and CRISPR/Cas-blocking mutation). To account for multiple HDR events after re-editing, reads were then separated into 32 unique categories covering

every possible combination of CRISPR/Cas-blocking mutations. **C**) Reads were aligned (bwa mem) and accurate HDR (perfect alignment) or indel distribution was reported (bam-readcount, R). HDR reads that had incorporated multiple CRISPR/Cas-blocking mutations were separately analyzed. **D**) For the mutation incorporation analyses performed in all other figures reads were filtered for the expected sequence and counted.

For the accurate HDR and indel analysis in Chapter II reads were filtered to assess the presence of HDR or NHEJ-induced indels. To isolate sequences with HDR, reads were first filtered to remove unedited wildtype reads. Next, HDR reads containing intended *APP* or *PSEN1* mutations were isolated by matching a 6-nt HDR motif around the pathogenic mutation. HDR reads were then analyzed for incorporation of CRISPR/Cas-blocking mutations by matching 6 to 8-nt HDR motifs around each mutation and categorized into unique groups of reads containing all possible combinations (32) of CRISPR/Cas-blocking mutations to account for measurable HDR after re-editing (**Figure 45B**). Each group of reads was then aligned to a corresponding reference sequence using *bwa mem* (Li and Durbin, 2010) (which has been successfully used for this purpose by others (Dow et al., 2015)) to determine the rate of accurate HDR and indel or substitution mutations (**Figure 45C**). Reads with multiple blocking mutations were analyzed separately. Accurate HDR reads were calculated in each group as the percentage of HDR reads without indels. To determine indel frequency, size and distribution, all edited reads from each experimental replicate were combined and aligned, as described above.

Indels were then marked at each base using bam-readcount (https://github.com/genome/bam-readcount), quantified in R (www.R–project.org) and plotted using Graphpad Prism.

In all other experiments assessing mutation incorporation for establishing the distance effect, reads were first filtered for experiment-specific barcode and quality as described above. Next, reads were considered to have HDR if they matched the repair ssODN template plus an additional 3-nt genomic sequence on each side to ensure proper genomic context during HDR and contained the pathogenic mutation and/or CRISPR/Cas-blocking silent mutation (**Figure 45D**). *n* values represent independent biological replicates.

To exclude a significant contribution of oligo synthesis and sequencing errors to our analysis, we sequenced *PSEN1* PCR amplicons from APP-edited iPSCs, and repair ssODNs annealed to a complementary ssODN. Errors introduced by sequencing were 2.7% ± 0.1% per 100bp, and 2.3% ± 1.7% of the 100bp ssODN sequences contained errors.

Calculation of optimal distance ranges for homo- or heterozygous genotypes.

Mutation scan data for *APP* and *PSEN1* loci determined by NGS for iPSCs from were combined to determine single allelic mutation incorporation probabilities p_a as a function of cut-to-mutation distance (p_a^{mut}). The probability of wildtype incorporation (p_a^{wt}) was determined as (p_a^{wt}= 1-p_a^{mut}). Assuming gene editing and HDR at each allele in a single cell are independent events, we calculated the

zygosity probabilities (p_z) for each allele combination given two alleles per cell. Specifically, probability of a homozygous, wildtype, and heterozygous zygosity was calculated as $p_z^{mut/mut}=p_a^{mut}xp_a^{mut}$, $p_z^{wt/wt}=p_a^{wt}xp_a^{wt}$ and $p_z^{wt/mut} = 2x(p_a^{wt}xp_a^{mut})$, respectively. These calculations were made using the entire range of data derived from **Figure 19B**, extrapolated for distance values above 36 and plotted in **Figure 22A** as fit curve ± SD of raw values.

RFLP analysis and Sanger sequencing for genotyping of single cell clones (Chapter II).

To facilitate single cell clone genotyping, the ssODN HDR templates used for gene editing were designed to introduce a restriction endonuclease motif with the blocking or pathogenic mutation. Genome edited single cell-derived iPSC clones grown on MEF-containing 10 cm plates (in HUESM + ROCK inhibitor) were manually picked into a single well of a U-bottom 96-well tissue culture plate in 100 μL HUESM + ROCK inhibitor. Cells were pelleted by centrifugation, and plates were immediately frozen in liquid N_2 and stored at -80 °C. Genomic DNA was extracted as previously described[44]. Briefly, cells were resuspended in 25 μL lysis buffer (0.75 μL 10 mg/mL Proteinase K (Ambion), 2.5 μL 10X PCR buffer (Sigma-Aldrich), transferred to 96-well PCR plates and incubated at 55 °C for 4 h. Proteinase K was inactivated by incubating plates at 96 °C for 10 min.

To identify clones with HDR events the genomic region surrounding the *APPswe* or *PSEN1-M146V,* loci were amplified (see primers in **Table 13**) by Taq

polymerase (Roche) and digested with restriction enzymes to screen for a novel restriction site introduced by the blocking or pathogenic mutation (primers, repair ssODNs and restriction enzymes used are listed in the above tables). Digested DNA was analyzed by agarose gel electrophoresis. The zygosity of the pathogenic mutation in clones that had undergone incorporation of the silent CRISPR/Cas-blocking mutations was determined by Sanger sequencing (Genewiz).

Table 13. Primers used for RFLP and Sanger sequencing of single-cell derived clones (Chapter II)

Name	purpose	sequence
APPswe-F	PCR/RFLP	GGGTAGGCTTTGTCTTACAGTGTTAT
APPswe-R	PCR/RFLP	ATCCTATAGGCAAGCATTGTATTTTTA
PS1-M146V-F	PCR/RFLP	GGTGAGTTGGGGAAAAGTGA
PS1-M146V-R	PCR/RFLP	CTGGCATTACACATGCACCT

To determine the frequency and distribution of indels in mono-allelic HDR single cell clones with NHEJ at the other allele, Sanger sequencing reads were separated into single reads for HDR and indel-containing alleles using PolyPeak Parser (Hill et al., 2014). Indel-containing reads were then combined into a single fasta file and analyzed for indel distribution by aligning to the reference sequence as described above.

CORRECT

Re-Guide and re-Cas utilize a two-step gene editing workflow: 2 million iPSCs were electroporated with sgRNA and Cas9 plasmids. In addition, during the first step a ssODN containing the intended mutation (M) and a CRISPR/Cas blocking mutation (B) was introduced (MB template). Cas9-eGFP expressing cells were FACS sorted and single cell iPSC clones were derived. The presence of B and M mutations was detected by RFLP. A single clone containing homozygous B and M mutations was then expanded for use in the second step of CORRECT. These "MB iPSCs" were then electroporated with re-sgRNA and wildtype Cas9 plasmids (for re-Guide) or wildtype sgRNA and mutant VRER Cas9 plasmids (for re-Cas). In addition, at this step the *CORRECT* template was provided to remove blocking mutation B. The efficacy of CRISPR/Cas blocking mutation removal was first determined by NGS. To isolate scarless edited "M iPSC clones" the second step of CORRECT editing was performed and single-cell-derived colonies were picked and expanded as described above. Genotypes were confirmed by sanger sequencing.

SURVEYOR assays

gDNA was extracted from gene edited iPSCs as described above. 300-500 bp around the gene edited locus were amplified by PCR using Herculase II (Agilent) and column purified. PCR amplicons were rehybridized and treated with SURVEYOR nuclease according to the manufacturers directions (IDT). Digested

DNA was separated on a 4-20% TBE polyacrylamide gel (BioRad) and imaged using SYBR Gold (Life Technologies). Densitometry was performed using Image J. Percent indel quantification was based on relative band intensities using the formula 100 x (1-(1-(*b*+*c*)/(*a*+*b*+*c*)$^{1/2}$, where *a* is the undigested PCR product intensity and *b* and *c* are the intensities of each cleavage product (Ran et al., 2013).

Isogenic *APP* and *PSEN1* mutant iPSC lines.

Generation of heterozygous and homozygous *APP* and *PSEN1* isogenic mutant iPSC lines was done using a combination of "distance effect" and oligo mixing based approaches as described above. Briefly, sgRNA sequences (see sgRNA sequences for Chapter IV in **Table 3**) were selected and cloned into plasmid MLM3636. 100-nt PAGE-purified ssODN repair templates were designed with homologous genomic flanking sequence centered around the predicted CRISPR cut site and containing pathogenic and/or CRISPR-blocking mutations (**Table 14**).

Table 14. ssODNs used for generation of isogenic *APP* and *PSEN1* mutant iPSC lines (Chapter IV).

* **guideRNA-binding site = 20-1, N = 0, G = -1, G = -2**
****bold** = cut site, **blue** = intended mutation, **red** = CRISPR/Cas-blocking mutation, **pink** = non-blocking control mutation, **green** = NGG
MB and M templates for CORRECT by re-Cas

locus	Strand	codon mutation	position of CRISPR/Cas-blocking mutation*	sequence**	Enzyme for RFLP
APP-A692G	+	GCA>G**G**A	-1 & 2	AAATTAAAATTCTTTTTCTTAATTTGTTTTCAAGGTGTTCTTTGGAGAA**G**ACGTAGGTTCAAACAAAGGTGCAATCATTGGACTCATGGTGGGCGGTGTT	**BmgBI**
APP-V717G (het)	+	GTC>G**G**C	-1	CATTGGACTCATGGTGGGCGGTGTTGTCATAGCGACAGTGATCGGCATC**A**C**C**TTAGTGATGCTGAAGAAGAAACAGTACACATCCATTCATCATGGTGTG	**DdeI**
APP-V717G (homo)	+	GTC>G**G**C	-1 & 2	CATTGGACTCATGGTGGGCGGTGTTGTCATAGCGACAGTGATCGGCATC**A**C**G**TTAGTGATGCTGAAGAAGAAACAGTACACATCCATTCATCATGGTGTG	**DdeI**
APPswe	+	none	none	CAGGTTCTGGGTTGACAAATATCAAGACGGAGGAGATCTCTGAAGTG**AA**T**C**T**G**GATGCAGAATTCCGACATGACTCAGGATATGAAGTTCATCATCAAAA	**TfiI**
APPswe	+	GAC>GA**T**	+3	CAAGACGGAGGAGATCTCTGAAGTGAA**T**CTGGATGCAGAATTCCGACATG**A**T**T**C**A**GGATATGAAGTTCATCATCAAAAATTGGTACGTAAAATAATTTAC	**TfiI**
PSEN1-M146V	+	CTG>CT**C**	-1	AATTCTGAATGCTGCCATCATGATCAGTGTCATTGTTGTC**G**TGACTATC**CT**CCT**C**GTGGTTCTGTATAAATACAGGTGCTATAAGGTGAGCATGAGACAC	**BsssI**
PSEN1-L166P	–	CTT>C**C**T	-1	AATTCTGAATGCTGCCATCATGATCAGTGTCATTGTTGTC**G**TGACTATC**CT**CCT**C**GTGGTTCTGTATAAATACAGGTGCTATAAGGTGAGCATGAGACAC	**NsiI**
PSEN1-M233L	+	ATG>C**T**G	-1	TCCACTTCGACTCCAGCAGGCATATCTCATTATGATTAGTGCCCTCA**T**G**G**CCT**A**GTGTTTATCAAGTACCTCCCTGAATGGACTGCGTGGCTCATCTTG	**ScrFI** (Loss of site)
PSEN1-A246E	+	GCG>GA**G**	-1, +1	CATGGCCCTGGTGTTTATCAAGTACCTCCCTGAATGGACTG**C**GTGGCTC**AT**CCT**A**GCTGTGATTTCAGTATATGGTAAAACCCAAGACTGATAATTTGTT	**FokI**
APP-A673T (MB)	+	TGG>TG**C**G	-2	TACAGGTTCTGGGTTGACAAATATCAAGACGGAGGAGATCTCTGAAGTG**AA**GATG**C**G**T**ACAGAATTCCGACATGACTCAGGATATGAAGTTCATCATCAA	**RsaI**
APP-A673T (CORRECT)	+	TG**C**G>TGG	-2,-3	TACAGGTTCTGGGTTGACAAATATCAAGACGGAGGAGATCTCTGAAGTG**AA**GATG**G**ATACAGAATTCCGACATGACTCAGGATATGAAGTTCATCATCAA	**BciVI**

iPSCs were transfected with Cas9-GFP and gRNA-expressing plasmids, and ssODNs by electroporation. After electroporation, GFP+ cells were FACS sorted and grown until single cell-derived colonies were detectable and picked. Identification of accurately edited iPSCs by RFLP analysis and Sanger sequencing was performed as described in (Kwart et al., 2017) using PCR amplification primers listed in **Table 15**. In all electroporations, 7889SA-derived iPSCs wildtype at genome-edited loci were used. *Swe/M146V* "double mutant" iPSCs were generated by a two-step editing approach. Homozygous *PSEN1-M146V* were re-edited to introduce the homozygous *APPswe* mutation.

Table 15. Primers used for RFLP analysis and Sanger sequencing of single-cell derived clones (Chapter IV).

Name	purpose	sequence
APPswe-F	PCR/RFLP	GGGTAGGCTTTGTCTTACAGTGTTAT
APPswe-R	PCR/RFLP	ATCCTATAGGCAAGCATTGTATTTTTA
APP-A692G-F	PCR/RFLP	CCAAATGTCCCCTGCATTTA
APP-A692G-R	PCR/RFLP	TGTAACCCAAGCATCATGGA
APP-V717G-F	PCR/RFLP	CCAAATGTCCCCTGCATTTA
APP-V717G-R	PCR/RFLP	TGTAACCCAAGCATCATGGA
APP-KO-F	PCR/RFLP	CGGCTTCTCTGCATTAAAGA
APP-KO-R	PCR/RFLP	GGGCTCCGTCAGTTTCCT
PS1-M146V-F	PCR/RFLP	GGTGAGTTGGGGAAAAGTGA
PS1-M146V-R	PCR/RFLP	CTGGCATTACACATGCACCT
PSEN1-L166P-F	PCR/RFLP	CGTGGTTCCACCTACTCAGG
PSEN1-L166P-R	PCR/RFLP	AAGCAAGGAGCAACAGAAGAA
PSEN1-M233L/A246E-F	PCR/RFLP	ATGTTTGGGAGCCATCACA
PSEN1-M233L/A246E-F	PCR/RFLP	CAGCCTCCCAAAGTGCTAAG

PSEN1-L166P, PSEN1-A246E and *PSEN1-M233L* iPSCs were generated in collaboration with Andrew Gregg, who recently presented preliminary data on these lines in his thesis (Gregg, 2017). To generate the *APP-KO* iPSC line, wildtype

iPSCs were electroporated with Cas9-GFP and gRNA-expressing plasmid only and identification of clones with frame-shift deletions was carried out by TOPO-cloning (**Figure 46**). One iPSC line per genotype was isolated and characterized. The newly established gene-edited lines displayed normal karyotypes and expressed pluripotency markers Oct4, Tra160, SSEA4, Nanog and Alkaline Phosphatase (data not shown).

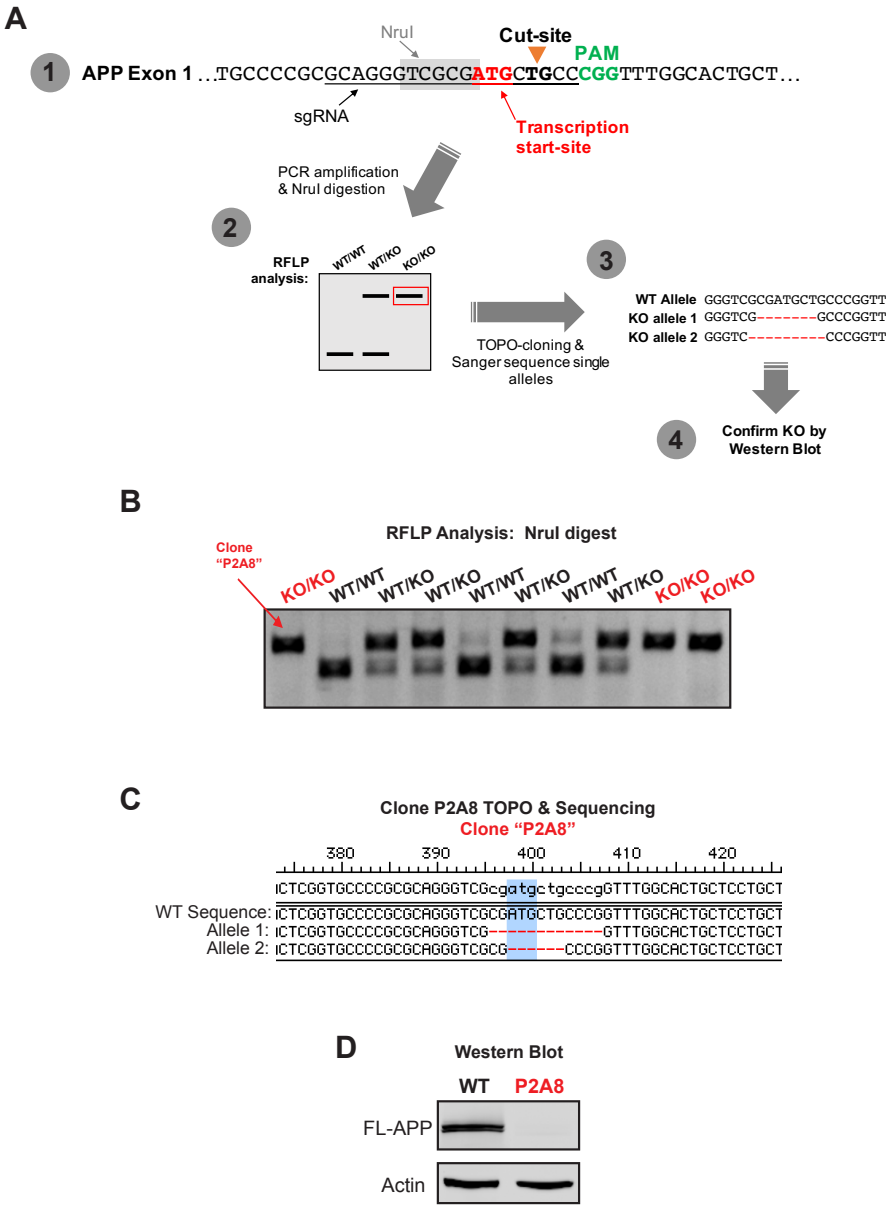

Figure 46. Generation of an *APP-KO* iPSC line.

A) Schematic describing the main steps in generating an isogenic APP knockout iPSC clone using CRISPR/Cas9. (1) We targeted the first conserved transcription start site (red) by using a sgRNA targeting a double stranded break at the indicated site. This ATG start site is adjacent to the Cas9 cleavage site, and therefore following non-homologous end joining mediated random deletion, we expected at some alleles the ATG would be

deleted. After isolating single cell-derived iPSC clones we can test loss for loss of ATG using an RFLP assay. We utilized the restriction enzyme NruI, which has a recognition sequence that includes the A of the ATG transcription start site. Therefore, we can look for loss of NruI cleavage as an indication of loss of ATG (2). (3) Following identification of putative knockout (loss of intact ATG) clones we utilized TOPO cloning technology to be able to analyze the editing outcome at each allele by Sanger sequencing. (4) Finally, to confirm knockout we performed a screen by western blot on iPSC lysates. **B**) An example of the RFLP assay from our gene editing experiment. Putative KO clones are highlighted in red. The clone we used in our experiments "P2A8" is indicated. **C**) TOPO cloning and Sanger sequencing alignment for each allele from the P2A8 KO clone compared to wildtype. Both alleles have a complete loss of the ATG sequence. **D**) Western blot analysis for full length APP (FL-APP) for wildtype and P2A8 iPSCs.

Cortical neuron differentiation

iPSC-derived cortical neurons were generated as previously described (Paquet et al., 2016) with modifications. Briefly, iPSCs were plated on 12-well tissue culture plates coated with Geltrex (Life Technologies) in MEF-conditioned HUESM with ROCK inhibitor. When cells were 100% confluent, medium was replaced with neural induction (NI) medium (day in vitro 0 (DIV0)) and maintained for 8 days. On DIV8 day cells were dissociated using Accutase (Life Technologies) and resuspended in NI medium at 30 million cells/mL. Cells were plated on dried poly-L-ornithine (Sigma-Aldrich) and laminin-coated (Life Technologies) 6-well plates in 200

μL spots. Cells were left to adhere for ~45 min and NI medium was added. On DIV10 NI was replaced with neural maintenance (NM) medium. Upon the appearance of neural rosettes, 20 ng/mL FGF2 was added for 2 days. When neurons started to form (~DIV21), rosettes were isolated manually after treatment with STEMdiff Neural Rosette Selection Reagent (STEMCELL Technologies) for 1 h. Rosettes were washed and plated on poly-L-ornithine/laminin-coated 6-well plates and grown for approximately 7 days. For cortical neuron maturation, ~675,000 NPCs/mL were plated on 6- or 12-well poly-L-ornithine/laminin-coated plates and maintained in Neurobasal medium supplemented with B-27 serum-free supplement, 2 mM Glutamax and 100 U/mL-0.1 mg/mL penicillin-streptomycin (all Life Technologies). For imaging experiments cells were plated in 24-well plates onto poly-L-ornithine/laminin-coated coverslips. During the first 7 days after plating, cells were treated with 10 μM DAPT (Sigma-Aldrich) to augment neuronal maturation, which was subsequently washed out with normal Neurobasal/B-27 medium.

Cortical neuron characterization

Canonical neural precursor cell markers (Nestin, Pax6, FoxG1, Otx2) and mature cortical neuronal markers (Tbr1, CTIP2, Satb2) were analyzed by immunofluorescence staining at DIV10 and DIV65, respectively (**Figure 47A-B**). Synapse marker expression was also analyzed by immunofluorescence at DIV65 (**Figure 47C**). Electrophysiological properties of iPSC-derived cortical neurons were assessed between DIV71 and 85 using a submerged recording chamber mounted

on an Olympus BX51 microscope equipped for infrared-DIC microscopy (**Figure 47D-H**). Neurons were perfused with 95% 0_2/5% CO_2 equilibrated ACSF (in mM): 119 NaCl, 2.5 KCl, 1.3 $MgSO_4$, 2.5 $CaCl_2$, 1 NaH_2PO_4, 26 $NaHCO_3$ and 11 glucose. Whole-cell patch clamp pipettes (5 MΩ) were filled with (in mM): 123 K-gluconate, 10 HEPES, 0.2 EGTA, 8 NaCl, 2 Na_2ATP, 0.3 Na_3GTP. Action potentials were elicited by step current injections and recorded in current-clamp mode (-65 mV). Properties (threshold, overshoot) of the largest action potential elicited in each cell were measured. Spontaneous synaptic activity was recorded in voltage-clamp mode (-70 mV). Data was digitized at 10 kHz and recorded using a Multiclamp 700B amplifier and Clampex 10.3.0.2 software (Molecular Devices). We also performed an analysis of Aβ production as a function of differentiation state. It was determined that Aβ production is considerably maturation-dependent and therefore we chose to analyze Aβ profiles from neurons at ~DIV70 (**Figure 47I**).

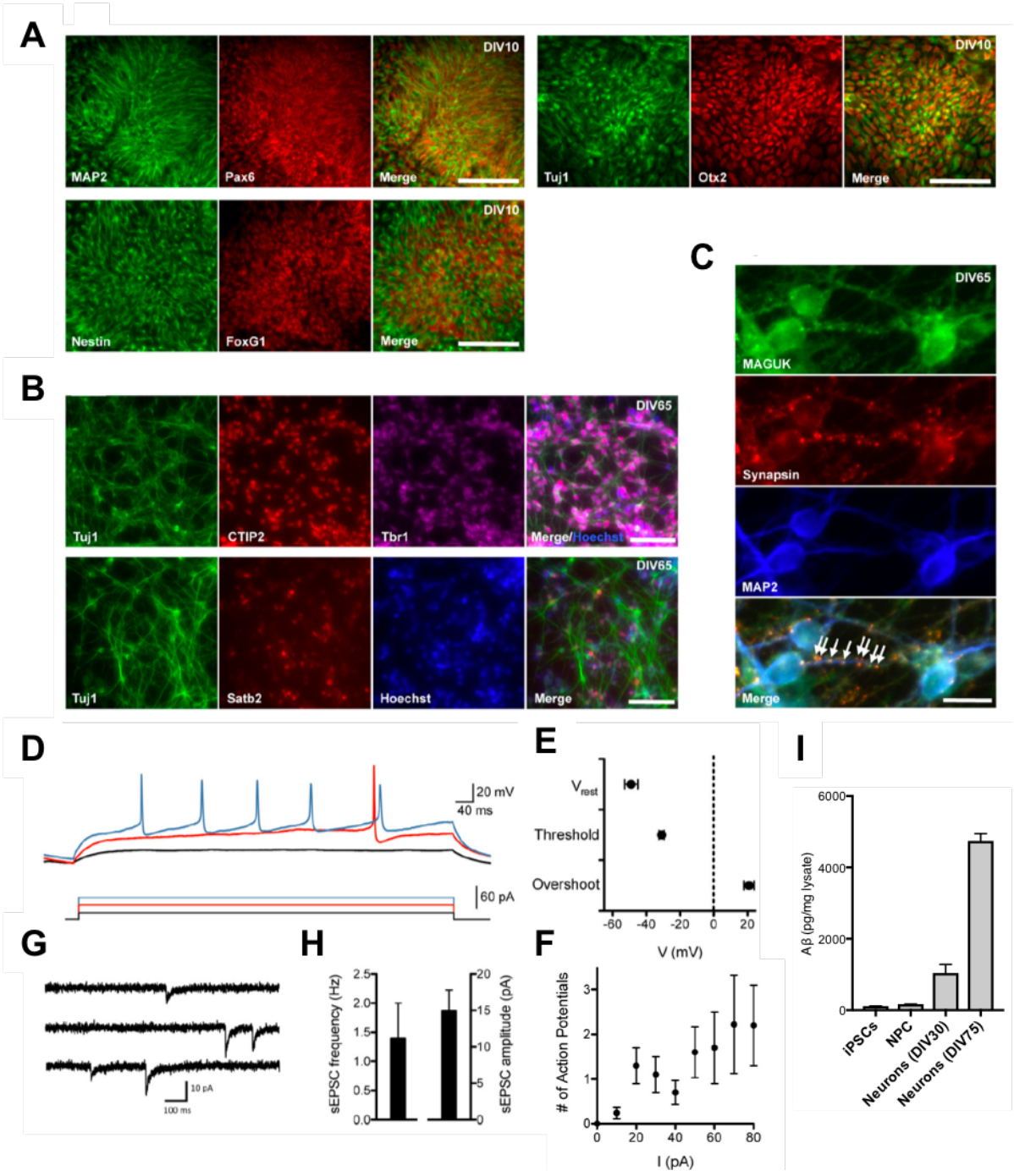

Figure 47. Characterization of iPSC-derived cortical neurons.

A-C) Immunofluorescence stainings of markers for neural precursors at DIV10 (**A**), cortical neurons at DIV65 (**B**) and functional synapses at DIV65 (**C**). Scale bars, 100 μm in A, B, 10 μm in C. **D**) Evoked action potentials recorded in a neuron current-clamped to -65 mV. **E**) Mean (± SEM) resting

membrane potential (V_{rest}), action potential threshold and action potential overshoot (DIV 71 – 85; n = 18). Properties of the largest action potential elicited in each cell were measured. **F**) Mean number of evoked action potentials increases with increasing stimulus strength. **G**) Spontaneous synaptic activity recorded in a neuron voltage-clamped to -70 mV. **H**) Mean (± SEM) frequency and amplitude of spontaneous excitatory postsynaptic currents (EPSCs) (DIV 71 - 85; n = 8). **I**) Total secreted Aβ levels from cells at different stages of the differentiation protocol.

Drug treatments

In all experiments, neurons were treated for 48h with 1 μM of drug in 0.1% DMSO. DMSO treatment alone was used as a vehicle control. Drugs used were β-Secretase inhibitor IV (Millipore), Compound E (Millipore). GSMs were obtained from Dr. Yeuming Li. A previously published GSM, GSM-I, was used in all experiments (Crump et al., 2011).

Whole transcriptomic RNA sequencing (RNA-seq)

RNA from DIV80 iPSC-derived neurons was extracted using Trizol (Invitrogen) and ribosomal RNA was removed with Ribo-Zero (Epicentre). RNA was DNAse-treated (Roche) sequencing libraries were generated as recommended by the Illumina High-throughput TruSeq sample preparation guidelines. 3 biological replicates, each consisting of 2 technical replicates, were used for sequencing. Stranded RNAseq was performed using an Illumina HiSeq 2500 at the New York

Genome Center generating 125-bp paired-end reads. Reads were aligned to the hg19 build of the human genome using Kallisto. All read counts, TPM and differential expression analysis was performed on R (www.R-project.org) using packages “Tximport” and “DESEQ2” (bioconductor.org). RNA-seq analysis was performed using R packages “ggplot”, “venneuler”, “pheatmap” or “pcaexplorer”. Quality control assessment of all RNA-seq libraries was performed as shown in **Figure 48.** *P*-values to assess statistically significant overlap between the AD gene lists was calculated with a hypergeometric test. The list of genes with AD-linked variants was obtained from https://www.ebi.ac.uk/gwas/ and is shown in **Table 16.** Gene expression heatmaps were generated using Prism. Metascape (Tripathi et al., 2015) (metascape.org) was used for GO pathway analysis and we included enriched terms down to $q < 0.01$ (p adjusted for multiple comparisons). The list of differentially expressed endocytic-related genes determined from metascape and used for RNA-seq analyses is shown in **Table 17**. Gene lists from **Tables 16** and **17** were used for hierarchical clustering analysis**.** A summary of Metascape GO terms identified when studying differentially expressed genes in *Swe/M146V* neurons compared to single mutant *APPswe* or *PSEN1-M146V* is shown in **Table 18**.

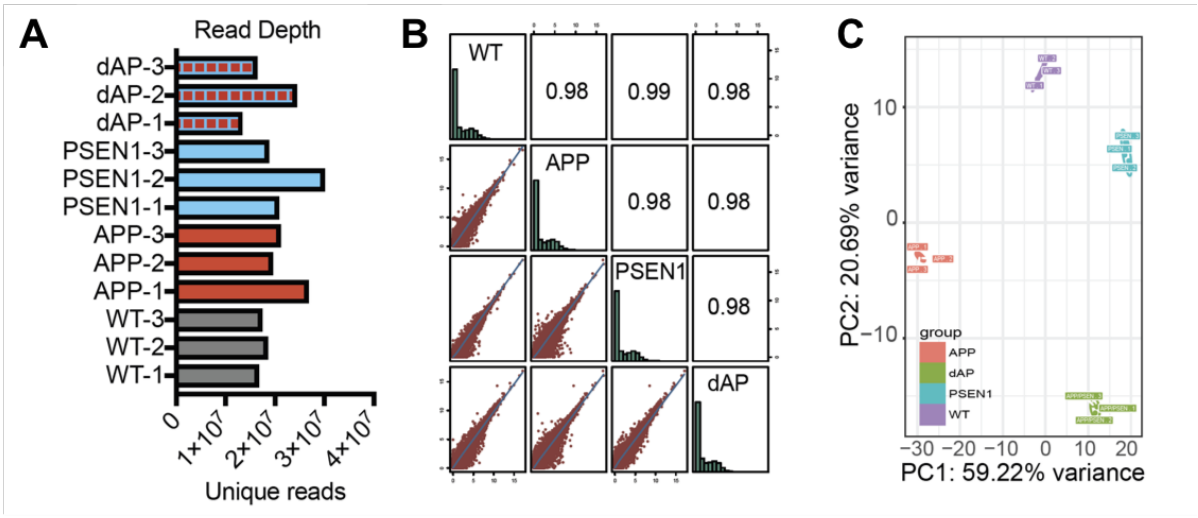

Figure 48. RNA-seq library quality control analysis.

A) Read depth (number of unique reads detected) of each biological replicate used for RNA-seq analysis. **B**) Diagonal: Distribution of each variable is shown via histogram for each of the respective iPSC-derived neuron genotypes of the RNA-sequencing libraries. Bottom panel: Scatter plot of log-transformed read counts per gene, displaying the relationship between each genotype. Upper panel: Correlation between RNA sequencing libraries per genotype, R = Pearson correlation coefficient. Abundance (TPM) averages per gene for all iPSC-derive neurons analyzed. **C**). Principal component analysis (PCA) plot displaying the projections of sample expression profiles

demonstrating overall effects of experimental and batch effects. Each of the 12 samples are plotted and spanned by their first two principle components. **D**) Scree plot of PC computed across samples. **E**) Top and bottom loadings of genes contributing to overall variances in the data. dAP = *Swe/M146V* double mutant.

Table 16. AD-linked genes used for hypergeometric test and hierarchical clustering analysis.

AD-linked genes (from EMBL-EBI "GWAS Catalog")				
ABCA7	APP	EPHA1	MAPT	RYR3
ABCA1	APPBP2	FAT1	MARK4	SEMA5A
ACE	ARAP3	FBXL7	MEF2C	SLC24A4
ADAM10	ARHGAP18	FERMT2	MS4A4A	SLC25A21
ADAM17	ATP5H	FGF1	MTHFD1	SORCS1
ADAM9	BAALC	FHIT	MTOR	SORCS2
ADAMTS20	BACE1	FSHR	MYO18B	SORCS3
ADAMTS9-AS2	BCHE	GAB2	NCSTN	SORL1
ADARB2	BIN1	GLIS3	NEGR1	SORT1
ADCY2	BLOC1S3	GRIN2B	NME8	TEK
AFF1	CADPS2	GRIN3A	NPAS3	TFAM
APBA1	CASS4	GRINL1A	NR3C2	TNK1
APBA2	CD2AP	GRM1	PARK2	TP53INP1
APBB1	CD33	HLA-DRB1	PDE1A	TP73
APBB2	CDH13	HLA-DRB5	PDGFD	TTBK2
APBB3	CELF1	HS3ST1	PICALM	UNC5C
APH1A	CELF2	IDE	PLXNA4	VPS35
APH1B	CLSTN2	IGHV1-67	PSEN1	XKR4
APLP1	CLU	IGSF21	PSEN2	ZCWPW1
APLP2	CR1	IL1B	PSENEN	
APOE	CST3	INPP5D	PTK2B	
	DLC1	KCTD2	PTPN5	
	DSG2	KIRREL3	PTPRD	
	DYNC1I1	LRP1	RAB20	
	EFNA1	MAB21L1	RIN3	

Table 17. Differentially-expressed endocytic-associated genes used for RNA-seq analysis.

Endocytic-associated genes (form Metascape GOs)				
ABCA1	CLU	GSN	NAPSA	SLC35D3
ACKR2	CLVS1	HIST1H1A	NRP1	SMO
ACKR3	CPNE6	HLA-A	NTRK1	SNCA
ADAM8	CTSH	HLA-B	OCLN	SPARC
ADRB1	CUBN	HLA-C	PDLIM4	STXBP2
ADRB2	CXCR4	HLA-E	PGA3	SYNDIG1
AMOT	CYBA	HLA-F	PLA2G4B	TAP1
ANGPT1	DIAPH2	IL12A	PLEKHG5	TAPBP
ANXA1	DKK1	ITGA2	PRLR	TCIRG1
ANXA11	DNER	ITGAV	PTX3	TLR4
ANXA2	DOCK2	ITGB5	RAB27A	TLR6
AP4B1	DRD2	KCNH1	RAB31	TLR7
APLN	EGF	KDR	RAB32	TMEM108
APOE	EGFR	KIAA0319	RAB34	TMEM163
ATP6V0E1	EPHA3	KIF16B	RAB38	TMEM184A
AXL	EPHB1	KIFC1	RAB8B	VCAM1
BOK	F2RL1	LAMP1	RAB3B	VEGFA
C3	FCGR1A	LAMP5	RAB27A	VIM
C4A	FGD5	LDLRAD4	RAB13	WLS
CALY	FLOT2	LIPG	RET	WNT1
CCL2	FZD4	LITAF	RFTN1	WNT3
CD163	FZD5	LPAR1	SAMD9	WNT4
CD207	GJA1	LRP2	SAMD9L	WNT5A
CD36	GPC3	MAGEL2	SCGB3A2	WNT7A
CD47	GPER1	MERTK	SELE	WNT7B
CFTR	GRIA1	MFGE8	SERPINE1	
	GRIA4	MSR1	SH3GL2	

Table 18. Sample of Metascape GO terms using input list of genes differentially expressed genes in *Swe/M146V* versus *APPswe* or *PSEN1-M146V* neurons.

Endosomal-lysosomal & Lipid trafficking GO terms			
GO	Description	LogP	# Genes
GO:0012506	vesicle membrane	-9.3237	142
GO:0030139	endocytic vesicle	-8.2469	53
GO:0045055	regulated exocytosis	-6.9176	132
GO:0030666	endocytic vesicle membrane	-6.4054	33
GO:0043087	regulation of GTPase activity	-6.1699	90
GO:1905954	positive regulation of lipid localization	-4.791	18
GO:0005769	early endosome	-4.4905	63
GO:0045807	positive regulation of endocytosis	-4.3651	30
GO:0060627	regulation of vesicle-mediated transport	-4.321	84
GO:0031901	early endosome membrane	-4.2981	32
GO:0043547	positive regulation of GTPase activity	-4.1397	72
GO:0005764	lysosome	-3.9922	82
GO:0005085	guanyl-nucleotide exchange factor activity	-3.7662	45
GO:1905952	regulation of lipid localization	-3.758	24
GO:0006869	lipid transport	-3.6272	60
GO:0032370	positive regulation of lipid transport	-3.5763	13
GO:0043202	lysosomal lumen	-3.5514	23
GO:0010876	lipid localization	-3.4713	64
GO:0031904	endosome lumen	-3.4072	10
GO:0030276	clathrin binding	-3.3195	18
GO:0006897	endocytosis	-3.1425	111
GO:0005096	GTPase activator activity	-2.9432	50
AD/Neurodeeneration GO terms			
GO	Description	LogP	# Genes
GO:0043408	regulation of MAPK cascade	-17.336	162
GO:0010942	positive regulation of cell death	-12.425	139
GO:0043065	positive regulation of apoptotic process	-9.9273	123
GO:0034599	cellular response to oxidative stress	-6.6819	62
GO:0051403	stress-activated MAPK cascade	-6.2771	58
GO:1901214	regulation of neuron death	-6.1453	60
GO:0001540	amyloid-beta binding	-5.8169	21
GO:0070997	neuron death	-5.3607	63
GO:0007568	aging	-5.0603	59
GO:0043523	regulation of neuron apoptotic process	-5.0166	43
hsa04730	Long-term depression	-4.7259	19
GO:0007254	JNK cascade	-3.8813	32
Synapse function			
GO	Description	LogP	# Genes
GO:0007268	chemical synaptic transmission	-25.663	163
GO:0098916	anterograde trans-synaptic signaling	-25.663	163
GO:0099537	trans-synaptic signaling	-25.495	163
GO:0099536	synaptic signaling	-25.495	163
GO:0044456	synapse part	-18.953	162
GO:0050808	synapse organization	-15.28	84
GO:0050804	modulation of chemical synaptic transmission	-14.766	85
GO:0099177	regulation of trans-synaptic signaling	-14.766	85
GO:0098793	presynapse	-13.557	91
GO:0098794	postsynapse	-11.285	97
GO:0097060	synaptic membrane	-11.014	75
GO:0007416	synapse assembly	-10.988	48
GO:0050807	regulation of synapse organization	-9.9973	48
GO:0045211	postsynaptic membrane	-8.5185	57
GO:0050806	positive regulation of synaptic transmission	-8.0496	39
GO:0048167	regulation of synaptic plasticity	-7.9323	44
R-HSA-112315	Transmission across Chemical Synapses	-6.4514	52
GO:0051965	positive regulation of synapse assembly	-6.2848	23
GO:0042133	neurotransmitter metabolic process	-6.1851	30
GO:0021766	hippocampus development	-5.8958	24
hsa04724	Glutamatergic synapse	-5.514	25
R-HSA-112314	Neurotransmitter receptors and postsynaptic signal transmission	-5.5896	38
GO:0051588	regulation of neurotransmitter transport	-5.3923	26
GO:0022843	voltage-gated cation channel activity	-5.3309	35
GPCR signalling			
GO	Description	LogP	# Genes
R-HSA-500792	GPCR ligand binding	-17.532	118
GO:0007187	G-protein coupled receptor signaling pathway, coupled to cyclic nucleotide second messenger	-15.145	67
GO:0007188	adenylate cyclase-modulating G-protein coupled receptor signaling pathway	-12.724	58
GO:0007264	small GTPase mediated signal transduction	-11.322	106
R-HSA-418594	G alpha (i) signalling events	-9.4897	88
GO:0051057	positive regulation of small GTPase mediated signal transduction	-5.8572	20
GO:0016907	G-protein coupled acetylcholine receptor activity	-5.4821	5
GO:0007189	adenylate cyclase-activating G-protein coupled receptor signaling pathway	-5.3308	27
R-HSA-1296059	G protein gated Potassium channels	-5.2913	12
R-HSA-1296041	Activation of G protein gated Potassium channels	-5.2913	12
GO:0008528	G-protein coupled peptide receptor activity	-4.7783	32
GO:0038037	G-protein coupled receptor dimeric complex	-4.5999	5
GO:0097648	G-protein coupled receptor complex	-4.5999	5
GO:0015467	G-protein activated inward rectifier potassium channel activity	-4.6988	7
R-HSA-418597	G alpha (z) signalling events	-3.5995	12
GO:0038042	dimeric G-protein coupled receptor signaling pathway	-3.262	4
GO:0045028	G-protein coupled purinergic nucleotide receptor activity	-3.1683	5
GO:0035589	G-protein coupled purinergic nucleotide receptor signaling pathway	-3.1683	5
GO:0001608	G-protein coupled nucleotide receptor activity	-3.1683	5

Immunocytochemistry and microscopy

Cells were fixed in 4% paraformaldehyde, permeabilized in PBS/0.1% TritonX-100 and stained with primary and secondary antibodies (see below). For low resolution microscopy (all experiments excluding endosome analyses) stained cells were imaged on a Nikon Eclipse Ti inverted microscope and acquired using NIS Elements imaging software (Nikon). For endosome analysis, stained cells were imaged on a DeltaVision inverted Olympus IX-70 microscope using a 100X oil objective with deconvolution. Rab5+ puncta quantifications were done using Imarus. Briefly, surface masks using the MAP2 staining to indicate neurons. Rab5+ puncta detection and quantification was automated and programmed using the Imarus spot detection function. Fiji (www.Fiji.sc / National Institutes of Health) and Adobe Photoshop were used to pseudo-color images, adjust contrast, and add scale bars.

Antibodies

The following antibodies were used: Oct4 (1:500, Stemgent S090023), Tra160 (1:500, Millipore MAB4360), SSEA4 (1:500, Abcam ab16287), Nanog (1:500, Cell Signaling 4903), MAP2 (1:2000, Abcam 5392), Pax6 (1:300, Covance PRB-278P), Tuj1 (mouse 1:1000, Covance MMS-435P / rabbit 1:1000, Covance MRB-435P), Otx2 (1:100, Millipore AB9566), Nestin (1:200, Millipore 2C13B9), FoxG1 (1:300, Abcam ab18259), CTIP2 (1:300, Abcam ab18465), Tbr1 (1:500, Millipore AB2261), SatB2 (1:100, Abcam ab51502), MAGUK (1:100, NeuroMab

K28_86), Synapsin (1:200, Cell Signalling Technologies 5297), APP C-term (1:10000, Abcam Y188 ab32136) Rab5 (1:200, Cell Signalling Technologies), anti-mouse/rabbit/rat/chicken Alexa Fluor 488/568/647 (Invitrogen 1:500.

Amyloid-β measurements

Aβ was measured in cell supernatant conditioned for 7 days (DIV62-72 cortical neurons). Experiments were performed in 3 biological replicates. Supernatants from experiments collected at different time points were frozen at -80 ˚C. Secreted Aβ1-38, Aβ1-40 and Aβ1-42 was measured with MSD Human (6E10) Aβ V-PLEX kits (Meso Scale Discovery) according to the manufacturer's directions. Aβ1-43 was measured using a colormetric ELISA (Takara) according to the manufacturer's directions. Secreted sAPPα and sAPPβ were also measured simultaneously, and from matching supernatants, with MSD sAPPα/sAPPβ kit (Meso Scale Discovery) according to the manufacturer's directions. For all experiments, Aβ levels were normalized to total sAPP levels unless otherwise stated.

Western Blotting

Neurons were lysed using the NucleoSpin RNA/Protein kit (Macherey Nagel) and total protein was isolated according to the manufacturer's instructions. Samples were run on Criterion™ Tris-Tricine 16.5% precast gels for SDS-PAGE at 125V (Bio-Rad). Gels were then blotted using standard techniques onto an Odyssey

nitrocellulose membrane (LI-COR). Membranes were blocked in 5% non-fat dairy milk in TBS-T, and were probed with primary antibodies listed below. IRDye conjugated secondary antibodies (LI-COR) were used at 1:10,000. Proteins were detected using the Odyssey CLx Imaging System (LI-COR).

Statistical Analysis

Experimental data was analyzed for significance using Graphpad Prism. $P<0.05$ was considered statistically significant. Sample sizes were chosen to be large enough to allow meaningful statistical analysis. In Chapter II, all experiments except the oligo scan were analyzed by one-way ANOVA followed by post testing with either Tukey's test, if multiple values were compared to each other, or Dunnett's method, if alterations were compared to controls. For the oligo scan, nonlinear regression analysis was performed to fit exponential decay equation model curves to experimental values; R square values were determined to test goodness of fit. To analyze if distance-incorporation relationships were significantly different for genomic loci, the rate constant k was determined for each individual data set and the k values of the two loci were compared using the unpaired t-test. For experiments in Chapter IV, data were analyzed by one-way or two-way ANOVA (as indicated) followed by post testing with Dunnett's method, as alterations were compared to controls. Outliers were identified by the ROUT method (Q=1%). T-tests were performed when only a single experimental group was being compared to control.

Appendix II: Rights and Permissions

Figure 4. Reprinted by permission from Cold Spring Harbor Laboratory Press: Cold Spring Harbor Perspectives in Medicine. Haass, C., Kaether, C., Thinakaran, G., and Sisodia, S. (2012). Trafficking and proteolytic processing of APP. Cold Spring Harb Perspect Med *2*, a006270–a006270., copyright (2012).

Figure 6. Reprinted by permission from Macmillan Publishers Ltd: Nature Reviews Neuroscience. Bu, G. (2009). Apolipoprotein E and its receptors in Alzheimer's disease: pathways, pathogenesis and therapy. Nat. Rev. Neurosci. *10*, 333–344., copyright (2009).

References

ADGC, Alzheimer's Disease Neuroimaging Initiative, Chapuis, J., Flaig, A., Grenier-Boley, B., Eysert, F., Pottiez, V., Deloison, G., Vandeputte, A., Ayral, A.-M., Mendes, T., et al. (2016). Genome-wide, high-content siRNA screening identifies the Alzheimer's genetic risk factor FERMT2 as a major modulator of APP metabolism. Acta Neuropathol. *133*, 955–966.

Aldudo, J., Bullido, M.J., and Valdivieso, F. (1999). DGGE method for the mutational analysis of the coding and proximal promoter regions of the Alzheimer's disease presenilin-1 gene: two novel mutations. Hum. Mutat. *14*, 433–439.

Alier, K.A., and Morris, B.J. (2005). Divergent regulation of Pyk2/CAKβ phosphorylation by Ca2+ and cAMP in the hippocampus. Biochimica Et Biophysica Acta (BBA) - Molecular Cell Research *1745*, 342–349.

Allen, M., Kachadoorian, M., Carrasquillo, M.M., Karhade, A., Manly, L., Burgess, J.D., Wang, C., Serie, D., Wang, X., Siuda, J., et al. (2015). Late-onset Alzheimer disease risk variants mark brain regulatory loci. Neurol Genet *1*, e15.

Alonso, A.D., Grundke-Iqbal, I., Barra, H.S., and Iqbal, K. (1997). Abnormal phosphorylation of tau and the mechanism of Alzheimer neurofibrillary degeneration: sequestration of microtubule-associated proteins 1 and 2 and the disassembly of microtubules by the abnormal tau. Proc. Natl. Acad. Sci. U.S.a. *94*, 298–303.

Alzheimer's Association (2017). 2017 Alzheimer's disease facts and figures. Alzheimer's & Dementia *13*, 325–373.

Alzheimer's Disease Collaborative Group (1995). The structure of the presenilin 1 (S182) gene and identification of six novel mutations in early onset AD families. Nat. Genet. *11*, 219–222.

Alzheimer, A. (1916). Über eine eigenartige erkrankung des zentralen nervensystems mit bulbären symptomen und schmerzhaften spastischen krampfzuständen der extremitäten. Zeitschrift Für Die Gesamte Neurologie Und Psychiatrie *33*, 45–59.

Alzheimer, A., Stelzmann, R.A., Schnitzlein, H.N., and Murtagh, F.R. (1995). An English translation of Alzheimer's 1907 paper, "Uber eine eigenartige Erkankung der Hirnrinde". (Wiley-Blackwell).

An, S.S., Cai, Y., and Kim, S. (2015). Mutations in presenilin 2 and its implications in Alzheimer’s disease and other dementia-associated disorders. Cia 1163.

Andersen, O.M., Reiche, J., Schmidt, V., Gotthardt, M., Spoelgen, R., Behlke, J., Arnim, von, C.A.F., Breiderhoff, T., Jansen, P., Wu, X., et al. (2005). Neuronal sorting protein-related receptor sorLA/LR11 regulates processing of the amyloid precursor protein. Proc. Natl. Acad. Sci. U.S.a. *102*, 13461–13466.

Antúnez, C., Boada, M., González-Pérez, A., Gayán, J., Ramírez-Lorca, R., Marín, J., Hernández, I., Moreno-Rey, C., Morón, F.J., López-Arrieta, J., et al. (2011). The membrane-spanning 4-domains, subfamily A (MS4A) gene cluster contains a common variant associated with Alzheimer's disease. Genome Med *3*, 33.

Apostolova, L.G., Risacher, S.L., Duran, T., Stage, E.C., Goukasian, N., West, J.D., Do, T.M., Grotts, J., Wilhalme, H., Nho, K., et al. (2018). Associations of the Top 20 Alzheimer Disease Risk Variants With Brain Amyloidosis. JAMA Neurol *75*, 328.

Avila, J., Lim, F., Moreno, F., Belmonte, C., and Cuello, A.C. (2002). Tau function and dysfunction in neurons: its role in neurodegenerative disorders. Mol. Neurobiol. *25*, 213–231.

Bahmad, H., Hadadeh, O., Chamaa, F., Cheaito, K., Darwish, B., Makkawi, A.-K., and Abou-Kheir, W. (2017). Modeling Human Neurological and Neurodegenerative Diseases: From Induced Pluripotent Stem Cells to Neuronal Differentiation and Its Applications in Neurotrauma. Frontiers in Molecular Neuroscience *10*, 1276.

Barber, R.C. (2012). The genetics of Alzheimer's disease. Scientifica (Cairo) *2012*, 246210–246214.

Beck, T.N., Nicolas, E., Kopp, M.C., and Golemis, E.A. (2014). Adaptors for disorders of the brain? The cancer signaling proteins NEDD9, CASS4, and PTK2B in Alzheimer's disease. Oncoscience *1*, 486–503.

Bellin, M., Marchetto, M.C., Gage, F.H., and Mummery, C.L. (2012). Induced pluripotent stem cells: the new patient? Nature Reviews Molecular Cell Biology *13*, 713–726.

Bennett, B.D., Babu-Khan, S., Loeloff, R., Louis, J.C., Curran, E., Citron, M., and Vassar, R. (2000). Expression analysis of BACE2 in brain and peripheral tissues. J. Biol. Chem. *275*, 20647–20651.

Beumer, K.J., Trautman, J.K., Mukherjee, K., and Carroll, D. (2013). Donor DNA Utilization During Gene Targeting with Zinc-Finger Nucleases. G3 (Bethesda) *3*, 657–664.

Bialk, P., Rivera-Torres, N., Strouse, B., and Kmiec, E.B. (2015). Regulation of Gene Editing Activity Directed by Single-Stranded Oligonucleotides and CRISPR/Cas9 Systems. PLoS ONE *10*, e0129308.

Biffi, A., Shulman, J.M., Jagiella, J.M., Cortellini, L., Ayres, A.M., Schwab, K., Brown, D.L., Silliman, S.L., Selim, M., Worrall, B.B., et al. (2012). Genetic variation at CR1 increases risk of cerebral amyloid angiopathy. Neurology *78*, 334–341.

Blankenberg, D., Gordon, A., Kuster, Von, G., Coraor, N., Taylor, J., Nekrutenko, A., Galaxy Team (2010a). Manipulation of FASTQ data with Galaxy. Bioinformatics *26*, 1783–1785.

Blankenberg, D., Kuster, Von, G., Coraor, N., Ananda, G., Lazarus, R., Mangan, M., Nekrutenko, A., and Taylor, J. (2010b). Galaxy: a web-based genome analysis tool for experimentalists. Curr Protoc Mol Biol *Chapter 19*, Unit19.10.1–Unit19.10.21.

Borchelt, D.R., Ratovitski, T., van Lare, J., Lee, M.K., Gonzales, V., Jenkins, N.A., Copeland, N.G., Price, D.L., and Sisodia, S.S. (1997). Accelerated amyloid deposition in the brains of transgenic mice coexpressing mutant presenilin 1 and amyloid precursor proteins. Neuron *19*, 939–945.

Borchelt, D.R., Thinakaran, G., Eckman, C.B., Lee, M.K., Davenport, F., Ratovitsky, T., Prada, C.M., Kim, G., Seekins, S., Yager, D., et al. (1996). Familial Alzheimer's disease-linked presenilin 1 variants elevate Abeta1-42/1-40 ratio in vitro and in vivo. Neuron *17*, 1005–1013.

Braak, H., and Braak, E. (1991). Neuropathological stageing of Alzheimer-related changes. Acta Neuropathol. *82*, 239–259.

Bu, G. (2009). Apolipoprotein E and its receptors in Alzheimer's disease: pathways, pathogenesis and therapy. Nat. Rev. Neurosci. *10*, 333–344.

Bugiani, O., Giaccone, G., Rossi, G., Mangieri, M., Capobianco, R., Morbin, M., Mazzoleni, G., Cupidi, C., Marcon, G., Giovagnoli, A., et al. (2010). Hereditary cerebral hemorrhage with amyloidosis associated with the E693K mutation of APP. Arch. Neurol. *67*, 987–995.

Byun, K., Gil, S.Y., Namkoong, C., Youn, B.-S., Huang, H., Shin, M.-S., Kang, G.M., Kim, H.-K., Lee, B., Kim, Y.-B., et al. (2014). Clusterin/ApoJ enhances central leptin signaling through Lrp2-mediated endocytosis. EMBO Rep. *15*, 801–808.

Calafate, S., Flavin, W., Verstreken, P., and Moechars, D. (2016). Loss of Bin1 Promotes the Propagation of Tau Pathology. CellReports *17*, 931–940.

Cam, J.A., Zerbinatti, C.V., Knisely, J.M., Hecimovic, S., Li, Y., and Bu, G. (2004). The low density lipoprotein receptor-related protein 1B retains beta-amyloid precursor protein at the cell surface and reduces amyloid-beta peptide production. J. Biol. Chem. *279*, 29639–29646.

Cam, J.A., Zerbinatti, C.V., Li, Y., and Bu, G. (2005). Rapid Endocytosis of the Low Density Lipoprotein Receptor-related Protein Modulates Cell Surface Distribution and Processing of the β-Amyloid Precursor Protein. J. Biol. Chem. *280*, 15464–15470.

Canver, M.C., Bauer, D.E., Dass, A., Yien, Y.Y., Chung, J., Masuda, T., Maeda, T., Paw, B.H., and Orkin, S.H. (2014). Characterization of genomic deletion efficiency mediated by clustered regularly interspaced short palindromic repeats (CRISPR)/Cas9 nuclease system in mammalian cells. J. Biol. Chem. *289*, 21312–21324.

Castellano, J.M., Kim, J., Stewart, F.R., Jiang, H., DeMattos, R.B., Patterson, B.W., Fagan, A.M., Morris, J.C., Mawuenyega, K.G., Cruchaga, C., et al. (2011). Human apoE isoforms differentially regulate brain amyloid-β peptide clearance. Sci Transl Med *3*, 89ra57–89ra57.

Cataldo, A.M., Peterhoff, C.M., Troncoso, J.C., Gomez-Isla, T., Hyman, B.T., and Nixon, R.A. (2000). Endocytic pathway abnormalities precede amyloid beta deposition in sporadic Alzheimer's disease and Down syndrome: differential effects of APOE genotype and presenilin mutations. Am. J. Pathol. *157*, 277–286.

Cataldo, A.M., Mathews, P.M., Boiteau, A.B., Hassinger, L.C., Peterhoff, C.M., Jiang, Y., Mullaney, K., Neve, R.L., Gruenberg, J., and Nixon, R.A. (2008). Down syndrome fibroblast model of Alzheimer-related endosome pathology: accelerated endocytosis promotes late endocytic defects. Am. J. Pathol. *173*, 370–384.

Chartier-Harlin, M.C., Crawford, F., Houlden, H., Warren, A., Hughes, D., Fidani, L., Goate, A., Rossor, M., Roques, P., and Hardy, J. (1991). Early-onset Alzheimer's disease caused by mutations at codon 717 of the beta-amyloid precursor protein gene. Nature *353*, 844–846.

Chen, H., Wu, G., Jiang, Y., Feng, R., Liao, M., Zhang, L., Ma, G., Chen, Z., Zhao, B., Li, K., et al. (2015). Analyzing 54,936 Samples Supports the Association Between CD2AP rs9349407 Polymorphism and Alzheimer's Disease Susceptibility. Mol. Neurobiol. *52*, 1–7.

Chen, Y., Durakoglugil, M.S., Xian, X., and Herz, J. (2010). ApoE4 reduces glutamate receptor function and synaptic plasticity by selectively impairing ApoE receptor recycling. Proceedings of the National Academy of Sciences *107*, 12011–12016.

Cho, S.W., Kim, S., Kim, J.M., and Kim, J.-S. (2013). Targeted genome engineering in human cells with the Cas9 RNA-guided endonuclease. Nat. Biotechnol. *31*, 230–232.

Choy, R.W.-Y., Cheng, Z., and Schekman, R. (2012). Amyloid precursor protein (APP) traffics from the cell surface via endosomes for amyloid β (Aβ) production in the trans-Golgi network. Proc. Natl. Acad. Sci. U.S.a. *109*, E2077–E2082.

Chu, V.T., Weber, T., Wefers, B., Wurst, W., Sander, S., Rajewsky, K., and Kühn, R. (2015). Increasing the efficiency of homology-directed repair for CRISPR-Cas9-induced precise gene editing in mammalian cells. Nat. Biotechnol. *33*, 543–548.

Chung, W.-S., Verghese, P.B., Chakraborty, C., Joung, J., Hyman, B.T., Ulrich, J.D., Holtzman, D.M., and Barres, B.A. (2016). Novel allele-dependent role for APOE in controlling the rate of synapse pruning by astrocytes. Proc. Natl. Acad. Sci. U.S.a. *113*, 10186–10191.

Citron, M., Oltersdorf, T., Haass, C., McConlogue, L., Hung, A.Y., Seubert, P., Vigo-Pelfrey, C., Lieberburg, I., and Selkoe, D.J. (1992). Mutation of the beta-amyloid precursor protein in familial Alzheimer's disease increases beta-protein production. Nature *360*, 672–674.

Citron, M., Vigo-Pelfrey, C., Teplow, D.B., Miller, C., Schenk, D., Johnston, J., Winblad, B., Venizelos, N., Lannfelt, L., and Selkoe, D.J. (1994). Excessive production of amyloid beta-protein by peripheral cells of symptomatic and presymptomatic patients carrying the Swedish familial Alzheimer disease mutation. Proc. Natl. Acad. Sci. U.S.a. *91*, 11993–11997.

Clark, R.I., Tan, S.W.S., Péan, C.B., Roostalu, U., Vivancos, V., Bronda, K., Pilátová, M., Fu, J., Walker, D.W., Berdeaux, R., et al. (2013). MEF2 is an in vivo immune-metabolic switch. Cell *155*, 435–447.

Condello, C., Yuan, P., Schain, A., and Grutzendler, J. (2015). Microglia constitute a barrier that prevents neurotoxic protofibrillar Aβ42 hotspots around plaques. Nature Communications *6*, 6176.

Cong, L., Ran, F.A., Cox, D., Lin, S., Barretto, R., Habib, N., Hsu, P.D., Wu, X., Jiang, W., Marraffini, L.A., et al. (2013). Multiplex genome engineering using CRISPR/Cas systems. Science *339*, 819–823.

Corder, E.H., Saunders, A.M., Risch, N.J., Strittmatter, W.J., Schmechel, D.E., Gaskell, P.C., Rimmler, J.B., Locke, P.A., Conneally, P.M., Schmader, K.E., et al. (1994). Protective effect of apolipoprotein E type 2 allele for late onset Alzheimer disease. Nat. Genet. *7*, 180–184.

Corder, E.H., Saunders, A.M., Strittmatter, W.J., Schmechel, D.E., Gaskell, P.C., Small, G.W., Roses, A.D., Haines, J.L., and Pericak-Vance, M.A. (1993). Gene dose of apolipoprotein E type 4 allele and the risk of Alzheimer's disease in late onset families. Science *261*, 921–923.

Cormont, M., Metón, I., Mari, M., Monzo, P., Keslair, F., Gaskin, C., McGraw, T.E., and Le Marchand-Brustel, Y. (2003). CD2AP/CMS Regulates Endosome Morphology and Traffic to the Degradative Pathway Through its Interaction with Rab4 and c-Cbl. Traffic *4*, 97–112.

Cosker, K.E., and Segal, R.A. (2014). Neuronal signaling through endocytosis. Cold Spring Harb Perspect Biol *6*, a020669–a020669.

Cowan, C.A., Klimanskaya, I., McMahon, J., Atienza, J., Witmyer, J., Zucker, J.P., Wang, S., Morton, C.C., McMahon, A.P., Powers, D., et al. (2004). Derivation of embryonic stem-cell lines from human blastocysts. N. Engl. J. Med. *350*, 1353–1356.

Cruchaga, C., Karch, C.M., Jin, S.C., Benitez, B.A., Cai, Y., Guerreiro, R., Harari, O., Norton, J., Budde, J., Bertelsen, S., et al. (2014). Rare coding variants in the phospholipase D3 gene confer risk for Alzheimer's disease. Nature *505*, 550–554.

Crump, C.J., Fish, B.A., Castro, S.V., Chau, D.-M., Gertsik, N., Ahn, K., Stiff, C., Pozdnyakov, N., Bales, K.R., Johnson, D.S., et al. (2011). Piperidine acetic acid based γ-secretase modulators directly bind to Presenilin-1. ACS Chem Neurosci *2*, 705–710.

Crump, C.J., Johnson, D.S., and Li, Y.-M. (2013). Development and Mechanism of γ-Secretase Modulators for Alzheimer's Disease. Biochemistry *52*, 3197–3216.

Cuccaro, M.L., Carney, R.M., Zhang, Y., Bohm, C., Kunkle, B.W., Vardarajan, B.N., Whitehead, P.L., Cukier, H.N., Mayeux, R., St George-Hyslop, P., et al. (2016). SORL1 mutations in early- and late-onset Alzheimer disease. Neurol Genet *2*, e116.

Davis, D.G., Schmitt, F.A., Wekstein, D.R., and Markesbery, W.R. (1999). Alzheimer neuropathologic alterations in aged cognitively normal subjects. J. Neuropathol. Exp. Neurol. *58*, 376–388.

De Jonghe, C., Esselens, C., Kumar-Singh, S., Craessaerts, K., Serneels, S., Checler, F., Annaert, W., Van Broeckhoven, C., and De Strooper, B. (2001). Pathogenic APP mutations near the gamma-secretase cleavage site differentially affect Abeta secretion and APP C-terminal fragment stability. Human Molecular Genetics *10*, 1665–1671.

De Jonghe, C., Zehr, C., Yager, D., Prada, C.M., Younkin, S., Hendriks, L., Van Broeckhoven, C., and Eckman, C.B. (1998). Flemish and Dutch mutations in amyloid beta precursor protein have different effects on amyloid beta secretion. Neurobiol. Dis. *5*, 281–286.

De Strooper, B., Saftig, P., Craessaerts, K., Vanderstichele, H., Guhde, G., Annaert, W., Figura, Von, K., and Van Leuven, F. (1998). Deficiency of presenilin-1 inhibits the normal cleavage of amyloid precursor protein. Nature *391*, 387–390.

De Strooper, B. (2007). Loss-of-function presenilin mutations in Alzheimer disease. Talking Point on the role of presenilin mutations in Alzheimer disease. EMBO Rep. *8*, 141–146.

De Strooper, B., Iwatsubo, T., and Wolfe, M.S. (2012). Presenilins and γ-secretase: structure, function, and role in Alzheimer Disease. Cold Spring Harb Perspect Med *2*, a006304–a006304.

DeMattos, R.B., Cirrito, J.R., Parsadanian, M., May, P.C., O'Dell, M.A., Taylor, J.W., Harmony, J.A.K., Aronow, B.J., Bales, K.R., Paul, S.M., et al. (2004). ApoE and clusterin cooperatively suppress Abeta levels and deposition: evidence that ApoE regulates extracellular Abeta metabolism in vivo. Neuron *41*, 193–202.

Di Paolo, G., Sankaranarayanan, S., Wenk, M.R., Daniell, L., Perucco, E., Caldarone, B.J., Flavell, R., Picciotto, M.R., Ryan, T.A., Cremona, O., et al. (2002). Decreased synaptic vesicle recycling efficiency and cognitive deficits in amphiphysin 1 knockout mice. Neuron *33*, 789–804.

Ding, Q., Regan, S.N., Xia, Y., Oostrom, L.A., Cowan, C.A., and Musunuru, K. (2013). Enhanced efficiency of human pluripotent stem cell genome editing through replacing TALENs with CRISPRs. Cell Stem Cell *12*, 393–394.

Doherty, G.J., and McMahon, H.T. (2009). Mechanisms of endocytosis. Annu. Rev. Biochem. *78*, 857–902.

Dow, L.E., Fisher, J., O'Rourke, K.P., Muley, A., Kastenhuber, E.R., Livshits, G., Tschaharganeh, D.F., Socci, N.D., and Lowe, S.W. (2015). Inducible in vivo genome editing with CRISPR-Cas9. Nat. Biotechnol. *33*, 390–394.

Dries, D., and Yu, G. (2008). Assembly, Maturation, and Trafficking of the gamma-Secretase Complex in Alzheimers Disease. Current Alzheimer Research *5*, 132–146.

Duan, L., Bhattacharyya, B.J., Belmadani, A., Pan, L., Miller, R.J., and Kessler, J.A. (2014). Stem cell derived basal forebrain cholinergic neurons from Alzheimer's disease patients are more susceptible to cell death. Mol Neurodegener *9*, 3.

Duff, K., Eckman, C., Zehr, C., Yu, X., Prada, C.M., Perez-tur, J., Hutton, M., Buee, L., Harigaya, Y., Yager, D., et al. (1996). Increased amyloid-beta42(43) in brains of mice expressing mutant presenilin 1. Nature *383*, 710–713.

Dumanchin, C., Camuzat, A., Campion, D., Verpillat, P., Hannequin, D., Dubois, B., Saugier-Veber, P., Martin, C., Penet, C., Charbonnier, F., et al. (1998). Segregation of a missense mutation in the microtubule-associated protein tau gene with familial frontotemporal dementia and parkinsonism. Human Molecular Genetics *7*, 1825–1829.

Dustin, M.L., Olszowy, M.W., Holdorf, A.D., Li, J., Bromley, S., Desai, N., Widder, P., Rosenberger, F., van der Merwe, P.A., Allen, P.M., et al. (1998). A Novel Adaptor Protein Orchestrates Receptor Patterning and Cytoskeletal Polarity in T-Cell Contacts. Cell *94*, 667–677.

Ebneth, A., Godemann, R., Stamer, K., Illenberger, S., Trinczek, B., and Mandelkow, E. (1998). Overexpression of tau protein inhibits kinesin-dependent trafficking of vesicles, mitochondria, and endoplasmic reticulum: implications for Alzheimer's disease. J. Cell Biol. *143*, 777–794.

Eckman, C.B., Mehta, N.D., Crook, R., Perez-tur, J., Prihar, G., Pfeiffer, E., Graff-Radford, N., Hinder, P., Yager, D., Zenk, B., et al. (1997). A new pathogenic mutation in the APP gene (I716V) increases the relative proportion of A beta 42(43). Human Molecular Genetics *6*, 2087–2089.

Efthymiou, A.G., and Goate, A.M. (2017). Late onset Alzheimer's disease genetics implicates microglial pathways in disease risk. Mol Neurodegener *12*, 704.

Egan, M.F., Kost, J., Tariot, P.N., Aisen, P.S., Cummings, J.L., Vellas, B., Sur, C., Mukai, Y., Voss, T., Furtek, C., et al. (2018). Randomized Trial of Verubecestat for Mild-to-Moderate Alzheimer's Disease. N. Engl. J. Med. *378*, 1691–1703.

Eikelenboom, P., Hack, C.E., Rozemuller, J.M., and Stam, F.C. (1989). Complement activation in amyloid plaques in Alzheimer's dementia. Virchows Arch., B, Cell Pathol. *56*, 259–262.

Elliott, B., Richardson, C., Winderbaum, J., Nickoloff, J.A., and Jasin, M. (1998). Gene conversion tracts from double-strand break repair in mammalian cells. Molecular and Cellular Biology *18*, 93–101.

Evans, L.D., Wassmer, T., Fraser, G., Smith, J., Perkinton, M., Billinton, A., and Livesey, F.J. (2018). Extracellular Monomeric and Aggregated Tau Efficiently Enter Human Neurons through Overlapping but Distinct Pathways. CellReports *22*, 3612–3624.

Fazzari, P., Horré, K., Arranz, A.M., Frigerio, C.S., Saito, T., Saido, T.C., and De Strooper, B. (2017). PLD3 gene and processing of APP. Nature *541*, E1–E2.

Fu, H., Hussaini, S.A., Wegmann, S., Profaci, C., Daniels, J.D., Herman, M., Emrani, S., Figueroa, H.Y., Hyman, B.T., Davies, P., et al. (2016). 3D Visualization of the

Temporal and Spatial Spread of Tau Pathology Reveals Extensive Sites of Tau Accumulation Associated with Neuronal Loss and Recognition Memory Deficit in Aged Tau Transgenic Mice. PLoS ONE *11*, e0159463.

Fu, Y., Foden, J.A., Khayter, C., Maeder, M.L., Reyon, D., Joung, J.K., and Sander, J.D. (2013). High-frequency off-target mutagenesis induced by CRISPR-Cas nucleases in human cells. Nat. Biotechnol. *31*, 822–826.

Games, D., Adams, D., Alessandrini, R., Barbour, R., Berthelette, P., Blackwell, C., Carr, T., Clemens, J., Donaldson, T., and Gillespie, F. (1995). Alzheimer-type neuropathology in transgenic mice overexpressing V717F beta-amyloid precursor protein. Nature *373*, 523–527.

Gandy, S., and Greengard, P. (1994). Processing of Alzheimer Aβ-Amyloid Precursor Protein: Cell Biology, Regulation, and Role in Alzheimer's Disease. In Amyloid Protein Precursor in Development, Aging and Alzheimer's Disease, (Berlin, Heidelberg: Springer Berlin Heidelberg), pp. 100–120.

Gaudelli, N.M., Komor, A.C., Rees, H.A., Packer, M.S., Badran, A.H., Bryson, D.I., and Liu, D.R. (2017). Programmable base editing of A•T to G•C in genomic DNA without DNA cleavage. Nature *551*, 464–471.

Ginsberg, S.D., Alldred, M.J., Counts, S.E., Cataldo, A.M., Neve, R.L., Jiang, Y., Wuu, J., Chao, M.V., Mufson, E.J., Nixon, R.A., et al. (2010a). Microarray analysis of hippocampal CA1 neurons implicates early endosomal dysfunction during Alzheimer's disease progression. Biological Psychiatry *68*, 885–893.

Ginsberg, S.D., Mufson, E.J., Counts, S.E., Wuu, J., Alldred, M.J., Nixon, R.A., and Che, S. (2010b). Regional selectivity of rab5 and rab7 protein upregulation in mild cognitive impairment and Alzheimer's disease. J. Alzheimers Dis. *22*, 631–639.

Giri, M., Lü, Y., and Zhang, M. (2016). Genes associated with Alzheimer's disease: an overview and current status. Cia 665–17.

Giudice, J., Xia, Z., Li, W., and Cooper, T.A. (2016). Neonatal cardiac dysfunction and transcriptome changes caused by the absence of Celf1. Scientific Reports *6*, 35550.

Goate, A., Chartier-Harlin, M.C., Mullan, M., Brown, J., Crawford, F., Fidani, L., Giuffra, L., Haynes, A., Irving, N., and James, L. (1991). Segregation of a missense mutation in the amyloid precursor protein gene with familial Alzheimer's disease. Nature *349*, 704–706.

Goecks, J., Nekrutenko, A., Taylor, J., Galaxy Team (2010). Galaxy: a comprehensive approach for supporting accessible, reproducible, and transparent computational research in the life sciences. Genome Biol. *11*, R86.

Goldgaber, D., Lerman, M.I., McBride, O.W., Saffiotti, U., and Gajdusek, D.C. (1987). Characterization and chromosomal localization of a cDNA encoding brain amyloid of Alzheimer's disease. Science *235*, 877–880.

Gopalraj, R.K., Zhu, H., Kelly, J.F., Mendiondo, M., Pulliam, J.F., Bennett, D.A., and Estus, S. (2005). Genetic association of low density lipoprotein receptor and Alzheimer's disease. Neurobiol. Aging *26*, 1–7.

Götz, J., Probst, A., Spillantini, M.G., Schäfer, T., Jakes, R., Bürki, K., and Goedert, M. (1995). Somatodendritic localization and hyperphosphorylation of tau protein in transgenic mice expressing the longest human brain tau isoform. Embo J. *14*, 1304–1313.

Götz, J., and Ittner, L.M. (2008). Animal models of Alzheimer's disease and frontotemporal dementia. Nat. Rev. Neurosci. *9*, 532–544.

Grabowski, T.J., Cho, H.S., Vonsattel, J.P., Rebeck, G.W., and Greenberg, S.M. (2001). Novel amyloid precursor protein mutation in an Iowa family with dementia and severe cerebral amyloid angiopathy. Ann. Neurol. *49*, 697–705.

Griciuc, A., Serrano-Pozo, A., Parrado, A.R., Lesinski, A.N., Asselin, C.N., Mullin, K., Hooli, B., Choi, S.H., Hyman, B.T., and Tanzi, R.E. (2013). Alzheimer's disease risk gene CD33 inhibits microglial uptake of amyloid beta. Neuron *78*, 631–643.

Grundke-Iqbal, I., Iqbal, K., Quinlan, M., Tung, Y.C., Zaidi, M.S., and Wisniewski, H.M. (1986). Microtubule-associated protein tau. A component of Alzheimer paired helical filaments. J. Biol. Chem. *261*, 6084–6089.

Guerreiro, R.J., Gustafson, D.R., and Hardy, J. (2012). The genetic architecture of Alzheimer's disease: beyond APP, PSENs and APOE. Neurobiol. Aging *33*, 437–456.

Guerreiro, R.J., Lohmann, E., Brás, J.M., Gibbs, J.R., Rohrer, J.D., Gurunlian, N., Dursun, B., Bilgic, B., Hanagasi, H., Gurvit, H., et al. (2013). Using Exome Sequencing to Reveal Mutations in TREM2 Presenting as a Frontotemporal Dementia–like Syndrome Without Bone Involvement. JAMA Neurol *70*, 78–84.

Guo, J.L., and Lee, V.M.Y. (2011). Seeding of normal Tau by pathological Tau conformers drives pathogenesis of Alzheimer-like tangles. J. Biol. Chem. *286*, 15317–15331.

Gustafsen, C., Glerup, S., Pallesen, L.T., Olsen, D., Andersen, O.M., Nykjaer, A., Madsen, P., and Petersen, C.M. (2013). Sortilin and SorLA display distinct roles in processing and trafficking of amyloid precursor protein. J. Neurosci. *33*, 64–71.

Haass, C., Kaether, C., Thinakaran, G., and Sisodia, S. (2012). Trafficking and proteolytic processing of APP. Cold Spring Harb Perspect Med *2*, a006270–a006270.

Hardy, J.A., and Higgins, G.A. (1992). Alzheimer's disease: the amyloid cascade hypothesis. Science *256*, 184–185.

Hardy, J. (2006). Alzheimer's disease: the amyloid cascade hypothesis: an update and reappraisal. J. Alzheimers Dis. *9*, 151–153.

Harel, A., Wu, F., Mattson, M.P., Morris, C.M., and Yao, P.J. (2008). Evidence for CALM in directing VAMP2 trafficking. Traffic *9*, 417–429.

Harold, D., Abraham, R., Hollingworth, P., Sims, R., Gerrish, A., Hamshere, M.L., Pahwa, J.S., Moskvina, V., Dowzell, K., Williams, A., et al. (2009). Genome-wide association study identifies variants at CLU and PICALM associated with Alzheimer's disease. Nat. Genet. *41*, 1088–1093.

Hartlieb, E., Rötzer, V., Radeva, M., Spindler, V., and Waschke, J. (2014). Desmoglein 2 compensates for desmoglein 3 but does not control cell adhesion via regulation of p38 mitogen-activated protein kinase in keratinocytes. J. Biol. Chem. *289*, 17043–17053.

Hartmann, T., Bieger, S.C., Brühl, B., Tienari, P.J., Ida, N., Allsop, D., Roberts, G.W., Masters, C.L., Dotti, C.G., Unsicker, K., et al. (1997). Distinct sites of intracellular production for Alzheimer's disease A beta40/42 amyloid peptides. Nat. Med. *3*, 1016–1020.

He, X., Cooley, K., Chung, C.H.Y., Dashti, N., and Tang, J. (2007). Apolipoprotein receptor 2 and X11 alpha/beta mediate apolipoprotein E-induced endocytosis of amyloid-beta precursor protein and beta-secretase, leading to amyloid-beta production. J. Neurosci. *27*, 4052–4060.

Hendriks, L., van Duijn, C.M., Cras, P., Cruts, M., Van Hul, W., van Harskamp, F., Warren, A., McInnis, M.G., Antonarakis, S.E., and Martin, J.J. (1992). Presenile dementia and cerebral haemorrhage linked to a mutation at codon 692 of the beta-amyloid precursor protein gene. Nat. Genet. *1*, 218–221.

Herl, L., Thomas, A.V., Lill, C.M., Banks, M., Deng, A., Jones, P.B., Spoelgen, R., Hyman, B.T., and Berezovska, O. (2009). Mutations in amyloid precursor protein affect its interactions with presenilin/gamma-secretase. Mol. Cell. Neurosci. *41*, 166–174.

Hickman, S.E., Allison, E.K., and Khoury, El, J. (2008). Microglial dysfunction and defective beta-amyloid clearance pathways in aging Alzheimer's disease mice. J. Neurosci. *28*, 8354–8360.

Hill, J.T., Demarest, B.L., Bisgrove, B.W., Su, Y.-C., Smith, M., and Yost, H.J. (2014). Poly peak parser: Method and software for identification of unknown indels using sanger sequencing of polymerase chain reaction products. Dev. Dyn. *243*, 1632–1636.

Hinney, A., Albayrak, O., Antel, J., Volckmar, A.-L., Sims, R., Chapman, J., Harold, D., Gerrish, A., Heid, I.M., Winkler, T.W., et al. (2014). Genetic variation at the CELF1 (CUGBP, elav-like family member 1 gene) locus is genome-wide associated with Alzheimer's disease and obesity. Am. J. Med. Genet. B Neuropsychiatr. Genet. *165B*, 283–293.

Hoe, H.-S., Wessner, D., Beffert, U., Becker, A.G., Matsuoka, Y., and Rebeck, G.W. (2005). F-spondin interaction with the apolipoprotein E receptor ApoEr2 affects processing of amyloid precursor protein. Molecular and Cellular Biology *25*, 9259–9268.

Holcomb, L., Gordon, M.N., McGowan, E., Yu, X., Benkovic, S., Jantzen, P., Wright, K., Saad, I., Mueller, R., Morgan, D., et al. (1998). Accelerated Alzheimer-type phenotype in transgenic mice carrying both mutant amyloid precursor protein and presenilin 1 transgenes. Nat. Med. *4*, 97–100.

Hollingworth, P., Harold, D., Sims, R., Gerrish, A., Lambert, J.-C., Carrasquillo, M.M., Abraham, R., Hamshere, M.L., Pahwa, J.S., Moskvina, V., et al. (2011). Common variants at ABCA7, MS4A6A/MS4A4E, EPHA1, CD33 and CD2AP are associated with Alzheimer's disease. Nat. Genet. *43*, 429–435.

Holton, P., Ryten, M., Nalls, M., Trabzuni, D., Weale, M.E., Hernandez, D., Crehan, H., Gibbs, J.R., Mayeux, R., Haines, J.L., et al. (2013). Initial Assessment of the Pathogenic Mechanisms of the Recently Identified Alzheimer Risk Loci. Annals of Human Genetics *77*, 85–105.

Holtzman, D.M., Herz, J., and Bu, G. (2012). Apolipoprotein E and apolipoprotein E receptors: normal biology and roles in Alzheimer disease. Cold Spring Harb Perspect Med *2*, a006312–a006312.

Honda, M., Minami, I., Tooi, N., Morone, N., Nishioka, H., Uemura, K., Kinoshita, A., Heuser, J.E., Nakatsuji, N., and Aiba, K. (2016). The modeling of Alzheimer's disease by the overexpression of mutant Presenilin 1 in human embryonic stem cells. Biochem. Biophys. Res. Commun. *469*, 587–592.

Hong, M., Zhukareva, V., Vogelsberg-Ragaglia, V., Wszolek, Z., Reed, L., Miller, B.I., Geschwind, D.H., Bird, T.D., McKeel, D., Goate, A., et al. (1998). Mutation-specific functional impairments in distinct tau isoforms of hereditary FTDP-17. Science *282*, 1914–1917.

Hong, S., Beja-Glasser, V.F., Nfonoyim, B.M., Frouin, A., Li, S., Ramakrishnan, S., Merry, K.M., Shi, Q., Rosenthal, A., Barres, B.A., et al. (2016). Complement and microglia mediate early synapse loss in Alzheimer mouse models. Science *352*, 712–716.

Hoover, B.R., Reed, M.N., Su, J., Penrod, R.D., Kotilinek, L.A., Grant, M.K., Pitstick, R., Carlson, G.A., Lanier, L.M., Yuan, L.-L., et al. (2010). Tau mislocalization to dendritic spines mediates synaptic dysfunction independently of neurodegeneration. Neuron *68*, 1067–1081.

Horvath, P., and Barrangou, R. (2010). CRISPR/Cas, the immune system of bacteria and archaea. Science *327*, 167–170.

Hruscha, A., Krawitz, P., Rechenberg, A., Heinrich, V., Hecht, J., Haass, C., and Schmid, B. (2013). Efficient CRISPR/Cas9 genome editing with low off-target effects in zebrafish. Development *140*, 4982–4987.

Hsiao, K., Chapman, P., Nilsen, S., Eckman, C., Harigaya, Y., Younkin, S., Yang, F., and Cole, G. (1996). Correlative memory deficits, Abeta elevation, and amyloid plaques in transgenic mice. Science *274*, 99–102.

Hsu, P.D., Lander, E.S., and Zhang, F. (2014). Development and applications of CRISPR-Cas9 for genome engineering. Cell *157*, 1262–1278.

Hsu, P.D., Scott, D.A., Weinstein, J.A., Ran, F.A., Konermann, S., Agarwala, V., Li, Y., Fine, E.J., Wu, X., Shalem, O., et al. (2013). DNA targeting specificity of RNA-guided Cas9 nucleases. Nat. Biotechnol. *31*, 827–832.

Hu, Y.-B., Dammer, E.B., Ren, R.-J., and Wang, G. (2015). The endosomal-lysosomal system: from acidification and cargo sorting to neurodegeneration. Transl Neurodegener *4*, 18.

Huse, J.T., Pijak, D.S., Leslie, G.J., Lee, V.M.Y., and Doms, R.W. (2000). Maturation and Endosomal Targeting of β-Site Amyloid Precursor Protein-cleaving Enzyme. J. Biol. Chem. *275*, 33729–33737.

Hutton, M., Lendon, C.L., Rizzu, P., Baker, M., Froelich, S., Houlden, H., Pickering-Brown, S., Chakraverty, S., Isaacs, A., Grover, A., et al. (1998). Association of missense and 5'-splice-site mutations in tau with the inherited dementia FTDP-17. Nature *393*, 702–705.

Inui, M., Miyado, M., Igarashi, M., Tamano, M., Kubo, A., Yamashita, S., Asahara, H., Fukami, M., and Takada, S. (2014). Rapid generation of mouse models with defined point mutations by the CRISPR/Cas9 system. Scientific Reports *4*, 5396.

Israel, M.A., Yuan, S.H., Bardy, C., Reyna, S.M., Mu, Y., Herrera, C., Hefferan, M.P., Van Gorp, S., Nazor, K.L., Boscolo, F.S., et al. (2012). Probing sporadic and familial Alzheimer's disease using induced pluripotent stem cells. Nature *482*, 216–220.

Iwatsubo, T., Mann, D.M., Odaka, A., Suzuki, N., and Ihara, Y. (1995). Amyloid beta protein (A beta) deposition: A beta 42(43) precedes A beta 40 in Down syndrome. Ann. Neurol. *37*, 294–299.

Jarrett, J.T., Berger, E.P., and Lansbury, P.T., Jr. (2002). The carboxy terminus of the .beta. amyloid protein is critical for the seeding of amyloid formation: Implications for the pathogenesis of Alzheimer's disease. Biochemistry *32*, 4693–4697.

Jiang, F., Zhou, K., Ma, L., Gressel, S., and Doudna, J.A. (2015). STRUCTURAL BIOLOGY. A Cas9-guide RNA complex preorganized for target DNA recognition. Science *348*, 1477–1481.

Jiang, W., Bikard, D., Cox, D., Zhang, F., and Marraffini, L.A. (2013). RNA-guided editing of bacterial genomes using CRISPR-Cas systems. Nat. Biotechnol. *31*, 233–239.

Jiang, Y., Mullaney, K.A., Peterhoff, C.M., Che, S., Schmidt, S.D., Boyer-Boiteau, A., Ginsberg, S.D., Cataldo, A.M., Mathews, P.M., and Nixon, R.A. (2010). Alzheimer's-related endosome dysfunction in Down syndrome is Abeta-independent but requires APP and is reversed by BACE-1 inhibition. Proc. Natl. Acad. Sci. U.S.a. *107*, 1630–1635.

Jiao, B., Liu, X., Zhou, L., Wang, M.H., Zhou, Y., Xiao, T., Zhang, W., Sun, R., Waye, M.M.Y., Tang, B., et al. (2015). Polygenic Analysis of Late-Onset Alzheimer's Disease from Mainland China. PLoS ONE *10*, e0144898.

Jin, L.-W., Maezawa, I., Vincent, I., and Bird, T. (2004). Intracellular Accumulation of Amyloidogenic Fragments of Amyloid-β Precursor Protein in Neurons with Niemann-Pick Type C Defects Is Associated with Endosomal Abnormalities. Am. J. Pathol. *164*, 975–985.

Jin, M., Shepardson, N., Yang, T., Chen, G., Walsh, D., and Selkoe, D.J. (2011). Soluble amyloid beta-protein dimers isolated from Alzheimer cortex directly induce Tau hyperphosphorylation and neuritic degeneration. Proc. Natl. Acad. Sci. U.S.a. *108*, 5819–5824.

Jinek, M., Chylinski, K., Fonfara, I., Hauer, M., Doudna, J.A., and Charpentier, E. (2012). A programmable dual-RNA-guided DNA endonuclease in adaptive bacterial immunity. Science *337*, 816–821.

Jinek, M., East, A., Cheng, A., Lin, S., Ma, E., and Doudna, J. (2013). RNA-programmed genome editing in human cells. Elife *2*, e00471.

Jing, H., Zhu, J.-X., Wang, H.-F., Zhang, W., Zheng, Z.-J., Kong, L.-L., Tan, C.-C., Wang, Z.-X., Tan, L., and Tan, L. (2016). INPP5D rs35349669 polymorphism with late-onset Alzheimer's disease: A replication study and meta-analysis. Oncotarget *7*, 69225–69230.

Jones, S.E., and Jomary, C. (2002). Clusterin. The International Journal of Biochemistry & Cell Biology *34*, 427–431.

Jonsson, T., Atwal, J.K., Steinberg, S., Snaedal, J., Jonsson, P.V., Bjornsson, S., Stefansson, H., Sulem, P., Gudbjartsson, D., Maloney, J., et al. (2012). A mutation in APP protects against Alzheimer's disease and age-related cognitive decline. Nature *488*, 96–99.

Jonsson, T., Stefansson, H., Steinberg, S., Jonsdottir, I., Jonsson, P.V., Snaedal, J., Bjornsson, S., Huttenlocher, J., Levey, A.I., Lah, J.J., et al. (2013). Variant of TREM2 associated with the risk of Alzheimer's disease. N. Engl. J. Med. *368*, 107–116.

Kaether, C., Haass, C., and Steiner, H. (2006). Assembly, trafficking and function of gamma-secretase. Neurodegenerative Diseases *3*, 275–283.

Kahler, D.J., Ahmad, F.S., Ritz, A., Hua, H., Moroziewicz, D.N., Sproul, A.A., Dusenberry, C.R., Shang, L., Paull, D., Zimmer, M., et al. (2013). Improved methods for reprogramming human dermal fibroblasts using fluorescence activated cell sorting. PLoS ONE *8*, e59867.

Kajiho, H., Saito, K., Tsujita, K., Kontani, K., Araki, Y., Kurosu, H., and Katada, T. (2003). RIN3: a novel Rab5 GEF interacting with amphiphysin II involved in the early endocytic pathway. J. Cell. Sci. *116*, 4159–4168.

Kajiho, H., Sakurai, K., Minoda, T., Yoshikawa, M., Nakagawa, S., Fukushima, S., Kontani, K., and Katada, T. (2011). Characterization of RIN3 as a guanine nucleotide exchange factor for the Rab5 subfamily GTPase Rab31. J. Biol. Chem. *286*, 24364–24373.

Kang, D.E., Saitoh, T., Chen, X., Xia, Y., Masliah, E., Hansen, L.A., Thomas, R.G., Thal, L.J., and Katzman, R. (1997). Genetic association of the low-density lipoprotein receptor-related protein gene (LRP), an apolipoprotein E receptor, with late-onset Alzheimer's disease. Neurology *49*, 56–61.

Kang, J., Lemaire, H.G., Unterbeck, A., Salbaum, J.M., Masters, C.L., Grzeschik, K.H., Multhaup, G., Beyreuther, K., and Müller-Hill, B. (1987). The precursor of Alzheimer's disease amyloid A4 protein resembles a cell-surface receptor. Nature *325*, 733–736.

Karch, C.M., and Goate, A.M. (2015). Alzheimer's Disease Risk Genes and Mechanisms of Disease Pathogenesis. Biological Psychiatry *77*, 43–51.

Karch, C.M., Ezerskiy, L.A., Bertelsen, S., Alzheimer's Disease Genetics Consortium (ADGC), and Goate, A.M. (2016). Alzheimer's Disease Risk Polymorphisms Regulate Gene Expression in the ZCWPW1 and the CELF1 Loci. PLoS ONE *11*, e0148717.

Karch, C.M., Jeng, A.T., Nowotny, P., Cady, J., Cruchaga, C., and Goate, A.M. (2012). Expression of Novel Alzheimer's Disease Risk Genes in Control and Alzheimer's Disease Brains. PLoS ONE *7*, e50976.

Kaufman, S.K., Sanders, D.W., Thomas, T.L., Ruchinskas, A.J., Vaquer-Alicea, J., Sharma, A.M., Miller, T.M., and Diamond, M.I. (2016). Tau Prion Strains Dictate Patterns of Cell Pathology, Progression Rate, and Regional Vulnerability In Vivo. Neuron *92*, 796–812.

Kelleher, R.J., III, and Shen, J. (2017a). Presenilin-1 mutations and Alzheimer's disease. Proc. Natl. Acad. Sci. U.S.a. *114*, 629–631.

Kim, M., Suh, J., Romano, D., Truong, M.H., Mullin, K., Hooli, B., Norton, D., Tesco, G., Elliott, K., Wagner, S.L., et al. (2009). Potential late-onset Alzheimer's disease-associated mutations in the ADAM10 gene attenuate {alpha}-secretase activity. Human Molecular Genetics *18*, 3987–3996.

Kim, S., Sato, Y., Mohan, P.S., Peterhoff, C., Pensalfini, A., Rigoglioso, A., Jiang, Y., and Nixon, R.A. (2015). Evidence that the rab5 effector APPL1 mediates APP- & beta CTF-induced dysfunction of endosomes in Down syndrome and Alzheimer's disease. *21*, 707–716.

Kim, S.H., Fountoulakis, M., Cairns, N.J., and Lubec, G. (2002). Human brain nucleoside diphosphate kinase activity is decreased in Alzheimer's disease and Down syndrome. Biochem. Biophys. Res. Commun. *296*, 970–975.

Kim, W.S., Li, H., Ruberu, K., Chan, S., Elliott, D.A., Low, J.K., Cheng, D., Karl, T., and Garner, B. (2013). Deletion of Abca7 increases cerebral amyloid-β accumulation in the J20 mouse model of Alzheimer's disease. J. Neurosci. *33*, 4387–4394.

Kleinstiver, B.P., Prew, M.S., Tsai, S.Q., Topkar, V.V., Nguyen, N.T., Zheng, Z., Gonzales, A.P.W., Li, Z., Peterson, R.T., Yeh, J.-R.J., et al. (2015). Engineered CRISPR-Cas9 nucleases with altered PAM specificities. Nature *523*, 481–485.

Koch, P., Tamboli, I.Y., Mertens, J., Wunderlich, P., Ladewig, J., Stüber, K., Esselmann, H., Wiltfang, J., Brüstle, O., and Walter, J. (2012). Presenilin-1 L166P mutant human pluripotent stem cell-derived neurons exhibit partial loss of γ-

secretase activity in endogenous amyloid-β generation. Am. J. Pathol. *180*, 2404–2416.

Koffie, R.M., Meyer-Luehmann, M., Hashimoto, T., Adams, K.W., Mielke, M.L., Garcia-Alloza, M., Micheva, K.D., Smith, S.J., Kim, M.L., Lee, V.M., et al. (2009). Oligomeric amyloid beta associates with postsynaptic densities and correlates with excitatory synapse loss near senile plaques. Proc. Natl. Acad. Sci. U.S.a. *106*, 4012–4017.

Kok, E.H., Luoto, T., Haikonen, S., Goebeler, S., Haapasalo, H., and Karhunen, P.J. (2011). CLU, CR1 and PICALM genes associate with Alzheimer's-related senile plaques. Alzheimers Res Ther *3*, 12.

Komor, A.C., Kim, Y.B., Packer, M.S., Zuris, J.A., and Liu, D.R. (2016). Programmable editing of a target base in genomic DNA without double-stranded DNA cleavage. Nature *533*, 420–424.

Kondo, T., Asai, M., Tsukita, K., Kutoku, Y., Ohsawa, Y., Sunada, Y., Imamura, K., Egawa, N., Yahata, N., Okita, K., et al. (2013). Modeling Alzheimer's disease with iPSCs reveals stress phenotypes associated with intracellular Aβ and differential drug responsiveness. Cell Stem Cell *12*, 487–496.

Krasemann, S., Madore, C., Cialic, R., Baufeld, C., Calcagno, N., Fatimy, El, R., Beckers, L., O'Loughlin, E., Xu, Y., Fanek, Z., et al. (2017). The TREM2-APOE Pathway Drives the Transcriptional Phenotype of Dysfunctional Microglia in Neurodegenerative Diseases. Immunity *47*, 566–581.e569.

Kucukkilic, E., Brookes, K., Barber, I., Guetta-Baranes, T., ARUK Consortium, Morgan, K., and Hollox, E.J. (2018). Complement receptor 1 gene (CR1) intragenic duplication and risk of Alzheimer's disease. Hum. Genet. *137*, 305–314.

Kuscu, C., Arslan, S., Singh, R., Thorpe, J., and Adli, M. (2014). Genome-wide analysis reveals characteristics of off-target sites bound by the Cas9 endonuclease. Nat. Biotechnol. *32*, 677–683.

Kuwano, R., Miyashita, A., Koike, A., Jun, G., Wang, L.-S., Takahashi, S., Kim, J.-W., George-Hyslop, P.S., Mayeux, R., Haines, J., et al. (2013). SORL1 is genetically associated with late-onset Alzheimer's disease in Japanese, Koreans and Caucasians. Alzheimer's & Dementia *9*, P693–P694.

Kwart, D., Paquet, D., Teo, S., and Tessier-Lavigne, M. (2017). Precise and efficient scarless genome editing in stem cells using CORRECT. Nat Protoc *12*, 329–354.

Lai, K.-O., and Ip, N.Y. (2009). Synapse development and plasticity: roles of ephrin/Eph receptor signaling. Curr. Opin. Neurobiol. *19*, 275–283.

Lambert, J.C., Ibrahim-Verbaas, C.A., Harold, D., Naj, A.C., Sims, R., Bellenguez, C., DeStafano, A.L., Bis, J.C., Beecham, G.W., Grenier-Boley, B., et al. (2013). Meta-analysis of 74,046 individuals identifies 11 new susceptibility loci for Alzheimer's disease. Nat. Genet. *45*, 1452–1458.

Levy, E., Carman, M.D., Fernandez-Madrid, I.J., Power, M.D., Lieberburg, I., van Duinen, S.G., Bots, G.T., Luyendijk, W., and Frangione, B. (1990). Mutation of the Alzheimer's disease amyloid gene in hereditary cerebral hemorrhage, Dutch type. Science *248*, 1124–1126.

Levy-Lahad, E., Wasco, W., Poorkaj, P., Romano, D.M., Oshima, J., Pettingell, W.H., Yu, C.E., Jondro, P.D., Schmidt, S.D., and Wang, K. (1995). Candidate gene for the chromosome 1 familial Alzheimer's disease locus. Science *269*, 973–977.

Li, H., and Durbin, R. (2010). Fast and accurate long-read alignment with Burrows-Wheeler transform. Bioinformatics *26*, 589–595.

Li, J., Kanekiyo, T., Shinohara, M., Zhang, Y., LaDu, M.J., Xu, H., and Bu, G. (2012). Differential regulation of amyloid-β endocytic trafficking and lysosomal degradation by apolipoprotein E isoforms. J. Biol. Chem. *287*, 44593–44601.

Li, Y., Lu, W., Marzolo, M.P., and Bu, G. (2001). Differential Functions of Members of the Low Density Lipoprotein Receptor Family Suggested by Their Distinct Endocytosis Rates. J. Biol. Chem. *276*, 18000–18006.

Lin, S., Staahl, B.T., Alla, R.K., and Doudna, J.A. (2014). Enhanced homology-directed human genome engineering by controlled timing of CRISPR/Cas9 delivery. Elife *3*, e04766.

Liu, C.-C., Kanekiyo, T., Xu, H., and Bu, G. (2013). Apolipoprotein E and Alzheimer disease: risk, mechanisms and therapy. Nature Reviews Neurology *9*, 106–118.

Liu, Q., Zerbinatti, C.V., Zhang, J., Hoe, H.-S., Wang, B., Cole, S.L., Herz, J., Muglia, L., and Bu, G. (2007). Amyloid Precursor Protein Regulates Brain Apolipoprotein E and Cholesterol Metabolism through Lipoprotein Receptor LRP1. Neuron *56*, 66–78.

Liu, Q., Waltz, S., Woodruff, G., Ouyang, J., Israel, M.A., Herrera, C., Sarsoza, F., Tanzi, R.E., Koo, E.H., Ringman, J.M., et al. (2014a). Effect of potent γ-secretase modulator in human neurons derived from multiple presenilin 1-induced pluripotent stem cell mutant carriers. JAMA Neurol *71*, 1481–1489.

Liu, S.-L., Wang, X.-C., Tan, M.-S., Wang, H.-F., Zhang, W., Wang, Z.-X., Yu, J.-T., and Tan, L. (2016). NME8 rs2718058 polymorphism with Alzheimer's disease risk: a replication and meta-analysis. Oncotarget *7*, 36014–36020.

Liu, Y., Yu, J.-T., Wang, H.-F., Hao, X.-K., Yang, Y.-F., Jiang, T., Zhu, X.-C., Cao, L., Zhang, D.-Q., and Tan, L. (2014b). Association between NME8 Locus Polymorphism and Cognitive Decline, Cerebrospinal Fluid and Neuroimaging Biomarkers in Alzheimer's Disease. PLoS ONE *9*, e114777.

Logue, M.W., Schu, M., Vardarajan, B.N., Farrell, J., Bennett, D.A., Buxbaum, J.D., Byrd, G.S., Ertekin-Taner, N., Evans, D., Foroud, T., et al. (2014). Two rare AKAP9 variants are associated with Alzheimer's disease in African Americans. Alzheimers Dement *10*, 609–618.e611.

Lu, R.-C., Yang, W., Tan, L., Sun, F.-R., Tan, M.-S., Zhang, W., Wang, H.-F., and Tan, L. (2017). Association of HLA-DRB1 polymorphism with Alzheimer's disease: a replication and meta-analysis. Oncotarget *8*, 93219–93226.

Ma, J., Yu, J.-T., and Tan, L. (2015). MS4A Cluster in Alzheimer's Disease. Mol. Neurobiol. *51*, 1240–1248.

Mali, P., Yang, L., Esvelt, K.M., Aach, J., Guell, M., DiCarlo, J.E., Norville, J.E., and Church, G.M. (2013). RNA-guided human genome engineering via Cas9. Science *339*, 823–826.

Maloney, J.A., Bainbridge, T., Gustafson, A., Zhang, S., Kyauk, R., Steiner, P., van der Brug, M., Liu, Y., Ernst, J.A., Watts, R.J., et al. (2014). Molecular mechanisms of Alzheimer disease protection by the A673T allele of amyloid precursor protein. J. Biol. Chem. *289*, 30990–31000.

Marquer, C., Laine, J., Dauphinot, L., Hanbouch, L., Lemercier-Neuillet, C., Pierrot, N., Bossers, K., Le, M., Corlier, F., Benstaali, C., et al. (2014). Increasing membrane cholesterol of neurons in culture recapitulates Alzheimer's disease early phenotypes. Mol Neurodegener *9*, 60.

Marraffini, L.A., and Sontheimer, E.J. (2010). Self versus non-self discrimination during CRISPR RNA-directed immunity. Nature *463*, 568–571.

Martínez, A., Otal, R., Sieber, B.-A., Ibáñez, C., and Soriano, E. (2005). Disruption of ephrin-A/EphA binding alters synaptogenesis and neural connectivity in the hippocampus. Neuroscience *135*, 451–461.

Maruyama, T., Dougan, S.K., Truttmann, M.C., Bilate, A.M., Ingram, J.R., and Ploegh, H.L. (2015). Increasing the efficiency of precise genome editing with CRISPR-Cas9 by inhibition of nonhomologous end joining. Nat. Biotechnol. *33*, 538–542.

Masters, C.L., Simms, G., Weinman, N.A., Multhaup, G., McDonald, B.L., and Beyreuther, K. (1985). Amyloid plaque core protein in Alzheimer disease and Down syndrome. Proc. Natl. Acad. Sci. U.S.a. *82*, 4245–4249.

McColl, B.W., Graham, D.I., Weir, C.J., White, F., and Horsburgh, K. (2003). Endocytic Pathway Alterations in Human Hippocampus after Global Ischemia and the Influence of APOE Genotype. Am. J. Pathol. *162*, 273–281.

Millecamps, S., and Julien, J.-P. (2013). Axonal transport deficits and neurodegenerative diseases. Nat. Rev. Neurosci. *14*, 161–176.

Miller, E.C., Teravskis, P.J., Dummer, B.W., Zhao, X., Huganir, R.L., and Liao, D. (2014). Tau phosphorylation and tau mislocalization mediate soluble Aβ oligomer-induced AMPA glutamate receptor signaling deficits. Eur. J. Neurosci. *39*, 1214–1224.

Miyaoka, Y., Chan, A.H., Judge, L.M., Yoo, J., Huang, M., Nguyen, T.D., Lizarraga, P.P., So, P.-L., and Conklin, B.R. (2014). Isolation of single-base genome-edited human iPS cells without antibiotic selection. Nature Methods *11*, 291–293.

Moehlmann, T., Winkler, E., Xia, X., Edbauer, D., Murrell, J., Capell, A., Kaether, C., Zheng, H., Ghetti, B., Haass, C., et al. (2002). Presenilin-1 mutations of leucine 166 equally affect the generation of the Notch and APP intracellular domains independent of their effect on Abeta 42 production. Proc. Natl. Acad. Sci. U.S.a. *99*, 8025–8030.

Monzo, P., Gauthier, N.C., Keslair, F., Loubat, A., Field, C.M., Le Marchand-Brustel, Y., and Cormont, M. (2005). Clues to CD2-associated protein involvement in cytokinesis. Mol. Biol. Cell *16*, 2891–2902.

Moore, S., Evans, L.D.B., Andersson, T., Portelius, E., Smith, J., Dias, T.B., Saurat, N., McGlade, A., Kirwan, P., Blennow, K., et al. (2015). APP metabolism regulates tau proteostasis in human cerebral cortex neurons. CellReports *11*, 689–696.

Moreau, K., Fleming, A., Imarisio, S., Lopez Ramirez, A., Mercer, J.L., Jimenez-Sanchez, M., Bento, C.F., Puri, C., Zavodszky, E., Siddiqi, F., et al. (2014). PICALM modulates autophagy activity and tau accumulation. Nature Communications *5*, 4998.

Mullan, M., Crawford, F., Axelman, K., Houlden, H., Lilius, L., Winblad, B., and Lannfelt, L. (1992). A pathogenic mutation for probable Alzheimer's disease in the APP gene at the N-terminus of beta-amyloid. Nat. Genet. *1*, 345–347.

Mullard, A. (2017). BACE inhibitor bust in Alzheimer trial. Nat Rev Drug Discov *16*, 155–155.

Muratore, C.R., Rice, H.C., Srikanth, P., Callahan, D.G., Shin, T., Benjamin, L.N.P., Walsh, D.M., Selkoe, D.J., and Young-Pearse, T.L. (2014). The familial Alzheimer's disease APPV717I mutation alters APP processing and Tau expression in iPSC-derived neurons. Human Molecular Genetics *23*, 3523–3536.

Murrell, J.R., Hake, A.M., Quaid, K.A., Farlow, M.R., and Ghetti, B. (2000). Early-onset Alzheimer disease caused by a new mutation (V717L) in the amyloid precursor protein gene. Arch. Neurol. *57*, 885–887.

Murrell, J., Farlow, M., Ghetti, B., and Benson, M.D. (1991). A mutation in the amyloid precursor protein associated with hereditary Alzheimer's disease. Science *254*, 97–99.

Nieweg, K., Andreyeva, A., van Stegen, B., Tanriöver, G., and Gottmann, K. (2015). Alzheimer's disease-related amyloid-β induces synaptotoxicity in human iPS cell-derived neurons. Cell Death Dis *6*, e1709–e1709.

Nimmerjahn, A., Kirchhoff, F., and Helmchen, F. (2005). Resting microglial cells are highly dynamic surveillants of brain parenchyma in vivo. Science *308*, 1314–1318.

Nixon, R.A., Cataldo, A.M., and Mathews, P.M. (2000). The endosomal-lysosomal system of neurons in Alzheimer's disease pathogenesis: a review. Neurochem. Res. *25*, 1161–1172.

Nixon, R.A. (2017). Amyloid precursor protein and endosomal–lysosomal dysfunction in Alzheimer's disease: inseparable partners in a multifactorial disease. The FASEB Journal *31*, 2729–2743.

Nowakowska, B.A., Obersztyn, E., Szymańska, K., Bekiesińska-Figatowska, M., Xia, Z., Ricks, C.B., Bocian, E., Stockton, D.W., Szczałuba, K., Nawara, M., et al. (2010). Severe mental retardation, seizures, and hypotonia due to deletions of MEF2C. Am. J. Med. Genet. B Neuropsychiatr. Genet. *153B*, 1042–1051.

Nuriel, T., Angulo, S.L., Khan, U., Ashok, A., Chen, Q., Figueroa, H.Y., Emrani, S., Liu, L., Herman, M., Barrett, G., et al. (2017a). Neuronal hyperactivity due to loss of inhibitory tone in APOE4 mice lacking Alzheimer's disease-like pathology. Nature Communications *8*, 1349.

Nuriel, T., Peng, K.Y., Ashok, A., Dillman, A.A., Figueroa, H.Y., Apuzzo, J., Ambat, J., Levy, E., Cookson, M.R., Mathews, P.M., et al. (2017b). The Endosomal-Lysosomal Pathway Is Dysregulated by APOE4 Expression in Vivo. Front Neurosci *11*, 702.

O'Brien, R.J., and Wong, P.C. (2011). Amyloid Precursor Protein Processing and Alzheimer's Disease. Annual Review of Neuroscience *34*, 185–204.

O'Connell, M.R., Oakes, B.L., Sternberg, S.H., East-Seletsky, A., Kaplan, M., and Doudna, J.A. (2014). Programmable RNA recognition and cleavage by CRISPR/Cas9. Nature *516*, 263–266.

O'Geen, H., Henry, I.M., Bhakta, M.S., Meckler, J.F., and Segal, D.J. (2015). A genome-wide analysis of Cas9 binding specificity using ChIP-seq and targeted sequence capture. Nucleic Acids Res. *43*, 3389–3404.

Oddo, S., Caccamo, A., Shepherd, J.D., Murphy, M.P., Golde, T.E., Kayed, R., Metherate, R., Mattson, M.P., Akbari, Y., and LaFerla, F.M. (2003). Triple-Transgenic Model of Alzheimer's Disease with Plaques and Tangles. Neuron *39*, 409–421.

Offe, K., Dodson, S.E., Shoemaker, J.T., Fritz, J.J., Gearing, M., Levey, A.I., and Lah, J.J. (2006). The lipoprotein receptor LR11 regulates amyloid beta production and amyloid precursor protein traffic in endosomal compartments. J. Neurosci. *26*, 1596–1603.

Oksanen, M., Petersen, A.J., Naumenko, N., Puttonen, K., Lehtonen, Š., Gubert Olivé, M., Shakirzyanova, A., Leskelä, S., Sarajärvi, T., Viitanen, M., et al. (2017). PSEN1 Mutant iPSC-Derived Model Reveals Severe Astrocyte Pathology in Alzheimer's Disease. Stem Cell Reports *9*, 1885–1897.

Ortiz-Virumbrales, M., Moreno, C.L., Kruglikov, I., Marazuela, P., Sproul, A., Jacob, S., Zimmer, M., Paull, D., Zhang, B., Schadt, E.E., et al. (2017). CRISPR/Cas9-Correctable mutation-related molecular and physiological phenotypes in iPSC-derived Alzheimer's PSEN2 N141I neurons. Acta Neuropathologica Communications *5*, 101.

Paquet, D., Kwart, D., Chen, A., Sproul, A., Jacob, S., Teo, S., Olsen, K.M., Gregg, A., Noggle, S., and Tessier-Lavigne, M. (2016). Efficient introduction of specific homozygous and heterozygous mutations using CRISPR/Cas9. Nature *533*, 125–129.

Paresce, D.M., Ghosh, R.N., and Maxfield, F.R. (1996). Microglial cells internalize aggregates of the Alzheimer's disease amyloid beta-protein via a scavenger receptor. Neuron *17*, 553–565.

Park, I.-H., Zhao, R., West, J.A., Yabuuchi, A., Huo, H., Ince, T.A., Lerou, P.H., Lensch, M.W., and Daley, G.Q. (2008). Reprogramming of human somatic cells to pluripotency with defined factors. Nature *451*, 141–146.

Parton, R.G., and Dotti, C.G. (1993). Cell biology of neuronal endocytosis. J. Neurosci. Res. *36*, 1–9.

Pattanayak, V., Lin, S., Guilinger, J.P., Ma, E., Doudna, J.A., and Liu, D.R. (2013). High-throughput profiling of off-target DNA cleavage reveals RNA-programmed Cas9 nuclease specificity. Nat. Biotechnol. *31*, 839–843.

Pearson, W.R., Wood, T., Zhang, Z., and Miller, W. (1997). Comparison of DNA sequences with protein sequences. Genomics *46*, 24–36.

Pitas, R.E., Boyles, J.K., Lee, S.H., Hui, D., and Weisgraber, K.H. (1987). Lipoproteins and their receptors in the central nervous system. Characterization of the lipoproteins in cerebrospinal fluid and identification of apolipoprotein B,E(LDL) receptors in the brain. J. Biol. Chem. *262*, 14352–14360.

Platt, R.J., Chen, S., Zhou, Y., Yim, M.J., Swiech, L., Kempton, H.R., Dahlman, J.E., Parnas, O., Eisenhaure, T.M., Jovanovic, M., et al. (2014). CRISPR-Cas9 knockin mice for genome editing and cancer modeling. Cell *159*, 440–455.

Qian, S., Jiang, P., Guan, X.-M., Singh, G., Trumbauer, M.E., Yu, H., Chen, H.Y., Van der Ploeg, L.H.T., and Zheng, H. (1998). Mutant Human Presenilin 1 Protects presenilin 1 Null Mouse against Embryonic Lethality and Elevates Aβ1–42/43 Expression. Neuron *20*, 611–617.

Quon, D., Wang, Y., Catalano, R., Scardina, J.M., Murakami, K., and Cordell, B. (1991). Formation of beta-amyloid protein deposits in brains of transgenic mice. Nature *352*, 239–241.

Raja, W.K., Mungenast, A.E., Lin, Y.-T., Ko, T., Abdurrob, F., Seo, J., and Tsai, L.-H. (2016). Self-Organizing 3D Human Neural Tissue Derived from Induced Pluripotent Stem Cells Recapitulate Alzheimer's Disease Phenotypes. PLoS ONE *11*, e0161969.

Rajendran, L., Schneider, A., Schlechtingen, G., Weidlich, S., Ries, J., Braxmeier, T., Schwille, P., Schulz, J.B., Schroeder, C., Simons, M., et al. (2008). Efficient inhibition of the Alzheimer's disease beta-secretase by membrane targeting. Science *320*, 520–523.

Ran, F.A., Hsu, P.D., Lin, C.-Y., Gootenberg, J.S., Konermann, S., Trevino, A.E., Scott, D.A., Inoue, A., Matoba, S., Zhang, Y., et al. (2013). Double nicking by RNA-guided CRISPR Cas9 for enhanced genome editing specificity. Cell *154*, 1380–1389.

Rapoport, M., Dawson, H.N., Binder, L.I., Vitek, M.P., and Ferreira, A. (2002). Tau is essential to beta -amyloid-induced neurotoxicity. Proc. Natl. Acad. Sci. U.S.a. *99*, 6364–6369.

Reitz, C., Tokuhiro, S., Clark, L.N., Conrad, C., Vonsattel, J.-P., Hazrati, L.-N., Palotás, A., Lantigua, R., Medrano, M., Z Jiménez Velázquez, I., et al. (2011). SORCS1 alters amyloid precursor protein processing and variants may increase Alzheimer's disease risk. Ann. Neurol. *69*, 47–64.

Richardson, C.D., Ray, G.J., DeWitt, M.A., Curie, G.L., and Corn, J.E. (2016). Enhancing homology-directed genome editing by catalytically active and inactive CRISPR-Cas9 using asymmetric donor DNA. Nat. Biotechnol. *34*, 339–344.

Rivera-Torres, N., Strouse, B., Bialk, P., Niamat, R.A., and Kmiec, E.B. (2014). The position of DNA cleavage by TALENs and cell synchronization influences the frequency of gene editing directed by single-stranded oligonucleotides. PLoS ONE *9*, e96483.

Rivest, S. (2015). TREM2 enables amyloid β clearance by microglia. Cell Res. *25*, 535–536.

Robakis, N.K., Ramakrishna, N., Wolfe, G., and Wisniewski, H.M. (1987). Molecular cloning and characterization of a cDNA encoding the cerebrovascular and the neuritic plaque amyloid peptides. Proc. Natl. Acad. Sci. U.S.a. *84*, 4190–4194.

Roberson, E.D., Scearce-Levie, K., Palop, J.J., Yan, F., Cheng, I.H., Wu, T., Gerstein, H., Yu, G.-Q., and Mucke, L. (2007). Reducing endogenous tau ameliorates amyloid beta-induced deficits in an Alzheimer's disease mouse model. Science *316*, 750–754.

Rockenstein, E.M., McConlogue, L., Tan, H., Power, M., Masliah, E., and Mucke, L. (1995). Levels and alternative splicing of amyloid beta protein precursor (APP) transcripts in brains of APP transgenic mice and humans with Alzheimer's disease. J. Biol. Chem. *270*, 28257–28267.

Rogaev, E.I., Sherrington, R., Rogaeva, E.A., Levesque, G., Ikeda, M., Liang, Y., Chi, H., Lin, C., Holman, K., and Tsuda, T. (1995). Familial Alzheimer“s disease in kindreds with missense mutations in a gene on chromosome 1 related to the Alzheimer”s disease type 3 gene. Nature *376*, 775–778.

Rogaeva, E., Meng, Y., Lee, J.H., Mayeux, R., Farrer, L.A., and George-Hyslop, P.S. (2009). The Sortilin-Related Receptor SORL1 is Functionally and Genetically Associated with Alzheimer's Disease. In Intracellular Traffic and Neurodegenerative Disorders, (Berlin, Heidelberg: Springer Berlin Heidelberg), pp. 157–165.

Roher, A., Wolfe, D., Palutke, M., and KuKuruga, D. (1986). Purification, ultrastructure, and chemical analysis of Alzheimer disease amyloid plaque core protein. Proc. Natl. Acad. Sci. U.S.a. *83*, 2662–2666.

Rosenberg, M.E., and Silkensen, J. (1995). Clusterin: Physiologic and pathophysiologic considerations. The International Journal of Biochemistry & Cell Biology *27*, 633–645.

Roses M D, A.D. (1996). APOLIPOPROTEIN E ALLELES AS RISK FACTORS IN ALZHEIMER'S DISEASE. Annual Review of Medicine *47*, 387–400.

Rovelet-Lecrux, A., Hannequin, D., Raux, G., Le Meur, N., Laquerrière, A., Vital, A., Dumanchin, C., Feuillette, S., Brice, A., Vercelletto, M., et al. (2006). APP locus duplication causes autosomal dominant early-onset Alzheimer disease with cerebral amyloid angiopathy. Nat. Genet. *38*, 24–26.

Ryman, D.C., Acosta-Baena, N., Aisen, P.S., Bird, T., Danek, A., Fox, N.C., Goate, A., Frommelt, P., Ghetti, B., Langbaum, J.B.S., et al. (2014). Symptom onset in autosomal dominant Alzheimer disease: a systematic review and meta-analysis. Neurology *83*, 253–260.

Sagare, A., Deane, R., Bell, R.D., Johnson, B., Hamm, K., Pendu, R., Marky, A., Lenting, P.J., Wu, Z., Zarcone, T., et al. (2007). Clearance of amyloid-beta by circulating lipoprotein receptors. Nat. Med. *13*, 1029–1031.

Saito, T., Matsuba, Y., Mihira, N., Takano, J., Nilsson, P., Itohara, S., Iwata, N., and Saido, T.C. (2014). Single App knock-in mouse models of Alzheimer's disease. Nat. Neurosci. *17*, 661–663.

Sakamoto, A., Sugamoto, Y., Tokunaga, Y., Yoshimuta, T., Hayashi, K., Konno, T., Kawashiri, M.A., Takeda, Y., and Yamagishi, M. (2011). Expression profiling of the ephrin (EFN) and Eph receptor (EPH) family of genes in atherosclerosis-related human cells. J. Int. Med. Res. *39*, 522–527.

Sanders, D.W., Kaufman, S.K., DeVos, S.L., Sharma, A.M., Mirbaha, H., Li, A., Barker, S.J., Foley, A.C., Thorpe, J.R., Serpell, L.C., et al. (2014). Distinct tau prion strains propagate in cells and mice and define different tauopathies. Neuron *82*, 1271–1288.

Sannerud, R., Esselens, C., Ejsmont, P., Mattera, R., Rochin, L., Tharkeshwar, A.K., De Baets, G., De Wever, V., Habets, R., Baert, V., et al. (2016). Restricted Location of PSEN2/γ-Secretase Determines Substrate Specificity and Generates an Intracellular Aβ Pool. Cell *166*, 193–208.

Saraceno, C., Musardo, S., Marcello, E., Pelucchi, S., and Luca, M.D. (2013). Modeling Alzheimer's disease: from past to future. Frontiers in Pharmacology *4*.

Saunders, A.M. (2000). Apolipoprotein E and Alzheimer disease: an update on genetic and functional analyses. J. Neuropathol. Exp. Neurol. *59*, 751–758.

Saunders, A.M., Strittmatter, W.J., Schmechel, D., George-Hyslop, P.H., Pericak-Vance, M.A., Joo, S.H., Rosi, B.L., Gusella, J.F., Crapper-MacLachlan, D.R., and Alberts, M.J. (1993). Association of apolipoprotein E allele epsilon 4 with late-onset familial and sporadic Alzheimer's disease. Neurology *43*, 1467–1472.

Schellenberg, G.D., Bird, T.D., Wijsman, E.M., Orr, H.T., Anderson, L., Nemens, E., White, J.A., Bonnycastle, L., Weber, J.L., and Alonso, M.E. (1992). Genetic linkage

evidence for a familial Alzheimer's disease locus on chromosome 14. Science *258*, 668–671.

Scheltens, P., Blennow, K., Breteler, M.M.B., de Strooper, B., Frisoni, G.M., Salloway, S., and Van der Flier, W.M. (2016). Alzheimer's disease. The Lancet *388*, 505–517.

Scheuner, D., Eckman, C., Jensen, M., Song, X., Citron, M., Suzuki, N., Bird, T.D., Hardy, J., Hutton, M., Kukull, W., et al. (1996a). Secreted amyloid β–protein similar to that in the senile plaques of Alzheimer"s disease is increased in vivo by the presenilin 1 and 2 and APP mutations linked to familial Alzheimer"s disease. Nat. Med. *2*, 864–870.

Scheuner, D., Eckman, C., Jensen, M., Song, X., Citron, M., Suzuki, N., Bird, T.D., Hardy, J., Hutton, M., Kukull, W., et al. (1996b). Secreted amyloid beta-protein similar to that in the senile plaques of Alzheimer"s disease is increased in vivo by the presenilin 1 and 2 and APP mutations linked to familial Alzheimer"s disease. Nat. Med. *2*, 864–870.

Schjeide, B.-M.M., Schnack, C., Lambert, J.-C., Lill, C.M., Kirchheiner, J., Tumani, H., Otto, M., Tanzi, R.E., Lehrach, H., Amouyel, P., et al. (2011). The Role of Clusterin, Complement Receptor 1, and Phosphatidylinositol Binding Clathrin Assembly Protein in Alzheimer Disease Risk and Cerebrospinal Fluid Biomarker Levels. Archives of General Psychiatry *68*, 207.

Selkoe, D.J. (2006). Toward a Comprehensive Theory for Alzheimer"s Disease. Hypothesis: Alzheimer"s Disease Is Caused by the Cerebral Accumulation and Cytotoxicity of Amyloid β-Protein. Annals of the New York Academy of Sciences *924*, 17–25.

Selkoe, D.J., and Hardy, J. (2016). The amyloid hypothesis of Alzheimer's disease at 25 years. EMBO Mol Med *8*, 595–608.

Semenova, E., Jore, M.M., Datsenko, K.A., Semenova, A., Westra, E.R., Wanner, B., van der Oost, J., Brouns, S.J.J., and Severinov, K. (2011). Interference by clustered regularly interspaced short palindromic repeat (CRISPR) RNA is governed by a seed sequence. Proc. Natl. Acad. Sci. U.S.a. *108*, 10098–10103.

Shea, Y.-F., Chu, L.-W., Chan, A.O.-K., Ha, J., Li, Y., and Song, Y.-Q. (2016). A systematic review of familial Alzheimer's disease: Differences in presentation of clinical features among three mutated genes and potential ethnic differences. J. Formos. Med. Assoc. *115*, 67–75.

Shen, Y., Li, R., McGeer, E.G., and McGeer, P.L. (1997). Neuronal expression of mRNAs for complement proteins of the classical pathway in Alzheimer brain. Brain Res. *769*, 391–395.

Sherrington, R., Rogaev, E.I., Liang, Y., Rogaeva, E.A., Levesque, G., Ikeda, M., Chi, H., Lin, C., Li, G., Holman, K., et al. (1995). Cloning of a gene bearing missense mutations in early-onset familial Alzheimer's disease. Nature *375*, 754–760.

Shi, Y., Yamada, K., Liddelow, S.A., Smith, S.T., Zhao, L., Luo, W., Tsai, R.M., Spina, S., Grinberg, L.T., Rojas, J.C., et al. (2017). ApoE4 markedly exacerbates tau-mediated neurodegeneration in a mouse model of tauopathy. Nature *549*, 523–527.

Shi, Y., Kirwan, P., Smith, J., MacLean, G., Orkin, S.H., and Livesey, F.J. (2012). A human stem cell model of early Alzheimer's disease pathology in Down syndrome. Sci Transl Med *4*, 124ra29–124ra29.

Shinohara, M., Tachibana, M., Kanekiyo, T., and Bu, G. (2017). Role of LRP1 in the pathogenesis of Alzheimer’s disease: evidence from clinical and preclinical studies. Journal of Lipid Research *58*, 1267–1281.

Shulman, J.M., Chen, K., Keenan, B.T., Chibnik, L.B., Fleisher, A., Thiyyagura, P., Roontiva, A., McCabe, C., Patsopoulos, N.A., Corneveaux, J.J., et al. (2013). Genetic susceptibility for Alzheimer disease neuritic plaque pathology. JAMA Neurol *70*, 1150–1157.

Siddiqui, S.S., Springer, S.A., Verhagen, A., Sundaramurthy, V., Alisson-Silva, F., Jiang, W., Ghosh, P., and Varki, A. (2017). The Alzheimer's disease–protective CD33 splice variant mediates adaptive loss of function via diversion to an intracellular pool. J. Biol. Chem. *292*, 15312–15320.

Sims, R., van der Lee, S.J., Naj, A.C., Bellenguez, C., Badarinarayan, N., Jakobsdottir, J., Kunkle, B.W., Boland, A., Raybould, R., Bis, J.C., et al. (2017). Rare coding variants in PLCG2, ABI3, and TREM2 implicate microglial-mediated innate immunity in Alzheimer's disease. Nat. Genet. *49*, 1373–1384.

Singh, V.K., Kalsan, M., Kumar, N., Saini, A., and Chandra, R. (2015). Induced pluripotent stem cells: applications in regenerative medicine, disease modeling, and drug discovery. Front Cell Dev Biol *3*, 2.

Sisodia, S.S. (1992). Beta-amyloid precursor protein cleavage by a membrane-bound protease. Proc. Natl. Acad. Sci. U.S.a. *89*, 6075–6079.

Small, S.A., and Petsko, G.A. (2015). Retromer in Alzheimer disease, Parkinson disease and other neurological disorders. Nat. Rev. Neurosci. *16*, 126–132.

Small, S.A., Simoes-Spassov, S., Mayeux, R., and Petsko, G.A. (2017). Endosomal Traffic Jams Represent a Pathogenic Hub and Therapeutic Target in Alzheimer’s Disease. Trends in Neurosciences *40*, 592–602.

Sondag, C.M., Dhawan, G., and Combs, C.K. (2009). Beta amyloid oligomers and fibrils stimulate differential activation of primary microglia. J Neuroinflammation *6*, 1.

Spires-Jones, T.L., and Hyman, B.T. (2014). The intersection of amyloid beta and tau at synapses in Alzheimer's disease. Neuron *82*, 756–771.

Sproul, A.A., Jacob, S., Pre, D., Kim, S.H., Nestor, M.W., Navarro-Sobrino, M., Santa-Maria, I., Zimmer, M., Aubry, S., Steele, J.W., et al. (2014). Characterization and molecular profiling of PSEN1 familial Alzheimer's disease iPSC-derived neural progenitors. PLoS ONE *9*, e84547.

St George-Hyslop, P., Haines, J., Rogaev, E., Mortilla, M., Vaula, G., Pericak-Vance, M., Foncin, J.F., Montesi, M., Bruni, A., Sorbi, S., et al. (1992). Genetic evidence for a novel familial Alzheimer's disease locus on chromosome 14. Nat. Genet. *2*, 330–334.

St George-Hyslop, P., Tanzi, R., Polinsky, R., Haines, J., Nee, L., Watkins, P., Myers, R., Feldman, R., Pollen, D., Drachman, D., et al. (1987). The genetic defect causing familial Alzheimer's disease maps on chromosome 21. Science *235*, 885–890.

Stenmark, H. (2009). Rab GTPases as coordinators of vesicle traffic. Nature Reviews Molecular Cell Biology *10*, 513–525.

Strittmatter, W.J., Saunders, A.M., Schmechel, D., Pericak-Vance, M., Enghild, J., Salvesen, G.S., and Roses, A.D. (1993). Apolipoprotein E: high-avidity binding to beta-amyloid and increased frequency of type 4 allele in late-onset familial Alzheimer disease. Proc. Natl. Acad. Sci. U.S.a. *90*, 1977–1981.

Suh, J., Choi, S.H., Romano, D.M., Gannon, M.A., Lesinski, A.N., Kim, D.Y., and Tanzi, R.E. (2013). ADAM10 missense mutations potentiate β-amyloid accumulation by impairing prodomain chaperone function. Neuron *80*, 385–401.

Sullivan, C.P., Jay, A.G., Stack, E.C., Pakaluk, M., Wadlinger, E., Fine, R.E., Wells, J.M., and Morin, P.J. (2011). Retromer disruption promotes amyloidogenic APP processing. Neurobiol. Dis. *43*, 338–345.

Sun, X., He, G., and Song, W. (2006). BACE2, as a novel APP θ-secretase, is not responsible for the pathogenesis of Alzheimer’s disease in Down syndrome. The FASEB Journal *20*, 1369–1376.

Sun, X., Wang, Y., Qing, H., Christensen, M.A., Liu, Y., Zhou, W., Tong, Y., Xiao, C., Huang, Y., Zhang, S., et al. (2005). Distinct transcriptional regulation and function of the human BACE2and BACE1genes. The FASEB Journal *19*, 739–749.

Szaruga, M., Munteanu, B., Lismont, S., Veugelen, S., Horré, K., Mercken, M., Saido, T.C., Ryan, N.S., De Vos, T., Savvides, S.N., et al. (2017). Alzheimer's-Causing Mutations Shift Aβ Length by Destabilizing γ-Secretase-Aβn Interactions. Cell *170*, 443–456.e14.

T Cuenco, K., Lunetta, K.L., Baldwin, C.T., McKee, A.C., Guo, J., Cupples, L.A., Green, R.C., St George-Hyslop, P.H., Chui, H., DeCarli, C., et al. (2008). Association of distinct variants in SORL1 with cerebrovascular and neurodegenerative changes related to Alzheimer disease. Arch. Neurol. *65*, 1640–1648.

Taghian, D.G., and Nickoloff, J.A. (1997). Chromosomal double-strand breaks induce gene conversion at high frequency in mammalian cells. Molecular and Cellular Biology *17*, 6386–6393.

Takahashi, K., and Yamanaka, S. (2006). Induction of pluripotent stem cells from mouse embryonic and adult fibroblast cultures by defined factors. Cell *126*, 663–676.

Takami, M., Nagashima, Y., Sano, Y., Ishihara, S., Morishima-Kawashima, M., Funamoto, S., and Ihara, Y. (2009). gamma-Secretase: successive tripeptide and tetrapeptide release from the transmembrane domain of beta-carboxyl terminal fragment. J. Neurosci. *29*, 13042–13052.

Tamaoka, A., Odaka, A., Ishibashi, Y., Usami, M., Sahara, N., Suzuki, N., Nukina, N., Mizusawa, H., Shoji, S., and Kanazawa, I. (1994). APP717 missense mutation affects the ratio of amyloid beta protein species (A beta 1-42/43 and a beta 1-40) in familial Alzheimer's disease brain. J. Biol. Chem. *269*, 32721–32724.

Tanzi, R.E., Gusella, J.F., Watkins, P.C., Bruns, G.A., St George-Hyslop, P., Van Keuren, M.L., Patterson, D., Pagan, S., Kurnit, D.M., and Neve, R.L. (1987). Amyloid beta protein gene: cDNA, mRNA distribution, and genetic linkage near the Alzheimer locus. Science *235*, 880–884.

Tarassishin, L., Yin, Y.I., Bassit, B., and Li, Y.-M. (2004). Processing of Notch and amyloid precursor protein by gamma-secretase is spatially distinct. Proc. Natl. Acad. Sci. U.S.a. *101*, 17050–17055.

The Alzheimer Disease Neuroimaging Initiative, Bradshaw, E.M., Chibnik, L.B., Keenan, B.T., Ottoboni, L., Raj, T., Tang, A., Rosenkrantz, L.L., Imboywa, S., Lee, M., et al. (2013). CD33 Alzheimer's disease locus: altered monocyte function and amyloid biology. Nat. Neurosci. *16*, 848–850.

Thinakaran, G., and Koo, E.H. (2008). Amyloid precursor protein trafficking, processing, and function. J. Biol. Chem. *283*, 29615–29619.

Thomas, R.S., Henson, A., Gerrish, A., Jones, L., Williams, J., and Kidd, E.J. (2016). Decreasing the expression of PICALM reduces endocytosis and the activity of β-secretase: implications for Alzheimer's disease. BMC Neuroscience *17*, 1094.

Tian, Y., Chang, J.C., Fan, E.Y., Flajolet, M., and Greengard, P. (2013). Adaptor complex AP2/PICALM, through interaction with LC3, targets Alzheimer's APP-CTF for terminal degradation via autophagy. Proc. Natl. Acad. Sci. U.S.a. *110*, 17071–17076.

Timmers, W.F., Tagliavini, F., Haan, J., and Frangione, B. (1990). Parenchymal preamyloid and amyloid deposits in the brains of patients with hereditary cerebral hemorrhage with amyloidosis--Dutch type. Neurosci. Lett. *118*, 223–226.

Tiscornia, G., Vivas, E.L., and Izpisúa Belmonte, J.C. (2011). Diseases in a dish: modeling human genetic disorders using induced pluripotent cells. Nat. Med. *17*, 1570–1576.

Treusch, S., Hamamichi, S., Goodman, J.L., Matlack, K.E.S., Chung, C.Y., Baru, V., Shulman, J.M., Parrado, A., Bevis, B.J., Valastyan, J.S., et al. (2011). Functional links between Aβ toxicity, endocytic trafficking, and Alzheimer's disease risk factors in yeast. Science *334*, 1241–1245.

Trinchese, F., Liu, S., Ninan, I., Puzzo, D., Jacob, J.P., and Arancio, O. (2004). Cell Cultures From Animal Models of Alzheimer's Disease as a Tool for Faster Screening and Testing of Drug Efficacy. Journal of Molecular Neuroscience *24*, 015–022.

Tripathi, S., Pohl, M.O., Zhou, Y., Rodriguez-Frandsen, A., Wang, G., Stein, D.A., Moulton, H.M., DeJesus, P., Che, J., Mulder, L.C.F., et al. (2015). Meta- and Orthogonal Integration of Influenza "OMICs" Data Defines a Role for UBR4 in Virus Budding. Cell Host Microbe *18*, 723–735.

Ubelmann, F., Burrinha, T., Salavessa, L., Gomes, R., Ferreira, C., Moreno, N., and Guimas Almeida, C. (2017). Bin1 and CD2AP polarise the endocytic generation of beta-amyloid. EMBO Rep. *18*, 102–122.

Ulrich, J.D., Ulland, T.K., Colonna, M., and Holtzman, D.M. (2017). Elucidating the Role of TREM2 in Alzheimer's Disease. Neuron *94*, 237–248.

Van Broeckhoven, C., Backhovens, H., Cruts, M., De Winter, G., Bruyland, M., Cras, P., and Martin, J.J. (1992). Mapping of a gene predisposing to early-onset Alzheimer's disease to chromosome 14q24.3. Nat. Genet. *2*, 335–339.

Van Broeckhoven, C., Haan, J., Bakker, E., Hardy, J.A., Van Hul, W., Wehnert, A., Vegter-Van der Vlis, M., and Roos, R.A. (1990). Amyloid beta protein precursor gene and hereditary cerebral hemorrhage with amyloidosis (Dutch). Science *248*, 1120–1122.

Van Der Kant, R., and Goldstein, L.S.B. (2015). Cellular Functions of the Amyloid Precursor Protein from Development to Dementia. Developmental Cell *32*, 502–515.

Van Nostrand, W.E., Melchor, J.P., Cho, H.S., Greenberg, S.M., and Rebeck, G.W. (2001). Pathogenic Effects of D23N Iowa Mutant Amyloid β-Protein. J. Biol. Chem. *276*, 32860–32866.

Van Nostrand, W.E., Melchor, J.P., Romanov, G., Zeigler, K., and Davis, J. (2002). Pathogenic effects of cerebral amyloid angiopathy mutations in the amyloid beta-protein precursor. Annals of the New York Academy of Sciences *977*, 258–265.

Vardarajan, B.N., Zhang, Y., Lee, J.H., Cheng, R., Bohm, C., Ghani, M., Reitz, C., Reyes-Dumeyer, D., Shen, Y., Rogaeva, E., et al. (2015). Coding mutations in SORL1 and Alzheimer disease. Ann. Neurol. *77*, 215–227.

Vardarajan, B.N., Zhang, Y., Lee, J.H., Cheng, R., Bohm, C., Reitz, C., Shen, Y., Rogaeva, E., George-Hyslop, P.S., and Mayeux, R. (2014). CODING MUTATIONS IN SORL1 IMPLICATE ALTERNATE APP PROCESSING MECHANISMS IN ALZHEIMER'S DISEASE. Alzheimer's & Dementia *10*, P134.

Vassar, R. (1999). Beta-Secretase Cleavage of Alzheimer's Amyloid Precursor Protein by the Transmembrane Aspartic Protease BACE. Science *286*, 735–741.

Vassar, R. (2013). ADAM10 prodomain mutations cause late-onset Alzheimer's disease: not just the latest FAD. Neuron *80*, 250–253.

Venkatesh, D., Mruk, D., Herter, J.M., Cullere, X., Chojnacka, K., Cheng, C.Y., and Mayadas, T.N. (2016). AKAP9, a Regulator of Microtubule Dynamics, Contributes to Blood-Testis Barrier Function. Am. J. Pathol. *186*, 270–284.

Verghese, P.B., Castellano, J.M., and Holtzman, D.M. (2011). Apolipoprotein E in Alzheimer's disease and other neurological disorders. The Lancet Neurology *10*, 241–252.

Verghese, P.B., Castellano, J.M., Garai, K., Wang, Y., Jiang, H., Shah, A., Bu, G., Frieden, C., and Holtzman, D.M. (2013). ApoE influences amyloid-β (Aβ) clearance despite minimal apoE/Aβ association in physiological conditions. Proc. Natl. Acad. Sci. U.S.a. *110*, E1807–E1816.

Veugelen, S., Saito, T., Saido, T.C., Chávez-Gutiérrez, L., and De Strooper, B. (2016). Familial Alzheimer's Disease Mutations in Presenilin Generate Amyloidogenic Aβ Peptide Seeds. Neuron *90*, 410–416.

Walker, E.S., Martinez, M., Brunkan, A.L., and Goate, A. (2005). Presenilin 2 familial Alzheimer's disease mutations result in partial loss of function and dramatic changes in Abeta 42/40 ratios. Journal of Neurochemistry *92*, 294–301.

Wang, H., Yang, H., Shivalila, C.S., Dawlaty, M.M., Cheng, A.W., Zhang, F., and Jaenisch, R. (2013). One-step generation of mice carrying mutations in multiple genes by CRISPR/Cas-mediated genome engineering. Cell *153*, 910–918.

Wang, H.-F., Tan, L., Hao, X.-K., Jiang, T., Tan, M.-S., Liu, Y., Zhang, D.-Q., Yu, J.-T., Alzheimer's Disease Neuroimaging Initiative (2015). Effect of EPHA1 genetic variation on cerebrospinal fluid and neuroimaging biomarkers in healthy, mild cognitive impairment and Alzheimer's disease cohorts. J. Alzheimers Dis. *44*, 115–123.

Wang, X., Huang, T., Bu, G., and Xu, H. (2014). Dysregulation of protein trafficking in neurodegeneration. Mol Neurodegener *9*, 31.

Wang, X., Zhou, X., Li, G., Zhang, Y., Wu, Y., and Song, W. (2017a). Modifications and Trafficking of APP in the Pathogenesis of Alzheimer's Disease. Frontiers in Molecular Neuroscience *10*, 329.

Wang, Y., Liu, S., Wang, J., Zhang, J., Hua, Y., Li, H., Tan, H., Kuai, B., Wang, B., and Sheng, S. (2017b). Association between LRP1 C766T polymorphism and Alzheimer's disease susceptibility: a meta-analysis. Scientific Reports *7*, 1082.

Weingarten, M.D., Lockwood, A.H., Hwo, S.Y., and Kirschner, M.W. (1975). A protein factor essential for microtubule assembly. Proc. Natl. Acad. Sci. U.S.a. *72*, 1858–1862.

Wetzel-Smith, M.K., Hunkapiller, J., Bhangale, T.R., Srinivasan, K., Maloney, J.A., Atwal, J.K., Sa, S.M., Yaylaoglu, M.B., Foreman, O., Ortmann, W., et al. (2014). A rare mutation in UNC5C predisposes to late-onset Alzheimer's disease and increases neuronal cell death. Nat. Med. *20*, 1452–1457.

Wilson, J.G., Andriopoulos, N.A., and Fearon, D.T. (1987). CR1 and the cell membrane proteins that bind C3 and C4. A basic and clinical review. Immunol. Res. *6*, 192–209.

Wischik, C.M., Novak, M., Thøgersen, H.C., Edwards, P.C., Runswick, M.J., Jakes, R., Walker, J.E., Milstein, C., Roth, M., and Klug, A. (1988). Isolation of a fragment of tau derived from the core of the paired helical filament of Alzheimer disease. Proc. Natl. Acad. Sci. U.S.a. *85*, 4506–4510.

Wisniewski, T., Ghiso, J., and Frangione, B. (1991). Peptides homologous to the amyloid protein of Alzheimer's disease containing a glutamine for glutamic acid substitution have accelerated amyloid fibril formation. Biochem. Biophys. Res. Commun. *180*, 1528.

Woodruff, G., Reyna, S.M., Dunlap, M., Van Der Kant, R., Callender, J.A., Young, J.E., Roberts, E.A., and Goldstein, L.S.B. (2016). Defective Transcytosis of APP and

Lipoproteins in Human iPSC-Derived Neurons with Familial Alzheimer's Disease Mutations. CellReports *17*, 759–773.

Woodruff, G., Young, J.E., Martinez, F.J., Buen, F., Gore, A., Kinaga, J., Li, Z., Yuan, S.H., Zhang, K., and Goldstein, L.S.B. (2013). The presenilin-1 ΔE9 mutation results in reduced γ-secretase activity, but not total loss of PS1 function, in isogenic human stem cells. CellReports *5*, 974–985.

Wu, J.W., Hussaini, S.A., Bastille, I.M., Rodriguez, G.A., Mrejeru, A., Rilett, K., Sanders, D.W., Cook, C., Fu, H., Boonen, R.A.C.M., et al. (2016). Neuronal activity enhances tau propagation and tau pathology in vivo. Nat. Neurosci. *19*, 1085–1092.

Wu, X., Scott, D.A., Kriz, A.J., Chiu, A.C., Hsu, P.D., Dadon, D.B., Cheng, A.W., Trevino, A.E., Konermann, S., Chen, S., et al. (2014). Genome-wide binding of the CRISPR endonuclease Cas9 in mammalian cells. Nat. Biotechnol. *32*, 670–676.

Wyss-Coray, T., Loike, J.D., Brionne, T.C., Lu, E., Anankov, R., Yan, F., Silverstein, S.C., and Husemann, J. (2003). Adult mouse astrocytes degrade amyloid-beta in vitro and in situ. Nat. Med. *9*, 453–457.

Xia, D., Watanabe, H., Wu, B., Lee, S.H., Li, Y., Tsvetkov, E., Bolshakov, V.Y., Shen, J., and Kelleher, R.J., III (2015). Presenilin-1 Knockin Mice Reveal Loss-of-Function Mechanism for Familial Alzheimer's Disease. Neuron *85*, 967–981.

Xiao, Q., Gil, S.-C., Yan, P., Wang, Y., Han, S., Gonzales, E., Perez, R., Cirrito, J.R., and Lee, J.-M. (2012). Role of phosphatidylinositol clathrin assembly lymphoid-myeloid leukemia (PICALM) in intracellular amyloid precursor protein (APP) processing and amyloid plaque pathogenesis. J. Biol. Chem. *287*, 21279–21289.

Xie, Y.Z., and Zhang, R.X. (2015). Neurodegenerative diseases in a dish: the promise of iPSC technology in disease modeling and therapeutic discovery. Neurol. Sci. *36*, 21–27.

Xu, H., Sweeney, D., Wang, R., Thinakaran, G., Lo, A.C., Sisodia, S.S., Greengard, P., and Gandy, S. (1997). Generation of Alzheimer beta-amyloid protein in the trans-Golgi network in the apparent absence of vesicle formation. Proc. Natl. Acad. Sci. U.S.a. *94*, 3748–3752.

Xu, W., Fang, F., Ding, J., and Wu, C. (2018). Dysregulation of Rab5-mediated endocytic pathways in Alzheimer's disease. Traffic *19*, 253–262.

Xu, W., Weissmiller, A.M., White, J.A., Fang, F., Wang, X., Wu, Y., Pearn, M.L., Zhao, X., Sawa, M., Chen, S., et al. (2016). Amyloid precursor protein-mediated endocytic pathway disruption induces axonal dysfunction and neurodegeneration. J. Clin. Invest. *126*, 1815–1833.

Xu, W., Xu, J., Wang, Y., Tang, H., Deng, Y., Ren, R., Wang, G., Niu, W., Ma, J., Wu, Y., et al. (2013). The Genetic Variation of SORCS1 Is Associated with Late-Onset Alzheimer's Disease in Chinese Han Population. PLoS ONE *8*, e63621.

Yagi, T., Ito, D., Okada, Y., Akamatsu, W., Nihei, Y., Yoshizaki, T., Yamanaka, S., Okano, H., and Suzuki, N. (2011). Modeling familial Alzheimer's disease with induced pluripotent stem cells. Human Molecular Genetics *20*, 4530–4539.

Yang, J., Li, S., He, X.-B., Cheng, C., and Le, W. (2016). Induced pluripotent stem cells in Alzheimer's disease: applications for disease modeling and cell-replacement therapy. Mol Neurodegener *11*, 239.

Yang, L., Guell, M., Byrne, S., Yang, J.L., De Los Angeles, A., Mali, P., Aach, J., Kim-Kiselak, C., Briggs, A.W., Rios, X., et al. (2013). Optimization of scarless human stem cell genome editing. Nucleic Acids Res. *41*, 9049–9061.

Ye, S., Huang, Y., Mullendorff, K., Dong, L., Giedt, G., Meng, E.C., Cohen, F.E., Kuntz, I.D., Weisgraber, K.H., and Mahley, R.W. (2005). Apolipoprotein (apo) E4 enhances amyloid peptide production in cultured neuronal cells: ApoE structure as a potential therapeutic target. Proceedings of the National Academy of Sciences *102*, 18700–18705.

Yoshino, Y., Yamazaki, K., Ozaki, Y., Sao, T., Yoshida, T., Mori, T., Mori, Y., Ochi, S., Iga, J.-I., and Ueno, S.-I. (2017). INPP5D mRNA Expression and Cognitive Decline in Japanese Alzheimer's Disease Subjects. J. Alzheimers Dis. *58*, 687–694.

Young, J.E., Boulanger-Weill, J., Williams, D.A., Woodruff, G., Buen, F., Revilla, A.C., Herrera, C., Israel, M.A., Yuan, S.H., Edland, S.D., et al. (2015). Elucidating molecular phenotypes caused by the SORL1 Alzheimer's disease genetic risk factor using human induced pluripotent stem cells. Cell Stem Cell *16*, 373–385.

Yu, C., Liu, Y., Ma, T., Liu, K., Xu, S., Zhang, Y., Liu, H., La Russa, M., Xie, M., Ding, S., et al. (2015). Small molecules enhance CRISPR genome editing in pluripotent stem cells. Cell Stem Cell *16*, 142–147.

Yuan, P., Condello, C., Keene, C.D., Wang, Y., Bird, T.D., Paul, S.M., Luo, W., Colonna, M., Baddeley, D., and Grutzendler, J. (2016). TREM2 Haplodeficiency in Mice and Humans Impairs the Microglia Barrier Function Leading to Decreased Amyloid Compaction and Severe Axonal Dystrophy. Neuron *92*, 252–264.

Yusa, K. (2013). Seamless genome editing in human pluripotent stem cells using custom endonuclease-based gene targeting and the piggyBac transposon. Nat Protoc *8*, 2061–2078.

Zandl-Lang, M., Fanaee-Danesh, E., Sun, Y., Albrecher, N.M., Gali, C.C., Čančar, I., Kober, A., Tam-Amersdorfer, C., Stracke, A., Storck, S.M., et al. (2018). Regulatory

effects of simvastatin and apoJ on APP processing and amyloid-β clearance in blood-brain barrier endothelial cells. Biochim. Biophys. Acta *1863*, 40–60.

Zetsche, B., Gootenberg, J.S., Abudayyeh, O.O., Slaymaker, I.M., Makarova, K.S., Essletzbichler, P., Volz, S.E., Joung, J., van der Oost, J., Regev, A., et al. (2015). Cpf1 is a single RNA-guided endonuclease of a class 2 CRISPR-Cas system. Cell *163*, 759–771.

Zhang, J., Kobert, K., Flouri, T., and Stamatakis, A. (2014). PEAR: a fast and accurate Illumina Paired-End reAd mergeR. Bioinformatics *30*, 614–620.

Zhao, N., Liu, C.-C., Van Ingelgom, A.J., Martens, Y.A., Linares, C., Knight, J.A., Painter, M.M., Sullivan, P.M., and Bu, G. (2017). Apolipoprotein E4 Impairs Neuronal Insulin Signaling by Trapping Insulin Receptor in the Endosomes. Neuron *96*, 115–129.e115.

Zhu, R., Liu, X., and He, Z. (2017). Association of rs610932 and rs670139 Polymorphisms in the MS4A Gene Cluster with Alzheimer's Disease: An Updated Meta-analysis. Current Alzheimer Research *14*, 335–344.